

Effect of TIG-dressing on fatigue strength and weld toe geometry of butt welded connections in high strength steel

Student:

S.H.J. van Es
sjorsvanes@hotmail.com
Student number: 1311255
March 2012

Graduation committee:

Prof. ir. F.S.K. Bijlaard
Dr. M.H. Kolstein
Dr. ir. R.J.M. Pijpers
Dr. ir. M.A.N. Hendriks
Ir. L.J.M. Houben

Structural Engineering, Delft University of Technology
Structural Engineering, Delft University of Technology
Structural Engineering, Delft University of Technology
Structural Mechanics, Delft University of Technology
Road and Railway Engineering, Delft University of Technology

Preface

During my bachelor thesis and my job as a student assistant I have experienced working in the Stevin II laboratory. When I needed to choose a subject for my master thesis, I quickly knew that I wanted experimental testing to be part of my project. After all, this may be the last chance to take part in experimental research with such depth and freedom of subject. My supervisor during my first two years as a student assistant was Richard Pijpers, who introduced me to his research of fatigue strength of welded connections in high strength steel. When there was an opportunity to perform a small experimental programme based on his larger database, this was a perfect chance for me to start my graduation thesis.

An experimental programme cannot be performed alone, so I would like to thank the laboratory staff: Arjen van Rhijn and John Hermsen who helped me preparing all specimens; Kees van Beek who programmed the software for the laser measurements and fatigue strength tests and finally Michele van Aggelen and Fred Schilperoort who have fixed many small problems I encountered in the laboratory.

Of course I also thank my exam committee for the guidance during my thesis: Prof. ir. Frans Bijlaard, Dr. Henk Kolstein, Dr. ir. Richard Pijpers and Dr. ir. Max Hendriks. The frequent meetings and the possibility to ask a quick question without appointment have been of great value.

Finally I would like to thank my girlfriend Greta and my parents for the support during this project.

Sjors van Es

March 2012

List of symbols and abbreviations

Latin symbols

a	crack length parameter	[mm]
a^*	material constant in notch stress approach	[mm]
a_i	initial crack size	[mm]
a_f	final crack size	[mm]
c	crack width parameters	[mm]
C_0	material constant in crack propagation calculation	[Nmm ^{-3/2}]
$d_{0,9}$	depth of $V_{0,9}$	[mm]
F	applied force	[kN]
$f_{lm;Ni}$	loading mode factor applicable to crack initiation life	[-]
$f_{lm;Np}$	loading mode factor applicable to crack propagation life	[-]
$f_{lm;Nf}$	loading mode factor applicable to total fatigue life	[-]
f_m	mean stress and residual stress factor	[-]
f_{mat}	material factor to determine fatigue limit of parent material	[-]
f_{Ni}	N_i/N_f	[-]
f_{Np}	N_p/N_f	[-]
$f_{t;Ni}$	thickness factor applicable to crack initiation life	[-]
$f_{t;Np}$	thickness factor applicable to crack propagation life	[-]
$f_{t;Nf}$	thickness factor applicable to total fatigue life	[-]
f_{uc}	influence factor for variation of undercut	[-]
f_{wh}	influence factor for variation of weld height	[-]
f_{θ}	influence factor for variation of weld toe angle	[-]
FAT-value	see $\Delta\sigma_c$	
h	weld height	[mm]
ΔK	range of stress intensity factor	[Nmm ^{-3/2}]
ΔK_{th}	threshold value of ΔK below which no crack propagation occurs	[Nmm ^{-3/2}]
K_f	fatigue notch factor	[-]
$K_{f,adj}$	increased value of fatigue notch factor after adjustment of the weld toe parameters in unfavourable direction	[-]
K_t	elastic stress concentration factor	[-]
$K_{t,adj}$	increased value of elastic stress concentration factor after adjustment of weld toe parameters in unfavourable direction	[-]
k_{hs}	stress concentration factor at hot spot	[-]
m	slope of S-N curve or material constant in crack propagation calculation	[-]
N	number of cycles	[-]
N_C	number of cycles at FAT-value	[-]
N_D	number of cycles at constant amplitude fatigue limit	[-]
N_i	number of cycles to crack initiation	[-]
N_{knee}	number of cycles at fatigue limit	[-]
N_L	number of cycles at cut-off limit	[-]
N_p	number of cycles during crack propagation	[-]
N_f	total number of cycles until failure	[-]
N_{up}	number of cycles at which the Basquin relation intersects with the yield line	[-]
P_s	probability of survival	[-]
R	stress ratio	[-]
R_{eh}	specified minimum yield strength	[N/mm ²]
$R_{0,2}$	specified offset yield strength at 0,2% strain after unloading	[N/mm ²]
R_m	ultimate tensile strength	[N/mm ²]
s	multiaxiality coefficient to determine fictitious notch radius	[-]
$V_{0,9}$	highly stressed volume	[mm ³]
w	width of highly stressed volume	[mm]
Y	compliance function in crack propagation calculation	[-]

Greek symbols

ε	strain	[-]
ρ	notch radius	[mm]

ρ_f	fictitious notch radius	[mm]
ρ^*	material constant to determine fictitious notch radius	[mm]
θ	weld toe angle; all angles are given in degrees	[-]
$\Delta\sigma$	stress range	[N/mm ²]
$\Delta\sigma_C$	stress range at FAT-value	[N/mm ²]
$\Delta\sigma_D$	stress range at constant amplitude fatigue limit	[N/mm ²]
$\Delta\sigma_L$	stress range at cut-off limit	[N/mm ²]
$\Delta\sigma_{\text{mean}}$	mean stress range	[N/mm ²]
$\Delta\sigma_{95\%}$	stress range with 95% survival probability	[N/mm ²]
$\sigma_{0,2\%}$	offset yield stress at 0,2% strain after unloading	[N/mm ²]
σ_a	stress amplitude	[N/mm ²]
$\sigma_{a;E}$	endurable stress amplitude in plain material	[N/mm ²]
$\sigma_{a;E;0}$	endurable stress amplitude in plain material at alternating load	[N/mm ²]
$\sigma_{E;\text{specimen}}$	endurable stress range in welded specimens	[N/mm ²]
σ_E	endurable stress range in plain material	[N/mm ²]
σ_f	stress below which infinite life is achieved	[N/mm ²]
σ_{hs}	stress at hot spot	[N/mm ²]
σ_{kaE}	endurable stress at the notch	[N/mm ²]
σ_m	mean stress	[N/mm ²]
σ_{nom}	nominal stress	[N/mm ²]
σ_{notch}	stress at notch root	[N/mm ²]
σ_r	residual stress	[N/mm ²]
σ_y	yield stress	[N/mm ²]
γ	safety factor	[-]

Abbreviations

AW	Indication that the value concerns as welded specimens
BM	Base material
FZ	Flusion zone or Fluid zone in case of TIG-dressing
HAZ	Heat affected zone
HSS	High strength steel
SG	Strain gauge
TIG	Indication that the value concerns TIG-dressed specimens (also: Tungsten Inert Gas)
UC	Undercut
VHSS	Very high strength steel
WT	Weld toe
WM	Weld material

Content

PREFACE	3
LIST OF SYMBOLS AND ABBREVIATIONS.....	5
CONTENT	7
1 INTRODUCTION, PROBLEM ANALYSIS AND OBJECTIVES	11
1.1 INTRODUCTION AND PROBLEM ANALYSIS	11
1.2 OBJECTIVES	11
2 INTRODUCTION IN HIGH STRENGTH STEEL, FATIGUE AND TIG DRESSING.....	13
2.1 CHAPTER OUTLINE	13
2.2 INTRODUCTION IN HIGH STRENGTH STEEL	13
2.2.1 <i>Material</i>	13
2.2.2 <i>Possibilities and limitations</i>	15
2.3 INTRODUCTION IN FATIGUE.....	16
2.3.1 <i>Definition</i>	16
2.3.2 <i>Parameters that influence the fatigue life</i>	16
2.3.3 <i>S-N curve</i>	19
2.3.4 <i>High strength steel and fatigue</i>	20
2.4 INTRODUCTION IN TIG-DRESSING	21
2.4.1 <i>Weld improvement techniques</i>	21
2.4.2 <i>TIG dressing process and influence on fatigue strength</i>	22
3 LITERATURE REVIEW: THEORY	23
3.1 INTRODUCTION AND CHAPTER OUTLINE.....	23
3.2 NOMINAL STRESS APPROACH	23
3.2.1 <i>Principles</i>	23
3.2.2 <i>Calculation procedure</i>	23
3.2.3 <i>Benefits, drawbacks and application</i>	24
3.3 STRUCTURAL STRESS APPROACH	25
3.3.1 <i>Principles</i>	25
3.3.2 <i>Calculation procedure</i>	25
3.3.3 <i>Benefits, drawbacks and application</i>	26
3.4 CRACK PROPAGATION APPROACH.....	27
3.4.1 <i>Principles</i>	27
3.4.2 <i>Calculation procedure</i>	29
3.4.3 <i>Benefits, drawbacks and application</i>	29
3.5 NOTCH STRESS APPROACH.....	29
3.5.1 <i>Principles</i>	29
3.5.2 <i>Calculation procedure</i>	36
3.5.3 <i>Benefits, drawbacks and application</i>	36
4 LITERATURE REVIEW: PRACTICE.....	37
4.1 CHAPTER OUTLINE	37
4.2 LITERATURE REGARDING FATIGUE AND HIGH STRENGTH STEEL.....	37
4.2.1 <i>Strength according to current design codes and recommendations</i>	37
4.2.2 <i>Behaviour of plain material</i>	37
4.2.3 <i>Behaviour of non-plain material</i>	38
4.3 LITERATURE REGARDING TIG-DRESSING AND HIGH STRENGTH STEEL	41
4.3.1 <i>TIG dressing process</i>	41
4.3.2 <i>Strength improvement according to current design codes and recommendations</i>	41
4.3.3 <i>Influences of TIG-dressing on material and geometry</i>	43
4.3.4 <i>Influences of TIG dressing on fatigue strength</i>	46

5 TEST SETUP.....	49
5.1 CHAPTER OUTLINE	49
5.2 TESTING PROGRAMME	49
5.2.1 Identification of test specimens	49
5.2.2 Preparation of specimens	49
5.3 TEST SETUP.....	50
5.3.1 Measurement of weld geometry.....	50
5.3.2 Measurement of fatigue life	51
5.3.3 Measurement of material hardness.....	52
6 PROCESSING AND RESULTS OF LASER MEASUREMENTS	53
6.1 CHAPTER OUTLINE	53
6.2 TEST OUTPUT AND PROCESSING LASER MEASUREMENTS.....	53
6.2.1 Test output.....	53
6.2.2 Determining the weld radius.....	55
6.2.3 Determining the weld toe angle, weld height and undercut.....	59
6.3 RESULTS	59
6.3.1 Observed geometries	59
6.3.2 Comparison between rolled and cast steel	60
6.3.3 Comparison between different steel grades	67
6.3.4 Distribution of weld geometry parameters.....	67
6.3.5 Evaluation of influence of TIG-dressing.....	72
7 PROCESSING AND RESULTS OF FATIGUE TESTS AND HARDNESS MEASUREMENTS.....	73
7.1 CHAPTER OUTLINE	73
7.2 TEST OUTPUT AND PROCESSING	73
7.2.1 Test output.....	73
7.2.2 Determining N_b , nominal stress and stress ratio.....	74
7.3 RESULTS OF FATIGUE TESTS	74
7.4 RESULTS OF HARDNESS MEASUREMENTS.....	76
7.5 RESULTS OF CRACK MONITORING	76
8 ANALYTICAL DETERMINATION OF FATIGUE STRENGTH.....	77
8.1 INTRODUCTION AND CHAPTER OUTLINE	77
8.2 FACTORS DETERMINING FATIGUE STRENGTH	77
8.3 DETERMINATION OF STRESS CONCENTRATION FACTOR AND FATIGUE NOTCH FACTOR	77
8.3.1 FEM analysis of weld toe.....	78
8.3.2 Determination of K_t	84
8.3.3 Determination of K_f	88
8.4 DETERMINATION OF MEAN STRESS FACTOR	91
8.5 DETERMINATION OF THICKNESS FACTOR	92
8.6 DETERMINATION OF LOADING MODE FACTOR	92
8.7 PREDICTION OF FATIGUE STRENGTH CURVE	92
9 ANALYSIS OF FATIGUE TEST RESULTS.....	93
9.1 CHAPTER OUTLINE	93
9.2 ANALYSIS OF RAW DATA	93
9.2.1 Exclusion of data	93
9.2.2 Adjustment of test data	95
9.2.3 Statistical analysis.....	97
9.3 FITTED S-N CURVES	99
9.3.1 Raw data.....	99
9.3.2 Adjusted data.....	100
9.3.3 Discussion	102
9.4 COMPARISON	102
9.4.1 Comparison of data with design codes	102
9.4.2 Comparison of data with as welded fatigue tests.....	106
9.4.3 Comparison of data with analytical determination of fatigue strength.....	115
9.5 EVALUATION OF TIG-DRESSING INFLUENCE	124

10 CONCLUSIONS AND RECOMMENDATIONS	125
10.1 CONCLUSIONS.....	125
10.1.1 <i>Influence of TIG-dressing of fatigue strength of butt welded specimens.....</i>	<i>125</i>
10.1.2 <i>Influence of TIG-dressing on weld geometry of butt welded specimens.....</i>	<i>125</i>
10.1.3 <i>Theoretical influence of changed weld geometry on behaviour of TIG-dressed specimens.....</i>	<i>126</i>
10.2 EVALUATION AND RECOMMENDATIONS.....	126
10.2.1 <i>Assumptions and approximations</i>	<i>126</i>
10.2.2 <i>Recommendations for further research.....</i>	<i>126</i>
ANNEX A : REFERENCES	129
ANNEX B : TEST SPECIMENS.....	131
ANNEX C : FATIGUE TEST DATA.....	133
ANNEX D : MATERIAL CERTIFICATES	135
ANNEX E : PRODUCTION DATA SHEETS TIG DRESSING	167
ANNEX F : MATLAB SCRIPTS TO PROCESS WELD GEOMETRY DATA	177
ANNEX G : COLLABORATION WITH TNO: ACOUSTIC EMISSION	183
ANNEX H : HARDNESS MEASUREMENTS	185
ANNEX I : CRACK MONITORING RESULTS.....	205
ANNEX J : DIANA MODEL.....	211

1 Introduction, problem analysis and objectives

1.1 Introduction and problem analysis

In most design codes and in common engineering practice, the fatigue strength of welded high strength steel structures is assumed to be comparable with the fatigue strength of mild steel structures.

It is shown in literature (Maddox, 1991; Gurney, 1979) that perfect smooth specimens of high strength steel perform better in fatigue tests than their mild steel counterparts. However, as soon as discontinuities, notches, surface roughness and all other imperfections that are unavoidable in practice are taken into account, the advantage of high strength steel quickly diminishes.

To recover some of the advantages of high strength steel, several options can be used. The combination of welds and other geometrical stress raisers can be omitted by design (for example by using cast steel nodes in trusses). Another possibility, which can also be combined with the aforementioned solution, is a weld improvement. Weld improvements are procedures executed after welding to improve the fatigue behaviour of the weld area by reducing tensile residual stresses, improving geometry, removing weld flaws and inclusions or a combination of these improvements. This research will focus on a weld improvement method called TIG dressing, in which the weld toe is remelted to provide a smoother weld profile. The procedure of TIG dressing has proven on fillet welds to be beneficial for both low strength and high strength steels in earlier research, but this effect is not always taken into account in current design codes and recommendations.

This research will compare TIG-dressed specimens with similar as welded specimens from the same material batches and will attempt to explain differences in fatigue strength, based mainly on geometry changes.

1.2 Objectives

The objectives of this study are:

- Determine the fatigue strength of TIG dressing on various high strength steel butt welded specimens in relation to the fatigue strength of similar, as welded specimens
- Describe the change of weld toe geometry due to the TIG dressing process on different high strength steel butt welded specimens
- Relate the alleged improved fatigue strength by TIG dressing to the changed geometry by means of a theoretical analysis

To accomplish these objectives, a method needs to be found to accurately measure and describe the weld profile in a consistent way. Furthermore fatigue tests will be executed on material from the same production batches as used in an earlier research by Pijpers (2011). From this research, fatigue data and adjustment factors for various geometrical and loading parameters will be used. To gain insight into the current state of knowledge and a theoretical background to couple the weld geometry to fatigue strength, this study will start with a literature research into fatigue, high strength steel and TIG-dressing.

2 Introduction in high strength steel, fatigue and TIG dressing

2.1 Chapter outline

This chapter gives a general introduction in high strength steel, its production processes, possibilities and limitations. Then a general introduction in fatigue is given, where the influencing factors of the fatigue process are discussed. The material and the process of fatigue are then combined. Finally a short explanation of the TIG-dressing process is given and its effects on the material and fatigue behaviour.

2.2 Introduction in high strength steel

2.2.1 Material

High strength steels are steels with a higher yield and tensile strength than the most commonly used steels. In current practice in Europe, the steel grades S235 and S355 are most commonly used for mild steel structures. These steel grades have a yield strength of at least 235 and 355 N/mm², respectively. High strength steels have a specified minimum yield strength (R_{eh}) higher than 355 N/mm². Common high strength steels (HSS) range from S355 to S690. Higher strength steels are referred to as very high strength steels (VHSS). Again the steel grade refers to a specified minimum strength, but because higher strength steels do not always show a clear yield point, the specified 'yield' strength is the stress at which after unloading a permanent deformation of 0.2% remains ($R_{0.2}$) (see figure 2.1).

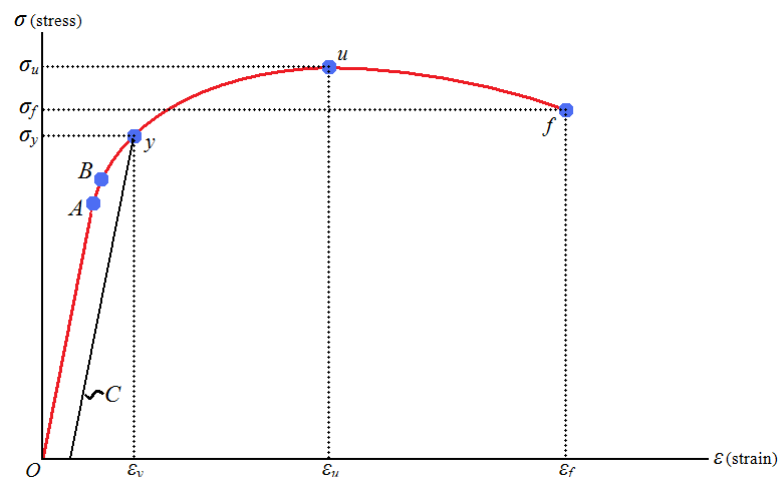


figure 2.1 Stress strain relationship for a high strength steel; A is the proportionality limit, B the elastic limit, y the yield point. Line C is used to determine the point where a permanent deformation of 0.2% remains: the specified 'yield' point. (source: Engineering Archives, 2008)

High strength steels can be manufactured in different ways. The most common high strength steels are normalized steel, thermomechanically rolled steel and quenched and tempered steel. All these manufacturing processes are focused on grain size reduction, which has a beneficial influence on the strength. Normalized steel and thermomechanically rolled steel are available in moderate high strengths (up to S460). Quenched and tempered steel is available in higher strengths (VM publication 125, 2008).

The different treatments have their influence on the microstructure of the material. The microstructure of steel depends, among other things, on the carbon content, temperature and cooling rate. In figure 2.2 the iron-carbon diagram is shown. The three important phases are liquid (L), ferrite (α) and austenite (γ). Other forms are cementite (Fe_3C) and pearlite ($\alpha+Fe_3C$). Austenite is formed above the transition temperature (for most carbon contents 723° C) and will transfer back to ferrite when cooled down. The possible excess of carbon, which is almost always the case when carbon is present, causes cementite to be formed. However, when the steel is cooled down fast, the austenite will change to ferrite oversaturated with carbon. This structure, called martensite, has a hard, crystalline and brittle structure with limited ductility. For this reason, steel consisting of martensite should be checked for sufficient ductility. As martensite is not an equilibrium phase, it is not visible in the iron-carbon diagram. Another possible crystalline structure is bainite. Bainite is created when austenite

is cooled quickly, but not so quickly that martensite forms. Bainite consists of ferrite with a lot of dislocations combined with cementite. The dislocations make the ferrite harder than ordinary ferrite.

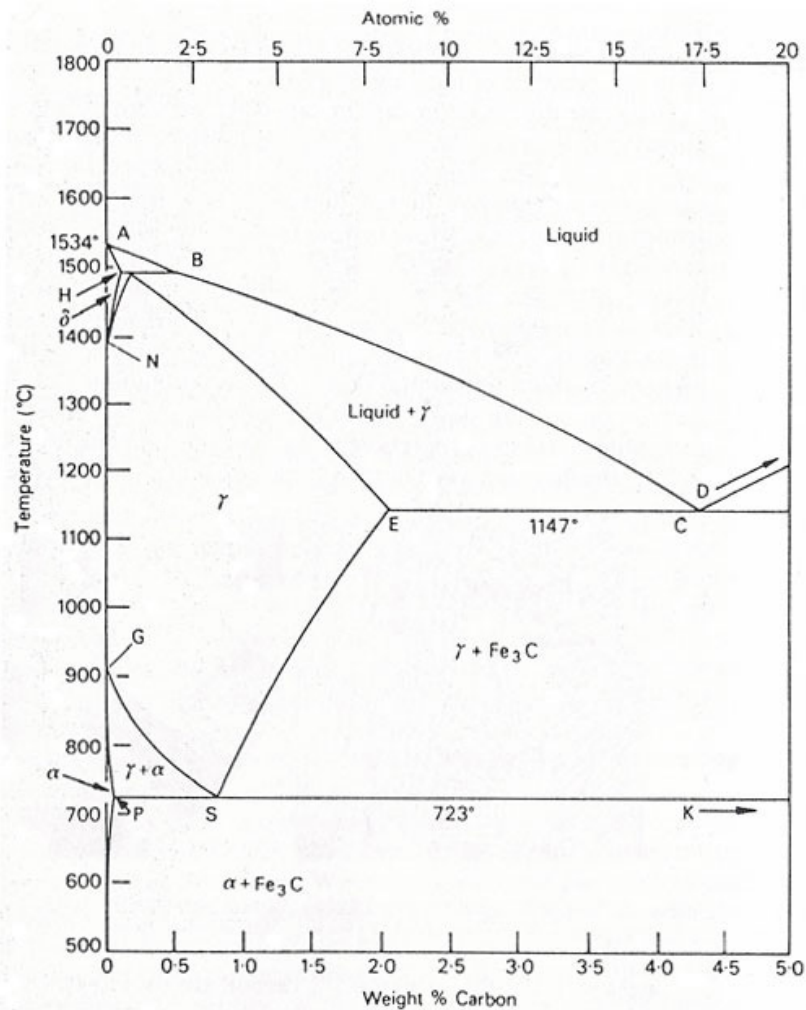


figure 2.2 The iron-carbon diagram (source: KEYtoMETALS.com)

Normalized steel mainly gains its strength by alloyed elements. The toughness of the steel is kept within boundaries by the normalizing treatment, but the treatment also raises the strength to a certain extent, especially the ultimate tensile strength. To normalize the steel it is heated to about 920° and then cooled by air.

Thermomechanically rolled steel has a low content of alloying elements and mainly gains its strength by grain size reduction. This is achieved by controlling and limiting the temperature during the end stages of the rolling. The relatively low temperature during the final deformation of the components requires rather strong rolling equipment. When the material is processed further, heating beyond the transition temperature is not allowed to prevent loss of strength.

Quenched and tempered steel is quickly cooled down to achieve high strength. This produces a very strong, very hard and very brittle material. To reduce hardness and restore ductility the material is reheated to a temperature below the transition temperature. The energy for reheating can also be supplied by the core of thicker materials when only the perimeters are quenched. This is called quenched self-tempered steel.

The three production methods each leave a characteristic microstructure. Normalized steel consist of fine grained ferrite and pearlite. Thermomechanically rolled steel starts with long austenite grains caused by the rolling processes. When cooled down a very fine grained ferrite structure is created. The microstructure of quenched and tempered steels mainly shows bainite and martensite in a crystalline structure. The different microstructures are depicted in figure 2.3.



figure 2.3 From left to right; microstructures of normalized S460, thermomechanically rolled S460 and quenched and tempered S1100 (source: VM publication 125, 2008)

2.2.2 Possibilities and limitations

Possibilities

High strength steel offers designers certain advantages, but it also has some drawbacks. The first advantage of high strength steel is directly related to its high strength: less material is needed to resist a certain force. Structures made of high strength steel can therefore be made lighter than their conventional counterparts. This is especially beneficial in movable structures, for example a movable bridge or mobile crane. Also most offshore structures benefit from this, because the transport to the building site on barges is an important part of the design. The second advantage is related to welded connections. In general, high strength steel structures have smaller plate thicknesses. Because the volume of added weld material increases quadratic with increasing thickness of the plates to be connected, a significant cost reduction could be made here, especially in western countries where wages are high.

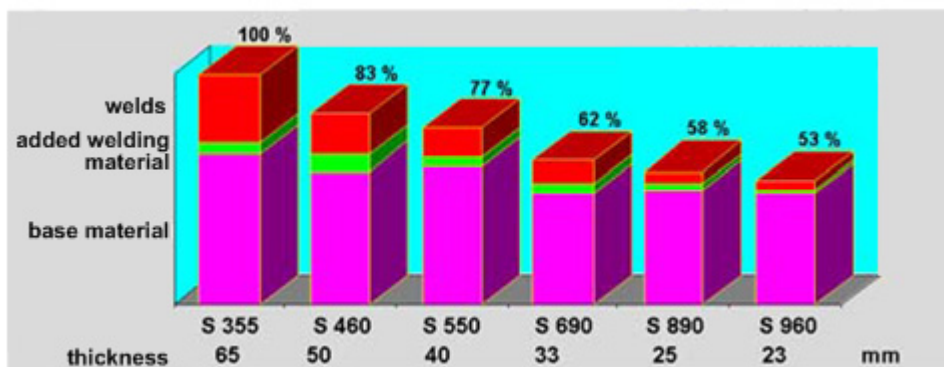


figure 2.4 Schematic view of the economic advantages of high strength steel (source: VM publication 125, 2008)

Limitations

A large disadvantage of high strength steel is the material cost and availability. Conventional mild steels are more readily available and more easily produced and are therefore cheaper. High strength steels that are available, are mostly only available as plate material and not as profiles. This disadvantage may be outweighed by the reduction of welding costs and transportation costs. Another aspect of high strength steel is the fact that the Young's modulus does not increase with increasing strength. For simple beam structures, high strength steel will therefore more easily reach the deformation limits set by the design code or dictated by secondary structures, such as internal walls and windows, than conventional steel structures. Structures that are stiff by their nature, such as truss structures, can overcome this problem. For the same reason, stability of high strength steel structures and components always needs attention. For columns, high strength steel therefore is only beneficial with highly loaded columns with relatively short buckling lengths, for example in high rise buildings. In beam structures, a high strength steel girder will probably not be a class 4 cross section. In tensile elements stability problems obviously cannot occur and therefore they can be very slender, with the exception of the area in which connections are made.

A bolted connection can cause problems, because the yield strength (or 0.2% proof stress) is much closer to the tensile strength than it is for ordinary steels. The reduction of this ratio with increasing strength is visible in figure 2.5. The allowable cross section reduction by holes is therefore limited. In general, all high strength steel structures and details should be checked for sufficient deformation capacity because of the lower ultimate strain of higher strength steels (see figure 2.5). Welded connections are possible in high strength steel, but current welding materials are limited to an ultimate strength of 900 N/mm². For steel grades higher than S890 this will have consequences for the welded connections.

Finally, the fatigue behaviour of high strength steel structures is commonly regarded as the same as for standard steel structures. While a plain, polished specimen does show increasing fatigue strength with increasing yield strength, the addition of surface roughness, imperfections, notches and residuals stresses, all caused by production or welding, severely

reduce the fatigue strength of real structures and limits it to a level comparable with the fatigue strength of mild steels. This will be elaborated on in paragraph 2.3.4.

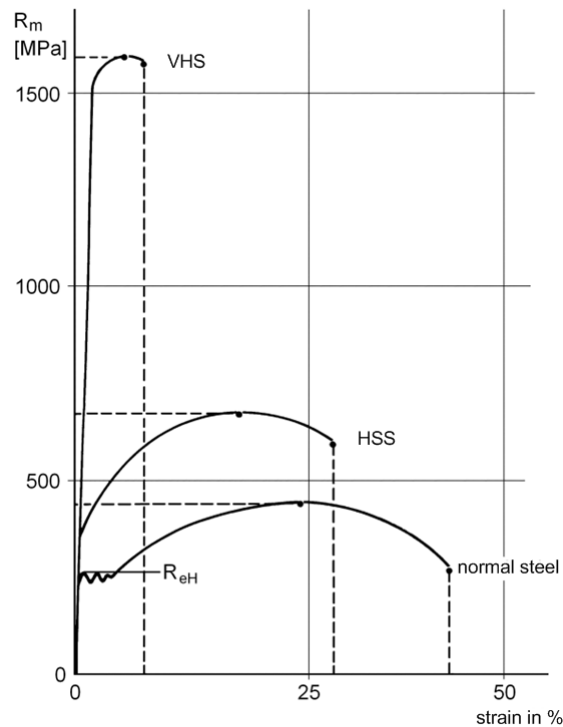


figure 2.5 Overview of material behaviour of steel with increasing strength (source: VM publication 125, 2008)

2.3 Introduction in fatigue

2.3.1 Definition

Fatigue can be defined as the mechanism whereby cracks grow in a structure (ESDEP). These cracks grow under fluctuating stresses, generated by fluctuating loads. Failure of a fatigue loaded structure occurs when the crack has reduced the cross section by such an amount, that the remaining cross section cannot carry the applied tensile loads.

Fatigue can occur after a relatively low amount of cycles to very large numbers of cycles. In general, fatigue can be divided into low cycle fatigue, medium cycle fatigue and high cycle fatigue. Exact boundaries between these three regimes are not apparent. Eurocode limits its use for applications with more than 10^4 cycles, which could be seen as a suitable boundary between low cycle and medium cycle fatigue.

2.3.2 Parameters that influence the fatigue life

In fatigue, a number of parameters are important, primarily regarding the stresses in the material (see figure 2.6):

N = the number of cycles

$\Delta\sigma$ = the stress range. The stress range is defined as the maximum stress minus the minimum stress

σ_m = the mean stress

σ_a = the stress amplitude (half of the stress range)

R = the stress ratio: $R = \frac{\sigma_{\min}}{\sigma_{\max}}$

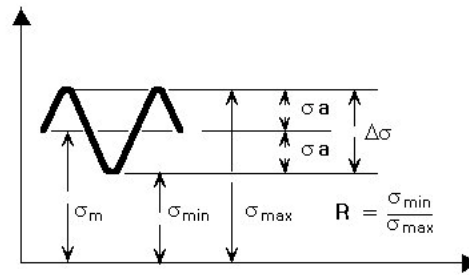


figure 2.6 Description of a fluctuating stress (source: ESDEP)

The mean stress influences the fatigue strength of the material. When the mean tensile stress increases, the fatigue capacity decreases. This has been derived by different authors, all showing roughly the same behaviour, see figure 2.7. When the static strength of steel increases, a higher mean stress in fatigue conditions can be endured. However, the sensitivity to the mean stress increases with increasing static strength (Haibach, 2006), resulting in a steeper line in figure 2.7.

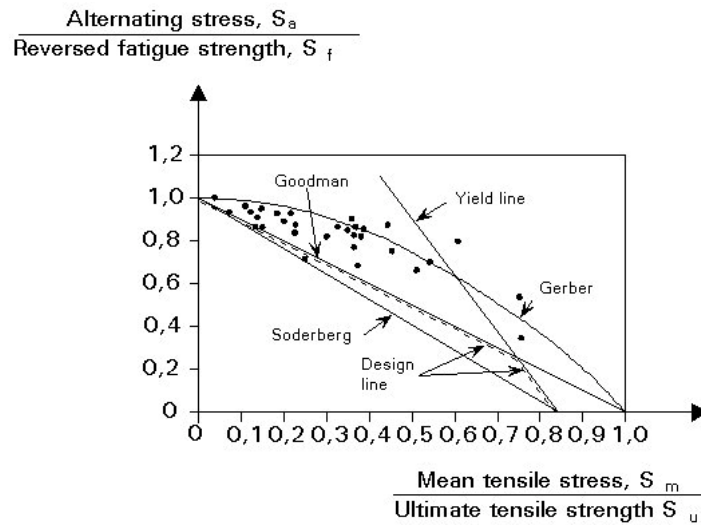


figure 2.7 Mean stress effect shown in a Haigh diagram (source: ESDEP)

In principle, compressive stresses prevent cracks from opening, and therefore growing. Therefore, compressive stresses in theory increase the fatigue life of components. However, in most structures residual tensile stresses are present as a result of production and welding. This means that cracks in areas of the structure that are nominally under constant compression can still show crack growth. Therefore the mean stress effect is not always present in actual structures. For welded structures the residual stresses can be in the order of the yield limit, which severely reduces the fatigue strength. This is closely related to the mean stress effect, because a crack cannot distinguish a residual stress from a mean stress, and is called residual stress effect.

Besides the stress also the geometry of the material has a large influence on the fatigue strength. Fatigue cracks start at small defects in the material. These defects, called notches, can occur at the surface of the material due to roughness, inclusions or surface defects, at large discontinuities such as bolt holes or at small discontinuities, for example near the weld. At these notches the stress is concentrated, thereby increasing the chance of a fatigue crack occurring in that area. This is known as the notch effect.

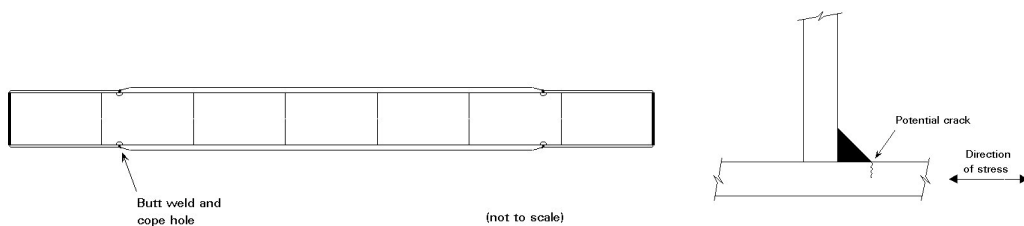


figure 2.8 Examples of discontinuities where cracks can occur; on the left a large discontinuity: a cope hole' on the right, on smaller scale, a small discontinuity: a weld (source: ESDEP)

Corrosion at these discontinuities can further decrease the fatigue strength. Also in plain specimens there is a clear influence of corrosion on the fatigue strength, see figure 2.9.

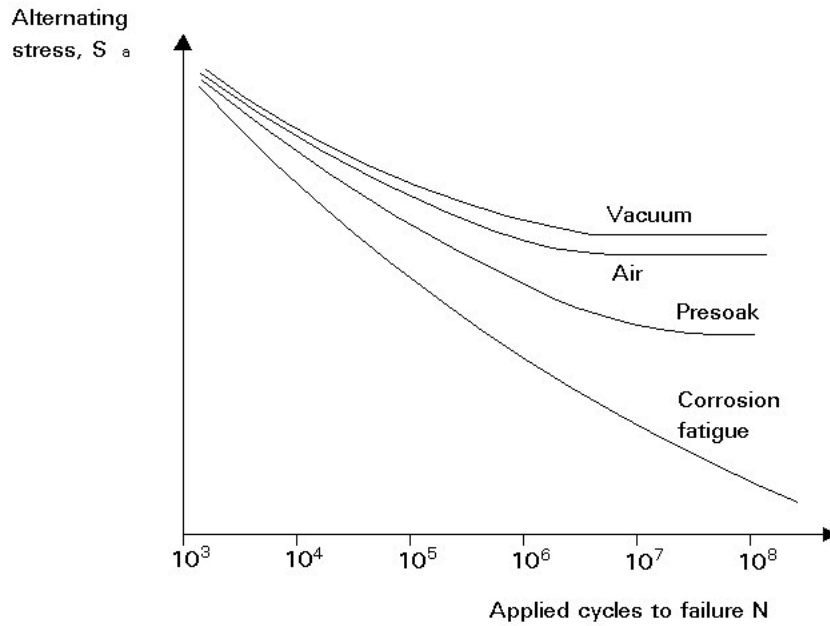


figure 2.9 Influence of corrosive environments on the fatigue strength of materials (source: ESDEP)

The size of the specimen also influences the fatigue strength. When the size of a specimen increases, the fatigue strength drops. The total strength of the component may increase, but the allowable stress decreases. This is known as the size effect, and is caused by (ESDEP):

- A statistical effect. When the size of a component increases, the chance of a 'weak link', in the form of a notch, small inclusion or residual stress, increases. Therefore also the chance of an initiating crack increases.
- A technological size effect. The production processes and their associated surface conditions upon delivery have an influence on the fatigue strength of a component.
- A geometrical size effect. When the thickness of a plate increases the stress gradient at a notch (in figure 2.10 a weld) decreases. When the inclusions or surface defects have the same size as they have in a thinner plate, the stresses at the tip of the defect are higher in the case of a thick plate (see figure 2.10).
- A stress increase effect. When the plate thickness increases, the notch size in general does not scale up to the same amount, or may not scale up at all.

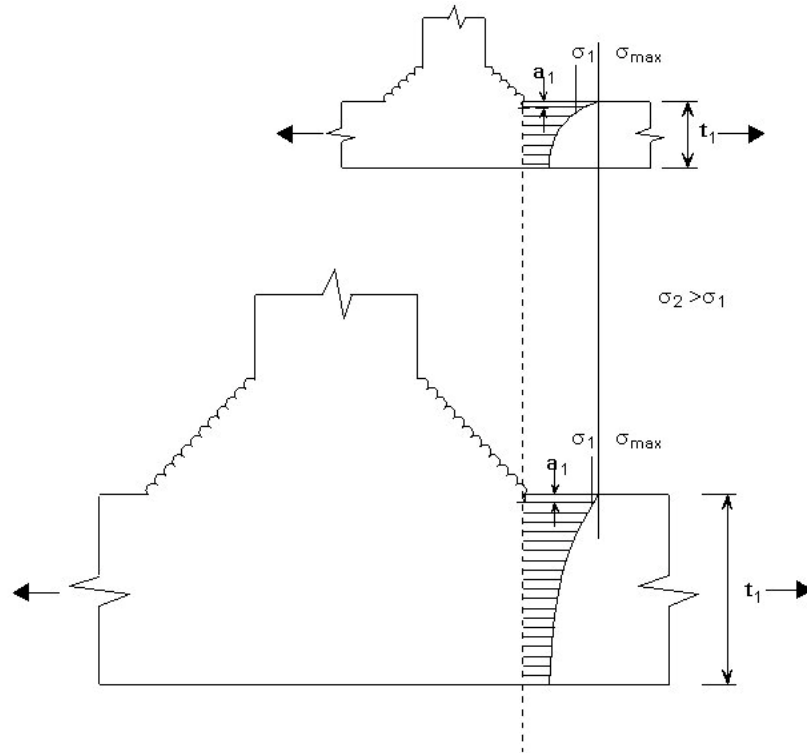


figure 2.10 Influence of the plate thickness on the fatigue strength (source: ESDEP)

Finally there is the effect of the material strength. When the material size increases the fatigue strength of the plain material also increases. However, when a crack occurs, the crack growth rate in all steels is roughly the same. This means that once a crack is initiated, all steels have a similar lifetime until failure when exposed to the same stress. Therefore high strength steels can only show a longer fatigue life if the material can longer resist crack initiation, this will be further elaborated on in 3.4. Because in actual structures plain steel always needs a connection, there will always be notches, stress raisers and, in the case of welding, inclusions present, which severely reduce the crack initiation life. Therefore, in current design codes, high strength steel structures mostly are regarded to have a fatigue strength comparable with standard steel structures. This subject is studied further in 2.3.4 and 4.2.

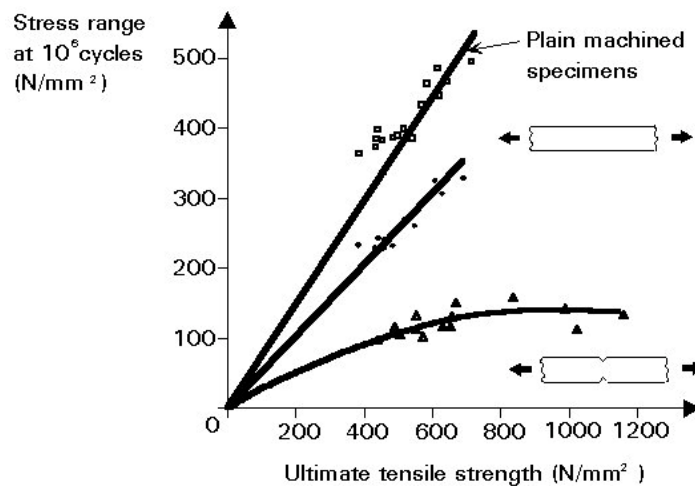


figure 2.11 Material strength effect. Plain machined specimens show a clear increase in fatigue strength when the material strength increases. At the same time it is clear that this increase is not entirely visible for notched specimens (source: ESDEP)

2.3.3 S-N curve

The S-N curve is the relation between a stress range ($\Delta\sigma$) or stress amplitude (σ_a) and the accompanying number of cycles to failure. S-N curve can be defined for plain material, simple details such as a welded plate or entire connections.

The S-N curves generally follow the form of Basquin's relation:

$$\sigma_a \cdot N^b = \text{constant} \quad (1.1)$$

Mostly both the horizontal axis and the vertical axis are shown in log-scale. Nowadays, most S-N curves are described by the formula:

$$\log N = \log a - m \cdot \log \Delta \sigma \quad (1.2)$$

The parameters a and m (equivalent to b in equation (1.1)) are determined based on tests or calculations. The parameters can for example depend on material, detail, post-weld treatments and weld quality guaranteed by certain inspection methods. As mentioned before, the material strength is regarded as unimportant in most design codes. A common example of an S-N curve is shown in figure 2.12. For loading with a constant amplitude the slope of the S-N curve (m) is 3 and below a certain stress level no damage occurs, this is shown in figure 2.12 as the constant amplitude fatigue limit. If the amplitude of the loading varies, there can be damage below this limit. The slope of the S-N curve changes and again, at a certain stress level no damage occurs, even in the case of variable amplitude loading. This limit is known as the cut-off limit. These characteristic points in the S-N curve are denoted with the symbols N_D for the constant amplitude fatigue limit and N_L for the cut-off limit with their accompanying stresses $\Delta\sigma_D$ and $\Delta\sigma_L$. The third characteristic point in the curve, denoted with N_C and $\Delta\sigma_C$ is the point that marks the detail category. Detail categories will be further explained chapter 3.2.

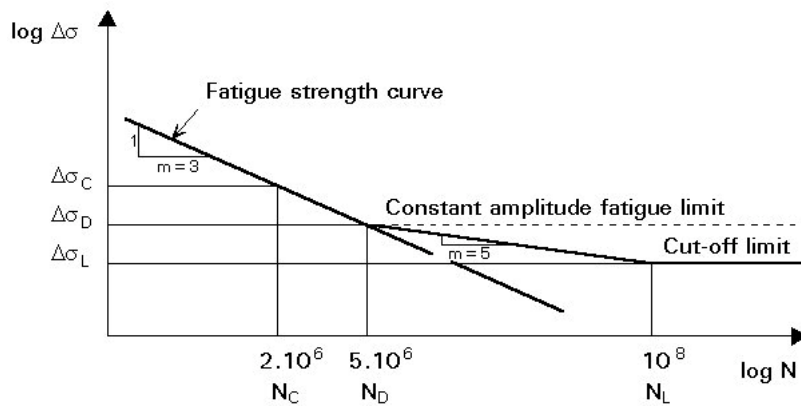


figure 2.12 An S-N curve (source ESDEP)

2.3.4 High strength steel and fatigue

Higher strength steels generally also have higher fatigue resistance. However, according to Pijpers (2011) this mainly affects the crack initiation period (N_i). After a crack has initiated, the crack growth rate is the same as for ordinary steels (see 3.4). Local notches in welded joints (see paragraph 2.3.2) effectively reduce the crack initiation time to a number of cycles which is negligible (ESDEP). Therefore, in conventional welded structures, where initial imperfections are always present, the material strength is of little influence on the fatigue strength. This effect is shown in figure 2.11. At very low (non practical) strength there is a clear influence of the material strength on notched specimens, but at the strength level of standard strength steels ($R_m > 400 \text{ N/mm}^2$) and high strength steels there is almost no influence of the material strength anymore.

Because of the effect shown in figure 2.11, most design codes do not distinguish standard steel from high strength steel when regarding fatigue and if an improvement is made, the code only shows improvements in the lower strength steels up to a certain steel grade. Above this steel grade (e.g. S355 in NPR-CEN/TS 13001-3-1) the fatigue performance of all materials is regarded to be the same.

Structures that can benefit greatly from the advantages of high strength steel (less material and therefore light; less welding) may also be loaded in fatigue. Examples of these structures are cranes, off-shore platforms and movable bridges. Because the cross sections of high strength steel are reduced in comparison with their standard steel counterparts, the stress range ($\Delta\sigma$) is much larger in the high strength steel structure. If the fatigue strength of a high strength steel structure is indeed not much different than from a standard steel structure, fatigue is potentially leading in the design of dynamically loaded structures.

To make full use of the high strength steels several options are available. The details of the structure can be adjusted to provide a smoother stress flow, thereby reducing stress concentrations. This geometrical improvement can be done on a small scale, for example by using tapered plates instead of butt-welding two plates together with different thicknesses. A geometrical improvement can also be used on a larger scale: adjust the design of the structure for fatigue. A good example of this approach is the use of cast steel nodes in trusses, by which the fatigue sensitive welds are removed from the highly stressed connection area (see figure 2.13). Another way to reduce the effective stresses is reducing the tensile residual stresses in a welded structure. This is not always possible, and the effect depends on the stress ratio and mean stress. A similar effect is reached if the mean stress caused by loading is less tensile, for example by lowering the self weight of the

structure. Finally, the specimens can be treated in such a way after fabrication that surface defects and microcracks are removed. This will increase the crack initiation time, and thereby the total fatigue life.



figure 2.13 A truss with cast steel nodes (source: Pijpers et al., 2010)

2.4 Introduction in TIG-dressing

2.4.1 Weld improvement techniques

In figure 2.11 it is clear that for plain specimens the fatigue strength increases with increasing material strength. However, if notches are introduced a strength plateau can be observed, which limits the fatigue strength for steels with an ultimate strength higher than approximately 400 N/mm^2 . These notches can be introduced by holes or changes in cross sections, but are, in civil engineering structures, mostly caused by welding. Welds have a very rough surface, caused by the nature of the process. Another drawback of the process is the possibility of small defects in the weld. These imperfections might have no or a small influence on static strength, but in fatigue loading they may form the one weak link that is needed to initiate a crack. Also, the weld itself causes a cross section change due to local thickening or the steep angle of a fillet weld. In addition, these welds are in general positioned at locations which suffer from stress concentrations due to global geometry of the structure. The notch effect is therefore very prominent in welded structures.

To reduce the strength reducing effects of the weld a number of weld improvement techniques can be used. The most important techniques are (Haagensen et al., 2001):

- Burr grinding
- Hammer peening
- Needle peening
- TIG dressing

Burr grinding

The aim of burr grinding is to remove possible weld flaws at the weld toe where fatigue cracks can initiate, by removing material with a high speed grinder. The stress concentration at the weld toe, caused by the sharp geometrical transition from parent material to weld material is reduced by smoothing the weld profile.

Hammer peening

The aim of hammer peening is to introduce compressive stresses in the weld toe region by repeatedly hammering this area with a pneumatic blunt-nosed chisel. The effect of the hammer peening process relies on the mean stress effect (see 2.3.2). Another beneficial effect may be the smoothing of the weld toe profile.

Needle peening

The aim of needle peening is also the introduction of compressive stresses in the weld toe region. In this case the single chisel is replaced by multiple, smaller chisels. This makes the process more suitable for larger areas to be treated. The effects of hammer peening and needle peening, and their aims in fatigue strength improvement are comparable.

TIG dressing

The aim of TIG dressing is to remove possible weld flaws by remelting the material at the weld toe. The remelting should also have a beneficial effect on stress concentrations because the weld geometry is made smoother. Although the process is carried out with welding equipment, no extra material is added. The melting of steel of course causes changes in the stress state of the material. If high residual stresses exist at the surface, they will be reduced to a certain extent (see 4.3.3). Also the heat affected zone will be enlarged. The effect of TIG-dressing will be discussed further in 2.4.2.

More information on all these processes can be found in the IIW recommendations on weld improvement techniques (Haagensen et al., 2001). Because in this study the focus lies on TIG dressing, the influence of this process on the material and geometry is explained more thoroughly in the next paragraph.

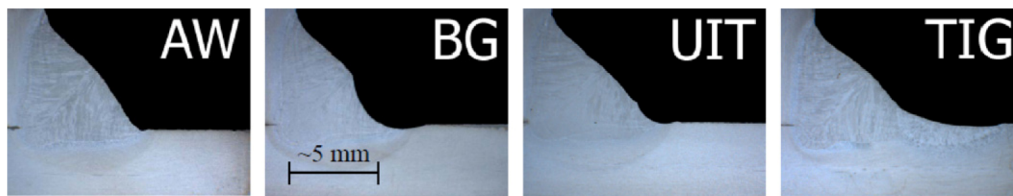


figure 2.14 Effect of different weld improvement techniques: as welded, burr grinding, ultrasonic impact treatment (comparable to the effects of hammer and needle peening) and TIG dressed (source Pedersen et al., 2010)

2.4.2 TIG dressing process and influence on fatigue strength

TIG dressing involves remelting of the material, which means that the original geometry of the weld toe is altered into a new geometry. It also means that any defects in the weld toe may be removed. To prevent the new weld toe from having the same imperfections and sharp geometry, some precautions must be taken.

The weld that is to be TIG dressed needs to be prepared by removing any mill scale, rust, oil, paint or any other possible weld contaminant. This can be done by wire brushing, but light grinding might also be necessary. If the cleaning process is not sufficient, gas inclusions in the weld can be the result, which severely lower the fatigue performance of the weld.

To guarantee the new geometry to be better than the original, a number of conditions must be met. The heat input must not be too high to prevent undercuts. To optimize the overall shape of the new weld toe the TIG torch must be positioned carefully. In IIW recommendations, the torch distance to the weld toe, angle of the torch in two directions and travel speed in combination with the welding current are specified (Haagensen et al., 2001).

TIG-dressing improves the weld toe in principle by improving the geometry and removing weld toe flaws. The smoothing of the geometry reduces the stress peak near the weld toe. This lower stress peak also has fewer flaws at which to cause a fatigue crack. A secondary benefit of TIG dressing may be the release of high tensile residual stresses caused by welding. These influences all mostly influence crack initiation time. Because crack initiation time is very important when high strength steel is considered (see 2.3.4) the beneficial effect of TIG dressing may be expected to be larger for high strength steel welded connections. This effect clearly shows when some previous research is studied where improvements of fatigue strength varying from 18% to 85% are found, even within the same research programme. This will be elaborated on in 4.3.4.

3 Literature review: Theory

3.1 Introduction and chapter outline

In all fatigue tests a wide scatter range is found because of the 'weakest link' process. A crack initiates at a location where global geometry, local geometry, surface defects, material defects and stress all combine to a worst case scenario. All these influences cannot exactly be modeled, because of the random nature of welding.

A number of different calculation models have been developed to calculate the fatigue strength of a component. The most common theories, nominal stress approach, structural stress approach and crack propagation approach, will be covered first. Subsequently, more in depth analyses will be treated, which is specifically used in this research.

3.2 Nominal stress approach

3.2.1 Principles

The nominal stress approach classifies a wide range of widely used details and specifies their fatigue strength at a certain number of cycles. In Eurocode 3 the fatigue strength of details is determined at $2 \cdot 10^6$ cycles. All S-N curves are parallel to each other, therefore only the fatigue strength at $2 \cdot 10^6$ cycles is needed to determine the S-N curve (see figure 3.1), which defines the allowable stress range at any number of cycles. The lines given in the code are design lines, which result in a sufficiently safe structure.

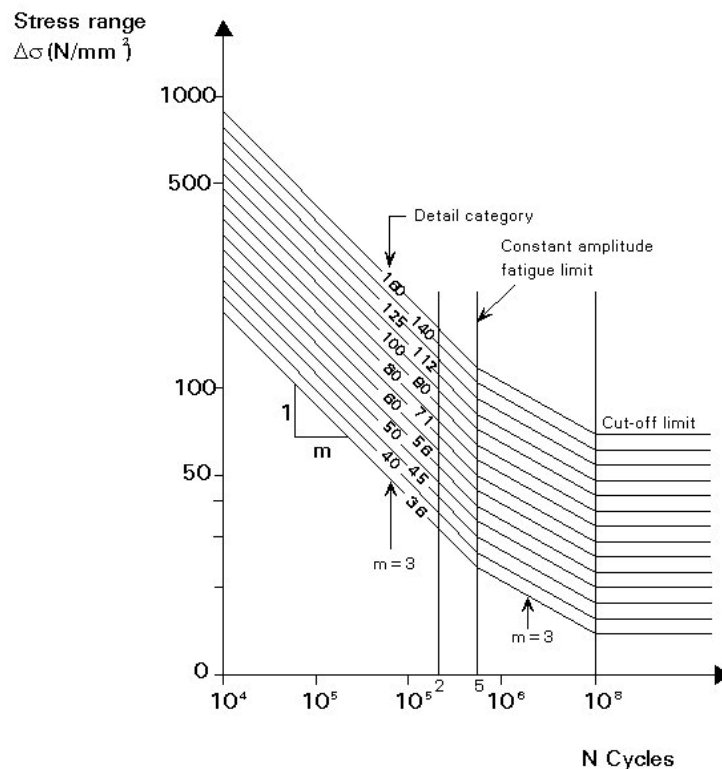


figure 3.1 A number of S-N curves belonging to different detail categories (source: ESDEP)

3.2.2 Calculation procedure

To design a structure, all stresses need to be determined and all details, welds and other discontinuities have to be classified in a certain detail category. Detail categories can depend for example on local geometry, weld type, weld quality, post weld treatments and define the maximum allowable stress at $2 \cdot 10^6$ cycles (see figure 3.2). Then for each detail the allowable number of cycles at the calculated stress level can be determined, by means of the standardized S-N curves as shown in figure 3.1. Possible misalignments and thickness effects have to be taken into account separately. This allowable number of cycles can then be compared with the needed number of cycles in the structures lifetime. A few examples of the

detail categories are shown in figure 3.2. The explained procedure is valid for normal stresses. Shear stresses can be taken into account with a similar procedure.

Detail category	Constructional detail	Description	Requirements
112	<p>1) Transverse splices in plates and flats. 2) Flange and web splices in plate girders before assembly. 3) Full cross-section butt welds of rolled sections without cope holes. 4) Transverse splices in plates or flats tapered in width or in thickness, with a slope $\leq 1/4$.</p>	<p><u>Without backing bar:</u></p> <p>1) Transverse splices in plates and flats. 2) Flange and web splices in plate girders before assembly. 3) Full cross-section butt welds of rolled sections without cope holes. 4) Transverse splices in plates or flats tapered in width or in thickness, with a slope $\leq 1/4$.</p>	<ul style="list-style-type: none"> - All welds ground flush to plate surface parallel to direction of the arrow. - Weld run-on and run-off pieces to be used and subsequently removed, plate edges to be ground flush in direction of stress. - Welded from both sides; checked by NDT. <p><u>Detail 3):</u> Applies only to joints of rolled sections, cut and rewelded.</p>
90	<p>5) Transverse splices in plates or flats. 6) Full cross-section butt welds of rolled sections without cope holes. 7) Transverse splices in plates or flats tapered in width or in thickness with a slope $\leq 1/4$. Translation of welds to be machined notch free.</p>	<p>5) Transverse splices in plates or flats. 6) Full cross-section butt welds of rolled sections without cope holes. 7) Transverse splices in plates or flats tapered in width or in thickness with a slope $\leq 1/4$. Translation of welds to be machined notch free.</p>	<ul style="list-style-type: none"> - The height of the weld convexity to be not greater than 10% of the weld width, with smooth transition to the plate surface. - Weld run-on and run-off pieces to be used and subsequently removed, plate edges to be ground flush in direction of stress. - Welded from both sides; checked by NDT. <p><u>Details 5 and 7:</u> Welds made in flat position.</p>
90	<p>8) As detail 3) but with cope holes.</p>	<p>8) As detail 3) but with cope holes.</p>	<ul style="list-style-type: none"> - All welds ground flush to plate surface parallel to direction of the arrow. - Weld run-on and run-off pieces to be used and subsequently removed, plate edges to be ground flush in direction of stress. - Welded from both sides; checked by NDT. - Rolled sections with the same dimensions without tolerance differences
80	<p>9) Transverse splices in welded plate girders without cope hole. 10) Full cross-section butt welds of rolled sections with cope holes. 11) Transverse splices in plates, flats, rolled sections or plate girders.</p>	<p>9) Transverse splices in welded plate girders without cope hole. 10) Full cross-section butt welds of rolled sections with cope holes. 11) Transverse splices in plates, flats, rolled sections or plate girders.</p>	<ul style="list-style-type: none"> - The height of the weld convexity to be not greater than 20% of the weld width, with smooth transition to the plate surface. - Weld not ground flush - Weld run-on and run-off pieces to be used and subsequently removed, plate edges to be ground flush in direction of stress. - Welded from both sides; checked by NDT. <p><u>Detail 10:</u> The height of the weld convexity to be not greater than 10% of the weld width, with smooth transition to the plate surface.</p>
63	<p>12) Full cross-section butt welds of rolled sections without cope hole.</p>	<p>12) Full cross-section butt welds of rolled sections without cope hole.</p>	<ul style="list-style-type: none"> - Weld run-on and run-off pieces to be used and subsequently removed, plate edges to be ground flush in direction of stress. - Welded from both sides.

figure 3.2 Detail categories for transverse butt welds (source: NEN-EN 1993-1-9)

3.2.3 Benefits, drawbacks and application

The nominal stress approach can easily be applied on a wide range of designs because most common details are incorporated in the codes. Calculations are relatively easy and quick to perform. When a detail is not classified, the nominal stress approach cannot be used.

In the widely used Eurocode 3-1-9 (2006) no distinction is made between different materials for the nominal stress design, and the calculation method is limited up to S700 since the issue of Eurocode 3-1-12 (2007). This means that the few high strength steels that can be designed according to Eurocode (e.g. S460 and S690) are assumed to show no better fatigue behaviour than standard steels. Also the use of post fabrication weld improvement techniques, other than stress relief, is not covered by Eurocode 3-1-9. For a more complete overview of the current design codes regarding fatigue, see 4.2.1. There will be explained that some codes do reward post weld treatments or high strength steels with higher fatigue strength to a certain extent. However, the nominal stress approach remains most useful for standard applications.

3.3 Structural stress approach

3.3.1 Principles

In this case the maximum stress at a so called 'hot spot' is determined, where the stress reaches a peak at a notch. This structural stress at the hot spot (σ_{hs}) includes all stress raising effects at the detail, except the stress raising effect of the weld geometry. This effect is left out of the analysis because the exact weld geometry differs greatly from weld to weld, and is therefore incorporated in the scatter of the fatigue strength curve. The method is thus very similar to the nominal stress approach, but applicable to all kinds of details, and not just the details listed in the design code.

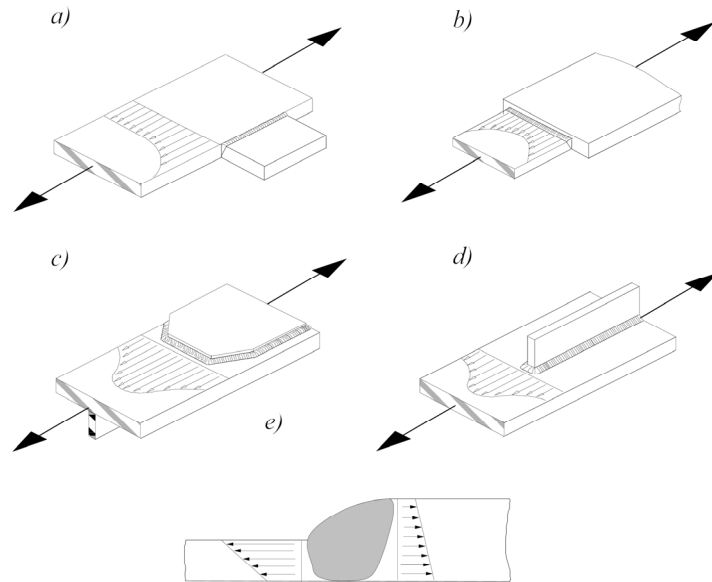


figure 3.3 Some examples of stress distribution at structural details (source: Hobbacher, 2007)

3.3.2 Calculation procedure

The structural stress can be determined by means of FEM analysis or by direct measurement on the component. From a certain number of measuring points the structural stress is then determined by extrapolation both in the case of FEM as with direct measurements. An alternative method is a parametric calculation where the structural stress is previously determined for a certain detail. A stress concentration factor (k_{hs}) can then be determined directly from a parametric formula. The structural stress can be calculated:

$$\sigma_{hs} = k_{hs} \cdot \sigma_{nom} \quad (3.1)$$

Once the structural hot spot stress is known the allowable number of cycles can be determined with the design S-N curves. Again these curves are dependent on the kind of detail but, as other stress raisers are already considered, only apply to simple welding details such as depicted in figure 3.4.

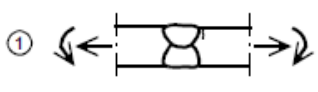
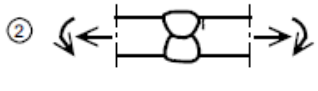
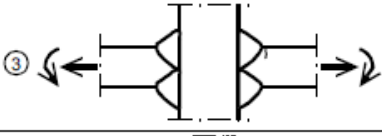
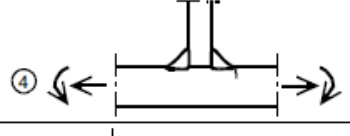
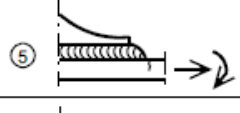
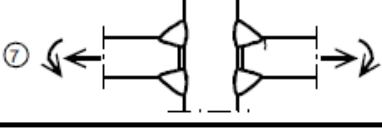
Detail category	Constructional detail	Description	Requirements
112		1) Full penetration butt joint.	1) -All welds ground flush to plate surface parallel to direction of the arrow. -Weld run-on and run-off pieces to be used and subsequently removed, plate edges to be ground flush in direction of stress. -Welded from both sides, checked by NDT. -For misalignment see NOTE 1.
100		2) Full penetration butt joint.	2) -Weld not ground flush -Weld run-on and run-off pieces to be used and subsequently removed, plate edges to be ground flush in direction of stress. -Welded from both sides. -For misalignment see NOTE 1.
100		3) Cruciform joint with full penetration K-butt welds.	3) -Weld toe angle $\leq 60^\circ$. -For misalignment see NOTE 1.
100		4) Non load-carrying fillet welds.	4) -Weld toe angle $\leq 60^\circ$. -See also NOTE 2.
100		5) Bracket ends, ends of longitudinal stiffeners.	5) -Weld toe angle $\leq 60^\circ$. -See also NOTE 2.
100		6) Cover plate ends and similar joints.	6) -Weld toe angle $\leq 60^\circ$. -See also NOTE 2.
90		7) Cruciform joints with load-carrying fillet welds.	7) -Weld toe angle $\leq 60^\circ$. -For misalignment see NOTE 1. -See also NOTE 2.

figure 3.4 Detail categories for the structural hot spot stress method (source: NEN-EN 1993-1-9)

3.3.3 Benefits, drawbacks and application

When a chosen detail does not exactly comply with the details given in the detail categories or where no clearly defined nominal stress exists, the nominal stress approach cannot be applied. Then the structural hot spot stress can be an adequate tool to analyze the fatigue strength of a component. A large drawback of this method is the extensive FEM research or actual tests that need to be executed when no parametric formulae are available to determine the hot spot stress.

The structural stress approach can only be applied to detail types where the crack grows from the weld toe, because the stress needs to be determined along a certain number of extrapolation points at the surface of a plate. In figure 3.5 this rules out details f to j. Therefore, to use this method, the designer must be sure the crack will initiate at the weld toe.

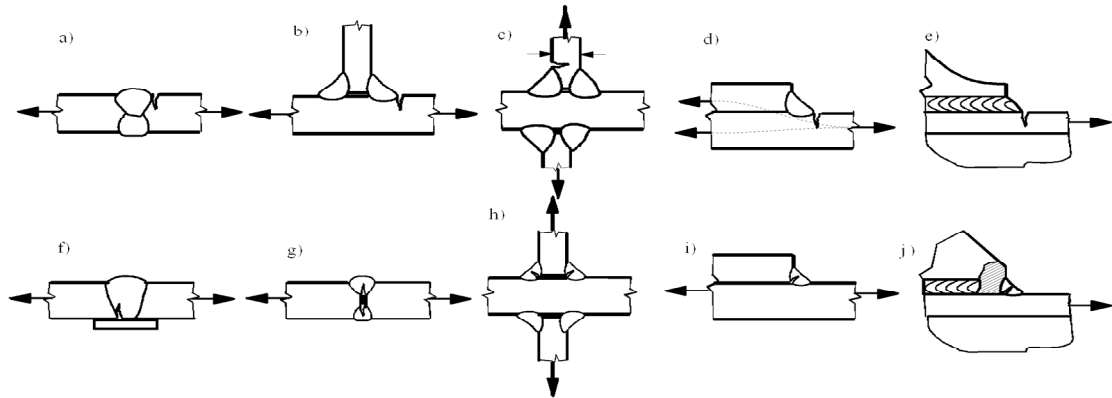


figure 3.5 Various locations where cracks may occur in welded joints (source: Hobbacher, 2007)

3.4 Crack propagation approach

3.4.1 Principles

The crack propagation approach treats the part of the fatigue life of a component from the initiation of a crack to failure. Both boundaries need to be determined in advance. For the initiation of a crack a commonly used crack length is 0.15 millimeter. The point at which a component is considered failed can be determined as the point where the crack is trough thickness, an actual failure or when the crack growth rate reaches a certain value after which relatively few remaining cycles are expected.

Once a crack has initiated the crack growth rate can be calculated with the Paris law:

$$\frac{da}{dN} = C_0 \cdot \Delta K^m \quad (3.2)$$

In which:

- a crack length parameter [mm]
- N number of cycles [-]
- ΔK range of stress intensity factor [$\text{Nmm}^{-3/2}$]
- C_0, m material constants [$\text{Nmm}^{-3/2}$], [-]

This relation holds if the crack is not too small (no crack propagation; $\Delta K < \Delta K_{th}$) or not too large. The Paris law and its limits for too small or too large cracks is shown in figure 3.6. From this figure it can clearly be seen that the number of cycles in region 1 (if $\Delta K > \Delta K_{th}$) and region 3 is relatively small. Therefore, the total number of cycles in the crack propagation stage (N_p) can be approximated with only the cracks in region 2 according to the Paris Law.

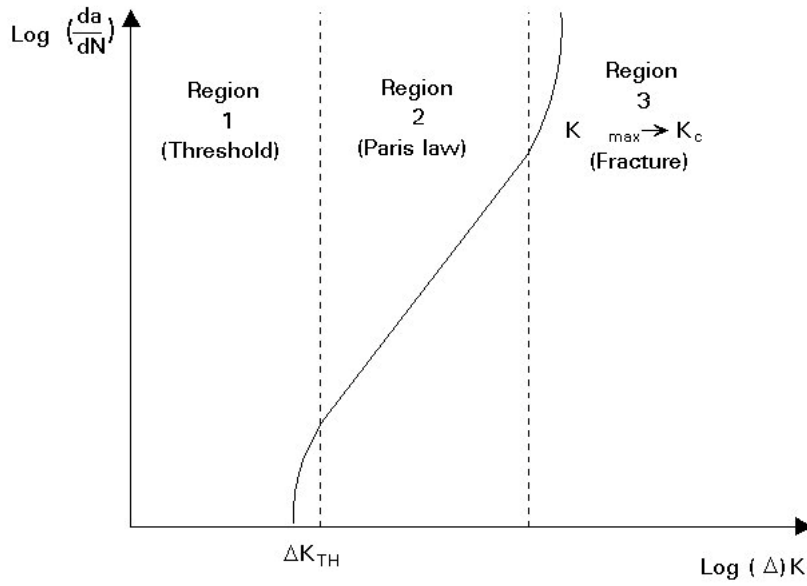


figure 3.6 Crack growth rate vs. stress intensity factor (Paris law) (source: ESDEP)

The material constants C_0 and m are material dependent, even between different types of steel, but do not differ much over the range of steels, see figure 3.7. This means that once a crack is initiated, it will propagate at approximately the same rate whether high strength or low strength steel is used.

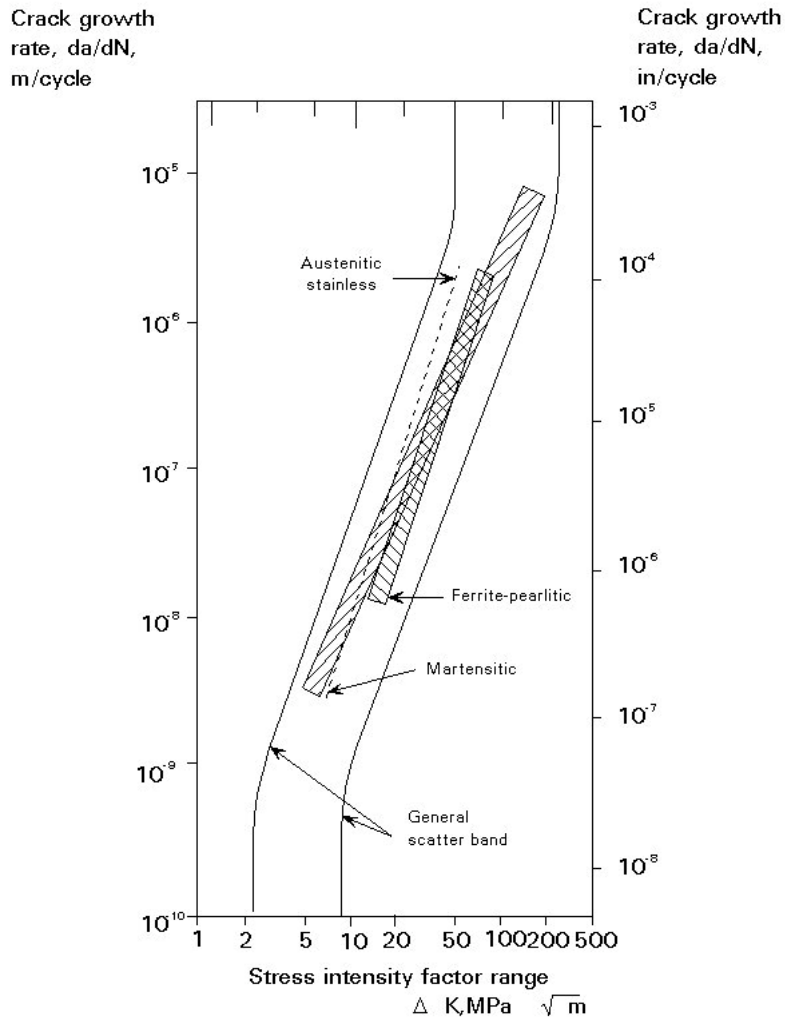


figure 3.7 Crack growth rate for different steels (source: ESDEP)

The stress intensity factor is used to describe the stress field around the crack tip, and depends on the geometry of the crack and the surrounding specimen. The stress intensity factor can be determined by means of FEM analysis, but for a wide range of joints the stress intensity factors can be directly calculated with parametric formulae. The threshold value of ΔK , below which no crack propagation occurs, depends on the mean stress and environmental conditions.

3.4.2 Calculation procedure

To start the calculation a description of the stress field around the crack tip is needed. This is done by means of the stress intensity factor K , which generally has the following form:

$$K = Y \cdot \Delta\sigma \sqrt{\pi a} \quad (3.3)$$

In which Y , called the compliance function, takes the crack shape and overall geometry of the surrounding material into account. If only propagating cracks are considered ($\Delta K > \Delta K_{th}$) the Paris law (equation (3.2)) can be rewritten to:

$$N = \frac{1}{C} \int_{a_i}^{a_f} \frac{da}{\Delta K^m} = \frac{1}{C} \int_{a_i}^{a_f} \frac{da}{\Delta\sigma^m Y^m (\sqrt{\pi a})^m} \quad (3.4)$$

Because the crack growth rate changes when the crack grows this integral cannot be solved directly, but must be approximated in small steps. In each of these steps the stress intensity factor is assumed constant.

$$\Delta N = \frac{1}{C \cdot \Delta\sigma^m \cdot \alpha \cdot \pi^{\frac{m}{2}} \cdot Y^m} \cdot \left(\frac{1}{a_i^{\frac{m}{2}-1}} - \frac{1}{a_f^{\frac{m}{2}-1}} \right) \quad (3.5)$$

In which:

- a_i the initial crack size [mm]
- a_f the final crack size [mm]

If a limit is set to the crack size at which the specimen is considered failed, or the critical crack length is reached after which unstable growth occurs (region 3 in figure 3.6), the total amount of cycles can be obtained by summation. To make the calculation, the material dependent parameters C and m need to be obtained. This can either be done directly from tests or from literature. Also the stress intensity factor can be obtained from literature, but a FEM-analysis can also be used. However, this FEM-analysis must be made for different crack depths of the same crack to determine the change of K when the crack dimensions increase.

3.4.3 Benefits, drawbacks and application

The crack propagation method can only calculate the number of cycles after crack initiation. Therefore, in design, it is only useful when the crack propagation phase is dominant. In normal welded connections, this is generally the case (ESDEP), in high strength steel welded connections this approximation can be too conservative.

If the compliance function is available from textbooks the analysis can be made rather quickly, especially when specialized software is used which already incorporates the 'small-step'-method depicted in equation (3.5). If the compliance function is not available, in most cases it must be derived from FEM analysis. Because the compliance function among other things depends on the crack depth, this analysis can be very time consuming.

The crack propagation approach can be used to determine the lives of already damaged structures. It can also be used to determine service intervals of structures. For this the time between a visible crack and failure is calculated.

3.5 Notch stress approach

3.5.1 Principles

As explained in 2.3.2, there is a clear notch effect in steel subjected to dynamic loading. At notches the stress is concentrated which facilitates the initiation of cracks. The principle of the notch stress approach is to compare this notch stress to the maximum stress a plain specimen can withstand. Therefore, at the root of a notch a small plain specimen is imagined which is subjected to the same stresses as the tip of the notch. In a simple assessment of these notches only the infinite fatigue life is considered and therefore only the fatigue limit is determined. If the plain machined specimens can endure a certain stress level without cracking, then this stress level can also be endured at the notch root. In this method one of the main assumptions is elasticity. This is not surprising, because (large) plastic deformations will eventually lead to

cracks and failure, which contradicts with the infinite life that was assumed. The method covers only the process of crack initiation.

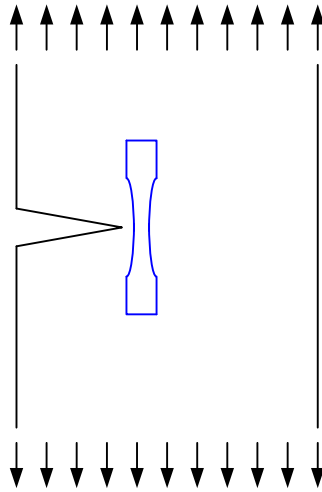


figure 3.8 At a notch the local stresses are determined and applied to a local 'plain specimen'

This does not take into account the fact that cracks may be initiated but do not propagate (dormant cracks) and that minor plastic deformation may take place without effect on the fatigue life (Radaj et al., 2006).

The stress concentration at the notch is calculated with the elastic stress concentration factor:

$$\sigma_{notch} = K_t \cdot \sigma_{nom} \quad (3.6)$$

Experiments have shown that this elastic notch stress does not determine the fatigue behaviour of the notched specimen. Instead, a somewhat lower stress can be linked to the fatigue behaviour of the specimen. This effect is called the 'microstructural support effect' (Radaj et al., 2006). The stress that governs the fatigue behaviour is a stress averaged over a small length or volume, characteristic for the considered material. This microstructural support does not only occur near very sharp notches (as shown in figure 3.8) but also at milder notches, provided that they are sufficiently small. The microstructural support effect therefore depends not only on the material but also the geometry of the specimen, specifically the radius of the considered notch (see figure 3.9)

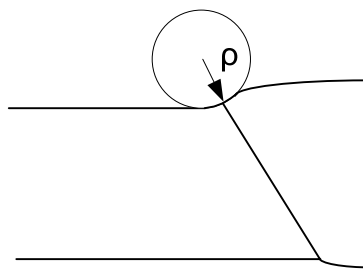


figure 3.9 One half of a butt weld and the corresponding notch radius (ρ) at the notch root

This microstructural support effect has been represented in different forms:

- Critical distance approach (Peterson, 1974)
- Stress averaging approach (Neuber 1937, 1946 and 1968)
- Stress gradient approach (Siebel et al., 1993)
- Highly stressed volume approach (Kuguel, 1961)

The stress at the notch that actually defines the fatigue behaviour of the component is expressed as:

$$\bar{\sigma}_{notch} = K_f \cdot \sigma_{nom} \quad (3.7)$$

Where the fatigue notch factor K_f is determined with one of the theories depicted above. The difference between K_f and K_t gives some information about the sensitivity of the material to notches. This is expressed in the notch sensitivity:

$$q = \frac{K_f - 1}{K_t - 1} \quad (3.8)$$

A notch factor of 1 represents a material that is fully sensitive to notches, because the fatigue notch factor K_f is equal to the elastic stress concentration factor. If $q=0$ the material is insensitive to notches because $K_f=K_t=1$.

Different calculation approaches have been developed, each based on one of the earlier mentioned representations of the microstructural support effects.

Critical distance approach

This method, developed by Lawrence from the original concept of Peterson, uses notch stress analysis to determine the fatigue notch factor (Radaj et al., 2006). From there the method continues with the notch strain approach, which is not covered by this research. Only the determination of K_f will be discussed here.

The first step in the analysis is to determine where the crack will arise. For these locations the elastic notch stress concentration factor needs to be determined. This can be done by FEM analysis or by using engineering formulae, if available for the considered joint. The fatigue notch factor is derived from K_t by using the critical distance approach developed by Peterson. This approach states that the ratio between K_t and K_f depends on the ratio between a material constant a^* and the notch radius ρ . The material constant is approximated by Lawrence, and has been applied on low and high strength steels:

$$a^* = 0.025 \left(\frac{2068}{R_M} \right)^{1.8} \quad (3.9)$$

Peterson also found a relation between the ultimate tensile strength and a^* . The two relations are depicted in table 3.1. Peterson also used some values based on hardness: $a^*=0.254$ millimeter for soft-annealed steel ($\approx 170\text{HB}$) and $a^*=0.0635$ millimeter for quenched and tempered steel ($\approx 360\text{HB}$) (Radaj et al., 2006). The values in table 3.1 differ greatly in the low strength range, but are very similar in the high strength range.

R_m [N/mm ²]		345	518	690	863	1035	1380	1725
a^* [mm]	Lawrence	0.628	0.302	0.180	0.121	0.087	0.052	0.035
	Peterson	0.380	0.250	0.180	0.130	0.089	0.051	0.033

table 3.1 Material constant a^* from Lawrence and Peterson (Peterson derived the data from bars loading in bending) (Radaj et al., 2006)

The relation between K_f and K_t is stated as:

$$K_f = 1 + \frac{K_t - 1}{1 + \frac{a^*}{\rho}} \quad (3.10)$$

The shape of this function is shown in figure 3.10. In this figure it can be seen that at a certain a^*/ρ ratio of about 1 the fatigue notch factor reaches its maximum. Because the notch radius scatters greatly at welds this worst case approach is applicable for design analysis. If the notch geometry and its scatter is accurately known, a realistic approach can be made.

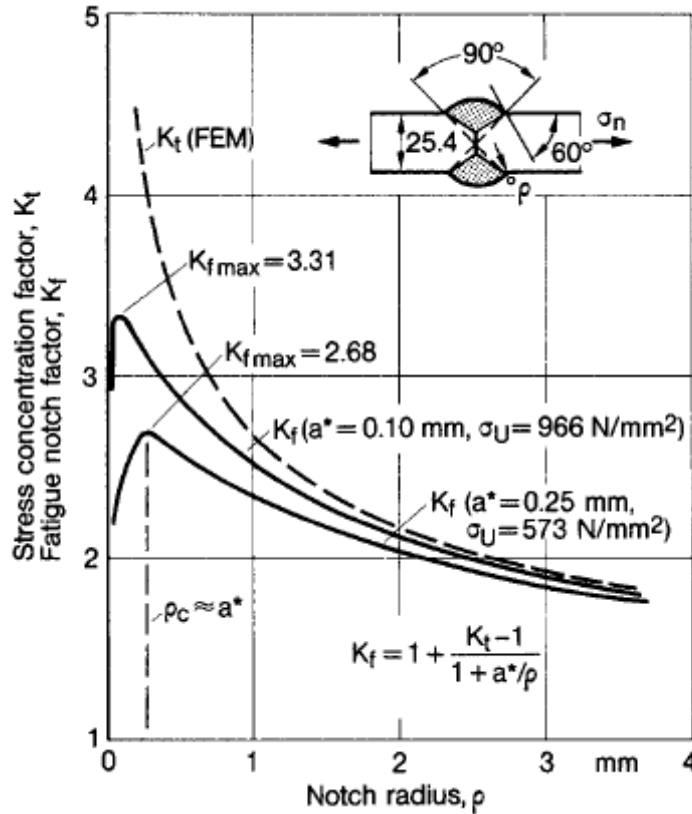


figure 3.10 Elastic stress concentration factor (K_t) for a butt joint and fatigue notch factor (K_f) for different materials (source: Radaj et al., 2006)

Because the method proceeds in the notch strain domain, no clear adjustments for mean and residual stresses are described for a direct notch stress analysis.

Fictitious notch rounding approach

This method is developed by Radaj and is based on the Neuber microstructural support hypothesis (Radaj et al., 2006). It has mainly been used for low strength steels, but is not restricted to these steels. To take account of the reduction of the elastic stress to an effective stress the notch is imagined less sharp. This fictitious rounded notch leads to a lower elastic stress concentration which is considered to approximate the fatigue notch factor of the original geometry.

The fictitious notch is given by:

$$\rho_f = \rho + s \cdot \rho^* \quad (3.11)$$

In which:

- ρ_f the fictitious notch radius [mm]
- ρ the original notch radius [mm]
- s a multiaxiality coefficient [-]
- ρ^* a material constant [mm]

It has been shown that if in the critical distance approach $a^*=0.25$ millimeter is chosen, this corresponds to a ρ_f of 1 millimeter, because it can analytically be derived that $\rho_f=4a^*$ (Radaj et al., 2006). The material constant ρ^* is considered to depend on the yield limit of the material, see figure 3.11. This figure only covers low strength steels, except for ferritic steels.

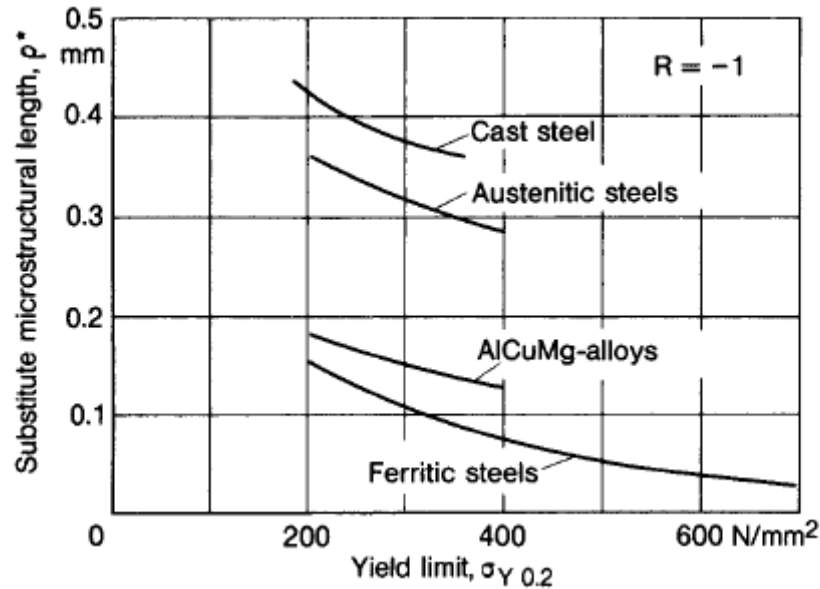


figure 3.11 Material constant ρ^* for different steel types and strengths (source: Radaj et al., 2006)

Radaj advises the use of a ρ^* of 0.4 millimeter in combination with $s=2.5$ when (low strength) steels are considered. This is based on the assumption of cast steel for the weld deposit (for ρ^*) and plane strain combined with the Von Mises multiaxial strength criterion (for s). If a worst case scenario of $\rho=0$ is considered, this leads to a ρ_f of 1 millimeter. This would, as described above, be equivalent to a value of a^* of 0.25 millimeter in the critical distance approach.

Static mean stresses can be taken into account via a Haigh diagram (see figure 2.7), but the Neuber microstructural support hypothesis, on which the method is based, has not been proven with the inclusion of these mean stresses.

The introduction of an enlarged radius can cause an undercut near the weld toe (see figure 3.12). This may cause extra stress concentration if this significantly reduces the load carrying cross section, especially when high stresses are involved. If the undercut occurs, correction terms are given by Radaj et al. (2006).

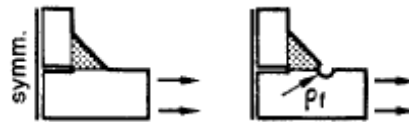


figure 3.12 Undercut caused by fictitious notch rounding (source: Radaj et al., 2006)

Highly stressed volume approach

Sonsino (1993) has developed methods that try to determine the statistical size effect (see 2.3.2) and the effect of multi-axial local stresses with in-phase and out-of-phase stress amplitudes with a calculation method based on the highly stressed volume approach. In this approach the statistical size effect is combined with the microstructural support hypothesis. It is assumed that the crack initiation time can be determined based on the stresses in a local volume of material. This volume has been determined by Sonsino as having a depth below the notch and a surface area where the notch stress has dropped to 90% of its maximum at the notch. Sonsino proposed the following relation for K_f :

$$K_f = \frac{\sigma_{\sigma E}}{\sigma_{k\sigma E}} K_t \quad (3.12)$$

In which:

- $\sigma_{\sigma E}$ the endurable stress amplitude in plain material [N/mm^2]
- $\sigma_{k\sigma E}$ the endurable stress at the notch [N/mm^2]

Equation (3.12) expresses the fact that the endurable notch stress seems higher than the endurable stress for plain material, instead of assuming that the stress at the notch is lower than elastically calculated, which was assumed in the previous approaches. The specimens for which the strength of plain material is determined, must of course not show the highly stressed volume effect themselves, therefore they must be of sufficient size. The endurable notch stress depends on the highly stressed volume ($V_{0.9}$):

$$\sigma_{kaE} = f(V_{0,9}) \quad (3.13)$$

The highly stressed volume is defined as the area where 90% of the maximum notch stress is exceeded. The depth of the region is determined by the normalized stress gradient (equations (3.15) and (3.16))

$$V_{0,9} = d_{0,9} w \cdot \frac{\pi \rho}{8} \quad (3.14)$$

$$d_{0,9} = \frac{0,1}{\chi} \quad (3.15)$$

$$\chi = \frac{1}{\sigma_{notch}} \frac{d\sigma_{notch}}{dn} \quad (3.16)$$

The notch stress gradient depends on the notch radius, cross section dimensions and loading type and can be found in literature or determined with a FEM analysis. The relation between highly stressed volume and allowable stress has been derived by Sonsino. The results are shown in figure 3.13.

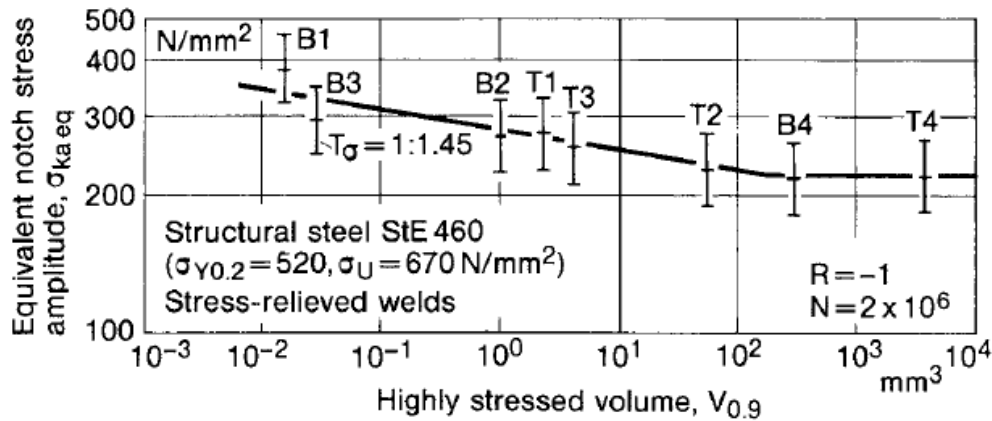


figure 3.13 Endurable notch stress amplitude at weld toes in structural steel as a function of the highly stressed volume; based on different tests including bending (B) and tension (T) loading (source: Radaj et al., 2006)

Now maximum stress for infinite fatigue life of the notched component can directly be derived from the infinite fatigue life of a plain machined specimen.

Extension into finite life

Although the notch stress approach was derived for infinite lives, there also have been attempts to extend the application into the finite life regime. Schijve proposes to construct an S-N curve on the basis of two asymptotes and the intermediate Basquin relation (Schijve, 2001), see figure 3.14. The upper asymptote is determined by the ultimate strength of the specimen and the mean stress. The lower asymptote can be calculated with the notch stress theory for infinite life, as has been treated in the previous section. To complete the S-N curve only the slope of the Basquin relation needs to be known. Schijve circumvents this and proposes to define a fixed number of relations for N_{up} and N_{knee} as shown in figure 3.14.

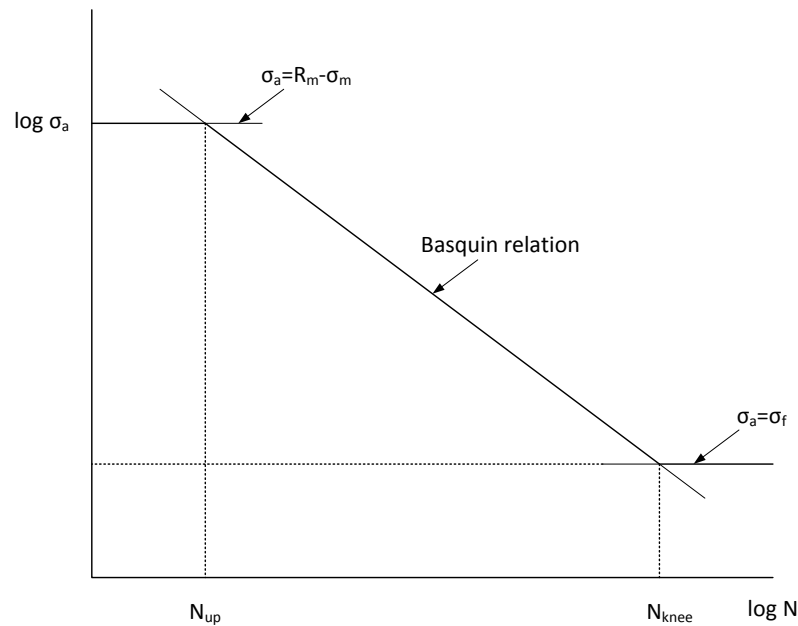


figure 3.14 Estimate of an S-N curve. Note the use of the stress amplitude (σ_a) instead of the stress range ($\Delta\sigma$)

The values proposed for N_{up} and N_{knee} are 10^2 and 10^6 respectively, based on tests on notched specimens. A remark is made that choosing 10^2 introduces a slight conservatism and that 10^3 would correspond better with test results. It must be noted that the method proposed is derived for 'notched specimens', which the author distinguishes from welded joints. In the chapter on welded joints a remark is made that the knee point (N_{knee}): "is found at a significantly higher fatigue life, about $2 \cdot 10^7$ ". For application for welded joints this most probably will be the more suitable value to use for N_{knee} when constructing the S-N curve. The normative values for the fatigue limit specified by Eurocode ($5 \cdot 10^6$) and IIW recommendations¹ (10^7) (Hobbacher, 2007) lie in between the proposed values of Schijve for constant amplitude fatigue loading.

Another method was proposed by Hück et al. (1981), which was summarized by Gudehus et al. (1999). Here the fatigue limit of a component is also determined by a notch stress analysis, but the slope of the Basquin relation also depends on the determined fatigue notch factor according to equation (3.17) for rolled steel and equation (3.18) for cast steel.

$$m = \frac{12}{K_f^2} + 3 \quad (3.17)$$

$$m = \frac{5.5}{K_f^2} + 6 \quad (3.18)$$

The knee point of the fatigue strength curve is depending on the slope of the curve according to this method. The knee point of the curve can be determined with equation (3.19) for rolled steel and equation (3.20) for cast steel.

$$N_{knee} = 10^{\frac{6.4 - 2.5}{m}} \quad (3.19)$$

$$N_{knee} = 10^{\frac{6.8 - 3.6}{m}} \quad (3.20)$$

With the use of these two equations, the slope and knee point of the fatigue strength curve are determined. When the fatigue limit has been determined with the notch stress analysis and the upper knee point (N_{up} , see figure 3.14) is ignored, the fatigue strength curve is determined. The neglect of the upper plateau by not using N_{up} results in a fatigue strength curve only usable in medium and high cycle regimes.

¹ The IIW recommendations only show a constant amplitude fatigue limit for standard applications. For very high cycle applications, also beyond 10^7 cycles the S-N curve shows a slope.

3.5.2 Calculation procedure

First the elastic notch stress concentration factor needs to be determined. This can be done with FEM-analysis, measuring or functional analysis methods based on theory of elasticity (Radaj et al., 2006). The elastic notch stress concentration factor is then defined as (rewritten from (3.6)):

$$K_t = \frac{\sigma_{notch}}{\sigma_{nom}} \quad (3.21)$$

From this elastic notch stress concentration factor the fatigue notch factor K_f needs to be determined. For this, one of the theories explained above can be used. The maximum stress at which no crack initiation ($\sigma_{notch;per}$) occurs can now directly be obtained:

$$\sigma_n = \frac{\sigma_{notch}}{K_f} \quad (3.22)$$

$$\sigma_{notch} \leq \sigma_{notch;per} \quad (3.23)$$

In which:

$\sigma_{notch;per}$ the permissible notch stress [N/mm²]

σ_{notch} the actual notch stress, based on the nominal stress and analyses with respect to K_f [N/mm²]

The permissible notch stress can be derived from tests on plain specimens, or by mathematical relations between the static strength and fatigue strength.

If any misalignments are present they must be taken into account. Formulas to take misalignments into account are given by Hobbacher (2007). Once the stress limit for infinite life is known, an estimate of the maximum stress for a certain finite life can be made by means of the method of Schijve, or the relations found by Hück.

3.5.3 Benefits, drawbacks and application

This method requires more effort than the 'standard' methods. Besides that, some information on the material and local geometry to determine the correct value of K_t and K_f is necessary. When these can be determined accurately enough, a reliable estimate can be made of the fatigue limit of the considered component.

The method was developed to determine the stress level below which no crack initiation occurs. This is of course a very important point in the S-N curve, but limits design possibilities to a 'fail-free' design. With the additions of Schijve and Haibach the method includes crack initiation over both the medium and high cycle domain. This means that for civil engineering structures the full fatigue life can be obtained if the analysis is combined with a crack propagation analysis.

This method currently does not find a lot of application in design, because of the required effort.

4 Literature review: Practice

4.1 Chapter outline

In paragraph 2.3.4 it was mentioned that high strength steel does not always show a significantly better fatigue behaviour than standard steel (see figure 2.11). In this chapter, this will be further investigated. First the current design codes and recommendations are discussed with regard to fatigue and high strength steel. Then the actual behaviour according to experiments will be discussed. First for plain material and then for non plain material, which contains both notched and welded specimens.

The effect of TIG-dressing was discussed in general in 2.4.2. In this chapter the current state of design codes and recommendations with regard to TIG-dressing and its beneficial effects is discussed. Then the influence of TIG dressing on the specimen is discussed, followed by the actual behaviour of TIG-dressed specimens, both for standard and high strength steel.

4.2 Literature regarding fatigue and high strength steel

4.2.1 Strength according to current design codes and recommendations

Three design codes will be discussed: Eurocode, IIW recommendations and NPR-CEN/TS 13001-3-1. Eurocode is taken into account because it is widely used in European steel structures. The IIW recommendations and the NPR design code are taken into account because they also cover very high strength steels.

Eurocode 1993-1-9 (2006)

Eurocode is applicable for steels up to S700 since the additional code NEN-EN 1993-1-12 (2007) was introduced. The code is mainly focused on the nominal stress approach, but also includes an annex addressing the structural stress approach. Both the detail categories specified for the nominal stress approach and the structural stress approach do not distinguish different detail categories for different steel grades. This means that any beneficial effect of the parent material strength is not referred to in the code. Therefore, two identical structures made from standard steel and high strength steel will have the same fatigue resistance according to Eurocode.

IIW recommendations

The design recommendations by the International Institute of Welding (Hobbacher, 2007) cover design of structures made of structural steels up to a yield strength of 960 N/mm². The document covers various fatigue approaches: nominal stress design, structural stress design, notch stress approach and crack propagation approach. If physical tests are necessary, the document gives some information on test procedures and statistical analysis.

The detail categories that are specified for the nominal stress approach and the structural stress approach do not distinguish different FAT-classes for high strength steel, and therefore do not differ from Eurocode in this aspect.

NPR-CEN/TS 13001-3-1

The CEN code is mainly applied to steel crane structures, but is interesting for this case because it, contrary to the Eurocode and IIW recommendations, adjusts the fatigue strength of a component to a certain extent, depending on the ultimate tensile strength of the material. The code is applicable to structures made of structural steels up to a yield strength of 960 N/mm² and covers the nominal stress design.

The code is different from the codes mentioned before, because it specifies the slope of the S-N curve depending on the detail that is used, and specifies the FAT-value depending on the ultimate tensile strength of the base material. This differentiation according to steel grade is only applied for plain material such as flat bars, plates and rolled profiles. The code distinguishes steels with a yield strength lower than 275 N/mm², between 275 N/mm² and 355 N/mm² and higher than 355 N/mm². The fact that this differentiation only takes place in the standard grades and classifies all high strength steels together may not be optimal, but is certainly less conservative than the approach of Eurocode and the IIW. An example of the design line of NPR-CEN/TS 13001-3-1 is shown in figure 4.2.

4.2.2 Behaviour of plain material

Different authors have found the fatigue strength of a plain specimen at a certain number of cycles to be increasing with increasing static strength (Maddox, 1991; Gurney, 1979). Gurney publishes a set of data from previous research, showing an approximate linear relation between fatigue strength and ultimate tensile strength (see figure 4.1).

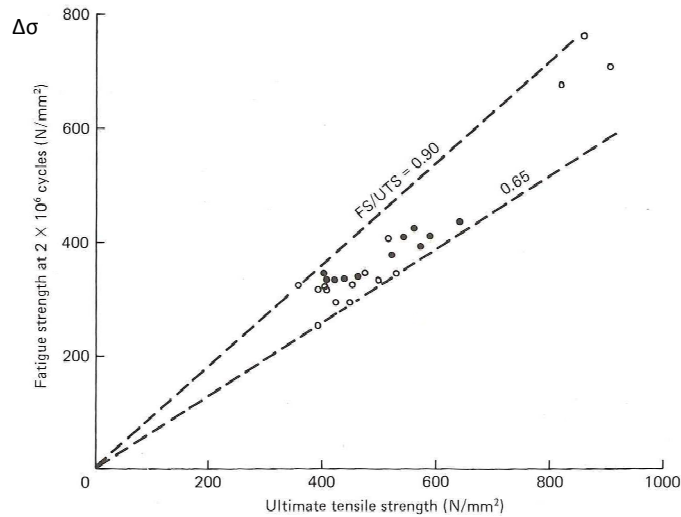


figure 4.1 Relation between ultimate tensile strength and fatigue strength of plain machined specimens. Black data points are originally bending tests, but analytically converted to tensile loading (source: Gurney, 1979)

Pijpers concluded not only that the fatigue strength of the plain specimens increases with increasing tensile strength, but also found a slope of the S-N curve less steep than specified in certain codes (Pijpers et al., 2009). The comparison between Eurocode, NPR-CEN/TS 13001-3-1 and the results are shown in figure 4.2. A comparison is not made with the IIW recommendations, this line will be similar to the one specified by Eurocode but marginally more conservative.

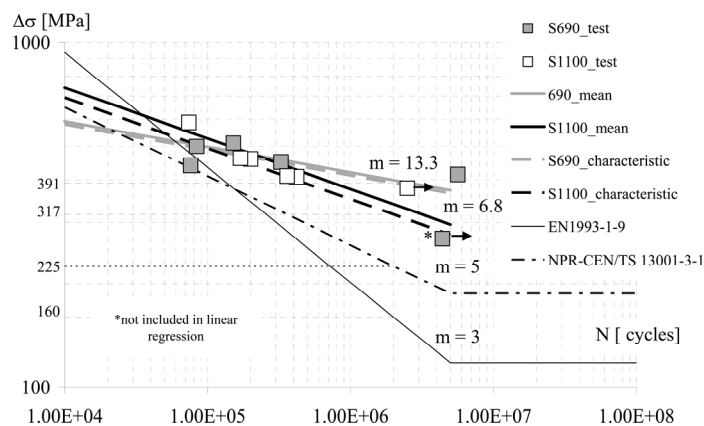


figure 4.2 S-N curve of base materials based on research from Pijpers (source: Pijpers et al., 2009)

In Pijpers' research the S1100 specimens do not seem to perform better than the S690 specimens. In fact, the calculated FAT-value for S690 was higher (391 N/mm^2) than for S1100 (317 N/mm^2). It was observed that in the S1100 specimens cracks occurred outside the tapered cross-section, which had been grounded to place strain gauges. The cracks occurred in the wider cross section where grinding had not taken place. Apparently these very high strength steels are very sensitive to surface roughness. Unfortunately, no data exists where cracks occurred in a smooth section of the S1100 specimens, but the fact that the cracks occurred outside the tapered sections, despite the higher stress in the tapered sections, shows that for smooth material higher fatigue strengths can be reached than depicted in figure 4.2.

Different data sets show what was already stated in 2.3.2: if the static strength of steel increases, the fatigue strength also increases for smooth specimens.

4.2.3 Behaviour of non-plain material

In practice, most structures will not be made of plain material. Structures are welded, with the associated microcracks and inclusions, have a certain surface roughness or other forms of notches. Gurney has collected data from previous experiments where specimens with machined surfaces are compared with specimens which are tested as produced. The effect of the present millscale and possible small defects is clear (see figure 4.3). Not only is the ratio between ultimate tensile strength and fatigue strength lowered from 0.9-0.625 to 0.625-0.4, but also above an ultimate strength of approximately 700 N/mm^2 the fatigue strength does no longer seem to increase with increasing ultimate strength.

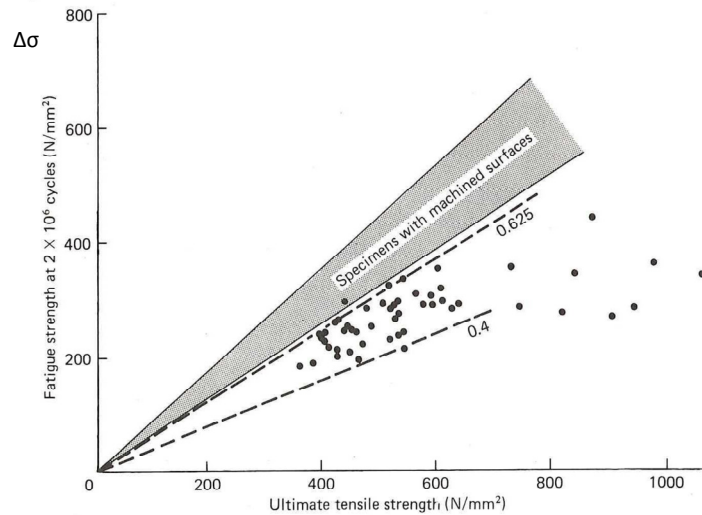


figure 4.3 Comparison of plain machined specimens with as-produced specimens. The scatter band for specimens with machined surfaces is derived from the data in figure 4.1 (source: Gurney, 1979)

The sensitivity to surface roughness that was assumed by Pijpers (see 4.2.2) is clearly shown in figure 4.3. Gurney found that this effect becomes visible above a certain ultimate tensile strength, which also matches with Pijpers research, where the S1100 specimens showed the very sensitive behaviour, while the S690 specimens cracked at the machined, reduced cross section.

Results of welded connections are also available from Gurney. These specimens have more severe notches than the plain machined specimens and as-produced specimens. Also, some residual stresses may be introduced and the microstructure of the heat affected zone may differ from the parent material. The effect of welding on the specimens is clearly visible in figure 4.4. The strength of the welded connections does not show the same increase of fatigue strength when the tensile strength of the parent material increases. In fact, the ultimate tensile strength of the material does not seem to have any influence at all.

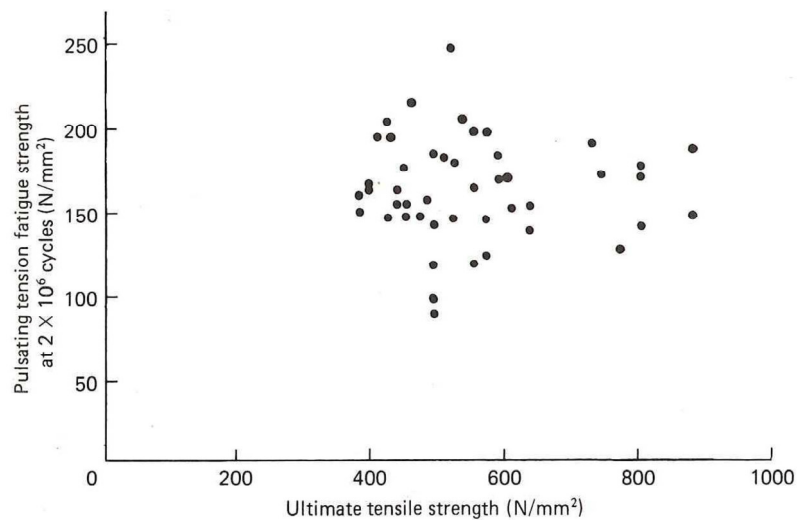


figure 4.4 Fatigue strength of welded specimens (source: Gurney, 1979)

Pijpers has collected data from different authors, which is very insightful in this matter, as shown in figure 4.5. The plain machined specimens show the linear relation as was earlier described. When some roughness, notch or weld defects are included the beneficial effect of high strength steel quickly diminishes.

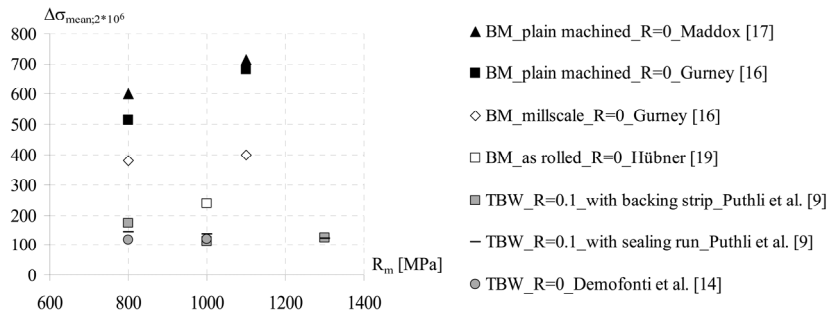


figure 4.5 Fatigue strength at $2 \cdot 10^6$ cycles for different specimens, both base material (BM) and transverse butt welded (TBW); the numbers between brackets refer to the sources of the data points in the original article (source: Pijpers et al., 2009)

Another large research project was executed by Anami, which focused only on welded joints. For different joints he tested local joint specimens and girder specimens which included the same type of joint. From the large amount of data the most striking examples are depicted in figure 4.6 and figure 4.7, in which it is clear that the high strength specimens mostly completely blend in with the lower strength specimens. He found that welded high strength steel structures might even behave worse than standard steel. This effect was most identifiable with the out of plane gusset girder specimens (a loaded plate with a gusset plate attached; non load carrying fillet welds), see the right diagram in figure 4.7. Anami suggests that this might be the case because in higher strength steel, higher residual stresses are possible. The fact that the effect is mostly visible in the girder specimens is because in these specimens the residual stresses could arise due to constraints. Other parameters, such as heat input and weld beat effects, were kept as constant as possible between the joints specimens and girder specimens. Unfortunately, the applied stress ratio is not stated.

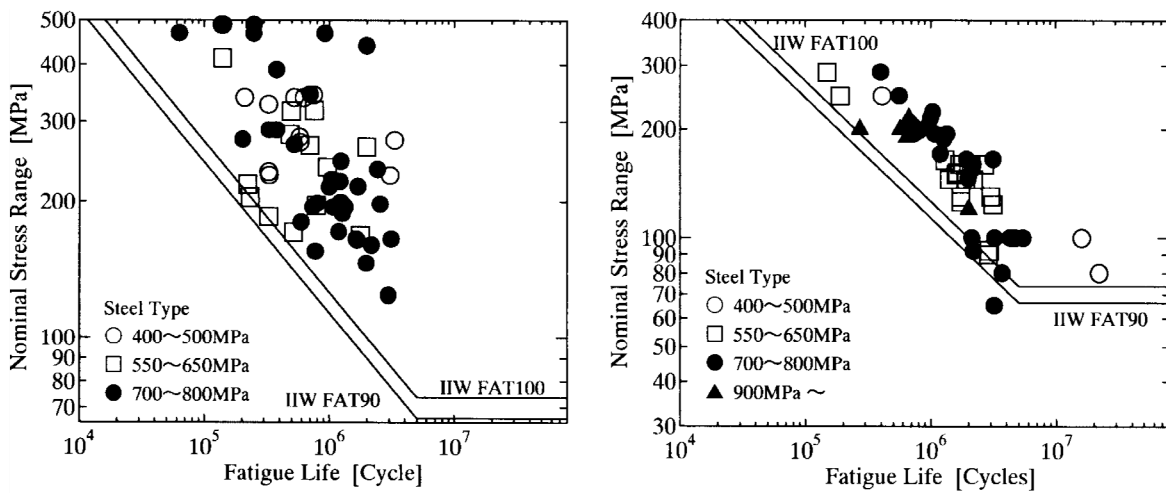


figure 4.6 Fatigue test data for longitudinal welded joints. Left: joint specimens, right: girder specimens. The mentioned strengths are tensile strengths (source: Anami et al., 2001)

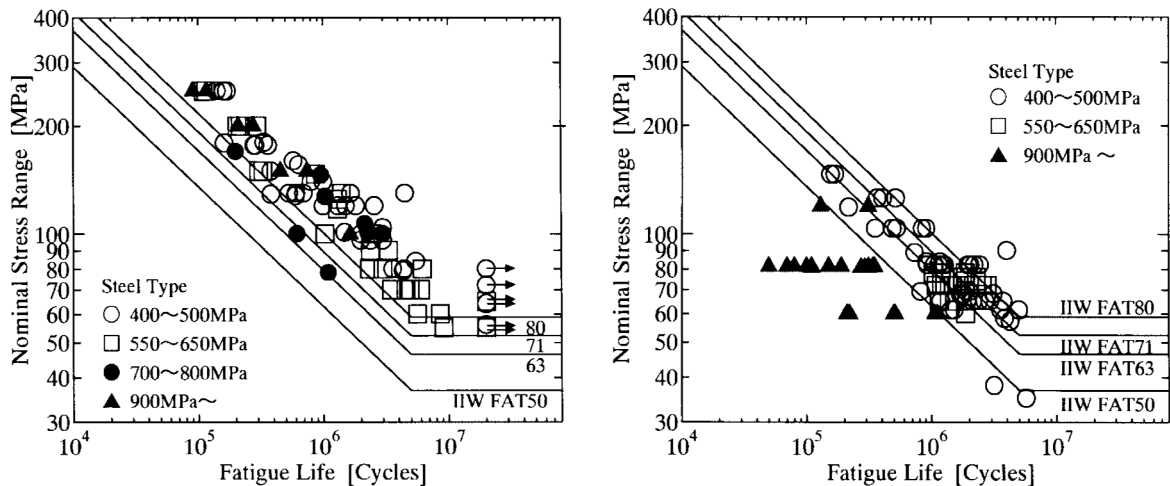


figure 4.7 Fatigue test data for out-of-plane gusset welded joints. Left: joint specimens, right: girder specimens. The mentioned strengths are tensile strengths (source: Anami et al., 2001)

From the information gathered two conclusions can be drawn. First, there is indeed an effect of the material strength on the fatigue strength of a component or joint. It is an approximately linear relation between fatigue strength and material tensile strength. However, in real constructions it will be very complicated to actually achieve this improvement, because high strength steels are more sensitive to roughness, notches and defects, caused by production or welding, which could easily lead to a fatigue strength comparable to the fatigue strength of standard steel.

4.3 Literature regarding TIG-dressing and high strength steel

4.3.1 TIG dressing process

According to IIV recommendations the aim of TIG dressing is 'to remove the weld toe flaws by re-melting the material at the weld toe. It also aims to reduce the local stress concentration effect of the local weld toe profile by providing a smooth transition between the plate and the weld face' (Haagensen et al., 2001).

The remelting of the weld toe is done with a standard TIG machine. The process is relatively sensitive to weld contaminants such as mill scale, rust, oil and paint. Therefore the area to be TIG dressed must be prepared by cleaning, wire brushing and light grinding. A lot of parameters are of influence on the end result, such as the shielding gas, travel speed, welding current, position of torch, etc. For exact specifications of the correct TIG-dressing procedure, reference is made to the IIV recommendations (Haagensen et al., 2001). An example of a TIG dressed specimen is shown in figure 4.8, where the right side of the weld has already been dressed and the left side is still in the as welded condition. The change in geometry regarding the weld toe is clear.

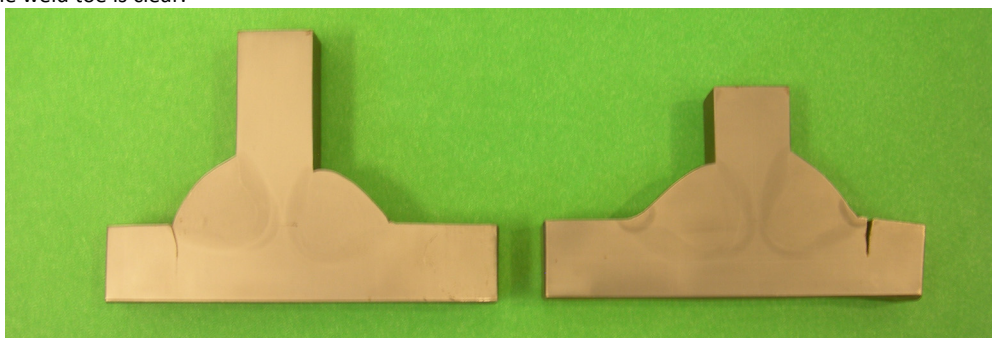


figure 4.8 Two polished specimens. On the left as welded, on the right TIG dressed.

4.3.2 Strength improvement according to current design codes and recommendations

Eurocode

Eurocode NEN-EN 1993-1-9 does not specify any benefit from weld improvement techniques, such as TIG-dressing. However, for certain detail categories grinding is specified. For example in table 8.3 of NEN-EN 1993-1-9, the detail category 112 is applicable for butt welds which, along with other quality specifications, have to be ground smooth. If this

specification is not met, the detail category is lowered. Unfortunately, burr grinding, TIG dressing or hammer peening is not appreciated in this manner.

IIW recommendations

The IIW recommendations acknowledge the possible beneficial effect of weld improvement techniques which are classified in three categories:

- Methods for improvement of the profile (machining the entire weld or weld toe and TIG/plasma/laser dressing)
- Methods for improvement of residual stress conditions (peening, overstressing, thermal stress relief)
- Methods for improvement of environmental conditions (painting, resin coating)

For the methods that improve the weld profile, recommendations are given. Only the possible improvements of TIG-dressing will be further explained here.

First the applicability is discussed. The application of the recommendations is limited to joints that are suitable for improvement, which are the ones where the crack starts from the weld toe. Furthermore, the recommendations are only applicable for steels with a yield strength lower than 900 N/mm², joints with plate thicknesses within specified boundaries and high cycle fatigue. Some other specifications can be found in the IIW document (Hobbacher, 2007). All improvements are given as an increase in fatigue strength with the as welded conditions as starting points and can only be used in the nominal stress approach or structural stress approach.

The improvement in nominal stress design by TIG dressing is specified as a factor 1.3 in fatigue class for fatigue classes with FAT ≤ 90, with a maximum possible fatigue class of 112 after improvement. In structural stress design table 4.1 is applicable. Note that no difference in improvement is specified between mild steel and higher strength steel, while for other improvement techniques, such as needle peening and hammer peening, high strength steel welded joints are assumed to have higher fatigue strength improvement. With both methods it must be noticed that the fatigue resistance of the improved joint is always limited by the fatigue resistance of the base material.

Material	Load carrying fillet welds	Non load carrying fillet welds and butt welds
Mild steel ($f_y < 350 \text{ N/mm}^2$)	112	125
Higher strength steel ($f_y > 350 \text{ N/mm}^2$)	112	125

table 4.1 FAT classes for use with structural stress approach at joints improved by TIG-dressing. For as welded connections the FAT classes are 90 or 100, depending on the specific detail (source: Hobbacher, 2007)

The beneficial effect of TIG-dressing is not taken into account in the notch stress approach as prescribed by the IIW because the actual weld geometry, which improves due to the dressing, is replaced in this code by an artificial geometry with a radius of 1 millimeter, because of the wide scatter and irregular geometry of a real weld profile.

NPR-CEN/TS 13001-3-1

In this design code the different weld classes specified in NEN-EN 25817 are used. To the different detail categories, different FAT values are given, depending on the weld quality. CEN/TS 13001-3-1 specifies another extra-high quality category for welds: B*. B* welds have to comply with, in addition to the B quality requirements:

- Full penetration without initial points
- Both surfaces machined flush ground down to plate surface; grinding in stress direction
- The weld toe post-treated by grinding, remelting by TIG, plasma welding or by needle peening
- Eccentricity of the joining plates less than 5% of thickness of greater plate
- Sum of lengths of concavities of weld less than 5% of total length of the weld
- 100% NDT (inspection along whole weld length)

These B* quality welds have a higher FAT-value, just as the B quality welds have a higher FAT-value than the C quality welds. Furthermore, the code allows C quality welds of any type to be upgraded to B quality welds for fatigue design if TIG dressing is applied at the potential crack initiation zone in order to increase the fatigue strength.

To illustrate the benefits of this quality improvement, an asymmetric butt joint with normal stress across the weld is taken as an example, see table 4.2. The 11% benefit of the upgrade from C quality to B quality is less than the 30% increase the IIW prescribes, but the application of the upgrade is not limited to a certain FAT-value, as is the case in the IIW recommendations. The extensive weld treatment to upgrade a weld to B* quality, including grinding and TIG dressing also grants about the same amount of extra fatigue strength.

FAT	Weld quality	Relative improvement
112	B* quality	1.12 (1.24 in relation to FAT140)
100	B quality	1.11
90	C quality	1.00

table 4.2 FAT values specified for different weld qualities (source: NPR-CEN/TS 13001-3-1)

4.3.3 Influences of TIG-dressing on material and geometry

Geometry

In the IIW recommendations on weld improvement techniques (Haagensen et al., 2001) detailed information is given on the TIG-dressing progress and some global information is given on the geometrical result of the process. The torch position resulting in the optimum shape in theory and an actual specimen are depicted in figure 4.9.

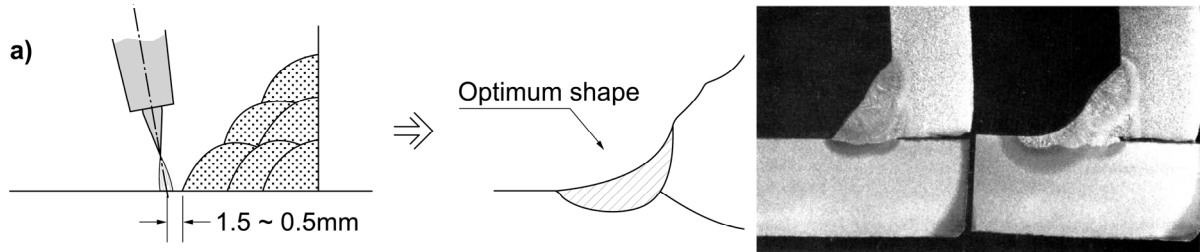


figure 4.9 Effect of TIG-dressing according to IIW recommendations (source: Haagensen et al., 2001)

The geometrical changes of TIG dressing can be quantified if the weld toe radius and weld toe angle are defined (see figure 4.10). The main effect of TIG dressing is the increase of the weld toe radius which results in a lower stress concentration at the weld toe. The weld toe angle remains approximately the same for fillet welds or butt welds with a cap that is high enough. For rather flat butt welds the angle will be reduced. The reduction of weld defects such as microcracks and small inclusions is more difficult to quantify, and is covered in the scatter of the results of most researches. In fact, the TIG dressing should reduce scatter by reducing the defects.

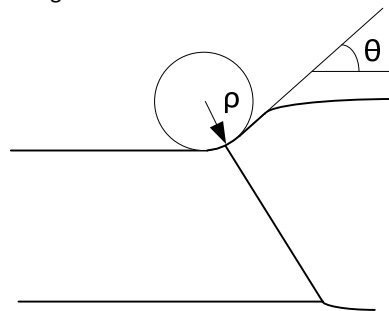


figure 4.10 Definition of weld toe radius and weld toe angle

Different authors have done research on the change of weld toe radius as a result of TIG dressing. Pedersen has collected a number of studies and has compared the weld toe radius of three weld improvement techniques with the as welded condition (Pedersen et al., 2010). His results are shown in figure 4.11. It is clear that a significant improvement in weld toe radius can be achieved by TIG dressing from an average of 1-1.5 millimeter to an average of 6 millimeter. However, the variation of the radius also increases much compared with the as welded condition. Unfortunately it is not clear on which weld type these analyses are made, but context suggest the considered studies are mostly focused on fillet welds. This would also clarify the absence of measured weld toe angles.

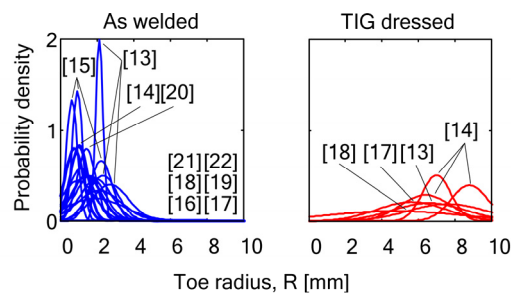


figure 4.11 Comparison of toe radii in as welded and TIG dressed condition; the numbers between brackets refer to the sources of the graphs in the original article (source: Pedersen et al., 2010)

Residual stresses and microstructure

The additional weld process will have its influence on the residual stress distribution in the specimen, the microstructure and the associated hardness of the material in the (new) fusion zone and HAZ. A concern when TIG dressing is applied to high strength steel connections is the possibility of excessive softening of material (Pedersen et al., 2009). His investigation showed a hardness drop of 15% to 20% in the TIG dressed area.

A numerical analysis of the influence of TIG dressing on S690 base material has been made by Hildebrand (Hildebrand et al., 2006). His results show a strong increase in martensitic structure in the TIG dressed region where the previous state was mainly bainite. He also found a reduction in residual stress at the surface of the joint, while internally the area with high residual stressed increased. The results of the simulation for a butt joint are shown in figure 4.12.

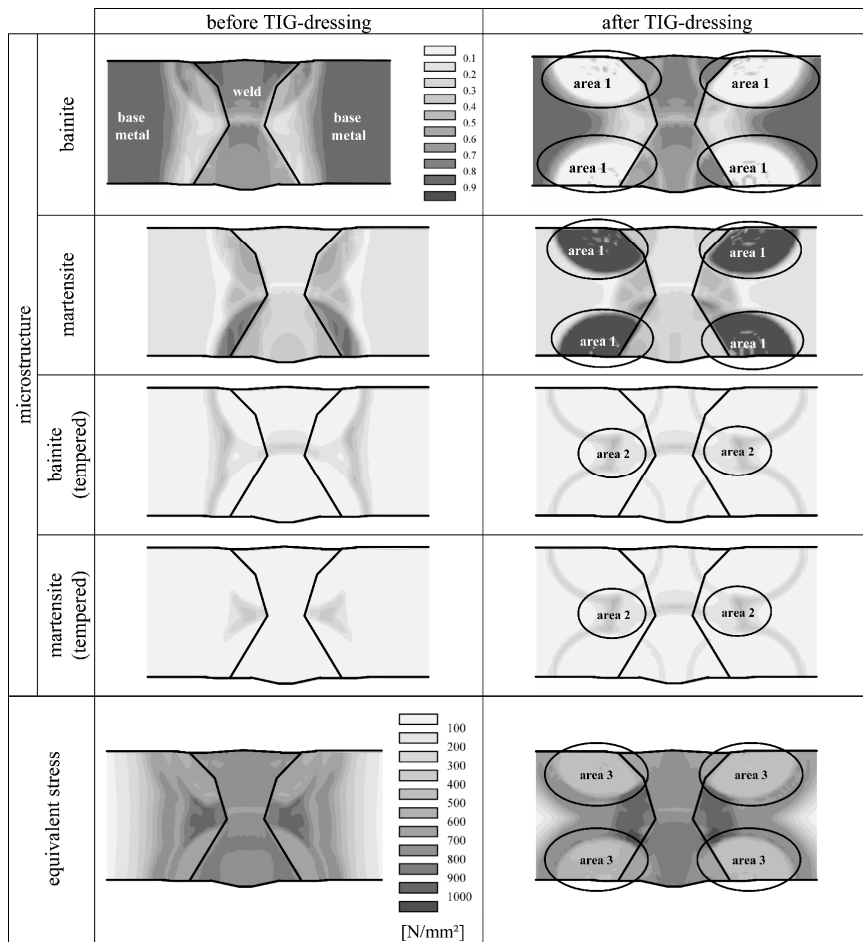


figure 4.12 Microstructure and residual stress in simulated, TIG-dressed butt joint (source: Hildebrand et al., 2006)

These results agree well with the research of Lopez Martinez (1997), where residual stresses were measured in actual specimens, before and after TIG-dressing. The material that was used has a yield strength of 590 N/mm² and a tensile strength of 757 N/mm². He also found evidence that TIG-dressing does not only influence the fatigue strength by geometrical modification of the joint, but also by lowering the residual stresses at the surface of the plates. The tests were executed on test specimens as shown in figure 4.13. In figure 4.15 to figure 4.18 his findings are shown.

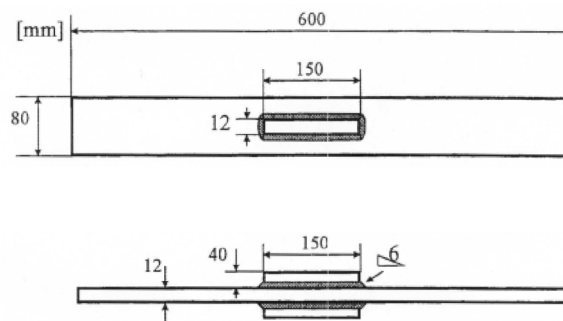


figure 4.13 Geometry of specimens tested by Martinez (source: Lopez Martinez et al., 1997)

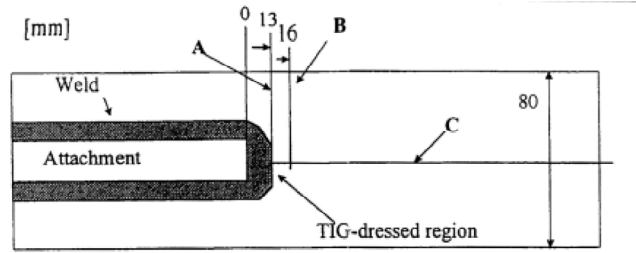


figure 4.14 Upper view of test specimen with locations for residual stress measurements (source: Lopez Martinez et al., 1997)

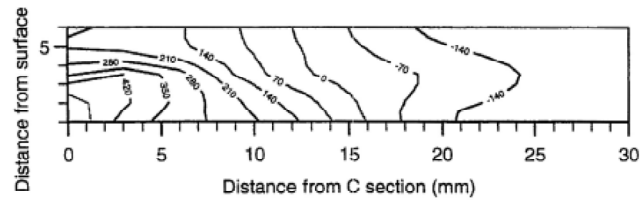


figure 4.15 Longitudinal residual stress distribution in A-section of as welded specimen (source: Lopez Martinez et al., 1997)

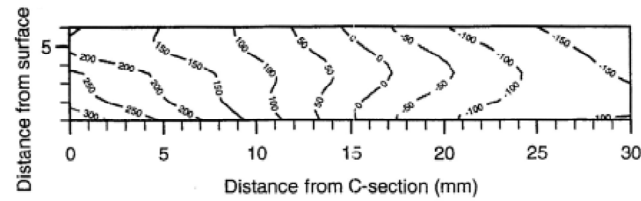


figure 4.16 Longitudinal residual stress distribution in B-section of as welded specimen (source: Lopez Martinez et al., 1997)

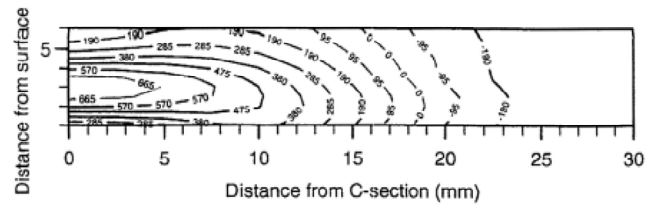


figure 4.17 Longitudinal residual stress distribution in A section of TIG-dressed specimen (source: Lopez Martinez et al., 1997)

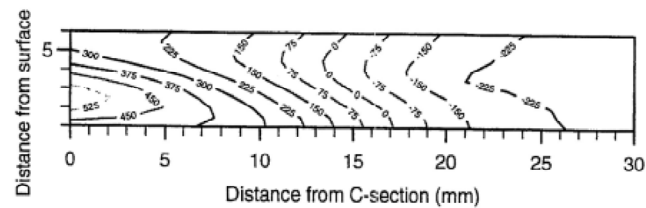


figure 4.18 Longitudinal residual stress distribution in B section of TIG-dressed specimen (source: Lopez Martinez et al., 1997)

It is clear that the maximum residual stress increases due to TIG-dressing. For example, the maximum stress in the stress state of figure 4.15 is 556 N/mm^2 while in the stress state of figure 4.17 this is increased to 699 N/mm^2 . At the surface however, the residual tensile stresses are reduced from 360 N/mm^2 to 256 N/mm^2 . As explained in 2.3.2, tensile residual stresses have a detrimental influence on the fatigue strength of a component. Therefore, a reduction of tensile residual stresses can increase the fatigue strength of the joint. At some distance from the weld toe, section B in figure 4.14, the tensile stresses at the surface increase due to the TIG-dressing, compare figure 4.16 and figure 4.18. This has of course the effect that the compressive residual stresses near the edge of the specimens increase. For welds, the most likely location

for crack initiation is at the weld toe at the surface. This is exactly the location where the residual stresses are reduced, which explains the beneficial effect of the change of the residual stress state.

4.3.4 Influences of TIG dressing on fatigue strength

In the previous paragraphs the main influences of TIG dressing are discussed:

- Increase of weld toe radius
- Change of residual stress state
- Change of microstructure
- Reduction of weld flaws and inclusions at the weld toe

Especially the reduction of weld flaws and inclusions in combination with the increase in weld toe radius is assumed to create the beneficial behaviour of TIG dressed specimens when compared with as welded specimens.

In general, two results are reported in research concerning the increase in fatigue strength: the fatigue strength at a certain number of cycles (usually $2 \cdot 10^6$ is taken as an example) increases and the fact that this strength increase is most notable at a high number of cycles. This second result means a higher m -value, or flatter S-N curves. Some examples of these effects are shown below, from a study by Dahle on fillet welds. The flatter appearance of the S-N curve is caused by the increase in crack initiation time, which mostly occurs at lower stresses and higher cycles. Because the high cycle regime has more benefit from the treatment, the S-N curve rotates and the m -value is increased. The fact that crack initiation becomes important means that the governing factors for fatigue are stress concentration factor, material strength, mean stress, residual stress, stress range, etc. (Dahle, 1998). For high strength steel the crack initiation time is more important with respect to the total fatigue life than it is for standard steel, therefore the high strength steel data show a clearer flattening of the S-N curve due to TIG dressing (see figure 4.19) and increase of fatigue strength than standard steel.

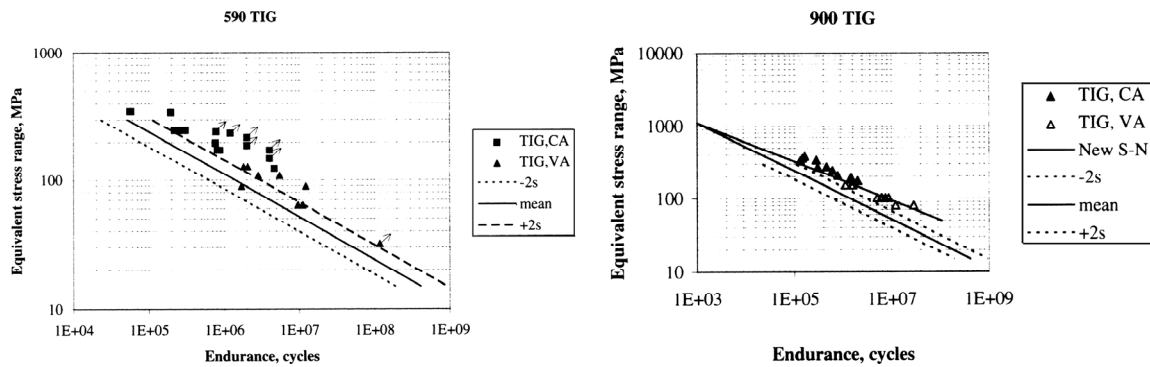


figure 4.19 S-N curves of TIG-dressed fillet weld specimens compared to an as welded reference scatter band. Left: S590 steel, right: S900 steel (source: Dahle, 1998)

Dahle has coupled the change in m -value, $\log(C)$ value and FAT-value to the material strength. The results of this regression are shown in figure 4.20. It is clear that both the m -value and the value of intersection with the vertical axis increase when the material strength increases. This will also result higher FAT values. The algebraic formula for the improvement of the FAT-value is:

$$\Delta \text{FAT} = 0,001056 \cdot R_{0,2} + 0,65982 \quad (4.1)$$

It must be noted that this FAT-value does not correspond directly to the standard detail categories, but is to be used with the also adjusted slope m and intersection $\log C$ as shown in figure 4.20.

This formula leads to a relatively low increase in fatigue strength for normal steel strengths, but matches with the data. A remark is made that the wide scatter of the data resulted in a very conservative design line.

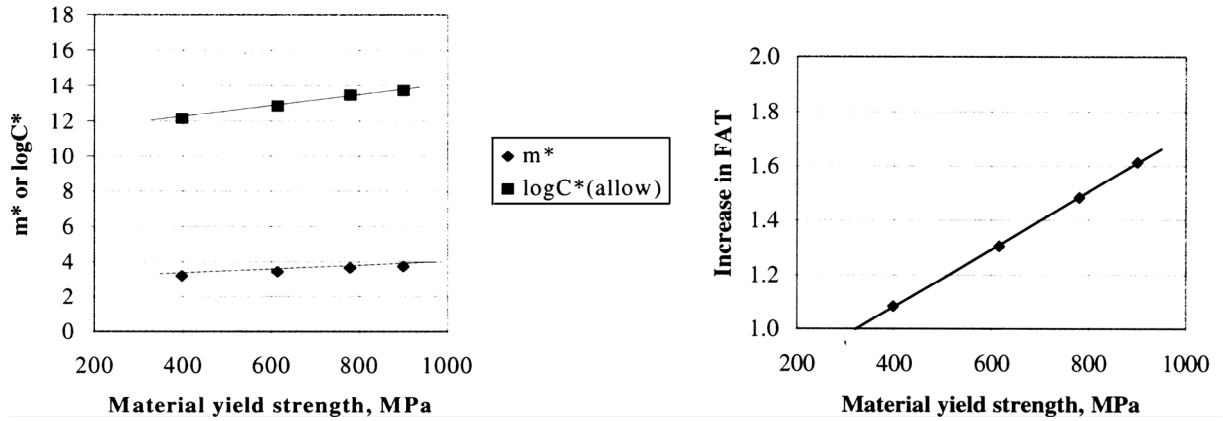


figure 4.20 Influence of material strength on S-N curve parameters. Left: m and C. Right: FAT-value. (source: Dahle, 1998)

Dahle also calculated the increase in fatigue strength of the individual data points with respect to the reference scattering band. In table 4.3 the average outcomes of this calculation are shown per steel grade. It is clear that the material strength has an influence on the beneficial effect from TIG dressing. Both data from constant amplitude loading and variable amplitude loading are incorporated in the calculation.

Steel Grade	Yield strength [N/mm ²]	Average improvement of fatigue strength
350	398	1.185
590	615	1.424
700	780	1.725
900	900	1.894

table 4.3 Increase in fatigue strength (source: Dahle, 1998)

Similar results arise from the research of Pedersen et al. (2009), where the free slope of the fatigue curve of TIG-dressed S700 grade specimens increases to 5.9 compared to 4.2 for as welded specimens of mixed steel grade. The reported beneficial effect at 10^5 cycles is around 38% and around 70% at $2 \cdot 10^6$. This research also considers fillet welds only

More research on the beneficial effect of TIG dressing on fillet welds has been done by Huo (2005). This research does not focus on high strength steel but distinguishes results for constant amplitude loading and variable amplitude loading. The results, comparing two post weld treatments to the as welded condition, are shown in figure 4.21. The test data show much less scatter than the low strength data of Dahle, which leads to a greater increase of the fatigue strength: approximately 37% for steel with $\sigma_y=390$ N/mm².

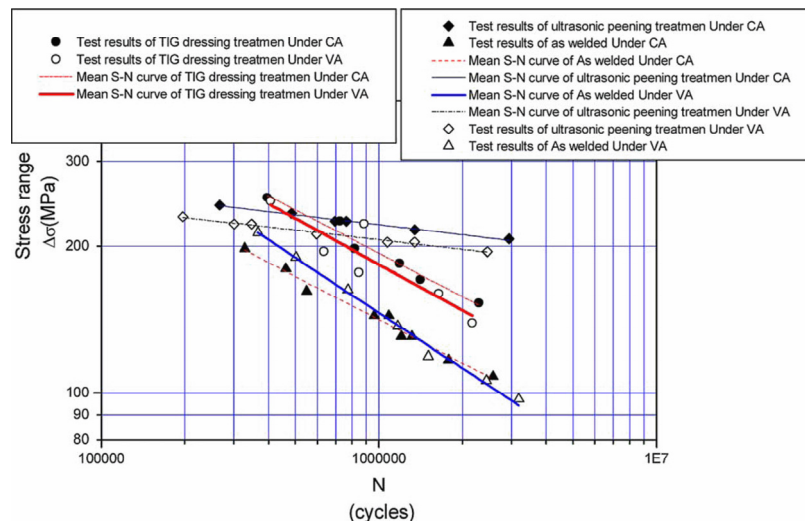


figure 4.21 Comparison of two weld improvement techniques with the as welded situation for a steel with a yield limit of 390 N/mm² and a tensile strength of 590 N/mm². Tested on fillet weld specimens (source: Huo et al., 2005)

The effects discussed by Dahle are partially visible in the data published by Huo. If only the constant amplitude (CA) data published by Huo are considered it is clear that the fatigue strength of the connection increases, but the higher m-value is barely visible. This might be due to the fact that the steel in question is of standard quality, while the flattening effect in the study of Dahle was most notable for higher strength steels.

Other results are published by Haagensen, who found an average increase of 44% in the fatigue strength of a fillet weld joint, but no change in slope of the S-N curve (Haagensen et al., 1987). This result was also found for standard steel with a yield strength of 365 N/mm^2 , which means it does not exclude the flattening effect for higher strength steels.

All research shows an increase in fatigue strength of TIG dressed specimens. The increase in fatigue strength differs from 20% to 40% for standard steels and can be as high as 90% for very high strength steels. The research data by Dahle and Pedersen also shows a rotation of the S-N curve, especially for high strength steels in the case of Dahle. Other researches do not show this effect, but also do not incorporate high strength steels, so they do not confirm nor refute the presence of this effect. All discussed researches consider fillet welds only. Whether the effect will be similar on butt welds shall have to show from this testing programme.

5 Test setup

5.1 Chapter outline

In this chapter the testing programme and test setup are discussed. In paragraph 5.2, the identification, dimensions and fabrication of the specimens is discussed. The test setups that have been used for the different experiments are shown and explained in paragraph 5.3.

5.2 Testing programme

5.2.1 Identification of test specimens

In total there were 11 plates available for testing, each with different specifications. The specimens indicated by a V consist of two rolled plates connected by a V-butt weld. The specimens indicated by a C consist of a rolled plate and a cast plate of similar static strength, connected by a V-butt weld. The cast steel plate is in general slightly thicker (about 5%) than the rolled steel plate. The number in the specimen identification code refers to the first two numbers of its steel grade. The available plates are:

- Plates V89, V46, V69, C69 and C46 with approximate dimensions 330 x 25 x 950 mm³.
- Plates C11 and V11 with approximate dimensions 330 x 20 x 950 mm³.
- Plate C89 with approximate dimensions 320 x 25 x 950 mm³, with a longitudinal cut along the full length except for the weld area.
- Plate C89a with approximate dimensions 160 x 25 x 950 mm³.

With the available material 24 strips with a width of approximately 100 millimeter were produced for fatigue testing. Each plate, except C89 and C89a, is therefore divided in three pieces of approximately 100 millimeter and one ±25 millimeter residual strip which can be used for hardness measurements. The C89 plate is divided in two specimens and the third C89 specimen is produced from plate C89a. The produced specimens are shown in Annex B in tabulated form. The material specifications can be found in the material certificates provided in Annex D.

5.2.2 Preparation of specimens

The specimens were prepared according to IIW recommendations on TIG dressing (Haagensen et al., 2001). Both the cap and root sides of the V-butt weld were TIG dressed. To provide a suitable geometry on which to apply TIG dressing, the weld root was ground off until a limited height remained. The weld roots of two specimens could not be TIG dressed:

- C69. After grinding the weld root, small porosities were visible. To prevent these gas inclusions swelling up during the TIG dressing process, resulting in an unsatisfactory end result, this root was not TIG dressed. It would be interesting to investigate whether these gas inclusions would indeed have spoiled the TIG dressing process, whether these inclusions would show up on an X-ray test and whether they would pass or fail this test. Depending on the answers on these questions these porosities could have serious consequences for the practical application of the TIG dressing process.
- C89. This plate consists of 2 butt welded specimens joined together longitudinally. One half of the plate had insufficient weld height to prevent the TIG dressing process causing undercut. Therefore, this half was not TIG dressed on the weld root.

In both these cases only the weld toes at the weld cap were TIG dressed. Because the misalignment due to welding will cause extra tensile stresses at the weld cap when the fatigue tests commence, the fatigue cracks are expected to initiate there. Therefore the decision not to TIG dress the weld roots will probably not have any influence on the outcome of the tests.

All plates were flame cut into strips of approximately 100 millimeter in width. Subsequently a reduction in cross section was made near the weld to prevent fatigue cracks in the parent material near or in the clamps of the testing rig. The final dimensions of all specimens are depicted in Annex B.

5.3 Test setup

5.3.1 Measurement of weld geometry

To make an accurate measurement of the weld geometry a sensor has been mounted to an X-Y motor. This laser sensor measures the distance from its own position to the object that is to be scanned. An overview of the measuring setup is shown in figure 5.1.



figure 5.1 Setup to measure the geometry of welds

The X-Y motor has a precision of 1/160 millimeter in both directions. The laser sensor has a resolution of 1/1000 millimeter over its full bandwidth which can be increased by sample averaging to 1/10000 millimeter. An overview of the type of laser sensor that has been used is shown in figure 5.2.

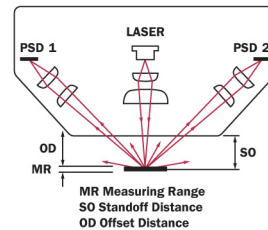


figure 5.2 Type of laser sensor used in measuring the weld geometry

Silicon rubber casts

To speed up the total process of measuring and preparation of the specimens and to make the changing of specimens more manageable, silicon rubber casts were made of the welds. The casts are an exact negative reproduction of the weld. The specifications of the used silicon rubber can be found in the manufacturer's website. The used rubber is of the type PS81020 from Polyservice in The Netherlands. In figure 5.3, laboratory staff is casting the silicon rubber onto the steel plates. The result of the casting is shown in figure 5.4.

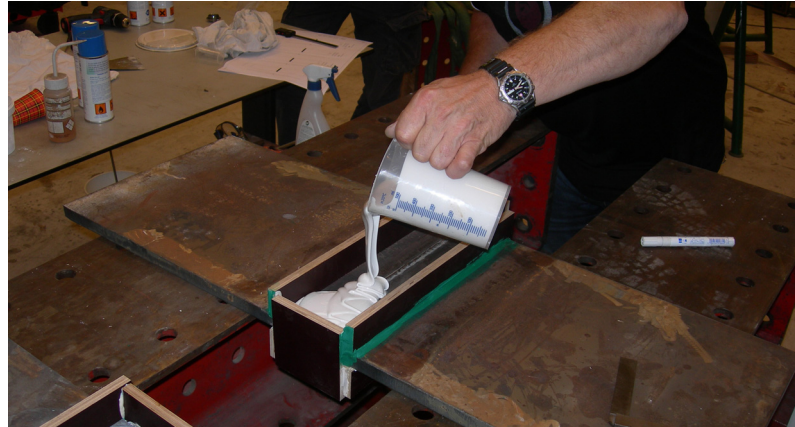


figure 5.3 Casting of the silicon rubber onto the steel plates



figure 5.4 Silicon rubber cast of C89a plate

5.3.2 Measurement of fatigue life

The prepared specimens are tested under axial loading in the Stevin Laboratory of the Delft University of Technology. The used test rig is depicted in figure 5.5. The testing rig has a maximum load of 600 kN.

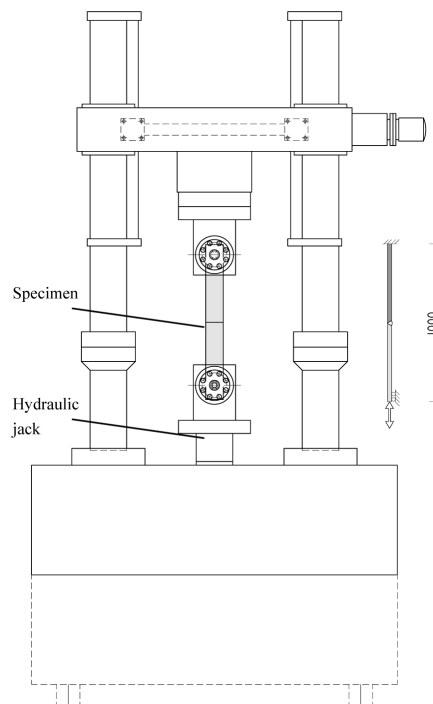


figure 5.5 Schematic of testing rig (image source: Pijpers, 2011)

The starting point of each measurement is the unclamped, unloaded specimen. This means that the deformation arising from the static clamping of the imperfect specimens already results in non-zero measured tensile strains at the weld cap.

For all specimens the intention is to test at $R=0.1$, but due to the aforementioned tensile strains and the resulting stresses, this requires the minimum load to be a compression load in many cases. This is deemed unpractical, and possibly unsafe, therefore a minimal tensile load of 10 kN is taken as a lower bound for the minimum load. The actual R-value is documented, based on both the strain gauges and the measured force.

Twelve strain gauges were placed on each specimen. The location of the strain gauges and global dimensions of the specimens are depicted in figure 5.6. The numbering of the strain gauges is depicted in Annex B.

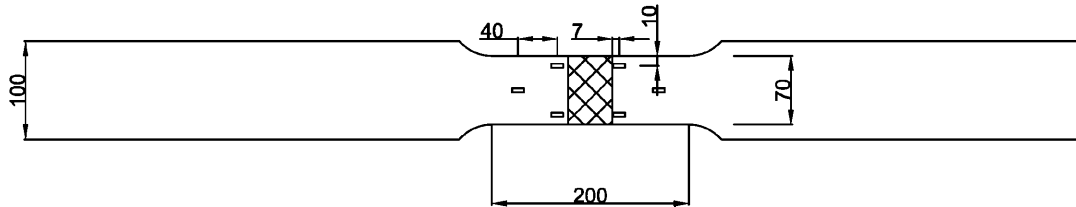


figure 5.6 Global dimensions of specimen and location of strain gauges

Crack monitoring

When one of the strain gauges starts showing a strain range which deflects significantly from its average, the system shuts down the test rig so that, when restarted, crack monitoring can take place. When the crack occurs near one of the strain gauges it can be detected at a crack length of about 10 millimeter. If the crack occurs further away, the crack length at detection can be much longer, up to 40 millimeter.

Cracks are monitored in two ways. To visualize the crack, some petroleum is brushed onto the surface of the specimen and subsequently wiped away. The length of the crack at the surface can then directly be measured with a vernier caliper. This measurement can be executed relatively frequent.

Another method to monitor cracks is crack marking. This involves raising the lower stress in the specimen to about 90% of the upper stress in the specimen, thereby greatly reducing the stress range, for 2% to 10% of the expected total number of cycles to failure. This results in visible 'beach marks' on the crack surface after failure of the specimen. Because the stress range is much lower during this procedure, the number of stress cycles made in this procedure can be neglected in the total amount of stress cycles before failure. A good example of the result of crack marking is shown in figure 5.7, but not all specimens give the good results as shown in the image. Some specimens fail rather quick after crack initiation, thus allowing only two or three crack markings. In other specimens, while the crack marking was executed more often, none or not all marks are visible. In general, crack marking cannot be executed as frequently as the surface measurement, because the markings must have some distance in between each other, preferable a few millimeters. Furthermore, the assumption that the number of cycles during marking can be neglected will become dubious if crack marking is executed to frequently.

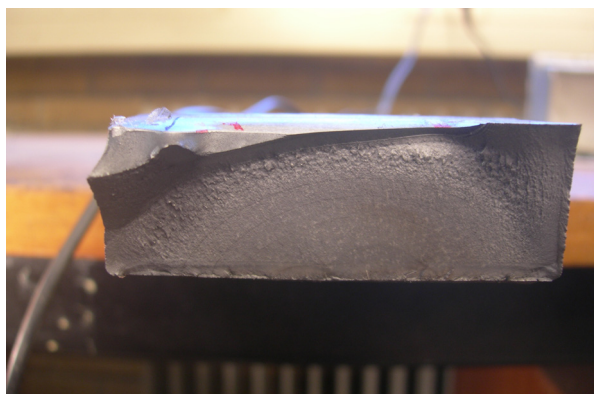


figure 5.7 Beach marks visible in a specimen

5.3.3 Measurement of material hardness

Of all plates a small piece of material has been polished and etched to distinguish the weld material, heat affected zone and parent material. On the different zones hardness measurements have been carried out. This is a standardized test and is executed according to the applying codes. For more details on the testing, reference is made to Annex H. The results are discussed in 7.4.

6 Processing and results of laser measurements

6.1 Chapter outline

In this chapter the results of the laser measurements are discussed. In paragraph 6.2 is discussed how the raw data is processed to usable results. Any issues that were encountered are discussed and a solution is presented. The distribution of the weld toe parameters and any differences between cast and rolled steels or different steel strengths are discussed in paragraph 6.3.

6.2 Test output and processing laser measurements

6.2.1 Test output

The direct output from the laser scan is a table containing the position of the laser and the measured distance. For post processing the laser position and measured distance are separated and the measured data are leveled out by subtracting a plane from the data in such a way that the parent plate has value 0. The matlab scripts to perform these actions, and all coming processing actions are shown in Annex F. Now the first results can be plotted in 3D, as shown in figure 6.1 and figure 6.2.

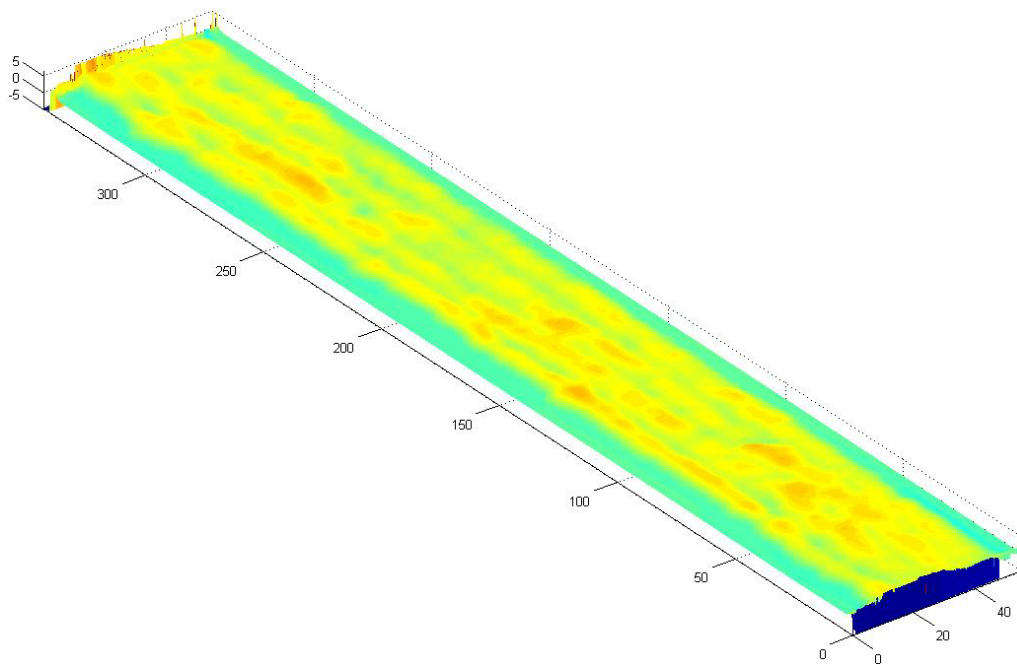


figure 6.1 3D overview of a the weld of plate V46 before TIG dressing, no gridlines are shown to keep the image clear

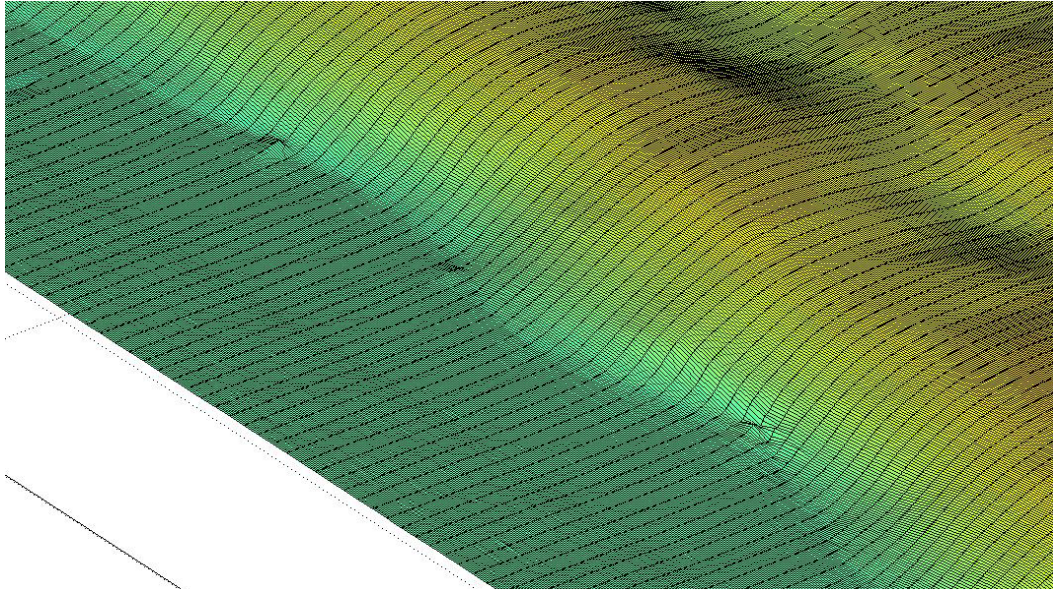


figure 6.2 Zoomed in on figure 6.1, with gridlines at a $0.05 \times 0.5 \text{ mm}^2$ grid

From the same datasets weld cross sections can be plotted (see figure 6.3), which can be used to determine the geometry of the weld toe.

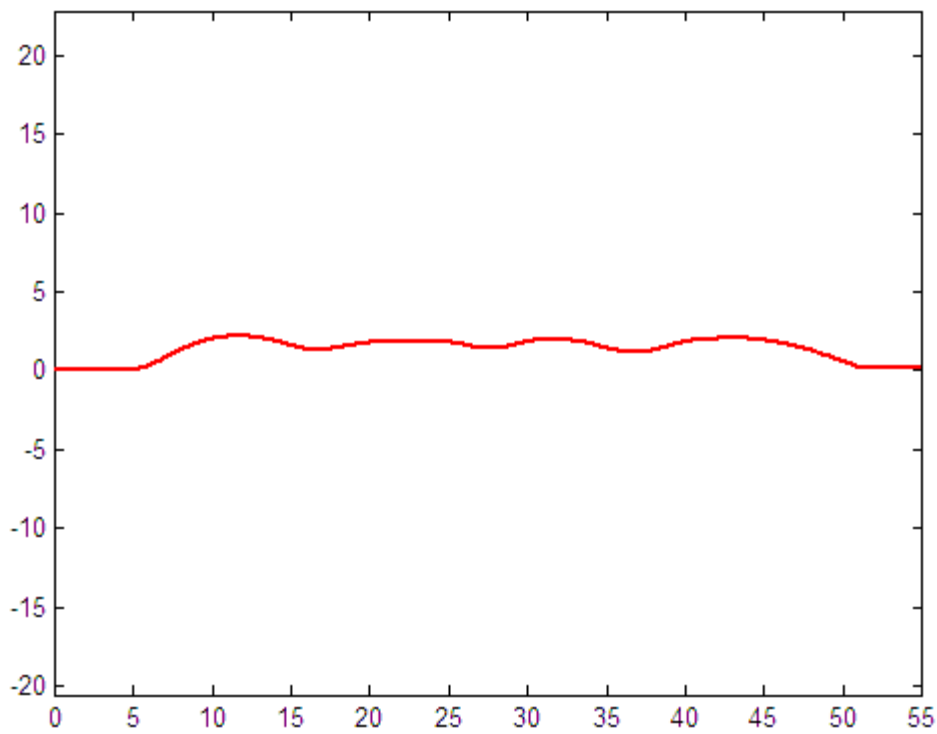


figure 6.3 Cross section of the weld of plate V46. Axes are in millimeters.

Four characteristic values have been chosen to describe the weld toe:

1. Weld toe radius
2. Weld toe angle
3. Weld height
4. Undercut

In figure 6.4 these characteristic values are shown on a fictive, exaggerated weld toe cross section.

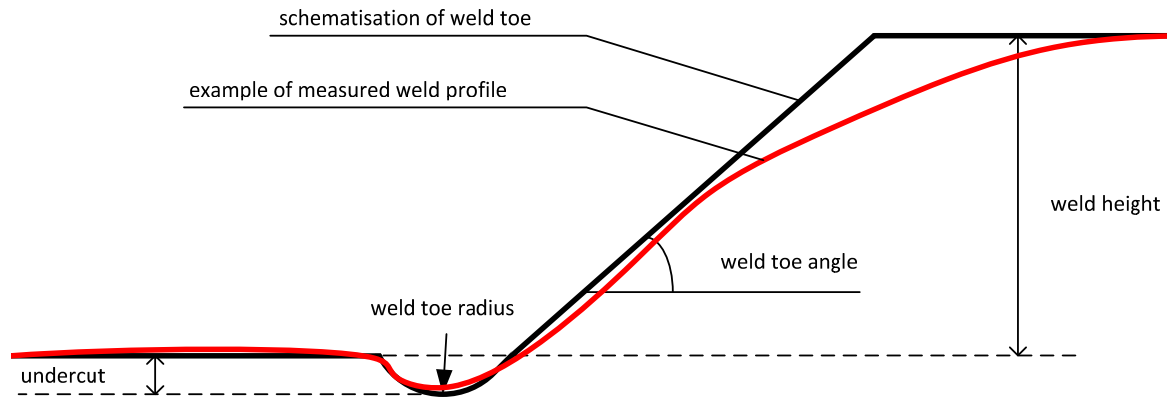


figure 6.4 Possible measured weld profile (exaggerated) and its accompanying schematization

6.2.2 Determining the weld radius

The radius is measured by creating a fine grid around an estimated midpoint for the circle which coincides with the notch root. For each grid point the distance to each data point of the weld geometry is calculated over a user specified section. The grid point that shows the least variation in these distances is the best suitable midpoint and the accompanying weld toe radius is determined by averaging all distances. The script of this process is shown in Annex F. Some steps of the process are shown in figure 6.3 and figure 6.5.

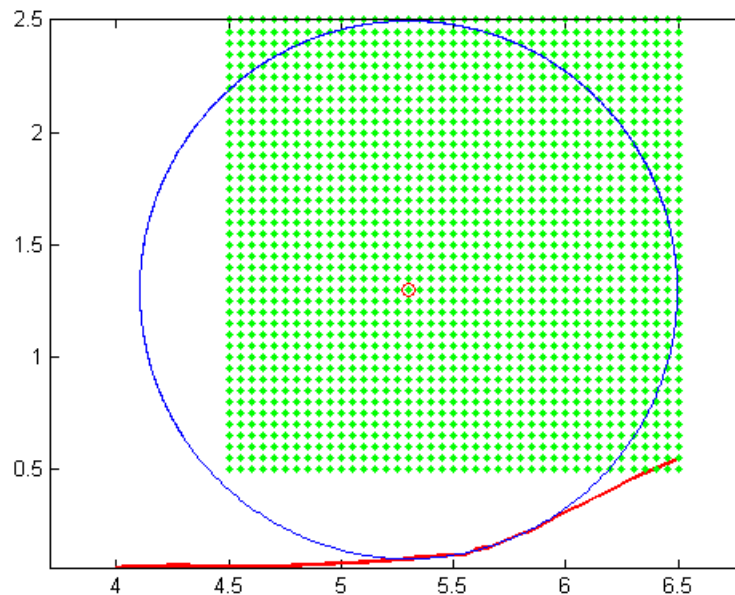


figure 6.5 Optimized circle for the left weld toe (red) of the same weld cross section as shown in figure 6.3. The optimal midpoint is marked. Axes are in millimeters

Unfortunately, the process is not completely automatic. The user must specify the boundaries of the grid by specifying an expected circle midpoint and the grid width and height. If this is not done properly the optimized midpoint will lie at the edge of the grid, because the actual optimal midpoint lies outside the grid. In this case the user can specify a larger grid or relocate the expected midpoint until the optimized midpoint lies at a satisfactory distance from the edge of the grid. The user must also specify boundaries between which the circle must be optimized. In figure 6.5 these boundaries are chosen as 5.25 millimeter and 5.75 millimeter. Of course these boundaries are estimates and could also be estimated at slightly different values. In figure 6.6 a plot is shown where the optimization boundaries were varied to a certain extent.

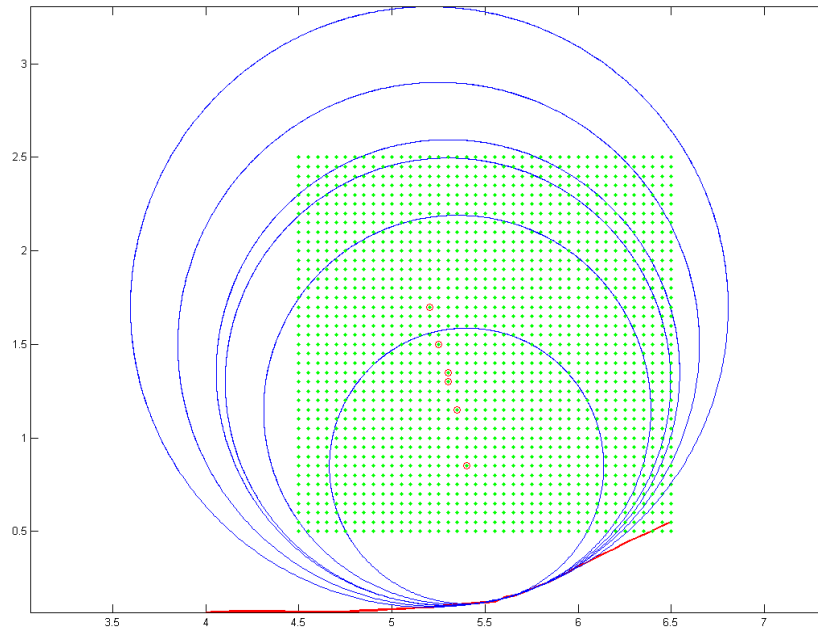


figure 6.6 Different radii for different optimisation boundaries. Axes are in millimeters.

In figure 6.6 different circles are shown as the result of different optimization boundaries. Unfortunately, there is no absolute way of determining which circle is the best optimization. An obvious indication of the best circle is the variation in the distances from its midpoint to the data points: the circle for which the total variation is the least fits the weld geometry the best. However, because the number of data points is reduced when the optimization boundaries are narrowed, it is easier for the program to make a better optimization. Therefore, narrower optimization boundaries will always result in a lower variation. From figure 6.6 can be concluded that rather large differences in weld toe radius can be found if the optimization boundaries are varied. The boundaries and their accompanying radii as drawn in figure 6.6 are shown in table 6.1.

Optimisation boundaries [mm]	Radius [mm]
5.15 – 5.85	1.61
5.20 – 5.80	1.40
5.25 – 5.75	1.20
5.30 – 5.70	1.24
5.35 – 5.65	1.04
5.40 – 5.60	0.74

table 6.1 Different determined radii for different optimisation boundaries

From figure 6.6 cannot clearly be concluded which of the circles fits best. If a zoomed in version of figure 6.6 is considered (figure 6.7) it is clear that the circle with the smallest radius (0.74 millimeter) is too pessimistic. The circle with the largest radius is too optimistic, especially on the right side of the figure. To the eye, the circles with radii 1.20, 1.24 and 1.40 millimeter seem to match best with the weld.

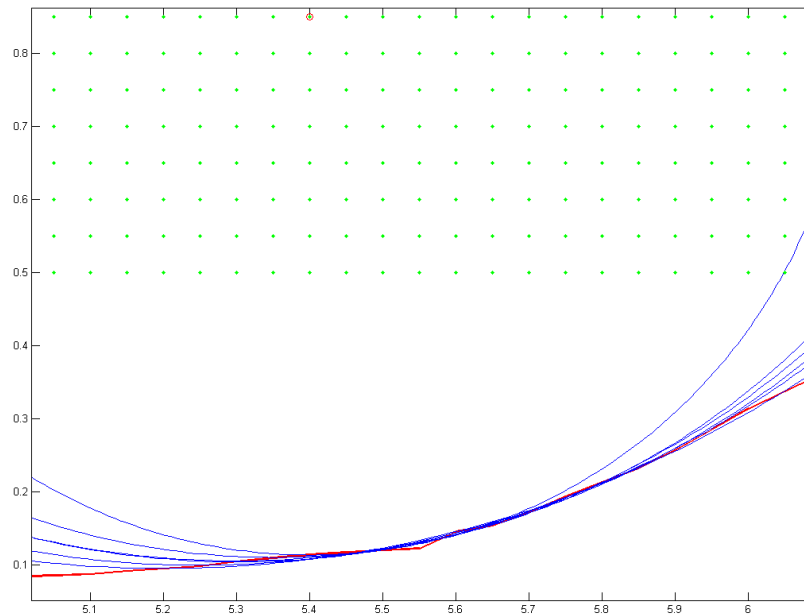


figure 6.7 Zoomed in on figure 6.6. Axes are in millimeters.

Another remark must be made on the small dimple in the weld geometry that can be seen around 5.55 on the horizontal axis of figure 6.7. This could also be regarded as a very small notch, with a very small radius. These types of dimples or other irregularities that could be interpreted as a small notch occur in a large number of weld cross sections, both as welded and TIG-dressed. A choice must be made to either use the large radius or use the small radii as characteristic value.

The following sections will first address the possible subjectivity of the determination of the radii and ways to make it as objective as possible. Then the issues concerning the additional smaller radii will be discussed.

Choosing the 'correct' radius for the weld toe

As described above, the determining of the weld toe radius cannot be done entirely automatic. The user of the program influences the outcome to a certain extent. To determine whether the found weld toe radius is acceptable, a number of checks can be made:

1. Where the found radius intersects or meets the measured weld profile, the tangent of the circle must coincide with the tangent of the measured weld profile.
2. When the boundaries are varied a small amount, the found radii must not greatly differ from each other. For example, the three radii in figure 6.7 which are deemed to fit rather well, are all determined with different boundaries but do not differ greatly. However, if the boundaries of the smallest circle are slightly enlarged the radius varies greatly. In this case, the smallest circle is influenced too much by the small dimple in the measured weld profile.
3. The overall image must be satisfactory. This is of course extremely subjective, but is one of the most important tools to judge a radius. For example: for the program it is very difficult to filter out the small dimple in the middle of figure 6.7, but a person can easily see that, if the large radius has to be determined, the small dimple can be ignored.

To get an estimate of the amount of subjectivity involved in the process, the analysis process has been carried out twice for one weld cast. The results of this are shown in table 6.2. It is clear that the differences in mean and standard deviation are very small. The differences in mean value can even be neglected when the size of the standard deviation is taken into account.

Measurement	Radius		Angle	
	1	2	1	2
Mean [mm]	1.26	1.28	25.64	24.98
Standard Deviation [mm]	1.12	1.02	5.40	5.07

table 6.2 Comparison of measured weld radii and angle for two different measurements of the same weld profile

This test does not prove that the weld profile measurements are fully objective, but can be used as an indication of the amount of variation to be expected in the weld toe parameters by the user input in the program.

Choosing between large and small radius

In figure 6.7 two radii can be seen, a large one, for which the circles are drawn, and a smaller dimple in the middle of the figure. Both these radii could be used to determine the ‘characteristic radius’ for this weld toe profile. This problem is not unique for the weld profile shown in the figure, but occurs regularly.

To solve the problem, experts on welding and fatigue at the faculty of mechanical engineering of Delft University of Technology were consulted. A suggestion was made that the small radius might be too small to have influence on the crack initiation of the specimen. In fracture mechanics this problem is addressed with the Kitagawa-Takahashi diagram (Janssen et al., 2002). This diagram describes the influence of a surface imperfection on the fatigue limit of the specimen. On the horizontal axis the size of the imperfection (a) is shown, which in this case is the depth of the small radius in relation to a ‘smooth’ larger radius. On the vertical axis the threshold stress range to initiate a crack in plain material is shown (σ_{th}). The diagram is build of out of two lines, one describing the fatigue limit, and one line depending on the threshold value of K, as used in fracture mechanics (see 3.4). In the example of figure 6.8 the threshold stress to initiate a crack lies around 350 N/mm² for small defects. When defects increase to a size greater than a certain value, the threshold stress will start to decline. As a rule of thumb we can state that below the intersection point of the two dotted lines, l_0 , the threshold stress does not decline by a large amount. This means that if a small defect (the small radius) is smaller than l_0 it will not influence the minimal stress to initiate a crack, and will therefore not influence the fatigue life.

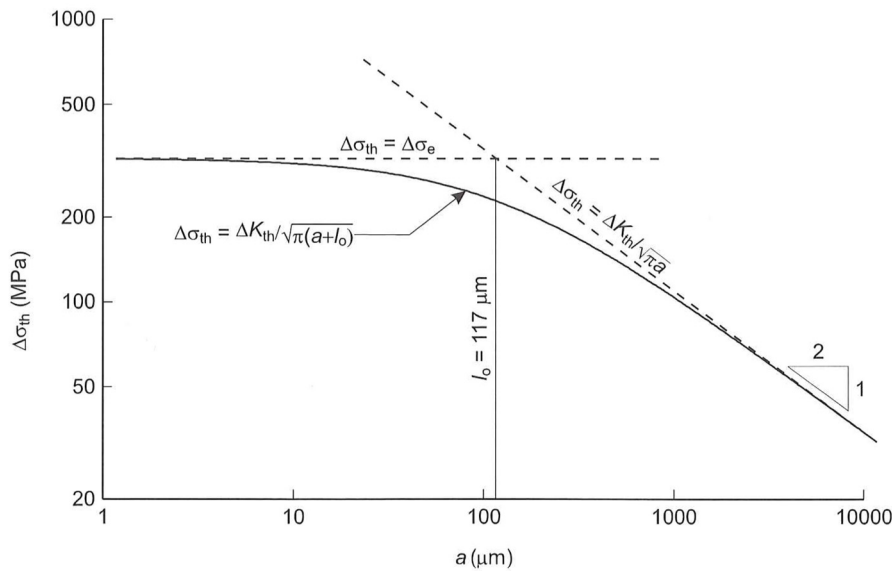


figure 6.8 Example of a Kitagawa-Takahashi diagram for a nodular cast iron ($\Delta\sigma_e = 320 \text{ MPa}$ $\Delta K_{th} = 6.2 \text{ MPa}\sqrt{\text{m}}$) (source: Janssen et al., 2002)

To determine whether the small radii have to be taken into account, first l_0 has to be determined for the different materials. When both σ_e and ΔK_{th} are known, the value of l_0 can be determined. To quickly assess the influence of the small radii not all materials are considered, but a selection of two materials is made: S690 and S1100. It is especially important that S1100 is considered because previous research (Pijpers, 2011) has shown that these specimens are very sensitive for surface roughness.

For the endurable stress range in plain material ($\sigma_{th} = \sigma_E$) reference is made to experiments carried out on this material (Pijpers, 2011). On plain specimens, with mill skin in place, tests were performed. For both materials a runout was found below a certain stress. This stress will here be used as σ_E . The values of the used fatigue limits are given in table 6.3.

Material	σ_E [N/mm ²]
S690	270
S1100	378

table 6.3 Endurable stresses on plain material

Different authors have reported on the value of ΔK_{th} . The different recommendations are shown in table 6.4. A remark must be made on the recommendation of the IIW (Hobbacher, 2007), in which for very small surface cracks it is reported that the K_{th} may be lower than specified in table 6.4. However, based on the experiences of all other authors, where no such remark is made, a value of 63 Nmm^{-3/2} is assumed to be sufficiently conservative.

ΔK_{th} [Nmm ^{-3/2}]	author
101 up to 120	Wanhill, 1991
102.2 up to 208.7	Romeijn, 2006
240-173·R	Gruney, 1979
170-214·R≥63	Hobbacher, 2007

table 6.4 Different estimates of ΔK_{th}

With these data the value of l_0 can be determined. For a limited number of weld cross sections an analysis is made of the depth of the 'small radius' if one is present. The results of this, and the calculated l_0 are shown in table 6.5. It is clear that most radii lie around the value of l_0 (note that the Kitagawa-Takahashi diagram uses log-scales on both axes). The small radii may therefore have an influence on the fatigue strength of that local material, but as this influence is relatively small it can probably be ignored, especially when it is taken into account that for ΔK_{th} values can occur which significantly increase the value of l_0 .

V11			V69		
x [mm]	toe radius [mm]	depth of 'small radius' [mm]	x[mm]	toe radius [mm]	depth of 'small radius' [mm]
30	4.5732	0.0255	30	0.9837	0.0086
60	0.1614	N/A	60	0.8090	0.0149
90	1.7606	0.0189	90	1.7725	0.0287
120	2.7126	0.0171	120	0.3471	N/A
150	0.9171	0.0086	150	0.5420	0.0056
180	1.3947	N/A	180	0.2387	N/A
210	2.2831	0.0088	210	0.5109	N/A
240	1.7988	0.0047	240	1.1260	N/A
270	1.0579	0.0066	270	1.7184	0.0227
300	0.6709	N/A	300	2.0000	0.0187
330	3.6710	0.0381	330	0.4925	N/A
Mean	1.9092	0.0160	Mean	0.9583	0.0165
Stdev	1.3260	0.0114	Stdev	0.6212	0.0086
l_0	0.0088		l_0	0.0173	

table 6.5 Analysis of occurring small radii and their depth in relation to a 'smooth' curve

Furthermore, these smaller radii occur mostly at some distance into the weld, where the maximum stress peak is not located, and therefore suffers from a lower stress range.

As a final argument to choose the larger radius as characteristic, is the fact that the smaller radii occur both in the as welded specimens and TIG-dressed specimens, with comparable regularity. Therefore, the large radius is the changing factor and thus interesting to record.

6.2.3 Determining the weld toe angle, weld height and undercut

For the determination of these three values a platform of straight parent material is used as base value. From this base the angle, height or undercut at the weld toe can be determined. To save time, the measurements only incorporate a limited distance of parent material (a few millimeters). This sometimes leads to difficulties because undercuts cannot always be distinguished from the straight parent material. If additional research is done on this topic, a wider measurement scope is highly recommended. About 10 millimeter of parent material, measured from the weld toe, will probably suffice. It might be possible to increase the across-the-weld grid size at distances greater than a few millimeters from the weld toe, to keep the measuring time within limits.

6.3 Results

6.3.1 Observed geometries

The analysis of weld geometries has resulted in around 750 radii, angles and undercuts and about 375 weld heights for both the as welded condition and the TIG-dressed condition. The as welded geometries all looked very similar, but the TIG-dressed geometries showed four characteristic shapes, which all appeared in different regularity. The global shape of the observed weld toe shapes for both the as welded and TIG-dressed condition are shown in figure 6.9.

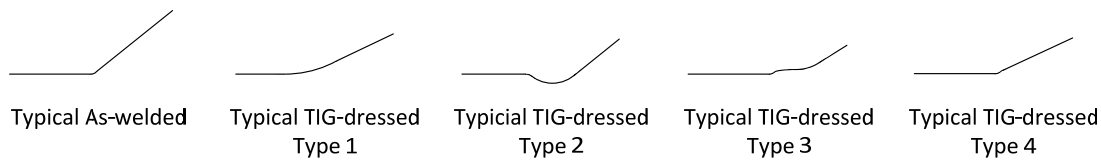


figure 6.9 Observed weld toe shapes (fictive geometries, for communication purposes)

- Typical As welded. The as welded specimens generally have, to the eye, the same geometry. The parent material shows no great undercuts. Then the weld material starts after a relatively small radius. The angle of the weld material is rather steep.
- Typical TIG-dressed, Type 1. This is the desired effect of TIG dressing (see 4.3.3, especially figure 4.9). The overall weld geometry is much smoother. The weld radius is much larger than in the as welded state, and the weld toe angle is reduced.
- Typical TIG-dressed, Type 2. A significant undercut is visible, even to the naked eye on the weld itself. The undercut has depths up to about 0.5 millimeter. The weld toe radius is generally larger than observed in Type 1, and the weld toe angle somewhat steeper than for Type 1. Type 2 does occur, but not very frequently, and also not in every weld.
- Typical TIG-dressed, Type 3. To the eye this looks very similar to Type 1. However, a small ridge can be felt with a sharp object or the fingernail. It seems the weld has solidified before an entirely smooth geometry was formed. In the measurements, the radius and angle of the first, and in all cases smallest, radius was measured. The weld angle of this type is similar to the weld angle of Type 1. Type 3 occurs rather frequently, and can be found in most, if not all studied welds.
- Typical TIG-dressed, Type 4. A small weld toe radius followed by a rather steep angle (similar to as welded) for a very short distance. After this, the angle declines back to similar values as found in Type 1 and Type 3. Type 4 occurs far less frequent than Type 1 and Type 3.

It would be very interesting to make an inventory of the exact frequency of the different types, which could be matched to fabricating conditions (experience of the welder, heat input, etc.) and to the point of crack initiation. Furthermore, it would be very interesting to investigate the existence and frequency of these typical geometries in TIG-dressed welds in practice. The welds studied in this research were all TIG-dressed by the same welder, under the same conditions on the same day. Furthermore, all considered weld cross sections are taken from a very limited number of welds, which could influence the results.

6.3.2 Comparison between rolled and cast steel

All data have been gathered and can be split in TIG-dressed and as welded or rolled and cast steels. It is visible to the eye that TIG-dressing has had great influence on the weld geometry. Whether there is a clear difference between rolled and cast steels has to result from the data from the weld geometry measurements. Only the parameters weld toe radius, weld toe angle and undercut will be compared, because the weld height is deemed independent from the parent material, especially since cast plates are always welded to a rolled plate in this research.

Weld toe radii

Bar diagrams of the density of measured radii for both rolled and cast steel are shown in figure 6.10. An overlay of these two diagrams is shown in figure 6.11. It is clear that the cast steel radii show a sharper peak, in contrast with the smoother diagram shown by the rolled steel data. The location of the peaks of both diagrams shows no large difference, especially when the spread of the data is taken into account.

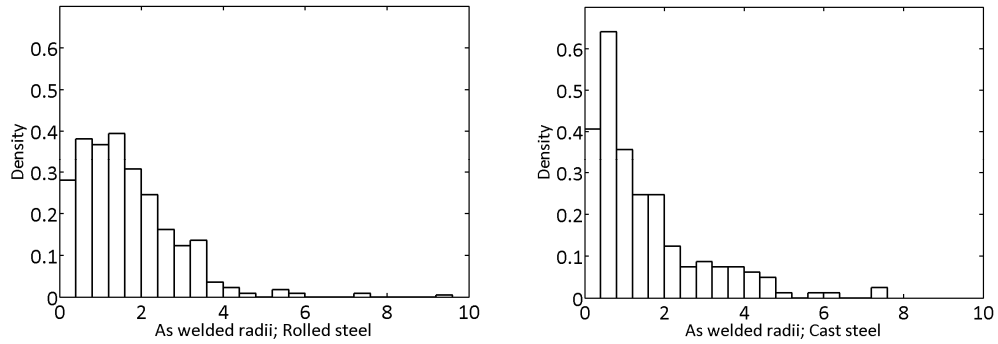


figure 6.10 Comparison of as welded radii between rolled steel and cast steel [mm]

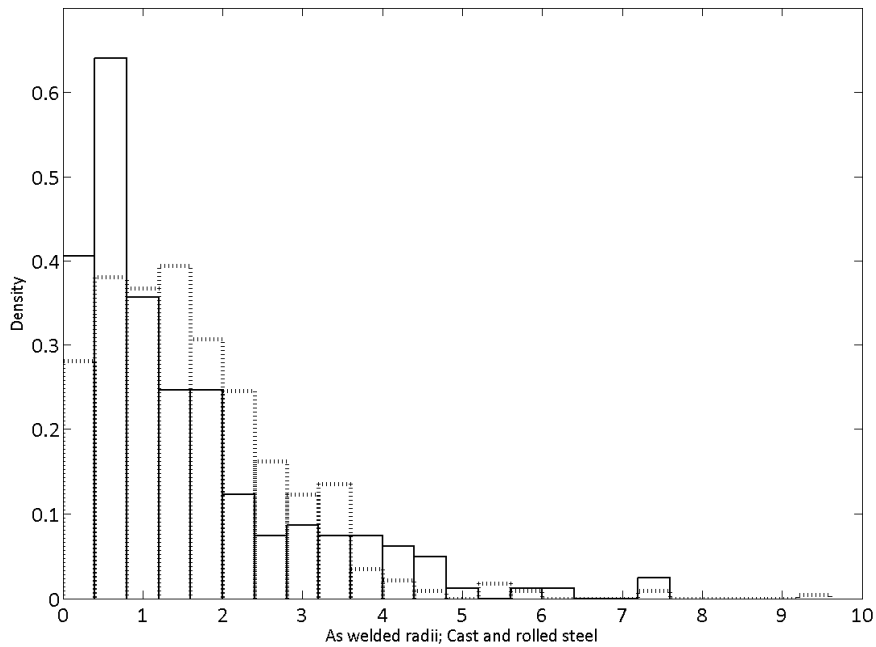


figure 6.11 Overlay of as welded radii; cast (—) and rolled (- -) steel [mm]

Density bar diagrams for TIG-dressed radii are depicted in figure 6.12 with an overlay in figure 6.13. The radii of the rolled steel show a density peak roughly at the same location as the cast steel and an additional peak of smaller radii. This can be a significant difference, but can also arise from the fact that all data result from a limited number of welds. One weld bead that has a lower quality, can easily influence the results to an extent that the differences between the two figures can be explained. Aside from the additional peak the global shape of the diagrams appears roughly the same.

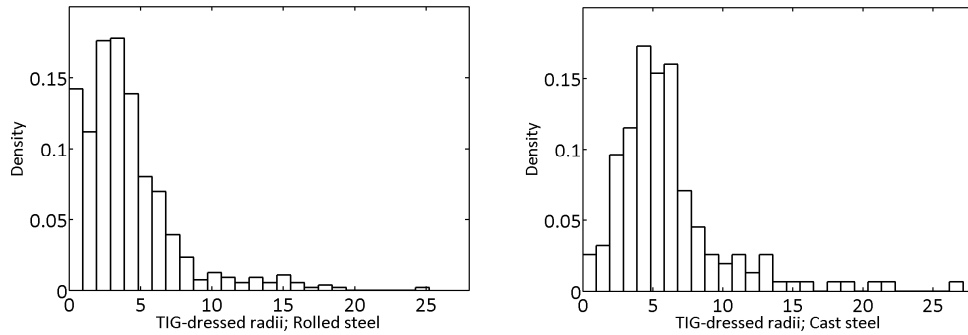


figure 6.12 Comparison of TIG-dressed radii between rolled steel and cast steel [mm]

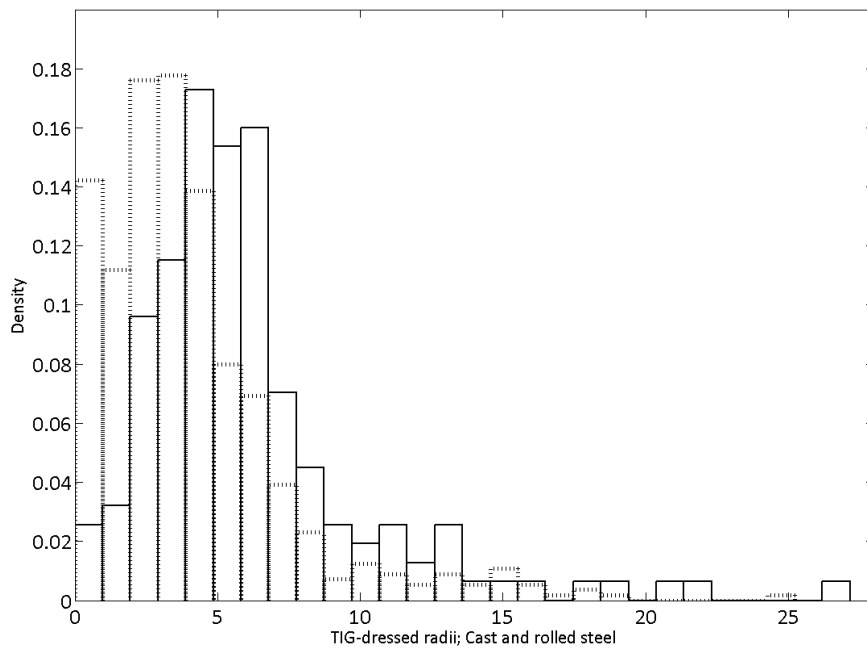


figure 6.13 Overlay of TIG-dressed radii of cast (—) and rolled (- -) steel [mm]

Weld toe angles

In figure 6.14 density bar diagrams are shown for the weld toe angles of as welded specimens. An overlay of both diagrams is shown in figure 6.15. It is clear that the diagrams are very similar.

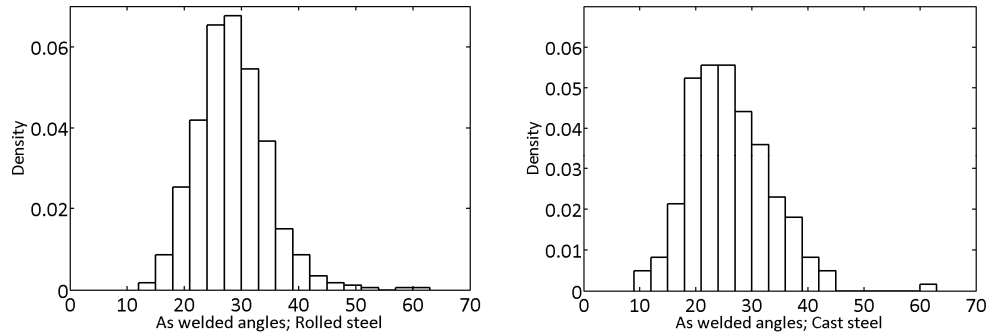


figure 6.14 Comparison of as welded angles between rolled steel and cast steel

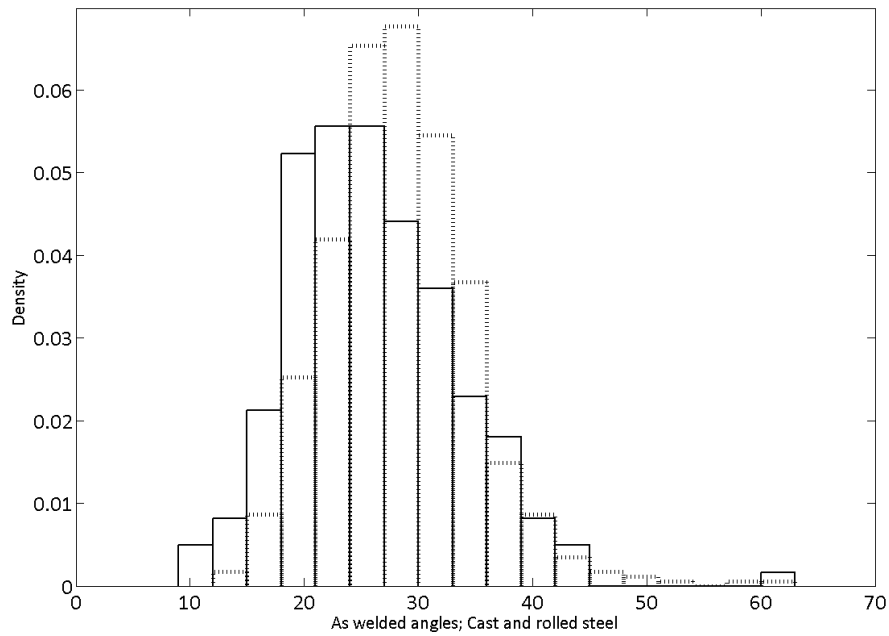


figure 6.15 Overlay of as welded angles of cast (—) and rolled (---) steel

In figure 6.16 density bar diagrams are shown for weld toe angles of TIG dressed specimens. An overlay is shown in figure 6.17. The peak of both data samples differs, but when the spread of the data is taken into account, it is questionable whether this is a significant difference.

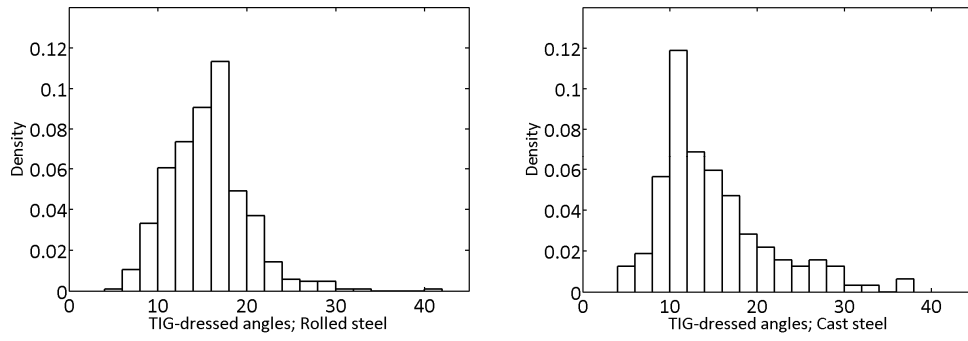


figure 6.16 Comparison of TIG-dressed angles between rolled steel and cast steel

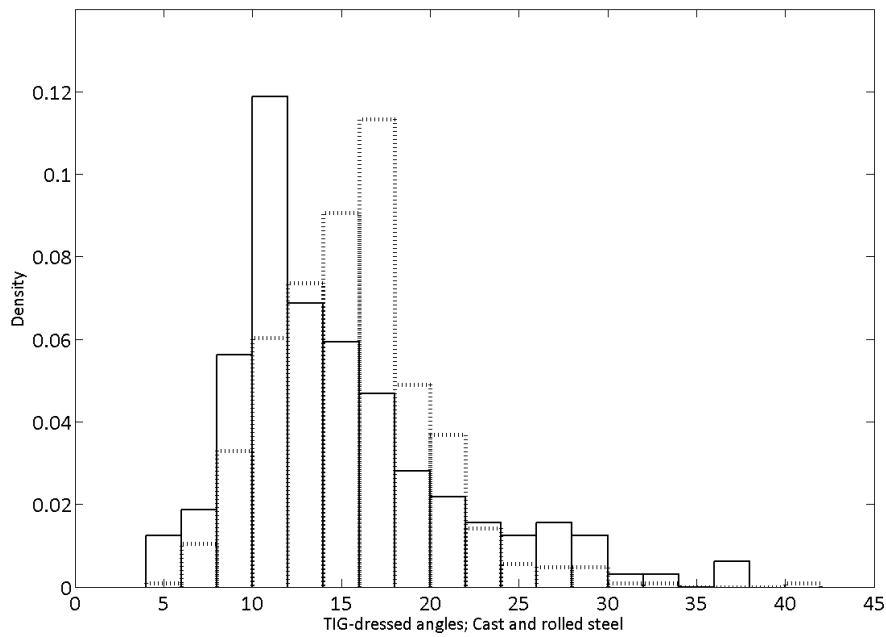


figure 6.17 Overlay of TIG-dressed angles of cast (—) and rolled (- -) steel

Undercuts

Density bar diagrams of the undercut of as welded specimens are shown in figure 6.18. An overlay of both diagrams is shown in figure 6.19. It is clear that the diagrams look very similar, with most undercuts being zero. It must be noted that both bar diagrams are cropped at 0.22 millimeter, while both the rolled steel and cast steel specimens shown a sporadic data point at deeper undercuts. For clarity of the comparison the diagrams are cropped.

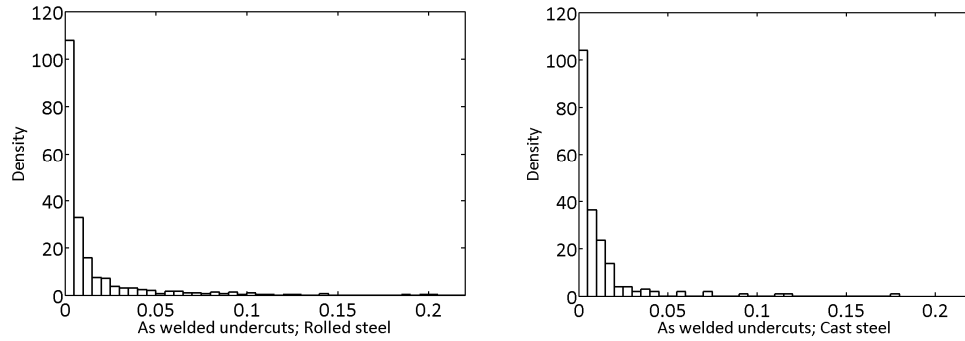


figure 6.18 Comparison of as welded undercuts between rolled steel and cast steel [mm]

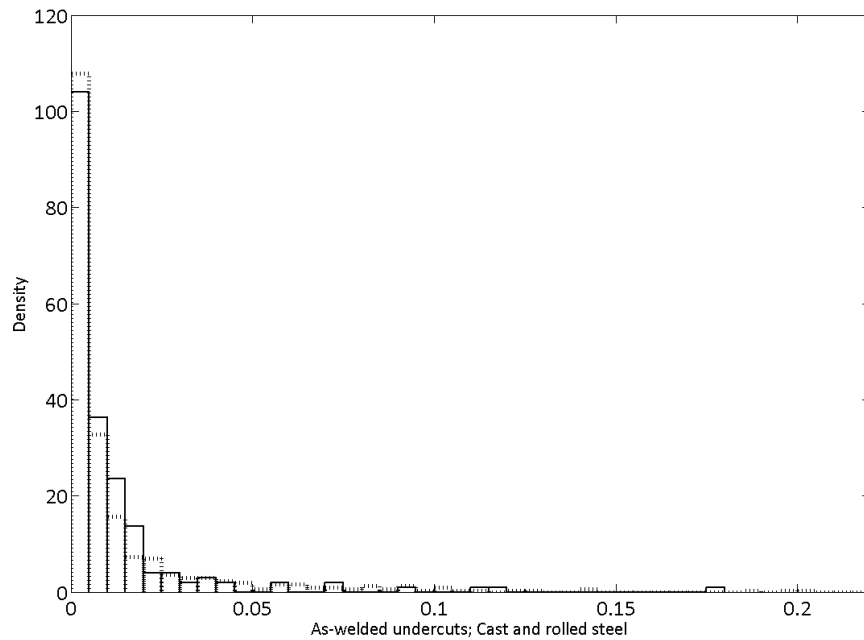


figure 6.19 Overlay of as welded undercuts of cast (—) and rolled (- - -) steel [mm]

The density bar diagrams of the undercuts of TIG-dressed specimens are shown in figure 6.20. An overlay of both diagrams is shown in figure 6.21. For small undercuts both diagrams show similar behaviour, but for deeper undercuts, the cast steel specimens show much more undercuts. This can be attributed to the fact that the large majority of typical TIG-dressed type 2 weld geometries (see figure 6.9) occurred in one weld in the C69TIG plate on the cast side.

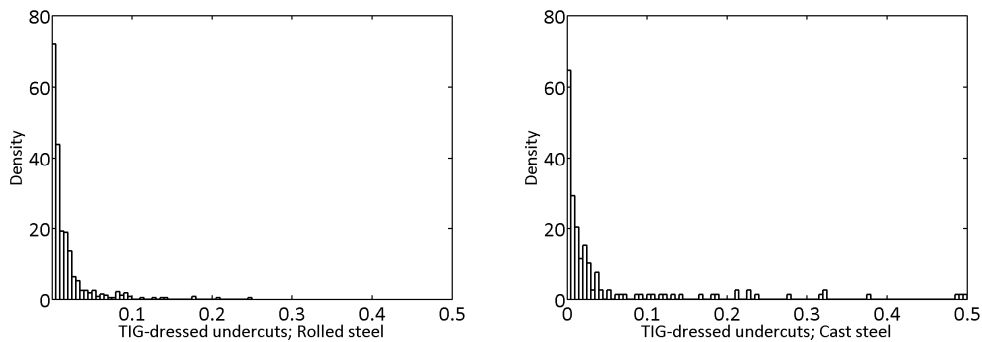


figure 6.20 Comparison of TIG-dressed undercuts between rolled steel and cast steel [mm]

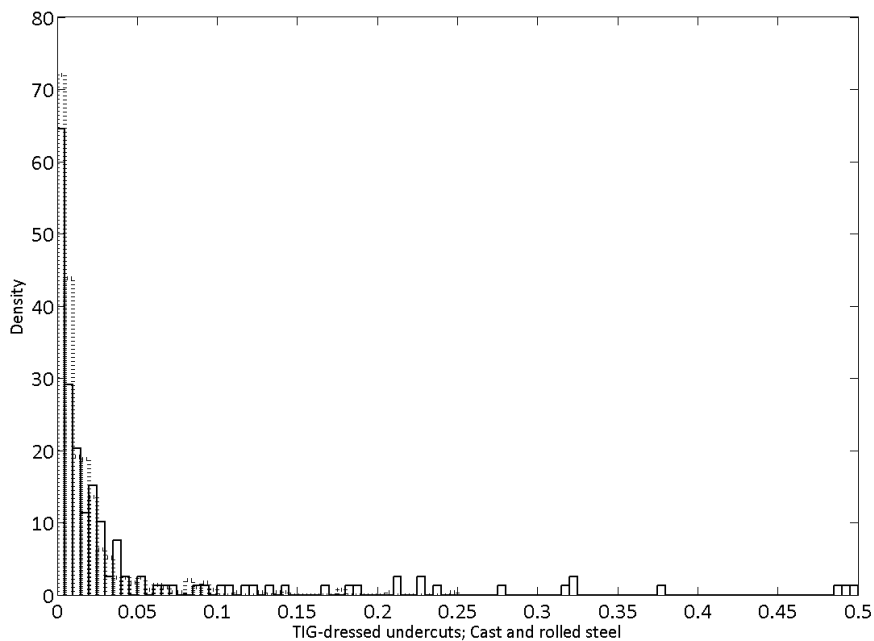


figure 6.21 Overlay of TIG-dressed undercuts of cast (—) and rolled (---) steel [mm]

Conclusion

The overlay diagrams of the weld toe radii, weld toe angles and undercuts show different results. In some cases the results match almost exactly, and in some cases the cast and rolled steels show rather different results. Before a conclusion can be drawn, a few factors must be considered.

First of all, the data set for cast steels is much smaller than for the rolled steels, since all cast steel plates are welded to a rolled steel plate. This results in a roughly three times larger data set for the rolled specimens. This could explain some of the sharp peaks the cast steel data show (e.g. see figure 6.11). Furthermore it must be noted that all data result from only nine welds in total, which in turn may be built up from multiple weld beads. This means that in total only eighteen weld beads have been measured (one for each weld toe). If one of those weld beads has been fabricated in a less than perfect way, this can very easily translate into large differences in the above analysis. For example, the large majority of large undercuts that are visible in cast steel appear in the C69TIG plate.

Based on these considerations and the fact that the differences between peaks generally do not exceed the standard deviation, it is assumed that the welds in cast steel and rolled steel have similar distributions of geometry.

6.3.3 Comparison between different steel grades

The data sets of the individual measured plates consist of relatively few data points. This will result in very rough bar diagrams. This effect was already noted in 6.3.2 where the rolled and cast measurements were compared. In this case there is not a difference in data size, but the small size of the data set severely distorts the overlay of two bar diagrams. Therefore, in this paragraph only mean values and standard deviations will be compared. The results for weld height are not taken into account, because this differs greatly between plates, and mainly depends on the skill of the welder and the amount of added weld material. In table 6.6 to table 6.8 the comparison between the different materials can be made, both for the as welded as TIG-dressed situation. For the weld toe radius and weld toe angle hardly any differences can be observed, and any differences are small when compared with the standard deviation. For the undercut in the as welded situation there seems to be a material dependent influence, but as this influence is not apparent in the TIG-dressed situation it is concluded that the steel grade has no influence on the weld toe parameters.

	As welded		TIG-dressed	
	mean [mm]	stdev [mm]	mean [mm]	stdev [mm]
S1100	1.4188	1.0184	4.5360	2.9817
S890	1.5691	0.9458	4.9847	4.4375
S690	1.5210	1.1274	4.5058	3.1078
S460	1.8761	1.6850	3.6718	3.2851

table 6.6 Comparison of mean value and standard deviation of weld toe radii. The given values are also applicable to the cast steel counterpart of the mentioned rolled steels.

	As welded		TIG-dressed	
	mean [-]	stdev [-]	mean [-]	stdev [-]
S1100	29.0235	5.9754	14.5088	4.2531
S890	28.3556	5.5604	14.1985	4.8029
S690	27.9500	6.2554	17.0907	6.0301
S460	26.0104	7.9736	15.7443	3.7348

table 6.7 Comparison of mean value and standard deviation of weld toe angles. The given values are also applicable to the cast steel counterpart of the mentioned rolled steels.

	As welded		TIG-dressed	
	mean [mm]	stdev [mm]	mean [mm]	stdev [mm]
S1100	0.0217	0.0534	0.0231	0.0369
S890	0.0176	0.0352	0.0161	0.0314
S690	0.0077	0.0120	0.0368	0.0850
S460	0.0067	0.0102	0.0142	0.0151

table 6.8 Comparison of mean value and standard deviation of undercuts. The given values are also applicable to the cast steel counterpart of the mentioned rolled steels.

6.3.4 Distribution of weld geometry parameters

Based on the previous paragraphs, the data for cast and rolled steel or different steel grades will not be analyzed separately. In this paragraph collected data of all weld geometry parameters will be plotted.

Weld toe radius

In figure 6.22 the results of the laser measurements are shown for as welded and TIG-dressed specimens. An overlay of both diagrams is shown in figure 6.23. The overall trend is what is to be expected from TIG-dressing: the weld toe radius increases. However, very small radii still occur and their numbers are still significant. This will be due to the occurrence of typical TIG-dressed geometries type 3 and 4 (see figure 6.9). The spread of the TIG-dressed radii is much larger than for the as welded radii with the occurrence of the aforementioned small radii, but also very large radii occur. A tabulated summary of the results is given in table 6.9. Note that the values of the weld toe radii are not normally distributed. The values in table 6.9 should therefore not be used as such.

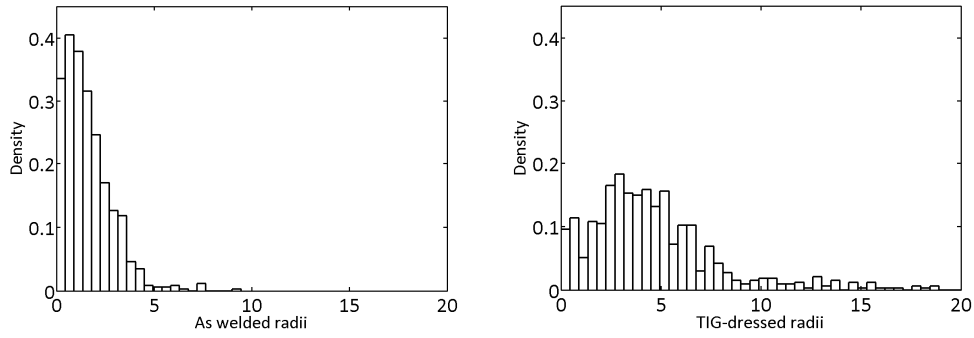


figure 6.22 Comparison of as welded and TIG-dressed radii [mm]

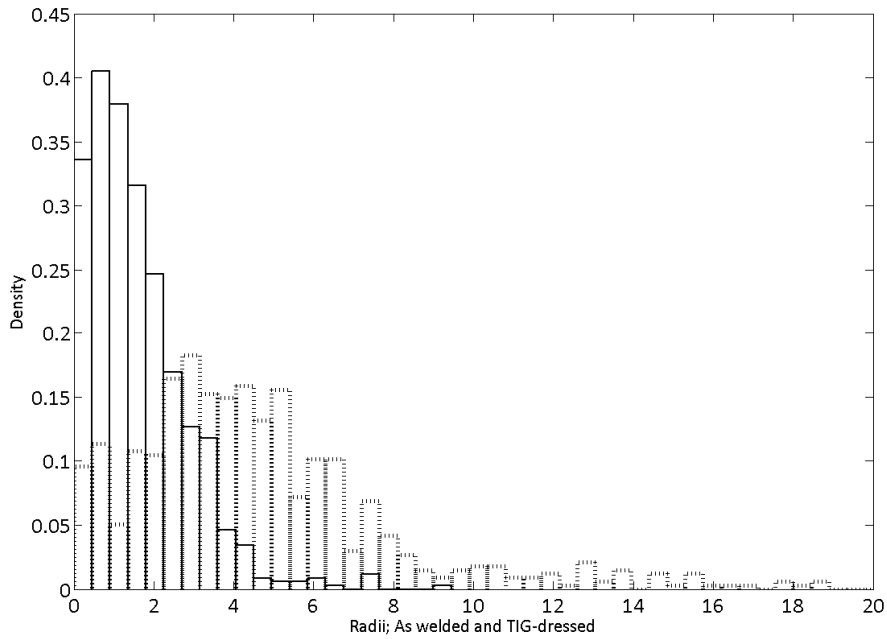


figure 6.23 Overlay radii of as welded (—) and TIG-dressed (- -) specimens [mm]

	Mean [mm]	Standard dev. [mm]
As welded	1.5940	1.2256
TIG-dressed	4.6807	3.5462

table 6.9 Mean and standard deviation of measured radii

Weld toe angle

In figure 6.24 the results of the laser measurements are shown for as welded and TIG-dressed specimens. An overlay of both diagrams is shown in figure 6.25. The trend is exactly as expected: the average angle decreases. Of course a few steeper angles occur in the TIG-dressed situation, but not with a frequency that is disproportionate with the overall shape of the distribution. The spread of both data is in the same order of magnitude. A tabulated summary of the results is given in table 6.10.

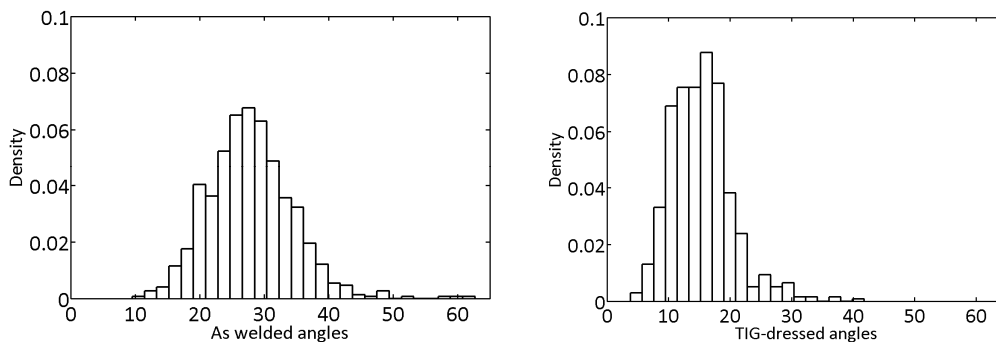


figure 6.24 Comparison of as welded and TIG-dressed angles [mm]

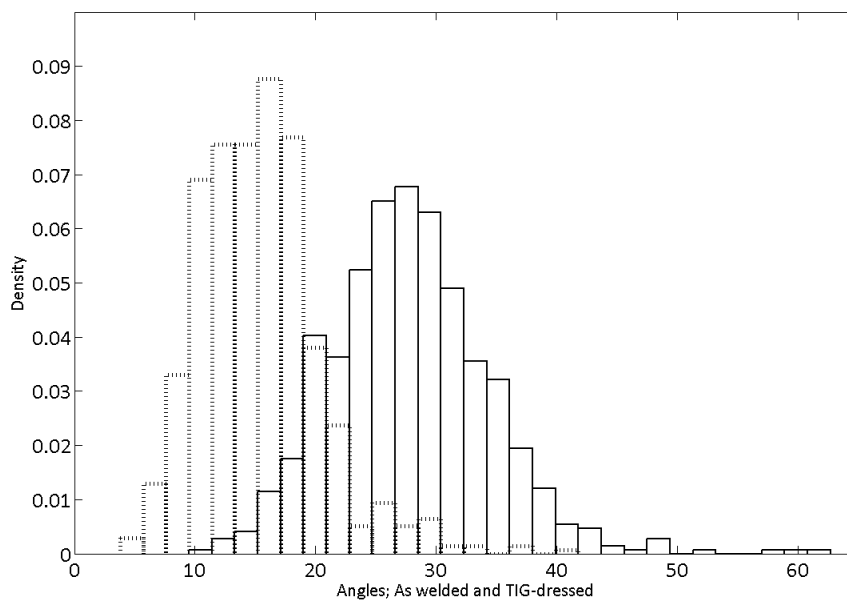


figure 6.25 Overlay angles of as welded (—) and TIG-dressed (- - -) specimens [mm]

	Mean [mm]	Standard dev. [mm]
As welded	27.8480	6.5577
TIG-dressed	15.3052	4.9701

table 6.10 Mean and standard deviation of measured angles

Undercut

In figure 6.26 the results of the laser measurements are shown for as welded and TIG-dressed specimens. An overlay of both diagrams is shown in figure 6.27. The diagrams show a slight increase in non zero undercuts for TIG-dressed specimens, but both TIG-dressed and as welded specimens have hardly any undercuts larger than 0.05-0.1 millimeter. The TIG-dressed specimens contain a few deeper undercuts as described above. A tabulated summary of the results is given in table 6.11.

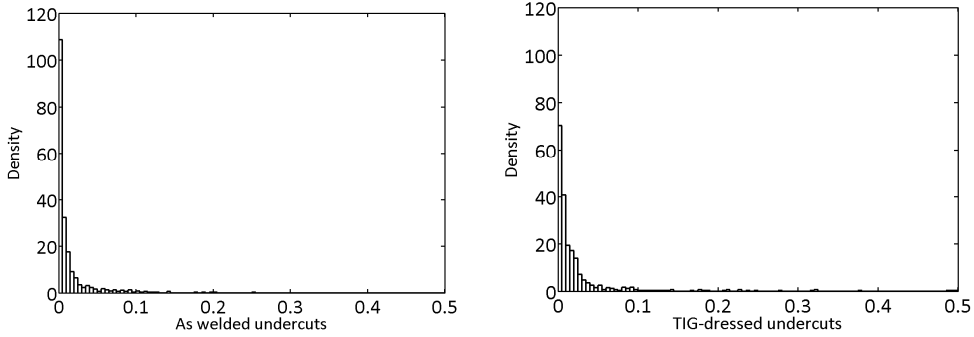


figure 6.26 Comparison of as welded and TIG-dressed undercuts [mm]

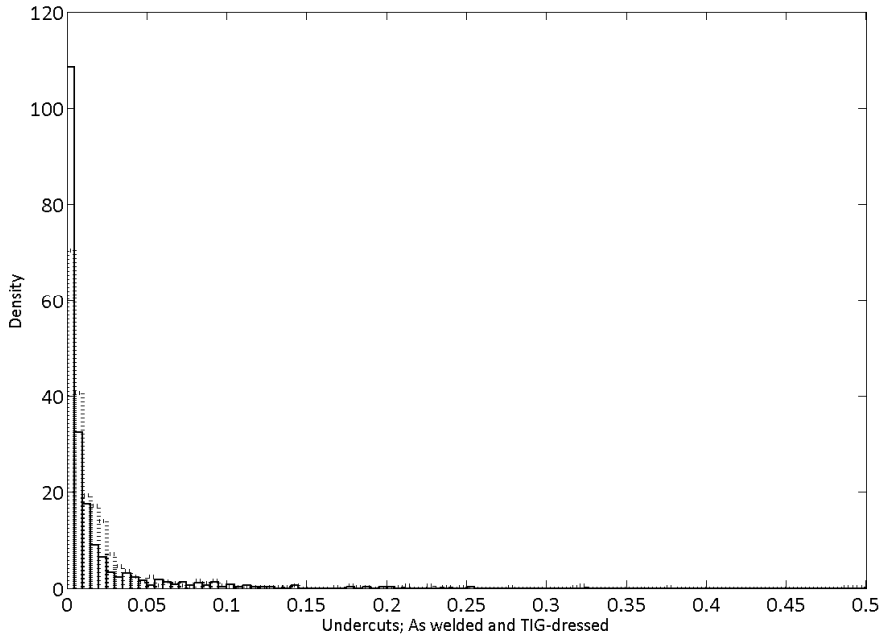


figure 6.27 angles of as welded (—) and TIG-dressed (- -) specimens [mm]

	Mean [mm]	Standard dev. [mm]
As welded	0.0136	0.0335
TIG-dressed	0.0229	0.0512

table 6.11 Mean and standard deviation of measured undercuts

Weld height

Because TIG-dressing takes place at the weld toe, the weld height is assumed not be influenced to a great extent. Therefore, only as welded data will be shown in diagrams. A comparison of mean and standard deviation of the weld height data between as welded and TIG-dressed specimens is shown in table 6.12. The results in this table strongly support the assumption that the weld height is not influenced by TIG-dressing.

	Mean [mm]		Standard Deviation [mm]	
	As welded	TIG-dressed	As welded	TIG-dressed
C11	3.9384	3.9188	0.4697	0.4557
C89	4.1151	4.1485	0.2928	0.2747
C89a	4.3455	4.3803	0.2212	0.1790
C69	2.3018	2.2875	0.1935	0.1943
C46	1.7768	1.7068	0.1662	0.1107
V11	3.6734	3.7067	0.2278	0.2193
V89	3.0152	3.0438	0.2569	0.2421
V69	2.4594	2.4965	0.1445	0.1342
V46	2.1462	2.1428	0.1875	0.2023

table 6.12 Comparison of mean and standard deviation of weld heights for as welded and TIG-dressed specimens

From the given values for the mean and standard deviation in table 6.12 can be deduced that the weld height can vary very significantly between welds, but shows very limited variation along one weld. Therefore, in figure 6.28 and figure 6.29 the distribution of weld heights is specified for each plate separately.

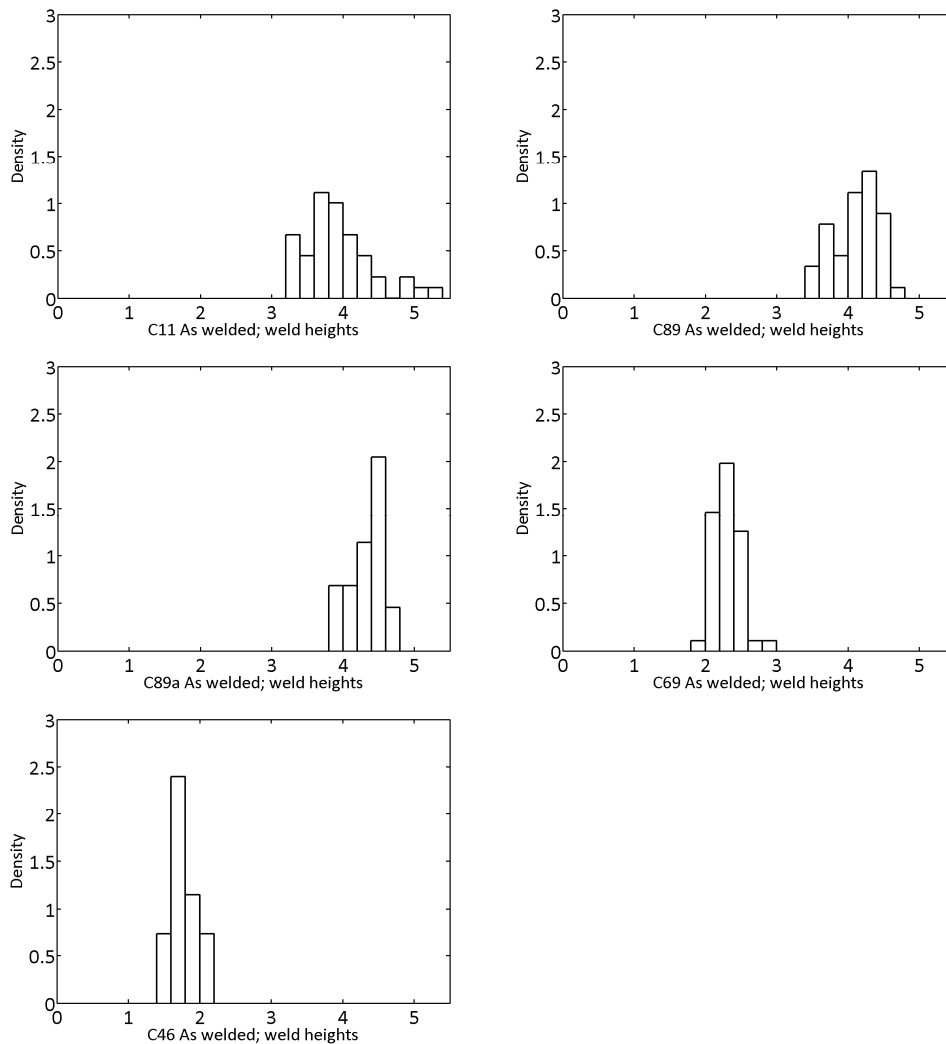


figure 6.28 Distribution of weld heights. Cast-rolled plates [mm]

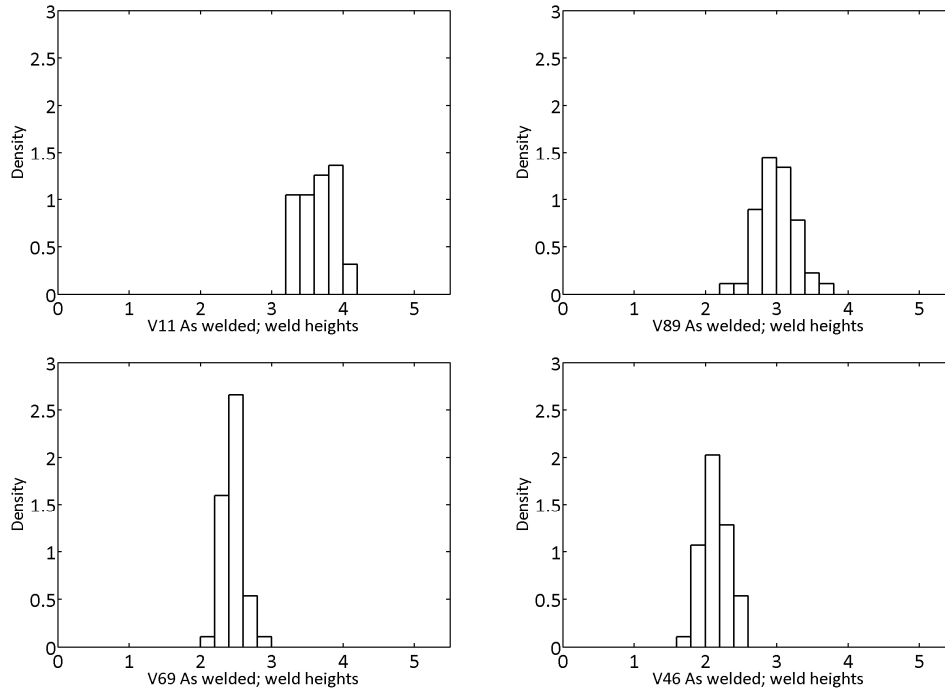


figure 6.29 Distribution of weld heights; Rolled-rolled plates [mm]

6.3.5 Evaluation of influence of TIG-dressing

The intention and expected result of TIG-dressing is the increase of the weld toe radius and, for butt welds, the reduction of the weld toe angle. Both these effects are clearly visible in the measured weld geometries.

The mean value and standard deviation that are found for the weld toe radius before and after weld improvement comply reasonably with earlier research (see figure 4.11) with the remark that the measured radius for TIG-dressed specimens is somewhat lower than is shown in earlier research. However, if the actual distribution of as welded and TIG-dressed specimens is observed it is clear that, although the average radius increases significantly, a large amount of small radii still occurs in the TIG-dressed specimens. The fitting of a statistical distribution has been omitted. While the as welded data comply reasonably well with a log-normal distribution, the TIG-dressed data shows an additional peak near the smaller radii which makes accurate mathematical description difficult.

The average weld toe angle has decreased significantly and shows smaller spread after TIG-dressing. The data sets before and after TIG-dressing show a distribution shape similar to a normal distribution. The distribution of undercuts after TIG-dressing shows similar behaviour as before the treatment, with the exception of an increase of very deep undercuts (typical TIG-dressed geometry type 2, see figure 6.9). The large majority of undercuts lies below 0.05 millimeters depth. The weld height of each separate weld does not seem to be influenced by TIG-dressing. The spread of weld heights over each weld is very small, but weld heights of different welds can show significant spread.

When fatigue is considered to be a weakest link process, it is questionable whether these results justify a fatigue strength increase due to changed geometry. The average weld geometry shows significant improvement with a larger weld toe radius and smaller weld toe angle, but in the worst case scenario this might not be the case. Especially the weld toe radii show a significant peak near the smaller radii.

A few remarks must be made concerning this conclusion. First of all, although the worst case radius does not seem to show improvement, it is very likely combined with a smaller weld toe angle, which reduces the stress concentration near the weld toe anyhow. Secondly, the measured smaller radii in the TIG-dressed specimens mainly occur in typical TIG-dressed geometries type 3 and 4 (see figure 6.9). In type 3 the stress concentration is expected to be lower due to the weld plateau directly after the weld toe. Type 4 is rather rare, and a worst case scenario with a combination of geometry type 4 and other parameters such as a large inclusion and high residual stresses, which makes it comparable with the as welded weld, is not very likely.

If a database would be made of the different occurring geometries (see figure 6.9), the dependencies between the weld toe parameters, which are very likely present, can be investigated and documented. This would make an analysis of the worst case scenario possible. This will be elaborated in 8.3.2.

7 Processing and results of fatigue tests and hardness measurements

7.1 Chapter outline

In this chapter the results of the fatigue tests are discussed. The output of the testing rig and determination of the values of N_f , R and σ_n is discussed the first two paragraphs. In paragraphs 7.3, 7.4 and 7.5 the results of the fatigue tests, hardness measurements and crack monitoring are presented.

7.2 Test output and processing

7.2.1 Test output

The fatigue tests result in data from the strain gauges, coupled to the number of cycles and notes made during the experiment which contain crack length at various stages during the crack propagation life and number of cycles at failure. When the specimen has failed it can be examined for beach marks, created by the crack marking procedure as described in 5.3.2. An example of the acquired strain gauge data is shown in figure 7.1, and an example of the acquired crack propagation data is shown in figure 7.2.

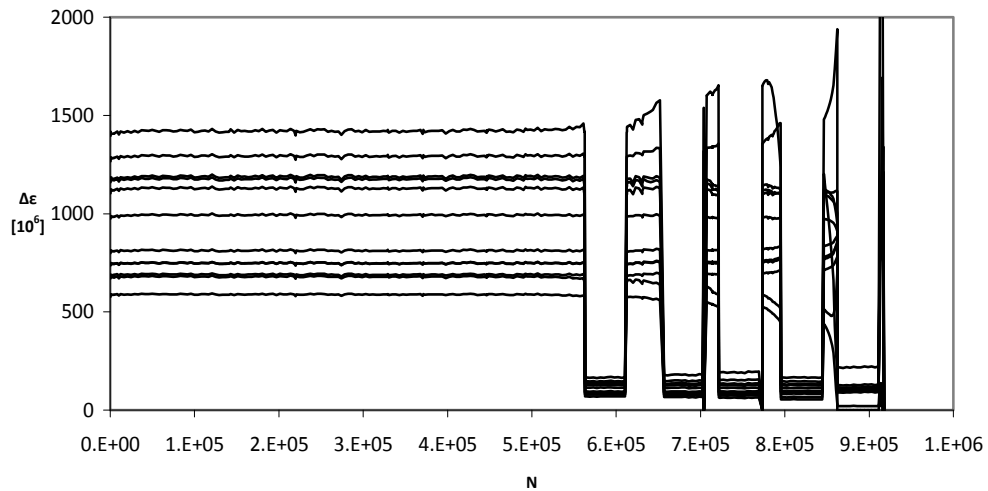


figure 7.1 Strain gauge data from specimen C69-2. The crack markings are clearly visible in the form of a lowered strain range.

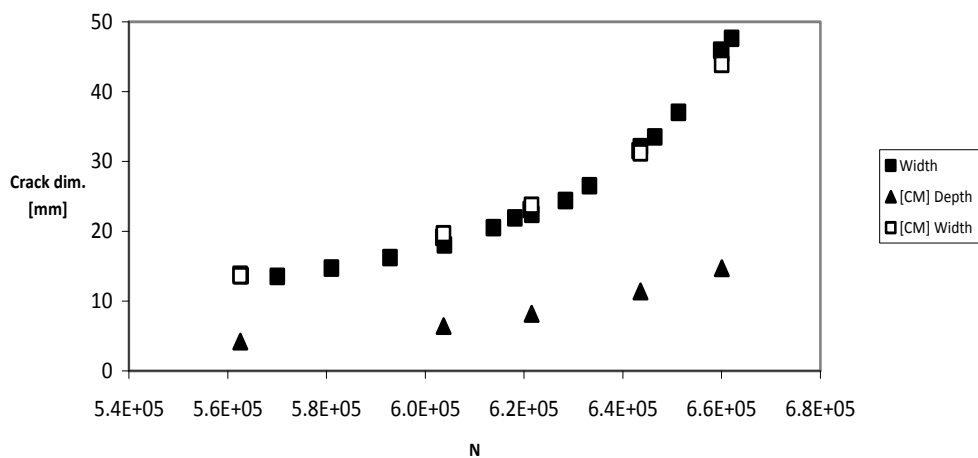


figure 7.2 Crack propagation data from specimen C69-2. Most data points are directly measured during the test. The crack marking data are rarer due to the complexity of the procedure, but fit in well with the other data.

7.2.2 Determining N_i , nominal stress and stress ratio

The test rig is programmed to shut down when the measured strain range deviates more than 5% from the average measured value. When the test rig shuts down to start crack monitoring (see 5.3.2), the crack size is fairly substantial most of the time. For example, the crack size at the first measurement in figure 7.2 is already 14 millimeter. Because TIG-dressing is expected to especially increase the crack initiation life of the specimens, the number of cycles at crack initiation (N_i) needs to be determined. This point is determined with the aid of the strain gauge data. The first point where one of the strain gauge lines starts to deflect from its average straight line is marked as the crack initiation point. In collaboration with TNO an alternate method to detect the crack initiation site and determine the number of cycles to crack initiation has been experimented with. Instead of the strain gauge data, acoustic emission of the crack was used. The procedure and experiences are added in Annex G.

After failure of the specimen the crack surface can be inspected more thoroughly to find the crack initiation site. This is usually darker due to the longer exposure to petroleum (see 5.3.2, crack monitoring). Also the presence of beach marks due to crack marking can help identify the crack initiation site. When the location of crack initiation is determined, the nominal stress is determined on the basis of measurements of the nearest strain gauge(s). In the tabulated fatigue test results in Annex C the used strain gauges are specified. Annex B shows the location of the numbered strain gauges.

In the tabulated fatigue test results, two different values of the stress ratio R are specified. One is based on the strain gauge(s) which were also used to determine the nominal stress. The other stress ratio is based on the measured values of the force.

7.3 Results of fatigue tests

In this paragraph only the results of the fatigue tests will be shown without any adjustments (see 9.2.2). The results will be split according to the static strength of the specimens. Cast and rolled results will be plotted in one graph. Based on certain considerations, some results will be excluded from the analysis later. In the figures below all results are plotted. The exclusion of data will be elaborated on in 9.2.1.

Three different failure mechanisms have been observed:

- Base material failure (indicated with BM in the graphs and Annex C)
- Weld toe failure (indicated with WT in Annex C)
- Weld material failure (indicated with WM in Annex C)

The first two mechanisms were also observed in the as welded tests by Pijpers (2011). The weld material failure mechanism was only very rarely observed in his quite substantial data set, while in the much smaller data set of this research seven of such failures are observed, which accounts for roughly 30% of all results. A total of five failures were found in the base material and only in the S890 and S1100 specimens. Several specimens have not failed and were stopped at a certain number of cycles. These runouts are marked in all graphs.

The total failure of specimens is marked as defined as the number of cycles to failure: N_f . The point where the first deviation of a strain range from its average can be noticed is defined as the number of cycles to crack initiation: N_i .

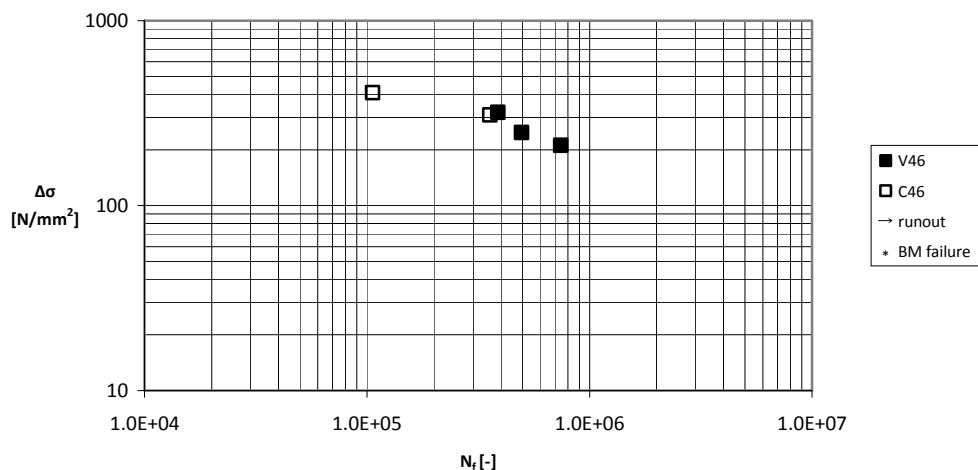


figure 7.3 Results of tests on S460 specimens.

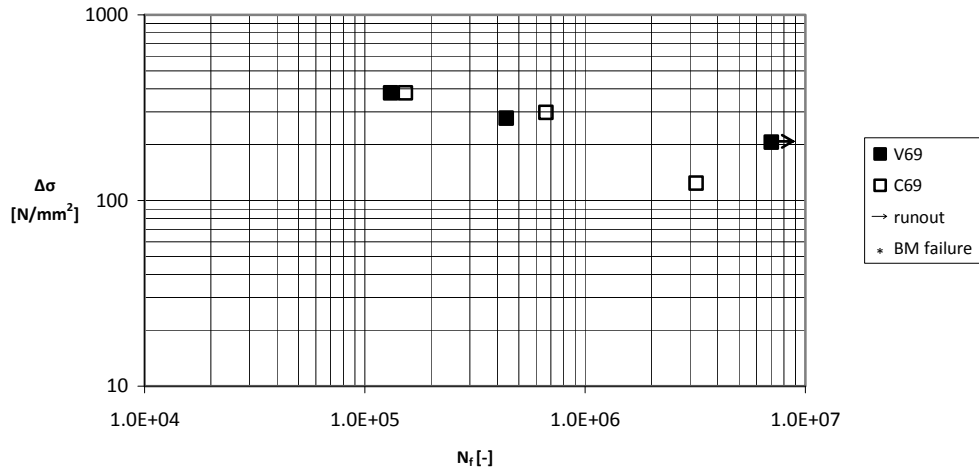


figure 7.4 Results of tests on S690 specimens

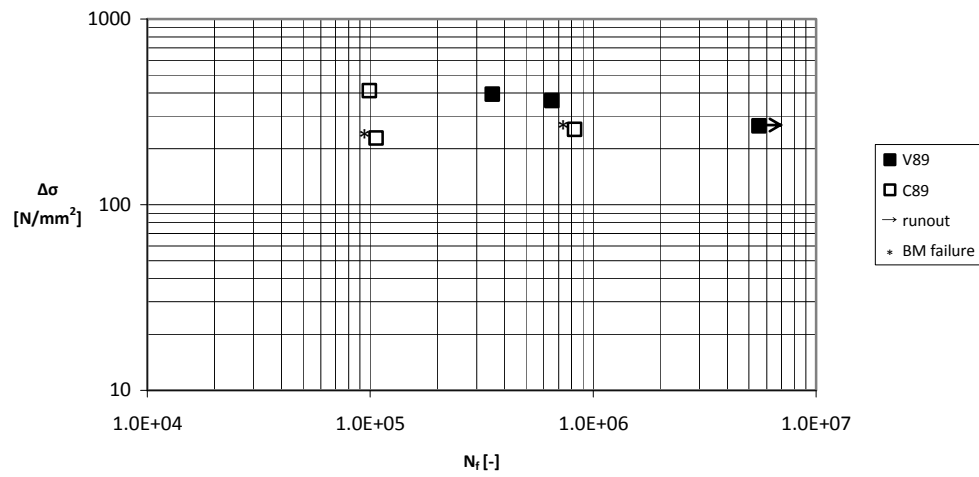


figure 7.5 Results of tests on S890 specimens

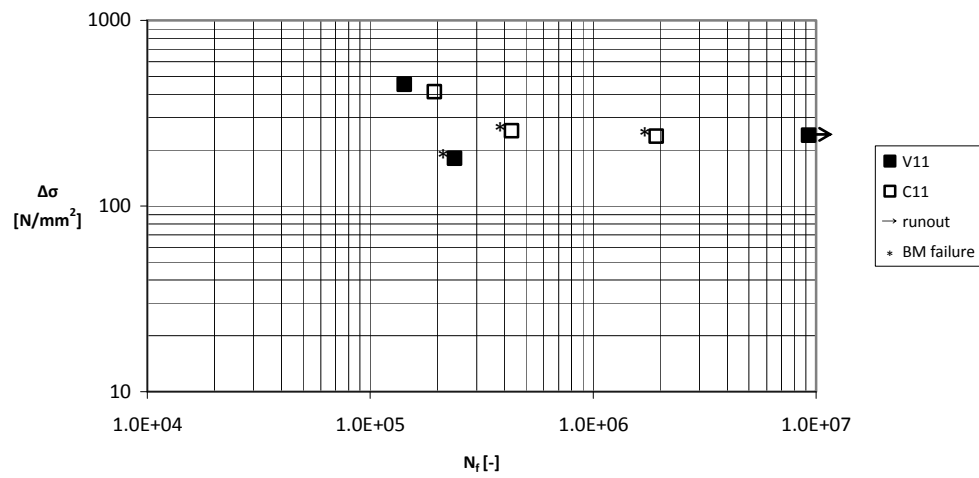


figure 7.6 Results of tests on S1100 specimens

7.4 Results of hardness measurements

The results of the hardness measurements are shown in Annex H, in this paragraph the results will be discussed. The general trend is that TIG-dressing increases the hardness of the material, both where the TIG-dressing has melted the material and where the material has been influenced by the heat of TIG-dressing. Exceptions to this trend are the specimens C89, C11 and V11, all of which are in the very high strength range. In these cases little to no hardness increase has been observed. In some exceptional cases, the hardness has been lowered by TIG-dressing on these specimens.

The extensive study of these results lies out of the scope of this study, but the results can lead to some interesting possible conclusions. The material hardness can be linked to the ultimate strength of the steel according to equation (7.1) (Van Wortel, 2006).

$$R_m = 3.02 \cdot HV10 \quad (7.1)$$

If the notch stress analysis is used, the ultimate strength is used in different steps of the calculation and directly linked to the fatigue strength. The material constant a^* , proposed by Lawrence (Radaj et al., 2006) (see 3.5.1 and equation (3.9)) depends on the ultimate strength. If the ultimate strength increases, a^* decreases, which results in a higher notch sensitivity of the material (see figure 3.10).

Different authors have reported on the relation between the static strength and fatigue strength (see figure 2.11). These relations generally take the form of a linear equation, where increasing static strength leads to increasing fatigue strength. This effect will be stronger than the effect of a^* (see figure 2.10, where a factor 2.5 in R_m leads to a factor of about 1.3 in K_f).

If both these relations can be proven to be valid in the conditions that are considered, the increased hardness caused by TIG-dressing may increase the fatigue strength of the weld, even when the changed weld geometry, residual stresses and reduced defects are absent.

Earlier research by Pedersen et al. (2010) has shown the opposite of the results from this research: there a hardness drop of 15 to 20% was shown (see 4.3.3). The exact effect of TIG-dressing on the hardness on the material and the consequences of these effects therefore deserves a more thorough research.

7.5 Results of crack monitoring

On all specimens crack monitoring has taken place. However, in some cases fewer data points are available because the crack had been detected in later stadium, or the beach marks which should be visible due to crack marking could not be found. All usable results are collected in Annex I. The results can be used to verify the number of cycles to crack initiation, or to determine material parameters needed for a crack propagation analysis. It could be investigated if the cracks grow in a different rate after TIG dressing, and to what extent this can be explained by the changed geometry only. This research will omit such calculations, because the focus lies on the extension of the crack initiation life.

8 Analytical determination of fatigue strength

8.1 Introduction and chapter outline

As previously discussed, TIG dressing has a number of possible influences on the weld toe:

- Geometry change
- Reduction of imperfections
- Change in residual stress state
- Change of metallurgical state

The laser measurements of the weld geometry (see 5.3.1) result in extensive data concerning the first parameter. Surface imperfections can possibly also be traced to a certain extent with the laser measurements, but this has not been done in this research because deeper imperfections (inclusions) cannot be traced in this manner. Non-destructive testing could give insight into the change in number and size of these imperfections, but to limit the duration of the research these tests have not been carried out. The hardness measurements (see 7.4) give insight into the change of metallurgical state of the weld toe. The change in residual stress shall be estimated, based on previous research.

In this chapter the fatigue strength of TIG-dressed specimens will be predicted based on the measured or estimated parameters stated above. Because most standard fatigue assessments incorporate the weld geometry and imperfections in the scatter, these methods for prediction cannot be used. The notch stress method (see 3.5) uses the actual geometry, stress range, residual stress state and metallurgical state at the crack initiation site. This method is therefore suitable to compare the state of the specimens before and after TIG dressing and predict the fatigue strength.

This chapter will first discuss the determination of the stress concentration factor and fatigue notch factor. Then other influence factors will follow, leading to a prediction of the fatigue strength of the considered specimens.

8.2 Factors determining fatigue strength

According to the notch stress approach, the crack initiation life of welded joints can be compared with the crack initiation life of plain material, if the corrections are made for the stress concentration effect of notches. However, as mentioned in 2.3.2 there are other factors influencing fatigue life. All these factors will be considered to determine the expected crack initiation life:

- Fatigue notch factor: K_f (depends on the elastic stress concentration factor: K_t)
- Mean stress factor: f_m
- Thickness factor: $f_{t,w;Ni}$ (only applicable to crack initiation life)
- Loading mode factor: $f_{lm,w;Ni}$ (only applicable to crack initiation life)

In the coming paragraphs each influence factor will be determined. Furthermore, the fatigue strength of the base material needs to be determined, to which is referred in the notch stress analysis. Different relations between the fatigue endurance limit and the static material strength have been developed. Pijpers (2011) has compared several formulas, and found equation (8.1), as proposed by Haibach 2006, to be most applicable because of the distinction between rolled and cast steel.

$$\sigma_{aE,0} = f_{mat} \cdot \sigma_u \quad (8.1)$$

In which:

f_{mat} material factor for either rolled steel (0.45) or cast steel (0.34) [-]

In equation (8.1), the used value for the ultimate strength is the value specified in the material certificates and has not been linked to the hardness measurements. When the fatigue limit of the base material is corrected for the influences described above, the fatigue strength curve can be determined using the approach by Schijve or Hück as described in 3.5.1.

8.3 Determination of stress concentration factor and fatigue notch factor

For butt welds without undercut, the elastic stress concentration factors have been studied before (Anthes et al., 1993) and have led to a formula to determine the elastic stress concentration factor at the weld toe.

$$K_t = \left[1 + b_1 \cdot \left(\frac{t}{r} \right)^{b_2} \right] \cdot \left[1 + \left(a_0 + a_1 \cdot \sin\left(\frac{\theta}{180} \cdot \pi \right) + a_2 \cdot \sin\left(\frac{\theta}{180} \cdot \pi \right)^2 + a_3 \cdot \sin\left(\frac{\theta}{180} \cdot \pi \right)^3 \right) \cdot \left(\frac{t}{r} \right)^{l_1 + l_2 \cdot \sin\left(\frac{\theta + l_3}{180} \cdot \pi \right)} \right] \quad (8.2)$$

In which:

- t the plate thickness [mm]
- r the weld toe radius [mm]
- θ the weld toe angle [-]; degrees

Other parameters are specified in the table below:

Factor	a_0	a_1	a_2	a_3	b_1	b_2	l_1	l_2	l_3
Tension	0.169	1.503	-1.968	0.713	-0.138	0.2131	0.2491	0.3556	6.1937
Bending	0.181	1.207	-1.737	0.689	-0.156	0.207	0.2919	0.3419	3.283

table 8.1 Influence factors for equation (8.2)

Unfortunately, this formula does not cover welds with undercuts. While the influence of small undercuts, such as found in most geometries, is unknown, the influence of the large undercut of Typical TIG-dressed type 2 (see figure 6.9) will certainly be significant. Furthermore, the weld height is not incorporated in the formula, as it is assumed by Anthes that weld height and weld angle are directly related. For the observed weld toe geometries after TIG-dressing (see figure 6.9) this is not the case, because the TIG-dressing process has changed the angle but not the weld height. To obtain stress concentration factors for the specific geometries which were found, a FEM model of the local weld geometry is made.

8.3.1 FEM analysis of weld toe

A parametric model has been set up in which the following parameters can be adjusted:

- Length
- Thickness
- Weld toe radius
- Weld toe angle
- Undercut
- Weld height

Because the weld is relatively long compared to the dimensions of the weld toe notch, a 2D model consisting of plane strain elements is chosen. An example of a possible weld geometry and the accompanying mesh are shown in figure 8.1. Only one side of the weld is modeled, and the assumption is made that this will not influence the result. This will be shown to be plausible later on.

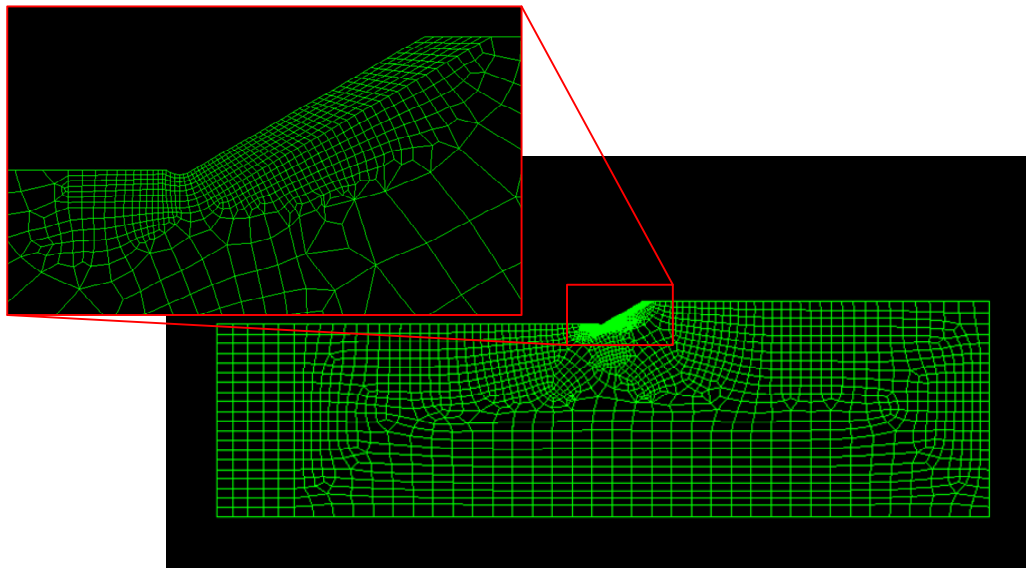


figure 8.1 Example of FEM model

The main concern when modeling the weld toe notch is the size of the elements near the expected location of the stress peak. IIW recommendations (Hobbacher, 2007) state that for linear elements the size of the elements should not exceed 1/6 of the weld toe radius, or 1/4 of the weld toe radius for higher order elements. To determine an acceptable mesh size, four geometries were analyzed three times, with radius to element size ratios of approximately 5, 10 and 15. In the

diagrams below the results of this investigation are shown. Each diagram shows three lines for the different radius to element size ratios. The lines show the value of the largest principal stress along the arc of the weld toe. In the accompanying legends the number of elements in the curve of the weld toe is also stated.

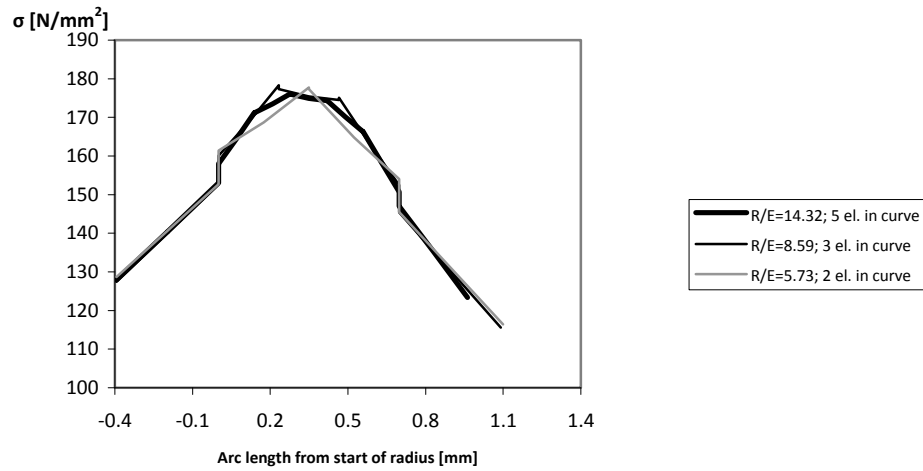


figure 8.2 Principal stress along notch radius. $\rho=2\text{mm}$, $\theta = 20^\circ$, no undercut

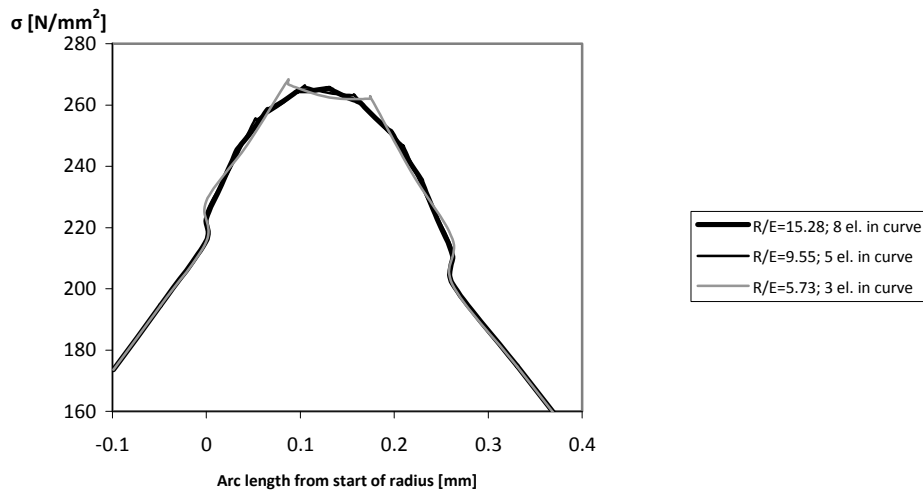


figure 8.3 Principal stress along notch radius. $\rho=0.5\text{mm}$, $\theta = 30^\circ$, no undercut

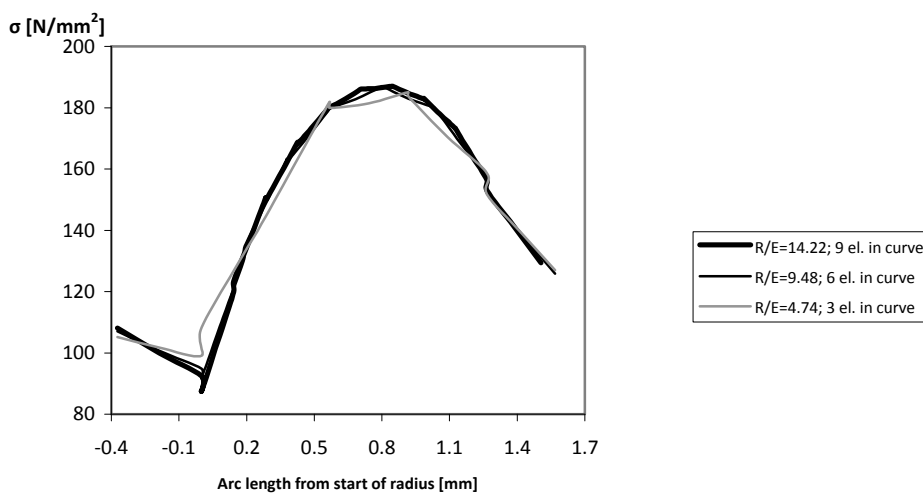


figure 8.4 Principal stress along notch radius. $\rho=2\text{mm}$, $\theta = 20^\circ$, Undercut= $R/25$

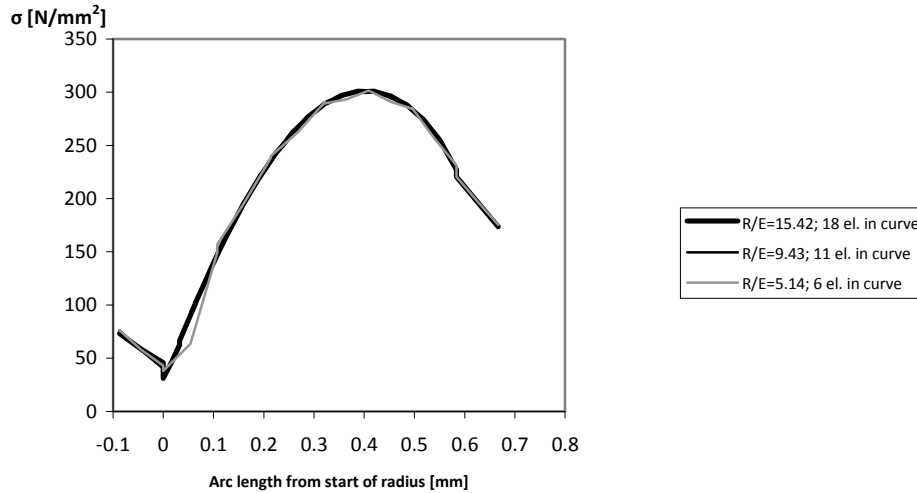


figure 8.5 Principal stress along notch radius. $\rho=0.5\text{mm}$, $\Theta = 30^\circ$, Undercut= $R/5$

From figure 8.2 till figure 8.5 can be concluded that the ratio between element size and weld toe radius (R/E) alone is not enough to judge the element size, because, although the three depicted R/E ratios are the same for each diagram, significant differences in smoothness of the stress diagram can be observed. The other parameter which is specified in the diagrams, the number of elements in the curve, provides a better guideline to the correctness of the element size. As a rule of thumb the maximum element size will be set at $R/E > 10$ and a minimum of 8 elements in the notch radius. A remark must be made that the height of the stress peak differs no more than 1.2% in the cases considered. The IIW guideline therefore seems to be applicable, but a smoother stress diagram gives more faith in the results, especially when in the coming analyses no mesh refinement is made. The choice for a possibly too fine mesh can be easily made, because the total calculation time of the model does not exceed one minute. Given the fact that further mesh refinement does not result in significantly different values and that the stress pattern is smooth, it can be concluded that the FEM model performs satisfactory.

In an overview of the results of the model (see figure 8.6) it is clear that for all applicable geometries the assumption that the other side of the weld does not have to be incorporated is reasonable, because after a very short distance the stress pattern recovers from the stress peak near the weld toe notch compared with the generally long width (>35 millimeter) of the weld.

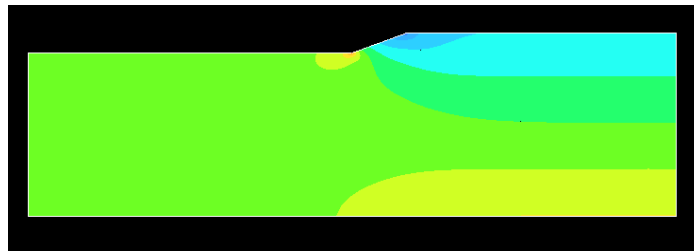


figure 8.6 Stress pattern in horizontal direction presented as contour levels. $\rho=2$, $\Theta=20^\circ$, no undercut

The developed model can be compared with the parametric formula by Anthes to see whether they give comparable results for a set of realistic parameters. A comparison for a weld profile with a height of 3 millimeter, a weld angle of 28° , a plate thickness of 25 millimeter and varying weld toe radius is made in figure 8.7. Obviously, no undercut is present, as the formula does not cover undercuts. Based on the comparison it can be assumed that the model and the formula give reasonably similar outcomes. The stress concentrations differ by about 5%, and a little more for radii larger than approximately 4 millimeter. This 5% difference between the parametric formula and actual results was already specified by Anthes when publishing his parametric formula. Some minor differences could also be attributed to a difference in Poisson-factor, which is not specified by Anthes, or the difference in analysis (Boundary Element Method by Anthes vs. plane strain FEM in this research). Most importantly it must be remarked that Anthes directly couples the weld toe angle Θ and the weld height, whereas in the FEM model they can be given values independently. The maximum difference lies around 5%, which is in line with the expected possible deviation specified by Anthes. However, if a non-regular weld is modeled, such as a TIG-dressed weld with a smaller angle but the same weld height as the as welded specimen, Anthes' formula predicts the stress concentration factor even better. This is remarkable because the fixed weld angle – weld height relation used by Anthes implies that for one of the analyzed situations the weld height used in the formula and the model should differ significantly. If the weld height has any influence on the elastic stress concentration factor, this should become clear by

means of a great difference between the formula by Anthes and the FEM results for one of both analyzed geometries. A more thorough investigation on the influence of the weld height is provided below.

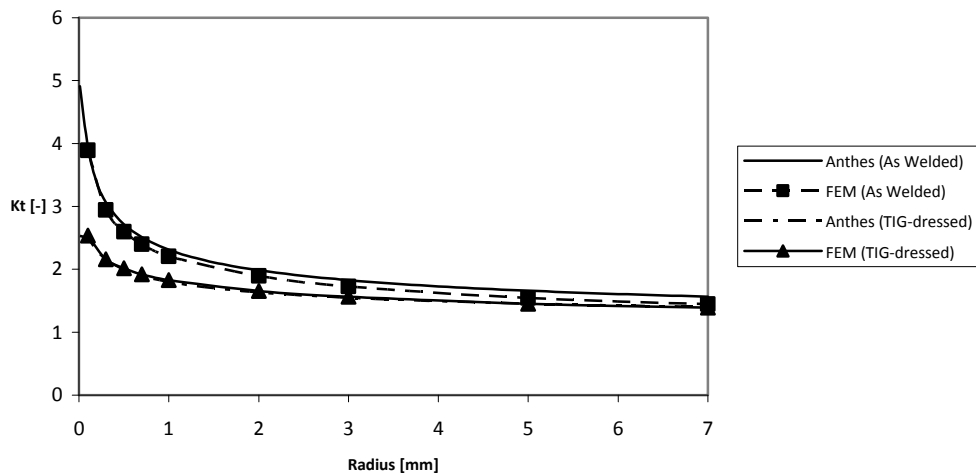


figure 8.7 Comparison of parametric formula (Anthes et al., 1993) and FEM model of weld toe. Parameters of analyzed geometries (weld toe angle, weld height, plate thickness, undercut): As Welded (28,3,25,0); TIG-dressed (15,3,25,0)

The influence of the weld toe radius and weld toe angle is clearly very large. Not only can this easily be seen in figure 8.7, but the presence of these two parameters in the formula of Anthes confirms that the value of K_t will be very sensitive to these parameters. The influence of the other parameters: weld height, plate thickness and undercut, is not apparent. To gain more insight in the behaviour of K_t under influence of changing parameters a short parameter study will follow. The influence of the plate thickness will not be considered, because these values are very accurately known, and show little variation, especially when compared with the variation of other parameters.

Influence of weld height

To study the influence of the weld height on the elastic stress concentration factor, a number of analyses has been executed on a typical as welded geometry and a typical TIG-dressed geometry. The results are shown in figure 8.8 and figure 8.9.

The typical as welded geometry (figure 8.8) shows limited sensitivity to the variation of weld height. As expected, a higher weld increases the stress concentration factor, and lowering the weld height decreases the stress concentration factor. From a certain weld height, in this case around 3 millimeter, increasing the weld height does not influence the stress concentration factor any more. Also a height of 2 millimeter shows limited variation from the base value of 3 millimeter, up to 6% for very small radii and no more than 4% for common radii (>0.5 millimeter). If the weld height is lowered to an extreme value of 0.25 millimeter, the maximum variation with respect to the base value of 3 millimeter is 35% which gradually decreases to 27% for very large radii. This is a considerable difference, but relatively limited considered that the weld height has reduced by more than a factor 10. It must be noted that any differences between the K_t curves will become smaller when the transformation to K_f is made. This also holds for differences due to weld toe angle, weld toe radius and undercut. This effect is most pronounced near the smaller radii.

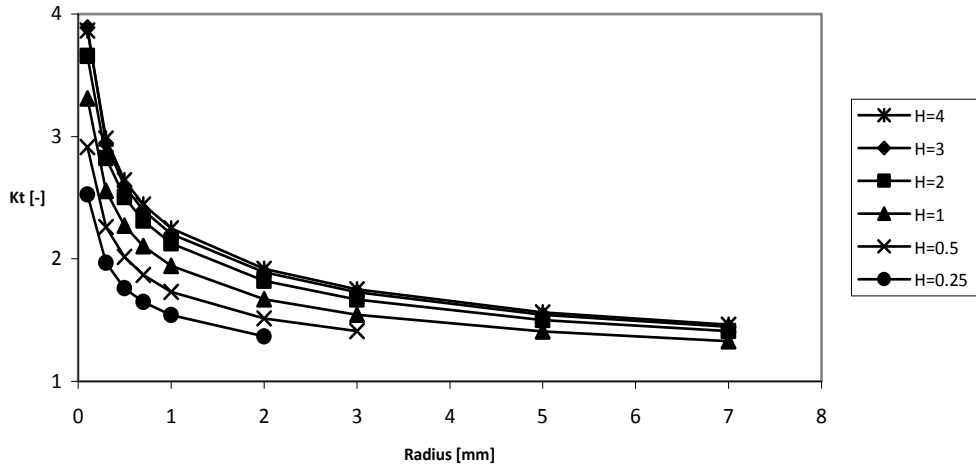


figure 8.8 Comparison of K_t for different weld heights for a typical as welded geometry. Parameters of analyzed geometries (weld toe angle, weld height, plate thickness, undercut): (28, ?, 25, 0)

The typical TIG-dressed geometry (figure 8.9) shows similar behaviour as the typical as welded geometry. From a certain weld height, in this case 2 millimeter, further increase of the height hardly influences the stress concentration factor. A height value of 1 millimeter shows relatively small variations to the base value of 3 millimeter of about 5% over the whole considered range of radii. The extreme case of a weld height of 0.25 millimeter leads to a variation of maximum 18% with respect to the base value of 3 millimeter.

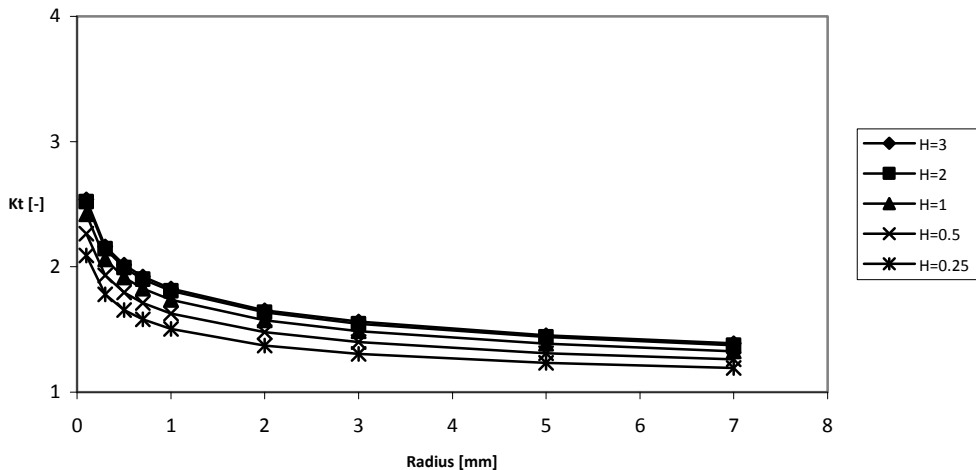


figure 8.9 Comparison of K_t for different weld heights for a typical TIG-dressed geometry. Parameters of analyzed geometries (weld toe angle, weld height, plate thickness, undercut): (15, ?, 25, 0)

Based on the parameter study it can be concluded that the stress concentration factor is relatively insensitive to weld height variations around commonly observed values. Because all weld heights are recorded they can relatively easily be incorporated in the model, but this conclusion is of great value when the model will be compared to reality later on. When weld heights as low as the weld plateau in typical TIG-dressed geometry number 3 (see figure 6.9) are considered, a significant influence is observed. This will be addressed later on.

It must be noted that this insensitivity of the model to weld height also explains why the model and Anthes' formula comply so well for varying weld toe angle while the weld height in the model did not change.

Influence of undercut

To study the influence of the undercut on the elastic stress concentration factor, a number of analyses has been executed on a typical as welded geometry and a typical TIG-dressed geometry, the results are shown in figure 8.10 and figure 8.11.

The stress concentration of the typical as welded geometry (see figure 8.10) increases as expected when an undercut arises, and increases further when the depth of this undercut increases. For all common measured undercuts (<0.06 millimeter) this variation with respect to the base value of no undercut is not larger than 20%. For common radii (>0.5 millimeter) the variation decreases to 10% or less.

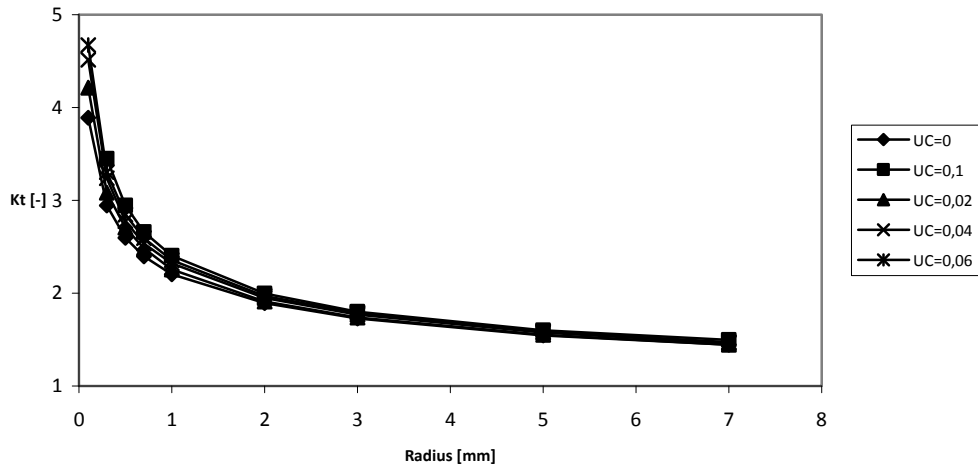


figure 8.10 Comparison of K_t for different weld heights for a typical as welded geometry. Parameters of analyzed geometries (weld toe angle, weld height, plate thickness, undercut): (28, 3, 25, ?)

The typical TIG-dressed geometry (see figure 8.11) shows similar behaviour to the as welded geometry, but is a bit more sensitive. For common undercuts the variation has a maximum value of 27%, which decreases to 12% or less when only common radii are considered.

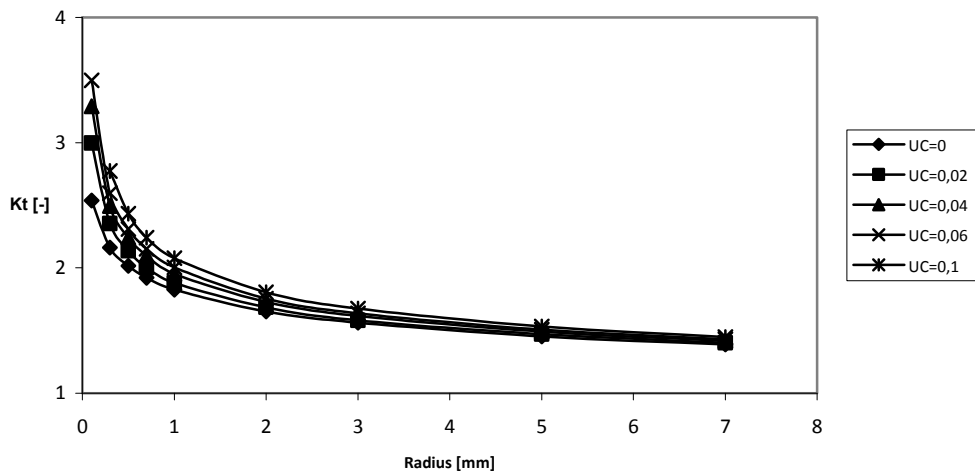


figure 8.11 Comparison of K_t for different weld heights for a typical TIG-dressed geometry. Parameters of analyzed geometries (weld toe angle, weld height, plate thickness, undercut): (15, 3, 25, ?)

Based on this analysis it can be concluded that the influence of the undercuts that were measured is relatively limited but has to be taken into account in the analysis, with the possible exception of typical TIG-dressed geometry type 2 (see figure 6.9) where the influence may be larger. While the influence may be limited, the undercut data is available and easily translated into the parametric model. Any influences of the undercut will therefore be taken into account in the fatigue strength prediction.

The larger undercuts, such as are present in typical TIG-dressed geometry type 2, are not present in this analysis. However, based on the behaviour for smaller undercuts it is very likely that the increase of K_t due to the larger undercut will very probably be smaller than the decrease of K_t due to the very large radius (>10 millimeter) which is commonly associated with this geometry.

Relation between model and reality

The model is of course a simplification of reality. In figure 8.12 a rough overlay of a possible weld geometry and its accompanying model is shown. In two areas the model shows a clear difference with reality. First in the transition from base material into the undercut (marked with line 1 in the figure). Secondly in the transition from the inclined weld material to the top of the weld material (marked with line 2 in the figure). The first difference is rather small, and does not lie in the area of the largest stress concentration. The second difference can be very large. However, the previous parameter study

has shown a relative insensitivity of the model to the weld height. The difference of between the two lines in figure 8.12 will therefore not have a large impact on the stress concentration factor at the weld toe. Furthermore, the top of the real weld profile consist of a number of side by side weld beads, and therefore is not completely flat (e.g. see figure 6.3). With the same reasoning as stated above, it can be argued that this will also not influence the stress concentration factor significantly.

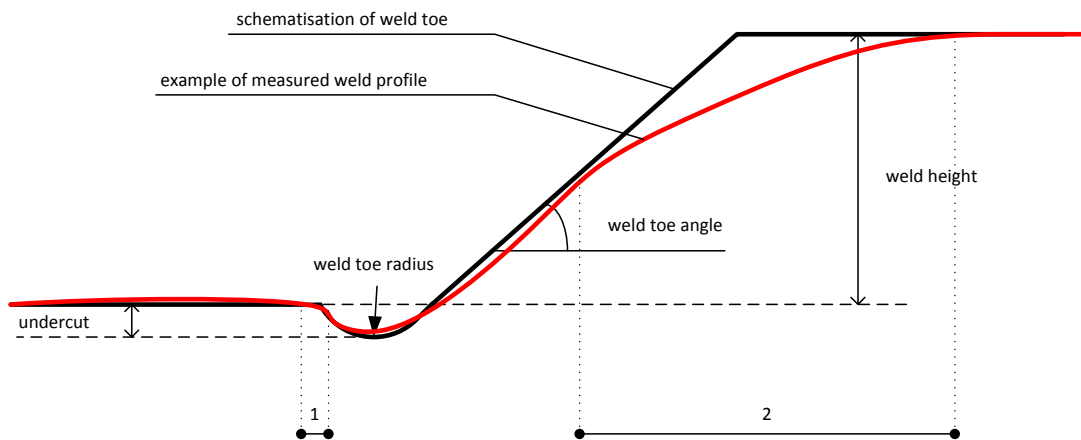


figure 8.12 Overlay of an exaggerated possible real weld geometry and the model used to represent this geometry

The possible weld geometry as shown in figure 8.12 can represent most measured geometries, except typical TIG-dressed type 3 (see figure 6.9). In this weld shape a clear plateau is visible after the weld toe radius. This can be modeled with the available model in two ways. The plateau can be ignored, resulting in too much weld material, or the plateau could be seen as the maximum height of the weld which results in ignoring most of the weld material. The two proposed models and a fictive ‘real’ weld are depicted in figure 8.13.

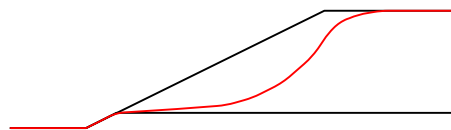


figure 8.13 Two possible representations of typical TIG-dressed type 3 and a fictive real weld profile (exaggerated drawings of the weld)

To analyze the consequences of choosing for one of those two models, one typical TIG-dressed geometry has been modeled to calculate how the stress concentration factor of this geometry will relate to the stress concentration factors of both proposed models. The results are presented in figure 8.14. It is clear that the ‘real’ model lies in between the two proposed models. Because of time constraints, in this research the choice will be made for one of both models. This will be the model on the right in figure 8.14 because here the difference with the ‘real’ model is the smallest. It must be noted that this approximation only has to be made for the specific geometries which show a plateau in the weld.

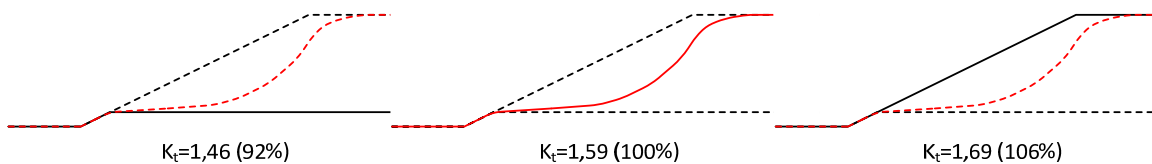


figure 8.14 Outcome of three different models for the same weld (exaggerated drawings of the weld)

8.3.2 Determination of K_t

Fatigue is a weakest link process. This property makes it very hard to predict the combination of geometry parameters which have to be taken into account to create the ‘characteristic weld toe’ in a model. The fact that the TIG-dressed weld toe radii showed significant spread and a small additional peak near the main peak of the as welded radii, indicating a possible lack of improvement of this ‘characteristic weld toe’, makes the analysis even more complicated.

The choice is made to execute two types of analyses, one where for all parameters the main peak value is considered both for as welded and TIG-dressed specimens and one where the radius of the TIG-dressed specimens has a similar value as the as welded radii while all other parameters are assumed to be at their peak value. Subsequently, influencing parameters will be varied, resulting in an expected bandwidth of K_t .

Some parameters will be calculated, such as the mean of the, nearly normal distributed, weld toe angles. Others will be estimated with the aid of the diagrams provided in 6.3.4. This introduces some extra uncertainty, but calculation would require the fitting of a probability density function, which also has an error margin, especially when the results do not fit the distribution very well. If the results of the laser measurements of the weld toe would have been categorized and any possible dependencies would have been documented, a statistic analysis could be performed which can, based on the occurrence of different geometries, more accurately predict the mean and standard deviation of K_t . Because such elaborate documentation of the weld toe parameters has been omitted in this research, the variation of K_t and K_f will be based on estimates.

First analysis, peak values

The base values of this analysis are depicted in table 8.2. It is indicated in the table for each variable how it has been determined.

		As welded	TIG-dressed	determined by
Weld toe radius [mm]		1.0	3.8	estimate
Weld toe angle [-]		27.8	15.3	calculated mean
Weld height [mm]	C11	3.9	3.9	calculated mean
	C89	4.1	4.1	calculated mean
	C89a	4.3	4.3	calculated mean
	C69	2.3	2.3	calculated mean
	C46	1.8	1.8	calculated mean
	V11	3.7	3.7	calculated mean
	V89	3.0	3.0	calculated mean
	V69	2.5	2.5	calculated mean
	V46	2.1	2.1	calculated mean
Undercut [mm]		0	0	estimate
Plate thickness [mm]	S1100	20	20	measured
	other	25	25	measured

table 8.2 Peak values of weld toes

The weld toe as described in table 8.2 will be considered as the base value. A short sensitivity analysis will follow, where all values are related to this base value. In figure 8.15 to figure 8.18 the results are presented for a variation of a certain amount to both sides of the chosen base value. The diagram shows the variation of K_t in relation to its base value as stated in table 8.2, when this base value is varied (see also equation (8.4)). For the weld toe angle and radius the values are varied for one standard deviation to both sides of the base value. For the undercut a value of 0.06 was chosen, based on the diagrams in 6.3.4. The weld height is varied over a wider band to cover the mean and standard deviation of all considered plates and has a base value (valued 1 in the graph) of 3. The assumption is that the influence of one parameter is not influenced by the change of another parameter. If for example the radius is determined at a slightly different value, it is assumed that the influence of the weld toe angle (see figure 8.16) is similar. Based on observations on the diagrams below, this seems a reasonable assumption because the diagrams all look similar while they are determined for two very different geometries.

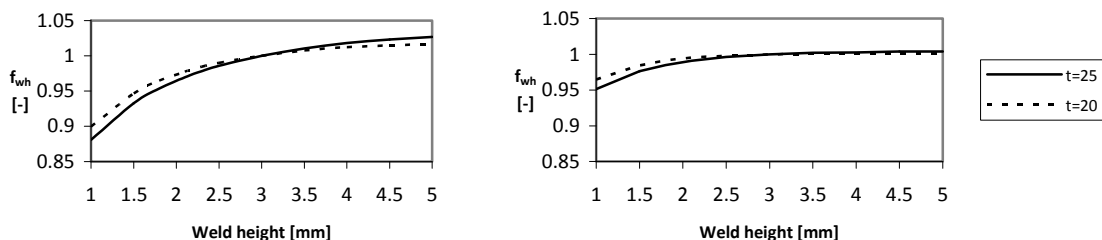


figure 8.15 Variation of K_t with varying weld height for as welded (left) and TIG-dressed joints (right)

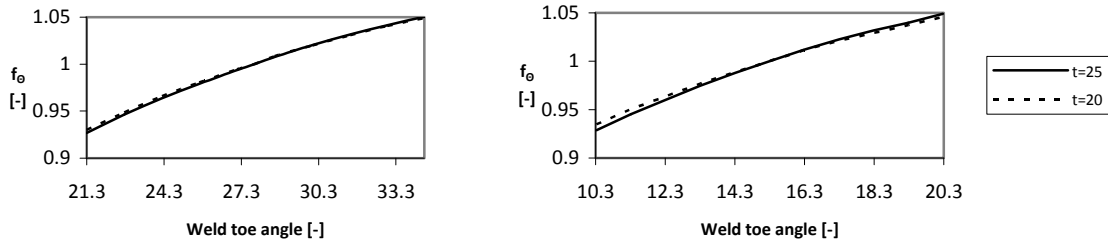


figure 8.16 Variation of K_t with varying weld height for as welded (left) and TIG-dressed joints (right)

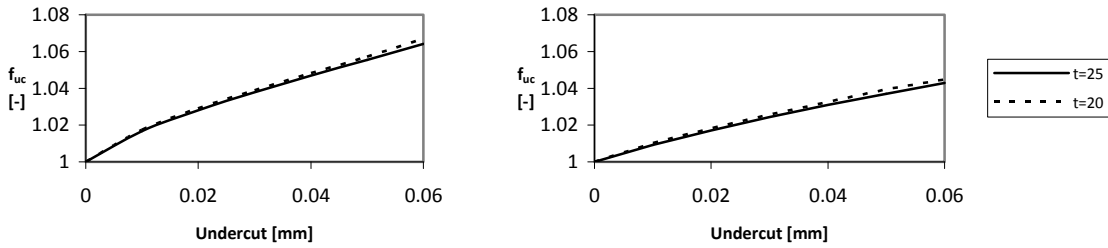


figure 8.17 Variation of K_t with varying weld height of as welded (left) and TIG-dressed joints (right)

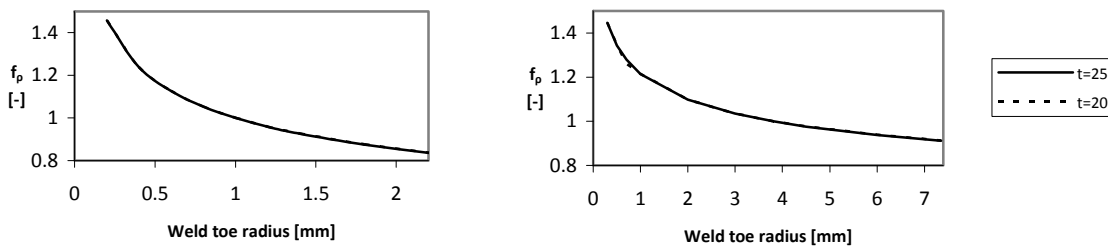


figure 8.18 Variation of K_t with varying weld height of as welded (left) and TIG-dressed joints (right)

With the aid of the graphs above, a larger K_t will be determined. The assumption is a variation of one standard deviation of all parameters, which results in multiplication factors for each weld toe variable. Because K_t also depends on the radius of the weld toe (see 3.5), the influence of radius variation will be covered in the next section. As can be seen in the diagrams above, the influence of the thickness on the influence of the weld toe radius, weld toe angle and undercut is very limited. Therefore no difference in thickness for these parameters will be made. For the weld height the differences are somewhat larger, therefore in these factors the difference between the 20 and 25 millimeter plates are incorporated. The different correction factors that are derived can be found in table 8.3. The total influence of weld toe angle, weld height and undercut variation seems limited and can be calculated with equation (8.3).

	As welded			TIG-dressed			
	Base value	Varied to	Factor f_i	Base value	Varied to	Factor f_i	
Weld toe angle [-]	27.8	34.4	1.05	15.3	20.2	1.05	
Weld height [mm]	C11	3.9	4.4	1	3.9	4.4	1
	C89	4.1	4.4	1	4.1	4.4	1
	C89a	4.3	4.5	1	4.3	4.5	1
	C69	2.3	2.5	1.01	2.3	2.5	1
	C46	1.8	2.0	1.01	1.8	2.0	1
	V11	3.7	3.9	1	3.7	3.9	1
	V89	3.0	3.3	1.01	3	3.3	1
	V69	2.5	2.6	1	2.5	2.6	1
	V46	2.1	2.3	1.01	2.1	2.3	1
Undercut [mm]	0	0.03	1.04	0	0.05	1.04	

table 8.3 Influence factors for variation of one standard deviation of weld toe angle, weld height and undercut

$$K_{t,adj} = f_{\theta} \cdot f_{uc} \cdot f_{wh} \tag{8.3}$$

In which:

f_{θ} = influence factor for variation of weld toe angle [-]

f_{uc} = influence factor for variation of undercut [-]

f_{wh} = influence factor for weld height [-]

$$f_i = \frac{K_i (i \neq \text{base value})}{K_i (i = \text{base value})} \tag{8.4}$$

Second analysis, no improvement in TIG-dressed radius

For this analysis all values of the as welded weld toe are the same as stated in table 8.2. The values of the TIG-dressed specimen are also assumed the same, with the exception of the weld toe radius. Based on observations on figure 6.22 it is very well possible that the weakest link radius of the TIG-dressed specimens has a similar value as in the as welded specimen, resulting in a base value radius of 1 millimeter. An additional sensitivity for the new TIG-dressed base geometry is presented in figure 8.19 and figure 8.20.

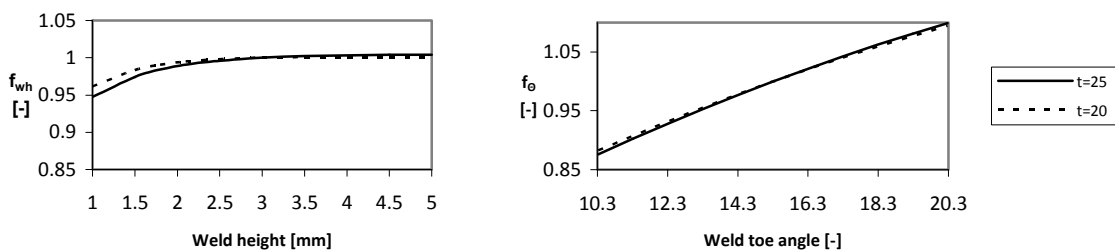


figure 8.19 Variation of K_t with varying weld height (left) and weld toe angle (right) for the TIG-dressed weld toe

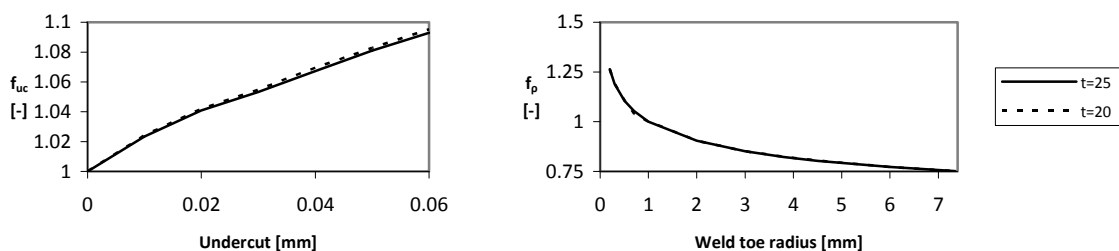


figure 8.20 Variation of K_t with varying undercut (left) and weld toe radius (right) for the TIG-dressed weld toe

A remark must be made on the variation of the weld toe angle and undercut which seem to have more influence for this geometry than they have for the standard as welded geometry or the previously considered TIG-dressed geometry. Furthermore, the weld toe radius influence seems far less, but this is fully caused by the change of base value ($\rho=1$ instead of $\rho=3.8$) which distorts the diagram. The correction factors for the adjusted TIG-dressed weld toe are given in table 8.4.

	TIG-dressed ($\rho=1$)		
	Base value	Varied to	Factor f_i
Weld toe angle [-]	15.3	20.2	1.1
Weld height [mm]			
C11	3.9	4.4	1
C89	4.1	4.4	1
C89a	4.3	4.5	1
C69	2.3	2.5	1
C46	1.8	2.0	1
V11	3.7	3.9	1
V89	3.0	3.3	1
V69	2.5	2.6	1
V46	2.1	2.3	1
Undercut [mm]	0.0	0.05	1.08

table 8.4 Influence factors for variation of one standard deviation of weld toe angle, weld height and undercut

8.3.3 Determination of K_f

For the determination of K_t the critical distance approach (see paragraph 3.5) will be used, because of the lack of experience with high strength steel in the fictitious notch rounding approach and the highly stressed volume approach would force the use of diagrams instead of formulas to determine the equivalent notch stress. These diagrams are not available for all steel grades. If equation (3.9) is used to determine a^* , the following values can be found for the different steel types:

Material	R_m [N/mm ²]	a^* [mm]
G20Mn5 (combined with S460)	622	0.217
	599	0.233
	611	0.224
G10MnMoV6-3 (combined with S690)	799	0.138
	785	0.143
	841	0.126
G18NiMoCr3-6 (combined with S890)	1042	0.086
	1052	0.084
	1070	0.082
G22NiMoCr5-6 (combined with S1100)	1185	0.068
	1163	0.070
	1171	0.070
S460	590	0.239
S690	843	0.126
S890	1065	0.083
	1051	0.085
S1100	1373	0.052

table 8.5 Calculated values of a^* for the different steel plates used

With the use of equation (3.10) the K_t of all possible geometries can be transformed into a fatigue notch factor K_f . Although the values of R_m and a^* for the paired cast steel and rolled steel of the C-specimens show some difference (see table 8.5) the difference in fatigue notch factor (K_f) is always less than 1% between the two halves of one C-plate in the cases considered. Therefore, no distinction is made between cast steel and rolled steel cracks with regard to the fatigue notch factor. In figure 8.21 to figure 8.23 the behaviour of K_t and K_f is shown for the four different considered steel grades, both for the peak values, as well as the adjusted values ($K_{t,adj}$ and $K_{f,adj}$) for deviating weld height, undercut and weld toe angle (see table 8.4 for the influence factors). The figures are depicted for the as welded situation, TIG-dressed situation

and TIG-dressed situation without radius improvement. All plates have slightly different weld height (see table 8.2), resulting in slightly different fatigue notch factors. These differences will be included in the analysis, but the differences between plates of the same steel grade (e.g. V890 and C890) are not shown here, because the overall shape of the diagrams is the same, and any quantitative differences are small.

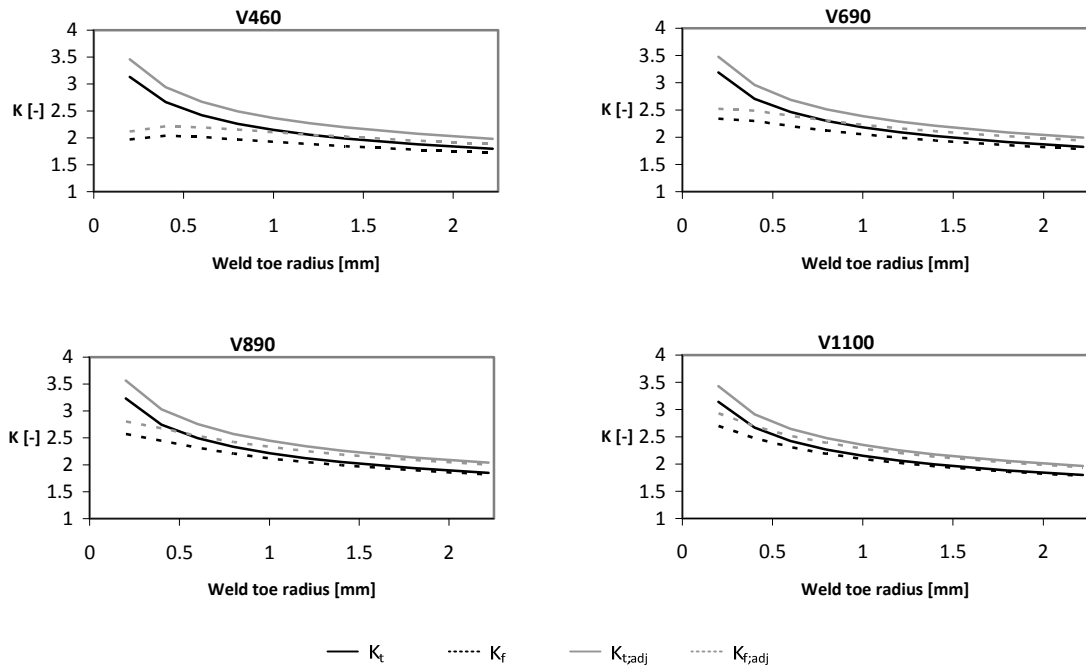


figure 8.21 Influence of radius variation on K_t (—) and K_f (- -) for different steel grades in the as welded situation. Peak values are plotted in black, adjusted values in grey.

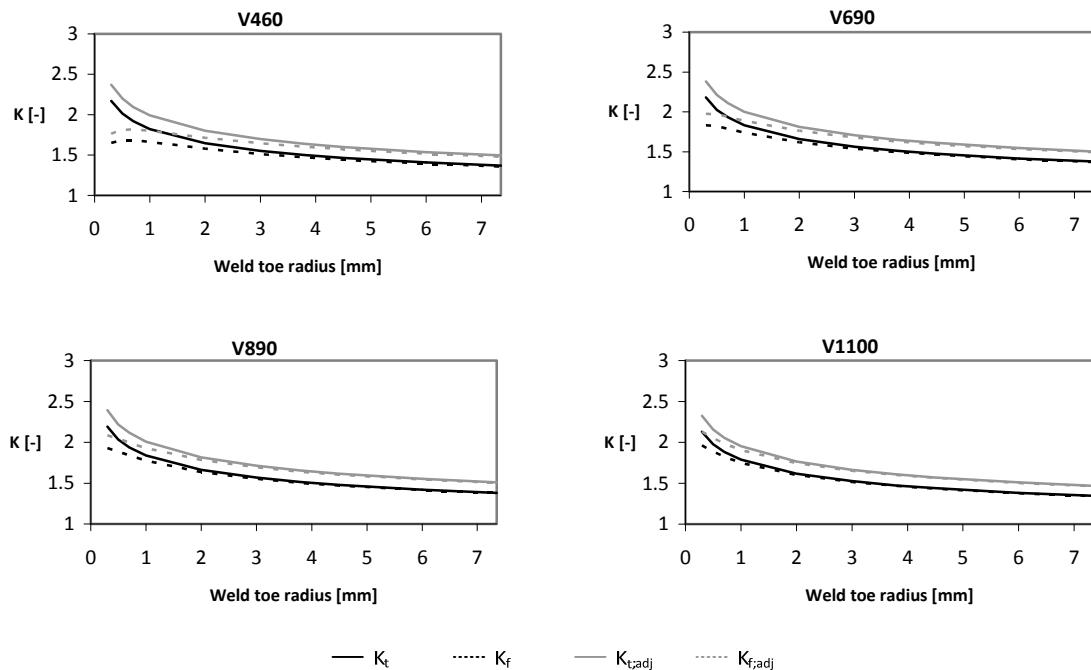


figure 8.22 Influence of radius variation on K_t (—) and K_f (- -) for different steel grades in the TIG-dressed situation. Peak values are plotted in black, adjusted values in grey.

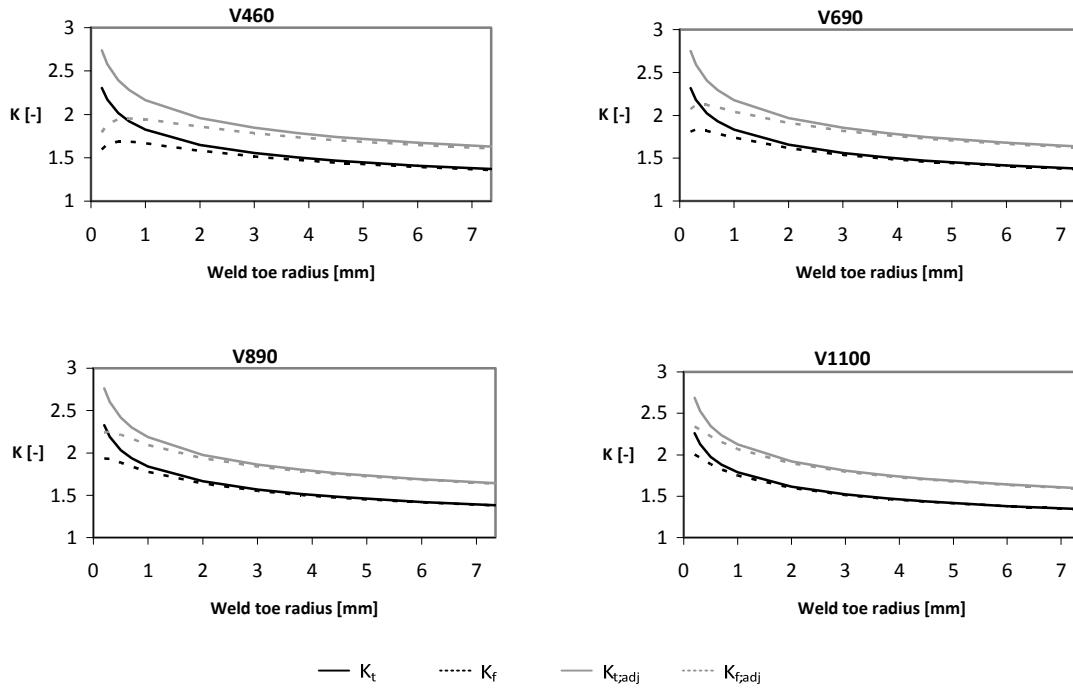


figure 8.23 Influence of radius variation on K_t (—) and K_f (- -) for different steel grades in the TIG-dressed situation without radius improvement. Peak values are plotted in black, adjusted values in grey.

The fatigue strength curve of each material will be determined for different cases. One analysis uses the peak value of the weld toe radius, combined with the peak value of all other weld toe parameters. In case of the TIG-dressed situation without radius improvement an exception is made for the weld toe radius, which is kept at the peak value of the as welded situation. Another analysis will be made using the weld toe parameters which are corrected to simulate the possibility of a ‘weakest link’. All parameters except the weld toe radius were already varied over a value of one standard deviation in 8.3.2. A similar variation of the weld toe radius would lead to very small differences between the three considered situations, because especially the TIG-dressed radii show a large standard deviation. Because small radii in combination with other TIG-dressed weld toe parameters are already covered in a separate situation, such a large variation is deemed too conservative and is therefore omitted. The chosen variation of the weld toe radius is determined at half of its peak value, which covers the bulk of the weld toe radii (see 6.3.4). This leads to an adjusted weld toe radius of 0.5 millimeter for the as welded situation and an adjusted weld toe radius of 1.9 millimeter for the TIG-dressed situation. The calculated stress concentration factors and fatigue notch factors for both the peak values (K_t and K_f) and the corrected values after variation of the weld toe parameters ($K_{t,adj}$ and $K_{f,adj}$) can be found in table 8.6 and table 8.7. Some slight differences may exist between the cast and rolled side of the specimens. This is not depicted in table 8.6 and table 8.7, but is incorporated in the model and the comparison with the fatigue tests in 9.4.3.

	As welded		TIG-dressed		TIG-dressed ($\rho=1$)	
	K_t	$K_{t,adj}$	K_t	$K_{t,adj}$	K_t	$K_{t,adj}$
C1100	2.16	2.79	1.47	1.78	1.79	2.35
C890	2.26	2.92	1.52	1.84	1.85	2.43
C890a	2.26	2.92	1.52	1.84	1.85	2.42
C690	2.17	2.83	1.50	1.82	1.83	2.40
C460	2.11	2.75	1.49	1.81	1.81	2.38
V1100	2.15	2.78	1.47	1.78	1.79	2.35
V890	2.22	2.89	1.52	1.84	1.84	2.42
V690	2.19	2.82	1.51	1.83	1.83	2.41
V460	2.15	2.80	1.50	1.82	1.82	2.39

table 8.6 Calculated elastic stress concentration factors for the three distinguished situations for peak values and adjusted values

	As welded		TIG-dressed		TIG-dressed ($\rho=1$)	
	K_f	$K_{f,adj}$	K_f	$K_{f,adj}$	K_f	$K_{f,adj}$
C1100	2.10	2.61	1.47	1.76	1.75	2.22
C890	2.16	2.63	1.51	1.80	1.78	2.22
C890a	2.16	2.64	1.51	1.80	1.78	2.22
C690	2.04	2.45	1.49	1.77	1.74	2.12
C460	1.91	2.19	1.46	1.72	1.66	1.95
V1100	2.10	2.61	1.47	1.76	1.75	2.22
V890	2.12	2.61	1.50	1.80	1.77	2.21
V690	2.05	2.44	1.49	1.77	1.74	2.12
V460	1.93	2.20	1.47	1.72	1.66	1.94

table 8.7 Calculated fatigue notch factors for the three distinguished situations for peak values and adjusted values

8.4 Determination of mean stress factor

The fatigue strength of specimens is also influenced by a mean stress (see figure 2.7). This mean stress is determined by the stress ratio R (see 2.3.2) and by the residual stress σ_r . For welded connections, a residual stress equal in magnitude to the yield stress is usually assumed. The TIG-dressing process is expected to lower residual stresses. Due to time limitations, measurements on residual stresses could not be done. To make a reasonable assumption, reference is made to literature. As shown in 4.3.3, Lopez Martinez has investigated the residual stress before and after TIG dressing. Before TIG-dressing he found a residual stress at the surface of $0.61\sigma_y$, which was reduced to $0.43\sigma_y$ after TIG-dressing. In deeper layers of the material the residual stress increased, but because the cracks are assumed to initiate at the surface, which is well supported by observations on the specimens, a similar residual stress reduction is assumed to occur in the specimens. When for the as welded specimens $\sigma_r = \sigma_y$ is assumed, the residual stress after TIG-dressing can be assumed as:

$$\sigma_r = \frac{0.43}{0.61}\sigma_y = 0.7\sigma_y \quad (8.5)$$

The mean stress of all specimens will be adjusted to a value of $\sigma_m = \frac{1}{2}\sigma_y$. Therefore the analytical values will also be adjusted to this value. Based on Haibach (2006), Pijpers (2011) proposed equation (8.6) to determine a mean stress factor including the effect of residual stresses:

$$f_{m,Haibach} = \begin{cases} \frac{1}{1-M_f} & \text{when } \frac{\sigma_m + \sigma_r}{\sigma_{aE;0}} < -1 \\ \frac{1}{1+M_f \cdot \frac{\sigma_m + \sigma_r}{\sigma_{aE;0}}} & \text{when } -1 < \frac{\sigma_m + \sigma_r}{\sigma_{aE;0}} < 1 \\ \frac{1 + \frac{M_f}{3}}{(1+M_f) \cdot \left(1 + \frac{M_f}{3} \cdot \frac{\sigma_m + \sigma_r}{\sigma_{aE;0}}\right)} & \text{when } 1 < \frac{\sigma_m + \sigma_r}{\sigma_{aE;0}} < 3 \\ \frac{1 + \frac{M_f}{3}}{(1+M_f)^2} & \text{when } 3 < \frac{\sigma_m + \sigma_r}{\sigma_{aE;0}} \end{cases} \quad (8.6)$$

$$\text{with } M_f = 0.00035 \cdot R_m - 0.1$$

In which:

$f_{m,Haibach}$	$\frac{\sigma_{aE;0}}{\sigma_{aE;0}}$ for $\sigma_m \neq 0$ and $\sigma_r \neq 0$ $\sigma_{aE;0}$ for $\sigma_m = 0$ and $\sigma_r = 0$
M_f	mean stress subfactor [N/mm ²]
σ_m	mean stress [N/mm ²]
σ_r	residual stress [N/mm ²]
$\sigma_{aE;0}$	fatigue endurance strength at alternating load [N/mm ²]

8.5 Determination of thickness factor

The plate thickness of a specimen can influence the fatigue strength. Thicker plates generally show less favourable fatigue behaviour. The calculation procedure as described in this chapter leads to the fatigue resistance at a reference thickness of 25 millimeter. Because the fatigue test results are all adjusted to a thickness of 25 millimeter, the fatigue strength prediction does not need to be adjusted. The determination and use of the thickness factor will be explained in 9.2.2.

8.6 Determination of loading mode factor

The method that is used refers to tensile loading of the specimens. In the fatigue testing in this research also only tensile loading will be applied. Due to misalignments the load will be partly in bending, but only the results of the actual tests will be adjusted for any influence of the bending loading mode. The fatigue strength prediction will refer to pure tension, thus eliminating the need for any loading mode factor. The correction of the fatigue test results will be explained in 9.2.2.

8.7 Prediction of fatigue strength curve

The fatigue strength curve for crack initiation is determined in several steps. First the fatigue limit of the base material is determined with equation (8.1). This value is then corrected for notches, mean and residual stress and displayed as a stress range instead of a stress amplitude, see equation (8.7).

$$\Delta\sigma_{E;specimen} = \frac{2}{K_f} \cdot f_m \cdot \sigma_{a;E;0} \quad (8.7)$$

Subsequently, the fatigue strength curve is determined with either the approach by Schijve or Hück et al. (see 3.5.1). The knee point for the fatigue strength curve in the approach by Schijve is set at $2 \cdot 10^7$ according to the recommendation in his publication (see 3.5.1).

This results in several design lines per plate. First of all there are the three considered situations: as welded, TIG-dressed, and TIG-dressed without radius improvement. Furthermore, to investigate the sensitivity of the fatigue strength to variation of the weld toe parameters, two values for K_f have been calculated in 8.3.2 and 8.3.3. One of these values, $K_{f,adj}$ is the result of an unfavourable variation of all weld toe parameters for a certain amount. This variation does not result in a specific failure chance, and has no more value than a sensitivity analysis. The difference between the lines determined with K_f and $K_{f,adj}$ gives insight in the sensitivity of the results for slight variation of the weld toe geometry. This will be commented on in 9.4.3.

9 Analysis of fatigue test results

9.1 Chapter outline

In this chapter the fatigue data will be analyzed. First, a selection and adjustment of the test data will be discussed. Then the statistical analysis of the data follows, which leads to mean and characteristic S-N curves. In paragraph 9.3, the data of the TIG-dressed specimens is compared with different design codes, as welded data and the analytical determination of the fatigue strength. The influence of TIG-dressing is summarized in paragraph 9.4.

9.2 Analysis of raw data

9.2.1 Exclusion of data

Not all data is deemed representative for analysis. In some cases the failure mechanism that was observed cannot occur in common practice. These data points will therefore be excluded and not be used in the statistical analysis of the fatigue data, but can still be found in the tabulated fatigue results in Annex C.

Excluded data

The data points of the following specimens have been excluded from analysis:

- C46-2
- C69-3
- C89-2
- V11-1

Due to a failure of the testing rig, specimen C46-2 has been compressed and has buckled (see figure 9.1). The permanent deformation resulting from this buckling or the straightening needed for testing will very probably influence the result, if the specimens is tested for fatigue strength. Therefore specimen C46-2 was not tested, and is thus absent in the fatigue data tabulation in Annex C.



figure 9.1 Damaged specimen C46-2

The backside of plate C69 could not be TIG-dressed (see 5.2.2). This resulted in a weld root with rather sharp notches (see figure 9.2). With specimen C69-1 this still resulted in weld cap failure, but at specimen C69-3 these notches initiated a crack on the back of the specimen. Because notches of these depth and sharpness will never pass quality control in any practical structure, this data point is eliminated. To prevent a similar failure with specimen C69-2, the weld root was ground smooth.



figure 9.2 Backside of specimen C69-1 with sharp notches at the weld root

C82-2 showed very large flaws in the cast plate, with depths of a few millimeters. To repair the plate these flaws were removed by milling and the resulting grooves were filled with weld material. Unfortunately, also the repaired specimen was not free of flaws in the cast base plate. Furthermore, the weld root could not be TIG-dressed (see also 5.2.2). This resulted in simultaneous crack initiation in the parent material and the weld root. Because both crack initiation sites would not have passed quality control in practice, this data point is eliminated.

In figure 7.6 it can clearly be seen that one data point does not cohere with the rest of the data. This specimen (V11-1) has failed in the parent material, on the root side of the weld. On the root side of the weld, stresses are much lower due to the misalignment. Although no clear defect could be found which can lead to exclusion of this data point, the data point will not be included in the analysis. It is reasonable to assume that the defect that caused the initiation of this crack has not been influenced by the TIG dressing because the crack occurred at the relatively large distance of a few centimeters from the weld toe. If this specimen had not been TIG-dressed, the crack would likely arise at the same location, because the data point also lies lower than most as welded data points which were tested by Pijpers (2011). Therefore, for the investigation of the influence of TIG-dressing, this specimen provides no useful information.

Reruns of specimens

Some specimens have shown crack initiation in the base material. Three of those base material cracks were outside of the cross section reduction. This concerns the specimens:

- C11-2
- C89-1
- C89-2

As described above, C89-2 will be excluded from the analysis. The remaining two specimens have a clear crack initiation site at a flaw in the material, which could have been visually assessed during quality control. Because the crack occurred at a significant distance from the cross section reduction it was possible to continue testing the specimen after it failed in the base material at approximately the same stress level. For several reasons the stress level of a second test will never be at exactly the same level. This is caused by the reduced specimen length, resulting in a changed misalignment, and the uncertainty where cracks will initiate. The stresses in the second test are matched to stresses in the first test from a strain gauge close to a likely, highly stressed, crack initiation point. This is not necessarily the crack initiation point of the second test. To calculate the combined stress for the final result, equation (9.1) has been used.

$$\Delta\sigma_{eq,S,d} = \sqrt[m_1]{\frac{1}{D} \cdot \frac{\sum(n_i \cdot \Delta\sigma_{i,S,d}^{m_1}) + \Delta\sigma_{L,d}^{(m_1-m_2)} \sum(n_j \cdot \Delta\sigma_{j,S,d}^{m_2})}{\sum n_i + \sum n_j}} \quad (\text{Hobbacher, 2007}) \quad (9.1)$$

In which:

- D Miner sum of total damage [-]
- $\Delta\sigma_{i,S,d}$ value of characteristic equivalent stress range [N/mm²]
- m_1 slope of S-N curve above the knee point [-]
- m_2 slope of S-N curve below the knee point [-]
- $\Delta\sigma_{i,S,d}$ stress ranges (loads) above the knee point [N/mm²]
- $\Delta\sigma_{j,S,d}$ stress ranges (loads) below the knee point [N/mm²]
- $\Delta\sigma_{L,d}$ stress range (resistance) at the knee point of the S-N curve [N/mm²]
- n_i number of cycles belonging to $\Delta\sigma_i$ [-]
- n_j number of cycles belonging to $\Delta\sigma_j$ [-]

In the calculation the Miner sum of total damage is assumed to be 1. All stress ranges are assumed to lie above the knee point of the S-N curve, thereby omitting the need for values of m_2 and $\Delta\sigma_{L,d}$. The slope of the S-N curve above the knee

point (m_1) is assumed to be 3. All these assumptions do not influence the result much because the stress ranges of the two tests are relatively close together. Other equivalent parameters are combined according to the number of cycles of each test, see equation (9.2). The limited influence of the assumptions for equation (9.1) show when equation (9.2) is used for the calculation of the combined stress: practically the same combined stress follows from both formulas.

$$X_{eq} = \frac{X_I \cdot n_I + X_{II} \cdot n_{II}}{n_I + n_{II}} \quad (9.2)$$

In which:

X_{eq}	equivalent parameter [-]
X_I	parameter value in first test [-]
N_I	number of cycles in first test [-]
X_{II}	parameter value in second test [-]
n_{II}	number of cycles in second test [-]

All presented results in graphs for specimen C11-2 and C89-1 represent the results of the final failure. In the tabulated test results in Annex C the values from the separated tests are available together with their combined value.

Failure outside weld region

Finally, some specimens must be mentioned which have shown failure outside the weld region, but will not be excluded from the data:

- C11-1
- C11-2 (after rerun)
- V11-1
- C89-1 (after rerun)

All specimens show a crack in the parent material, but inside the reduced cross section. Because there is no clear, large defect at which the crack has initiated which should not pass quality control in practice, these data points will not be excluded from the analysis. Their failure mode however, is different from all weld toe or weld material cracks. This could either be the result of a defect and the higher sensitivity of very high strength steels (especially S1100) for these defects (see 4.2.2) or an improvement of the fatigue strength in the weld region, caused by TIG-dressing. Such an improvement may have led to the base material being the weakest link. These data points will be marked in graphs to identify them if they show significant different behaviour than the other specimens. Any base material failures from the as welded tests will also be marked. If the base material failures after TIG-dressing show better fatigue behaviour than the as welded base material failures, this may be an indication that the base material failures in this research may have been caused by improving the weld toe, and shifting the weakest link to the base material. Failures in the weld material are considered to necessarily be an improvement of the connection, because such failures did not occur in the research by Pijpers. For this reason these results are judged as regular and will not be marked separately. In Annex C all different failure mechanisms are listed per specimen.

9.2.2 Adjustment of test data

To correctly compare the test data to the standardized cases in design codes, and to the previous experiments carried out by Pijpers (2011), the nominal stress levels will be adjusted. For the definition and determination of these factors this research relies to a great extent on the work by Pijpers (2011). Correction factors will be applied to correct for:

- Mean stress; nominal stresses are adjusted to a mean stress value of $\sigma_m = 0.5 \cdot \sigma_y$
- Residual stress; nominal stresses are adjusted to a loading with a certain representative residual stress
- Thickness; nominal stresses are adjusted to a reference thickness of 25 millimeter
- Loading mode; nominal stresses are adjusted to a pure tension loading mode

The adjusted nominal stress can then be calculated with the use of equation (9.3) for base material cracks and equation (9.4) for weld toe cracks.

$$\Delta\sigma_{n;u;Nf} = f_m \cdot \frac{1}{f_{t;u;Nf}} \cdot \frac{1}{f_{lm;u;Nf}} \cdot \Delta\sigma_n \quad (9.3)$$

In which:

f_m	Mean stress factor [-]
$f_{t;u;Nf}$	Thickness factor for fatigue life of base material cracks [-]
$f_{lm;u;Nf}$	Loading mode factor for fatigue life of base material cracks [-]

$$\Delta\sigma_{n,w;N_f} = f_m \cdot \frac{1}{f_{t,w;N_f}} \cdot \frac{1}{f_{lm,w;N_f}} \cdot \Delta\sigma_n \quad (9.4)$$

In which:

- f_m Mean stress factor [-]
 $f_{t,w;N_f}$ Thickness factor for fatigue life of weld toe cracks [-]
 $f_{lm,w;N_f}$ Loading mode factor for fatigue life of weld toe cracks [-]

Because the study of Pijpers showed no cracks in the weld material, no adjustment factors were derived for this failure mode. Due to time limitations, the choice is made to treat weld material cracks as weld toe cracks in this research. Furthermore, most correction factors derived by Pijpers show some variation for thickness and weld toe shape. The same corrections factors have been used in this research. It is recommended to investigate the change in these correction factors if the TIG-dressed geometries and weld material cracks are accounted for.

Mean stress factor

The as welded specimens tested by Pijpers (2011) were conservatively assumed to have a residual stress of 0 N/mm². Subsequently the results were adjusted to a value where $\sigma_r = \sigma_y$ and $\sigma_m = \frac{1}{2}\sigma_y$, which is the standard reference value for S-N curves. After TIG-dressing, the residual stresses are expected to be lower, but cannot become compressive, due to the still present cooling of the weld toe. Therefore, a reasonable and conservative assumption still is a residual stress of 0 N/mm² in the specimen. The TIG-dressed data are also adjusted to a reference value. For this, the residual stress reduction deducted from Lopez Martinez (see 8.4) is used. The test results are adjusted to $\sigma_r = 0.7\sigma_y$.

To adjust the test results, the assumed residual stress of 0 N/mm² and the measured value of σ_m were used in combination with equation (8.6) to obtain the equivalent stress for $\sigma_m = 0$ and $\sigma_r = 0$. From there adjustment to $\sigma_m = \frac{1}{2}\sigma_y$ and $\sigma_r = 0.7\sigma_y$ can be determined using the same equation. The total result of these adjustments is displayed as f_m in the tabulated fatigue test results.

Thickness factor

In general, if plate thicknesses increase, the resistance to fluctuating stresses at a notch decreases (see 2.3.1). The thickness effect is described in Eurocode according to equation (9.5). Note that this factor applies to the total fatigue life (N_f)

$$f_{t,w;N_f} = \left(\frac{25}{t}\right)^{0.2} \quad (9.5)$$

Pijpers (2011) used equation (9.6) and equation (9.7) to calculate the thickness effect for the crack initiation life, based on a parameter study. Pijpers did not find a confirmation of the thickness effect during the crack propagation life, resulting in $f_{t,w;N_p} = 1$. Equation (9.6) is valid for weld toe angles of 25°, and more pronounced thickness effects have been found for steeper angles (equation (9.7)). It therefore seems reasonable to expect a decreased thickness effect for TIG-dressed specimens due to the reduced weld toe angle.

$$f_{t,w;N_i} = \left(\frac{25}{t}\right)^{0.4} \quad \text{for } \Theta = 25^\circ \quad (9.6)$$

$$f_{t,w;N_i} = \left(\frac{25}{t}\right)^{0.7} \quad \text{for } \Theta = 65^\circ \quad (9.7)$$

Although Pijpers uses a factor which is more conservative than Eurocode, and there is reason to assume a less detrimental thickness effect because of the lower weld toe angle in TIG-dressed specimens, equation (9.6) will be used because of the differentiation between crack initiation life and crack propagation life. Equation (9.5) applies to the full fatigue life, while only the crack initiation life is covered by the notch stress approach and the alleged improvement of TIG-dressing applies mainly to the crack initiation life. Furthermore, the thickness effect proposed by Pijpers is more pronounced than stated in Eurocode which makes the use of equation (9.6) conservative, at least during the crack initiation life.

The adjustment for thickness is used to refer to a standard thickness of 25 millimeter. Most specimens approximate a thickness of 25 millimeter, except for the S1100 specimens, which have a thickness of 20 millimeter. The thickness adjustment factor consists of an adjustment factor which is applicable during the crack initiation life and an adjustment factor which is applicable during the crack propagation life. The thickness factor for the total fatigue life for weld toe cracks can then be calculated with the use of equation (9.8).

$$f_{t,w;N_f} = f_{t,w;N_i} \cdot f_{N_i} + f_{t,w;N_p} \cdot f_{N_p} \quad (9.8)$$

In which:

- $f_{t,w;Ni}$ Thickness factor for crack initiation life [-]
 f_{Ni} Crack initiation life ratio [-]
 $f_{t,w;Np}$ Thickness factor for crack propagation life [-]
 f_{Np} Crack propagation life ratio [-]

Pijpers did not find a thickness effect for base material cracks, resulting in $f_{t,u;Nf}=f_{t,u;Ni}=f_{t,u;Np}=1$.

Loading mode factor

The adjustment for loading mode is used to refer to a standard loading mode of pure tension. Because all specimens had a certain misalignment, part of the load was bending. The correction factor can be calculated with the use of equation (9.9) for base material cracks and equation (9.10) for weld toe cracks.

$$f_{lm;u;Nf} = f_{lm;u;Ni} \cdot f_{Ni} + f_{lm;u;Np} \cdot f_{Np} \quad (9.9)$$

In which:

- $f_{lm;u;Ni}$ Loading mode factor for crack initiation life; 1.0 (Pijpers, 2011) [-]
 f_{Ni} Crack initiation life ratio [-]
 $f_{lm;u;Np}$ Loading mode factor for crack propagation life; 1.09 (Pijpers, 2011) [-]
 f_{Np} Crack propagation life ratio [-]

$$f_{lm;w;Nf} = f_{lm;w;Ni} \cdot f_{Ni} + f_{lm;w;Np} \cdot f_{Np} \quad (9.10)$$

In which:

- $f_{lm;w;Ni}$ Loading mode factor for crack initiation life; 1.2 (Pijpers, 2011) [-]
 f_{Ni} Crack initiation life ratio [-]
 $f_{lm;w;Np}$ Loading mode factor for crack propagation life; 1.37 (Pijpers, 2011) [-]
 f_{Np} Crack propagation life ratio [-]

The applicable correction factor for the misaligned axially loaded specimens can be calculated with the use of equation (9.11).

$$f_{lm;w;Nf,ax} = \frac{K_m}{1 + \left(\frac{K_m - 1}{f_{lm;w;Nf}} \right)} \quad (9.11)$$

In which:

- K_m Misalignment factor. [-] Hobbacher (2007) proposed a formula based on geometry to calculate a stress increase factor. In this research K_m is based on the ratio between F/A and the measured stress near the weld [-]
 $f_{lm;w;Nf}$ Loading mode factor for total fatigue life for weld toe cracks. [-] If base material cracks are considered, $f_{lm;w;Nf}$ is replaced by $f_{lm;u;Nf}$ (cracks in the weld material will regarded as weld toe cracks) [-]

9.2.3 Statistical analysis

The fatigue data are analyzed according to the method described by Brozzetti et al. (1989) which is also prescribed by Eurocode. For a given dataset a mean regression line is constructed with a survival probability of 50% (see equation (9.12))

$$y_i = a_N + b \cdot x_i + \varepsilon \quad (9.12)$$

In which:

- y_i Log N_f [-]
 x_i Log $\Delta\sigma$ [-]
 a_N intersection on log N axis [-]
 b regression coefficient [-]
 ε sum of unknown random errors [-]

The residual random errors ε are minimized when a_N and b are estimated with the least squares method:

$$b = \frac{n \cdot \sum (x_i \cdot y_i) - \sum x_i \cdot \sum y_i}{n \cdot \sum x_i^2 - (\sum x_i)^2} \quad (9.13)$$

$$a_N = \frac{1}{n} \cdot (\sum y_i - b \cdot \sum x_i) \quad (9.14)$$

In which:

n number of specimens [-]

The slope of the S-N curve (b from equation (9.13)) can either be determined by the least squares method, or fixed to a certain value. Especially for small batches of fatigue tests (smaller than 10) the fixed value of the slope is a sensible solution. A common value for the slope is 3 for as welded joints. As mentioned in 4.3.4, different authors have found the slope to increase (i.e. a flatter S-N curve) when TIG-dressing is applied. Therefore, although the number of specimens is limited, an S-N curve with a free slope and a fixed slope of -3 will both be determined.

For comparison with Eurocode detail categories and as welded data, the mean stress range with a probability of survival of 50% and 95% at $N = 2 \cdot 10^6$ cycles is calculated. The mean stress with a 50% probability of survival at $2 \cdot 10^6$ is calculated with equations (9.15), (9.16) and (9.17).

$$\Delta\sigma_{50\%} = 10^{x_{50\%}} \quad (9.15)$$

$$x_{50\%} = \frac{y_{50\%} - a_N}{b} \quad (9.16)$$

$$y_{50\%} = \log(2 \cdot 10^6) \quad (9.17)$$

To calculate the stress range with a 95% survival probability, the coefficient of variation first needs to be determined. This can be done with equation (9.18).

$$s^2 = \begin{cases} \frac{\sum (y_i - (a_N + b \cdot x_i))^2}{n-2} & \text{when b is calculated} \\ \frac{\sum (y_i - (a_N + b \cdot x_i))^2}{n-1} & \text{when b is fixed} \end{cases} \quad (9.18)$$

In which:

s coefficient of variation [-]

Now the characteristic stress range at $2 \cdot 10^6$ cycles is calculated for a 75% confidence level of 95% probability of survival. As statistical distribution the student-t-distribution is used.

$$\Delta\sigma_{95\%} = 10^{x_{95\%}} \quad (9.19)$$

$$x_{95\%} = \frac{\log(y_{50\%}) - a_{95\%}}{b} \quad (9.20)$$

$$a_{95\%} = a_{50\%} - t_{0,95;n-f} \cdot s \quad (9.21)$$

In which:

$t_{0,95;n-f}$ The student-t-distribution factor for n-f degrees of freedom and a 95% probability of survival. n is the amount of data points, f is 1 for a fixed b-value and 2 for a calculated b value. [-]

Brozetti has stated some conditions for these formulas to give a reliable result. Runouts should not be considered, where all results with $N_f > 5 \cdot 10^5$ should be considered as such. The slope of the S-N curve should be fixed to -3 and the minimum sample size is 12. Because literature has shown that the use of high strength steel (Pijpers, 2011) and TIG-dressing (Dahle, 1998) can lead to higher m-values, two analyses have been carried out for each material, one with the prescribed fixed slope of -3, and one where the slope is optimized. The sample sizes of all fitted S-N curves will be much lower than the prescribed value of 12. Because of these differences, the results should not be seen as normative, but only as indicative.

9.3 Fitted S-N curves

9.3.1 Raw data

In the following graphs, S-N curves have been fitted for all non excluded data (see 9.2.1). This means that three failure mechanisms are considered:

- Weld toe failure
- Weld material failure
- Base material failure

All results are plotted together for two reasons. First of all, the number of data points for each failure mechanism would be very small, sometimes only one or two if each failure mechanism would be considered separately. This would make a decent analysis impossible. Secondly, the TIG-dressing is expected to significantly improve the fatigue resistance of the weld toe. This can lead to a change in the dominant failure mechanism, which still leads to the failure of the connection overall. The fatigue tests have shown that next to the two failure mechanisms which were observed during the as welded tests (weld toe and base material) another failure mechanism has presented itself: weld material failure. This mechanism has not been observed in the as welded tests, but has been responsible for seven of the twenty failed specimens during the TIG-dressed tests. Apparently the weld toe fatigue strength has been improved, causing failure in the next 'weakest link'. Because all three failure mechanisms lead to failure of the component, and non practical failures have been excluded, all data is analyzed together.

The characteristic values of the S-N curves that result from the statistic analysis are shown in table 9.1. The S-N curves are plotted with the accompanying data points in figure 9.3 to figure 9.6.

	calculated slope			fixed slope		
	$\Delta\sigma_{\text{mean}}$ [N/mm ²]	$\Delta\sigma_{95\%}$ [N/mm ²]	m [-]	$\Delta\sigma_{\text{mean}}$ [N/mm ²]	$\Delta\sigma_{95\%}$ [N/mm ²]	m [-]
S460	154	120	2.72	163	136	3
S690	212	165	4.45	171	126	3
S890	204	97	3.14	200	119	3
S1100	197	106	3.15	189	125	3

table 9.1 Characteristic values of fitted S-N curves. raw data

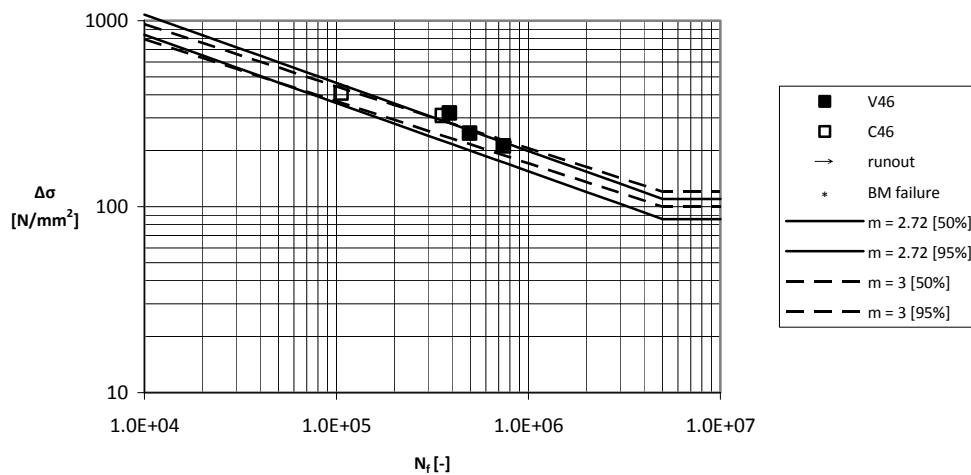


figure 9.3 Fitted S-N curves for S460, raw data

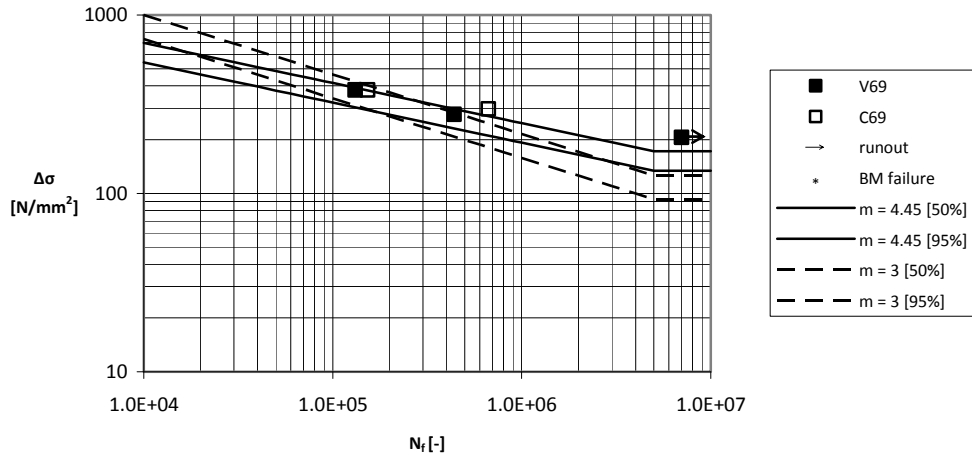


figure 9.4 Fitted S-N curves for S690, raw data

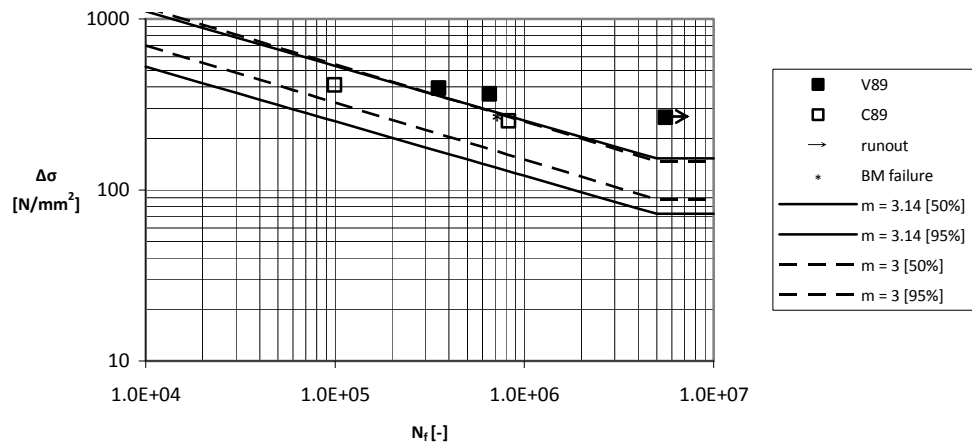


figure 9.5 Fitted S-N curves for S890, raw data

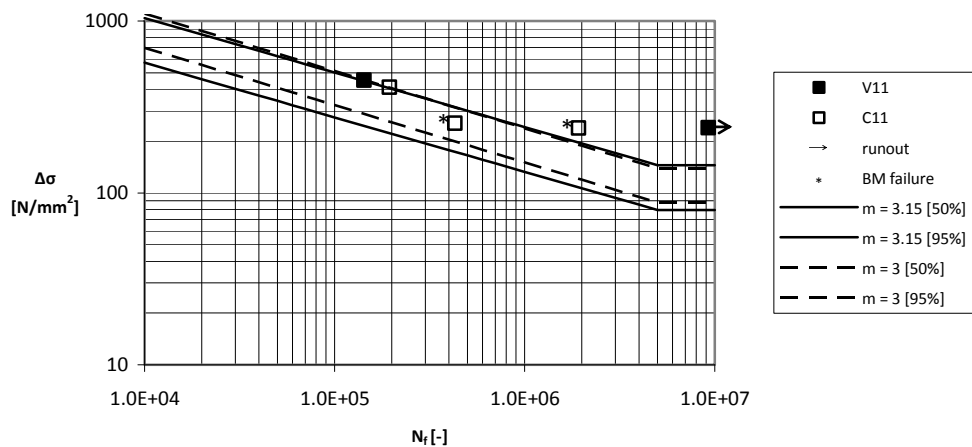


figure 9.6 Fitted S-N curves for S1100, raw data

9.3.2 Adjusted data

In the following graphs, S-N curves have been fitted for all non excluded data after adjustment. For the same reasons as explained in 9.3.1, all datapoints will be considered in one graph. The characteristic values of the S-N curves that result from

the statistic analysis are shown in table 9.2. The S-N curves are plotted with the accompanying data points in figure 9.7 to figure 9.6.

	calculated slope			fixed slope		
	$\Delta\sigma_{\text{mean}}$ [N/mm ²]	$\Delta\sigma_{95\%}$ [N/mm ²]	m [-]	$\Delta\sigma_{\text{mean}}$ [N/mm ²]	$\Delta\sigma_{95\%}$ [N/mm ²]	m [-]
S460	136	102	2.53	152	123	3
S690	169	129	4.06	142	107	3
S890	145	61	2.73	153	91	3
S1100	141	76	3.05	140	92	3

table 9.2 Characteristic values of fitted S-N curves. adjusted data

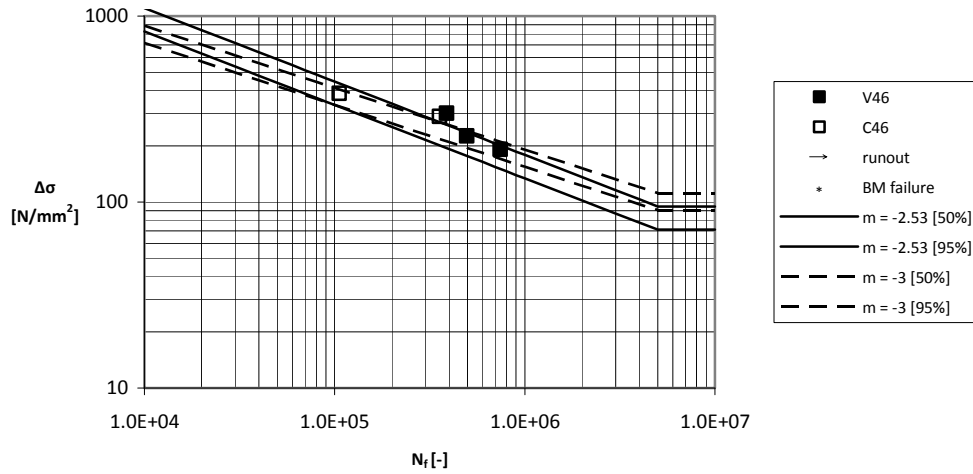


figure 9.7 Fitted S-N curve for S460, adjusted data

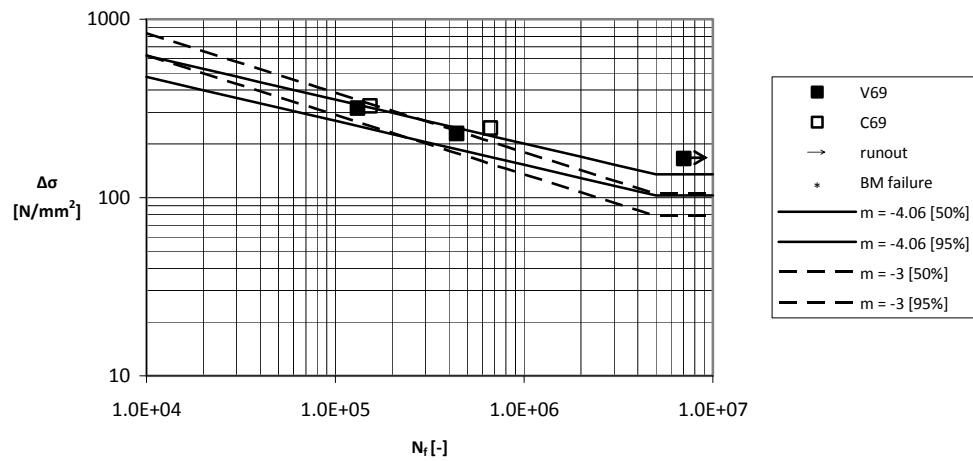


figure 9.8 Fitted S-N curve for S690, adjusted data

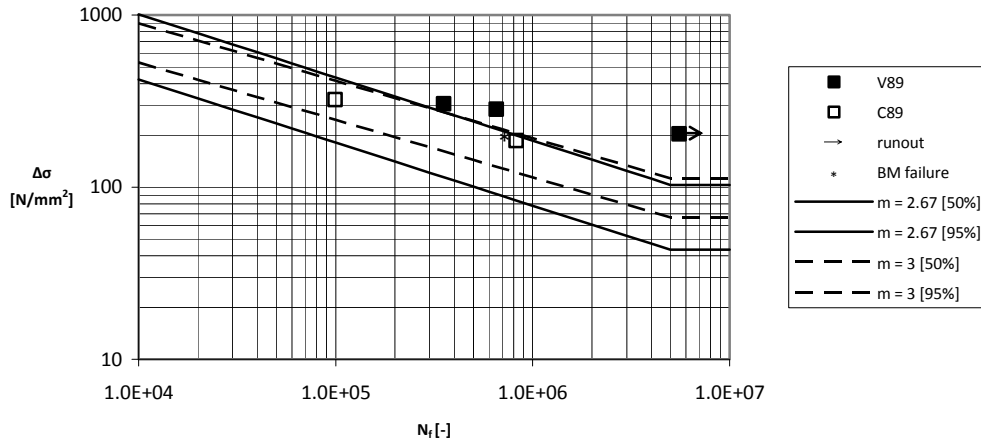


figure 9.9 Fitted S-N curve for S890, adjusted data

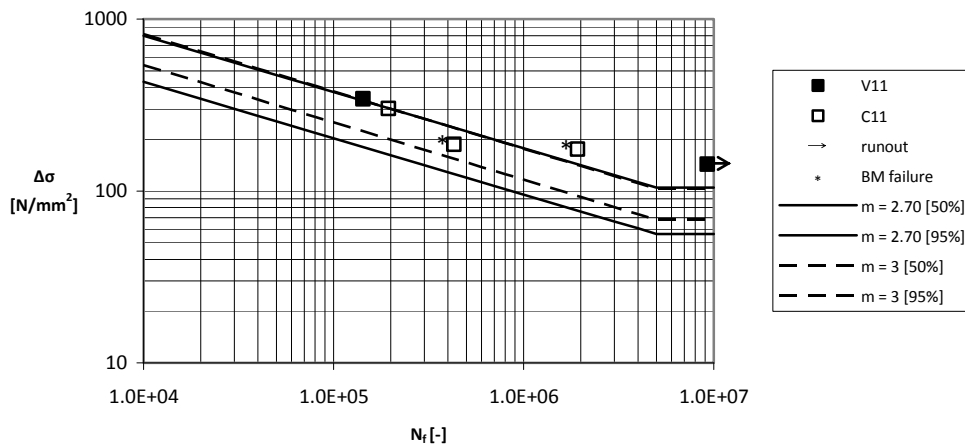


figure 9.10 Fitted S-N curve for S1100, adjusted data

9.3.3 Discussion

Some results show significant deviation from the total dataset (for example, the C89 point near $N=1 \cdot 10^5$). Some of these points contain base material failure, but others, such as the example point in figure 9.5, are other mechanisms. Because of the limited size of the dataset it is hard to determine whether these points are indeed a rare exception or part of a widely scattered dataset. Except for the excluded data as described in 9.2.1, no other data points are excluded from the regression in this paragraph or coming paragraphs.

The small data set leads to high values of $t_{0,95;n-f}$ (see 9.2.3), resulting in large difference between the mean and characteristic curve. This effect is even stronger because of the large influence single data points can have on the standard deviation due to the small sample size.

Furthermore, it must be noted that most observed runouts lie greatly above the fatigue limit which is derived from the value of the fitted S-N curve at $5 \cdot 10^6$ cycles. It is therefore questionable whether the chosen knee point is correct. Due to the limited number of results, especially for $N_f > 1 \cdot 10^6$ only a presumption with respect to the knee point can be expressed.

9.4 Comparison

9.4.1 Comparison of data with design codes

The connection that was tested, is judged by different design codes in different ways. In table 9.3 the characteristic data for a given probability of survival (P_s) are shown for the design S-N curves prescribed by different codes. The design curves are plotted and compared without any further safety factors.

	$\Delta\sigma_c$ [N/mm ²]	m [-]	P _s [-]
Eurocode*	71	3	95.0%
IIW**	92	3	95.0%
NPR-CEN/TS 13001-3-1***	100	3	97.7%

table 9.3 Characteristic values of design S-N curves for the tested specimens

*Welds checked by NDT from both sides, safety factor not considered. Design curve limited to steels up to R_{eh}=700 N/mm²

** Welds checked by NDT and misalignment <10% of plate thickness. This criterion is not met in the specimens. Design curve limited to steels up to R_{eh}=900 N/mm²

***Weld quality B. Detail category for asymmetric butt welds also incorporates asymmetric plate arrangement, which is not the case with the tested specimens. Design curve limited to steels up to R_{eh}=960 N/mm²

When table 9.1, table 9.2 and table 9.3 are compared, it is clear that the very high strength steel specimens (S890 and S1100) do not always match the codes when the characteristic strengths are compared. However, the characteristic curve value is influenced to a great extent by the uncertainty of the data caused by the small sample size. Below, all data points will be compared with the design lines specified in table 9.3.

Raw data

In figure 9.11 to figure 9.14 the raw data points are compared with the design lines of the different codes and recommendations as specified in table 9.3.

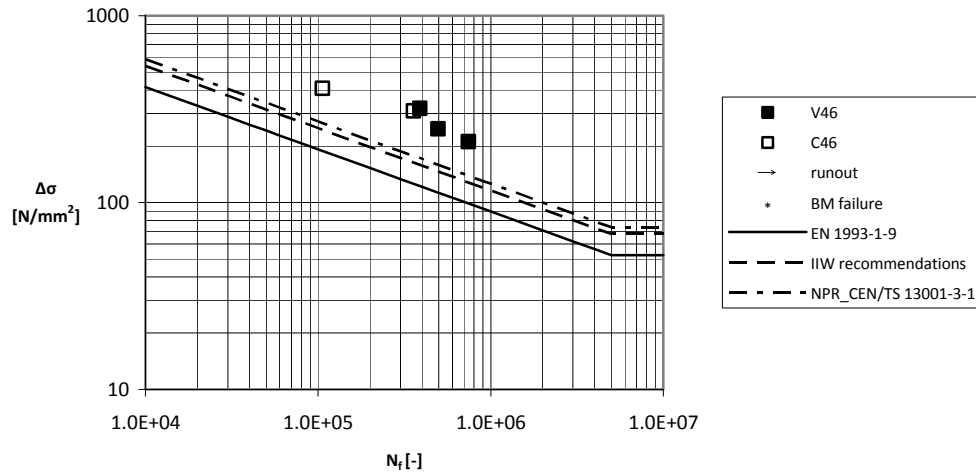


figure 9.11 S460 data points compared with design lines, raw data

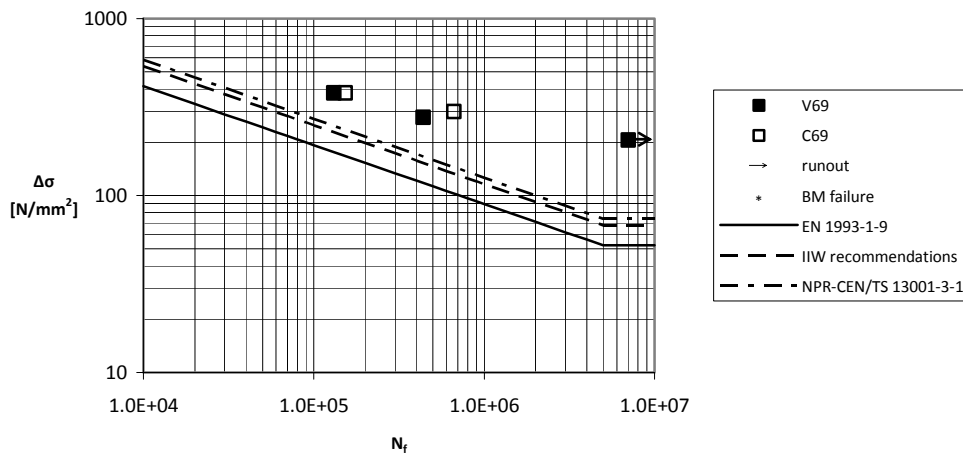


figure 9.12 S690 data points compared with design lines, raw data

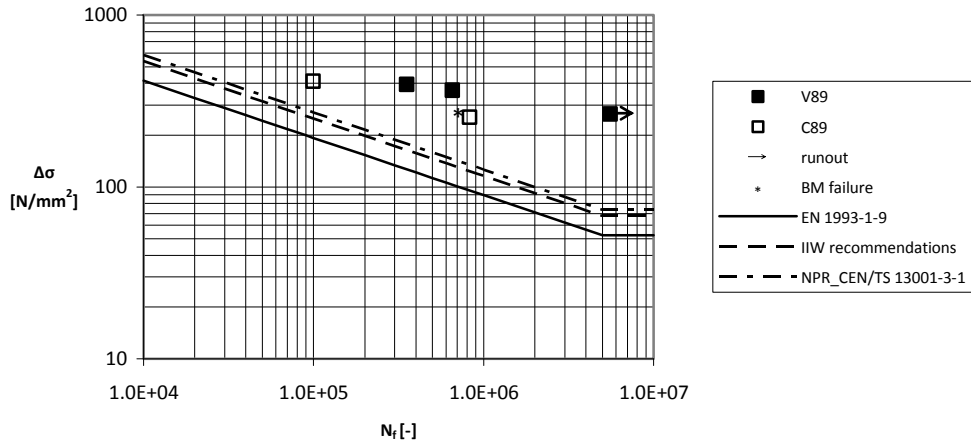


figure 9.13 S890 data points compared with design lines, raw data

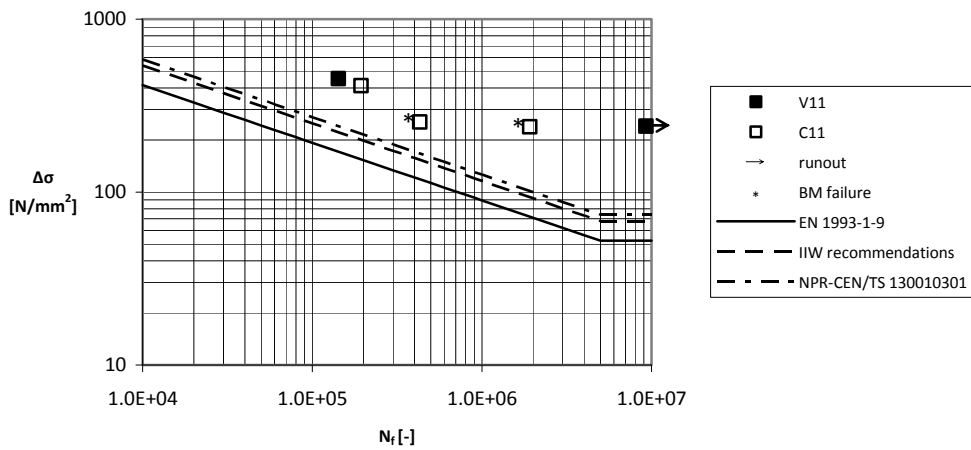


figure 9.14 S1100 data points compared with design lines, raw data

Adjusted results

In figure 9.15 to figure 9.18 the data points after adjustment are compared with the design lines of the different codes and recommendations as specified in table 9.3.

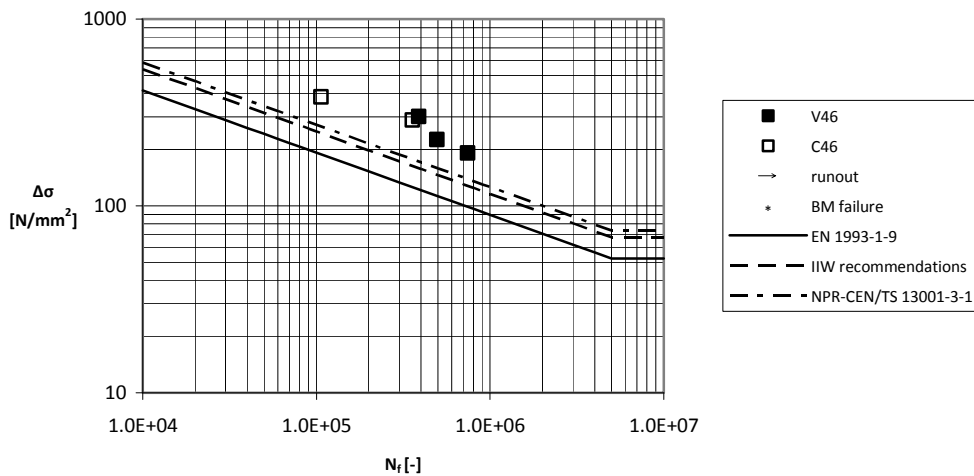


figure 9.15 S460 data points compared with design lines, adjusted data

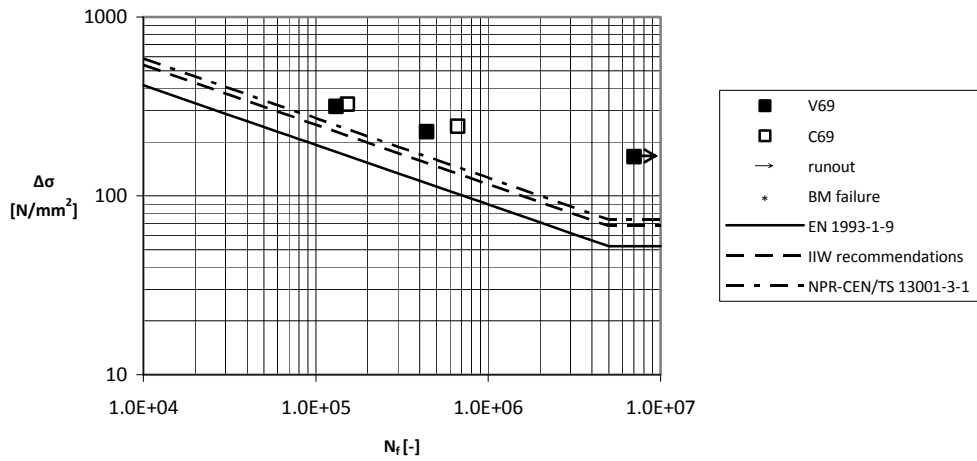


figure 9.16 S690 data points compared with design lines, adjusted data

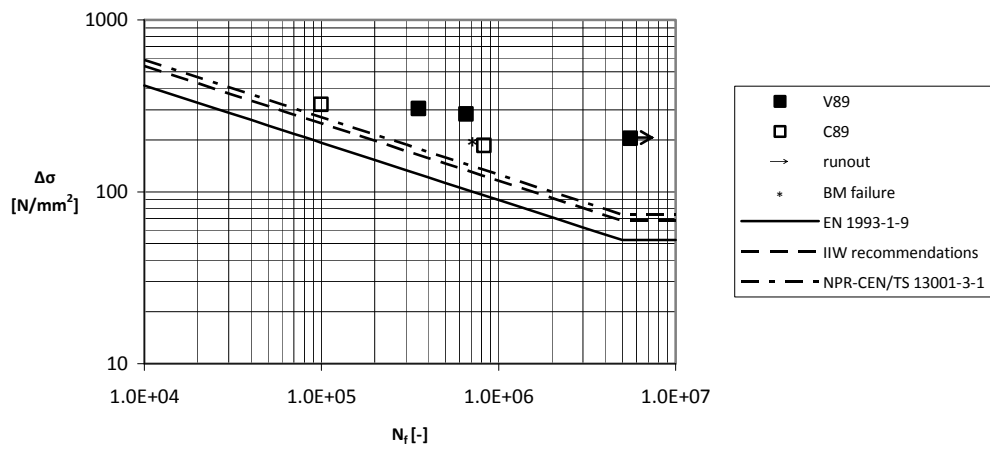


figure 9.17 S890 data points compared with design lines, adjusted data

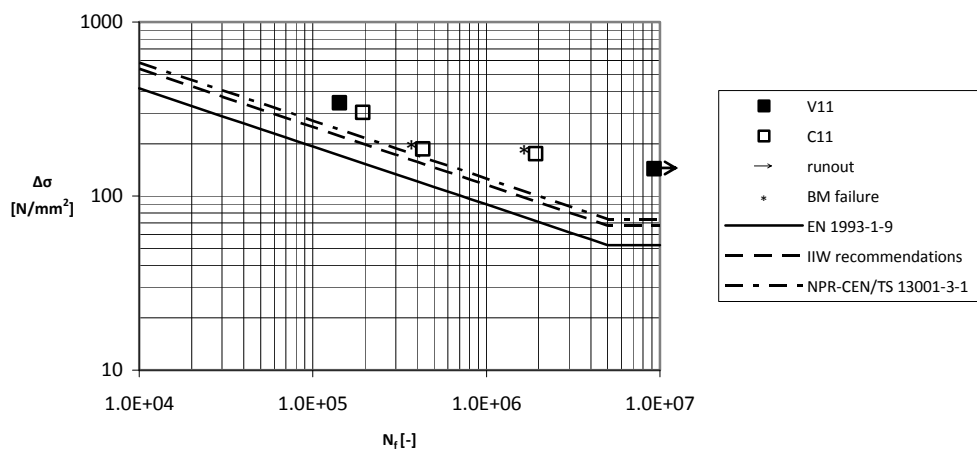


figure 9.18 S1100 data points compared with design lines, adjusted data

Discussion

All specimens have performed according to the three considered design codes or better, both before and after adjustment of the data. It is noteworthy that all found runout specimens show this behaviour at a significantly higher stress

range (factor 3-4 for raw data and a factor 2-3 for adjusted results) than specified in the design lines. A phenomenon which was also noticed when the data points were compared with the fitted S-N curves (see 9.3).

9.4.2 Comparison of data with as welded fatigue tests

From the TIG-dressed specimens all non excluded data are considered, for reasons explained in 9.3. In the study by Pijpers (2011), data were split according to their failure mechanism (base material or weld toe). The arguments to include all data in the analysis which were valid for TIG-dressed specimens, are not for the as welded data. Therefore, in principle it is only interesting to compare the results of this research with cap weld toe failures from the research by Pijpers. However, all base material failures that were found in this research can be the result of removing the weakest link from the chain by improving the weld toe, but could also already have been the weak link before TIG-dressing. Therefore, the weld toe failures from the cap side are plotted but also all base material failures are plotted. As was the case for the TIG-dressed data points, the base material failures will be marked in all diagrams.

Full fatigue life, raw data

In table 9.4 the mean stress range and characteristic stress range at $2 \cdot 10^6$ cycles are depicted for the as welded specimens and the TIG-dressed specimens. A graphic representation of the table can be found in figure 9.19. Although in figure 9.20 to figure 9.23 the TIG-dressed data points seem to lie in the middle and upper region of the as welded scatter band, the mean and characteristic values in table 9.4 and figure 9.19 do not show a strength increase due to TIG-dressing in most materials. This strength decrease may be explained by the fact that most as welded specimens were tested under bending, which in general gives better results in fatigue tests (see 9.2.2). The adjusted data therefore may show a different behaviour. The difference between as welded and TIG-dressed specimens increases when the characteristic stress range is considered for most materials. This can be caused by the fact that a small data set results in more uncertainty of the variation, and therefore results in a lower characteristic stress range. Furthermore, the flattening of the S-N curve due to TIG-dressing (see 4.3.4) cannot be observed in most results. Only the steel grade S690 behaves in a way that can be expected, based on literature research: the mean and characteristic strength increase, and the m-value of the S-N curve increases.

	calculated slope			fixed slope		
	$\Delta\sigma_{meanv}$ [N/mm ²]	$\Delta\sigma_{95\%}$ [N/mm ²]	m [-]	$\Delta\sigma_{mean}$ [N/mm ²]	$\Delta\sigma_{95\%}$ [N/mm ²]	m [-]
S460 TIG	154	120	2.72	163	136	3
S460 AW	192	165	3.99	171	138	3
S690 TIG	212	165	4.45	171	126	3
S690 AW	193	124	3.68	183	108	3
S890 TIG	204	97	3.14	200	119	3
S890 AW	259	222	6.95	208	138	3
S1100 TIG	197	106	3.15	189	125	3
S1100 AW	169	114	2.56	180	130	3

table 9.4 Comparison of mean and characteristic values at $2 \cdot 10^6$ cycles before and after TIG-dressing, raw data

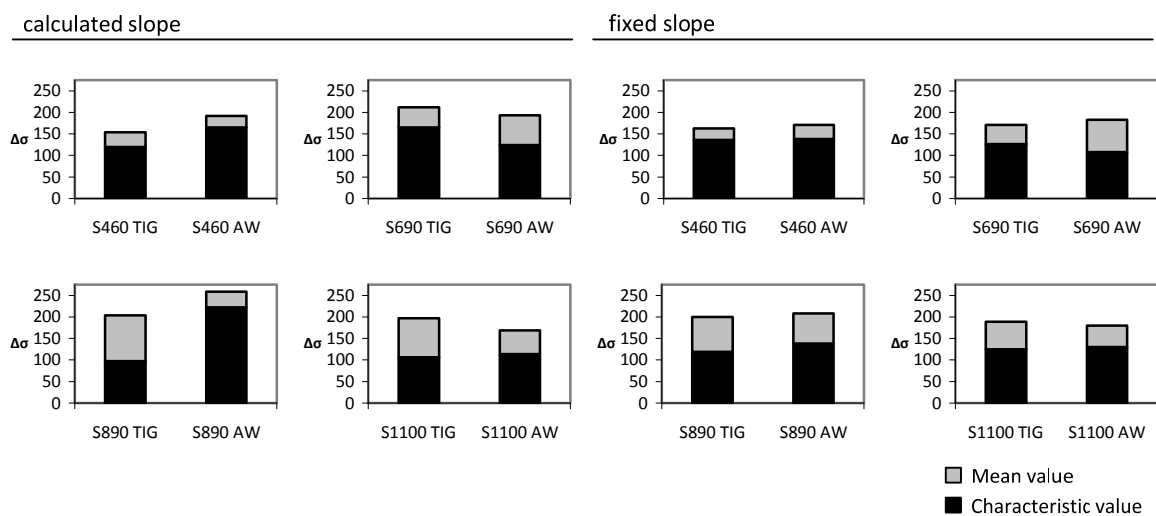


figure 9.19 Graphic overview of table 9.4: mean and characteristic stress range at $2 \cdot 10^6$ cycles, raw data

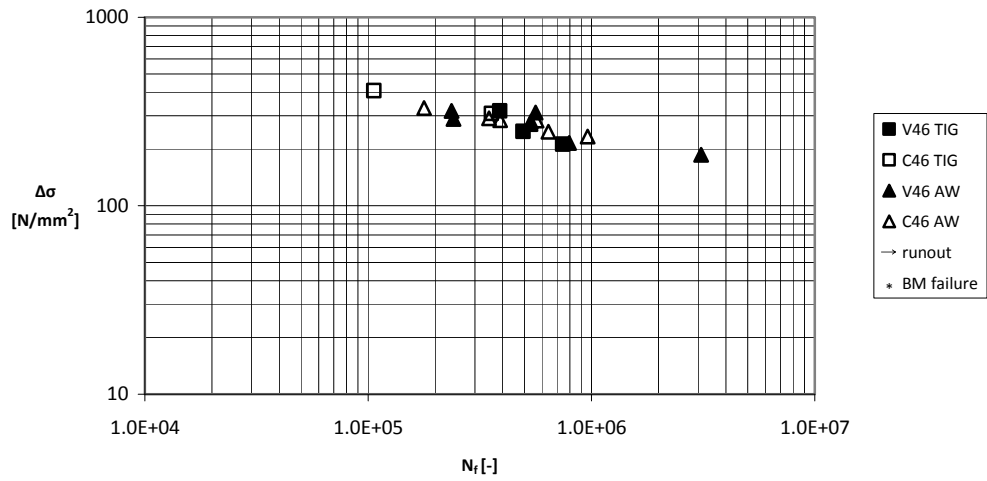


figure 9.20 Comparison between as welded data and TIG-dressed data, raw data

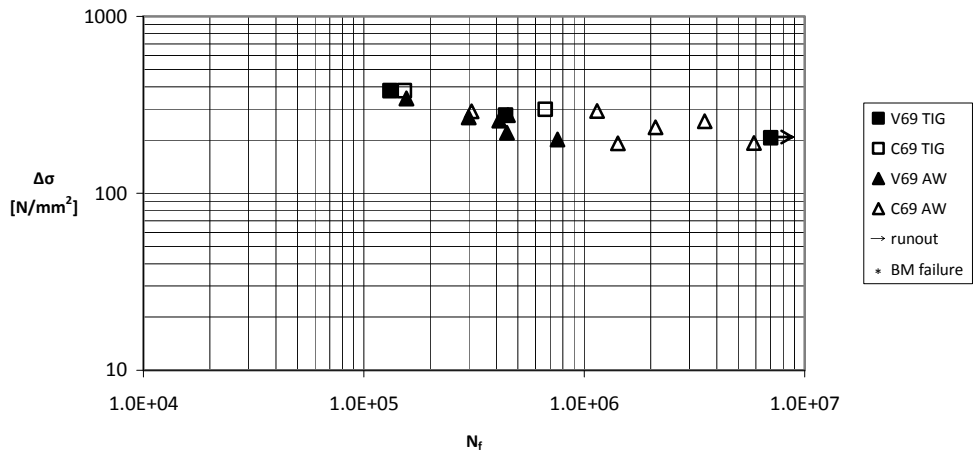


figure 9.21 Comparison between as welded data and TIG-dressed data, raw data

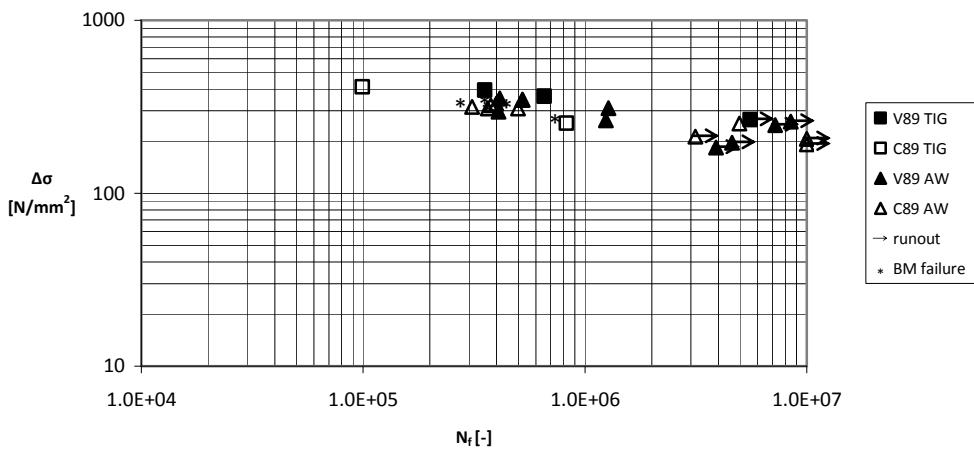


figure 9.22 Comparison of as welded data and TIG-dressed data, raw data

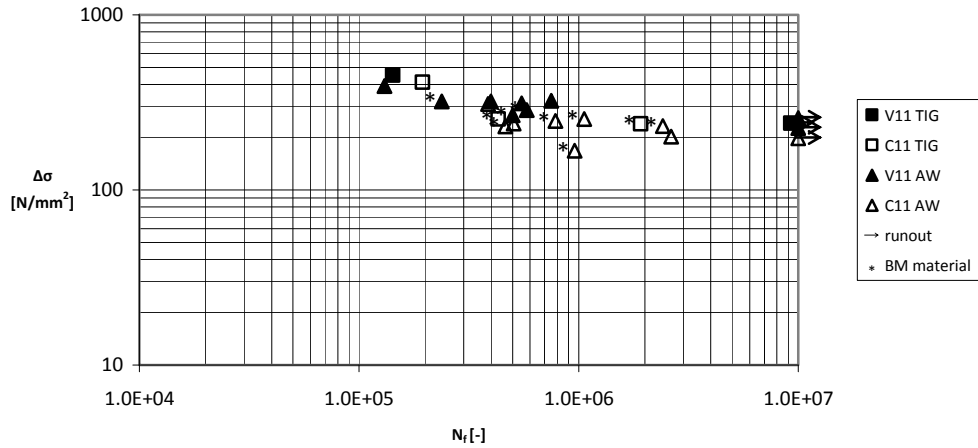


figure 9.23 Comparison of as welded data and TIG-dressed data, raw data

Full fatigue life, adjusted results

In table 9.5 the mean stress range and characteristic stress range at $2 \cdot 10^6$ cycles are depicted for the as welded specimens and the TIG-dressed specimens after adjustment of the data points. A graphic representation of the table can be found in figure 9.24. In the figure can be seen that still for most materials TIG-dressing does not seem to provide a significant increase in fatigue strength at $2 \cdot 10^6$ cycles, except for steel grade S690. It is remarkable that the fatigue strength increase at $2 \cdot 10^6$ cycles of TIG-dressed specimens seems to become larger when the S-N curve with a fixed slope is considered (see figure 9.24, right hand side), while a free slope is expected to perform better due to the flattening effect of the S-N curve (see 4.3.4). This flattening effect is not apparent in the results. When looking at the data points in figure 9.25 to figure 9.28 it is clear that the TIG-dressed data points generally lie in the upper part of the as welded scatter band with the S1100 data points as possible exception. Because the m -value of the curves decreases for all results and most data points lie in the region below $1 \cdot 10^6$ cycles, the characteristic strength at $2 \cdot 10^6$ is strongly influenced. Based on the observations of the scatter plots, a positive effect of TIG-dressing is likely.

	calculated slope			fixed slope		
	$\Delta\sigma_{\text{mean}}$ [N/mm ²]	$\Delta\sigma_{95\%}$ [N/mm ²]	m [-]	$\Delta\sigma_{\text{mean}}$ [N/mm ²]	$\Delta\sigma_{95\%}$ [N/mm ²]	m [-]
S460 TIG	136	102	2.53	152	123	3
S460 AW	150	127	4.72	127	96	3
S690 TIG	169	129	4.06	142	107	3
S690 AW	144	106	4.72	129	79	3
S890 TIG	145	61	2.73	153	91	3
S890 AW	168	122	3.77	155	106	3
S1100 TIG	141	76	3.05	140	92	3
S1100 AW	112	65	2.14	131	87	3

table 9.5 Comparison of mean and characteristic values at $2 \cdot 10^6$ cycles before and after TIG-dressing, adjusted data

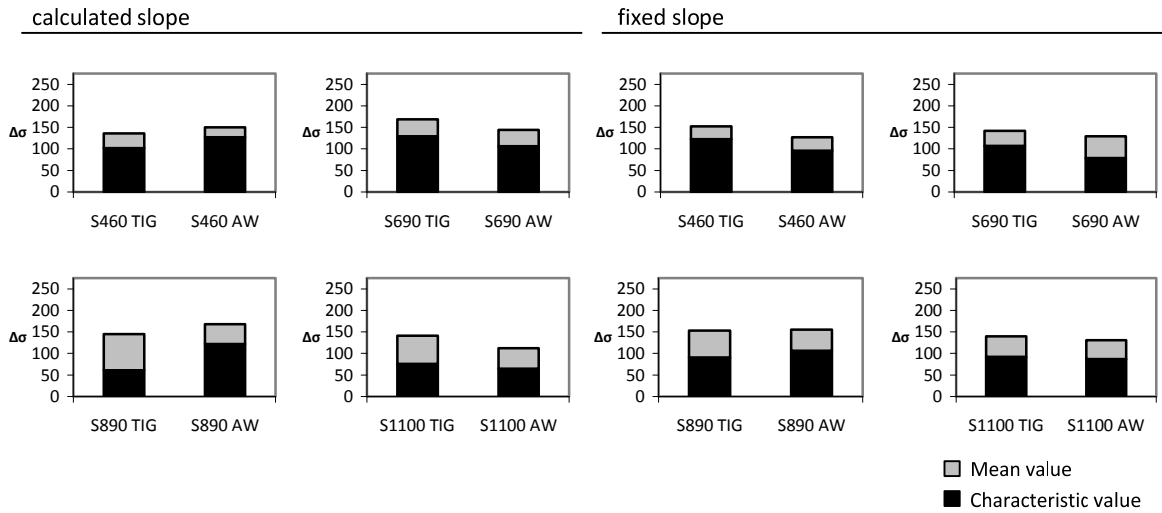


figure 9.24 Graphic overview of table 9.5: mean and characteristic stress range at $2 \cdot 10^6$ cycles, adjusted data

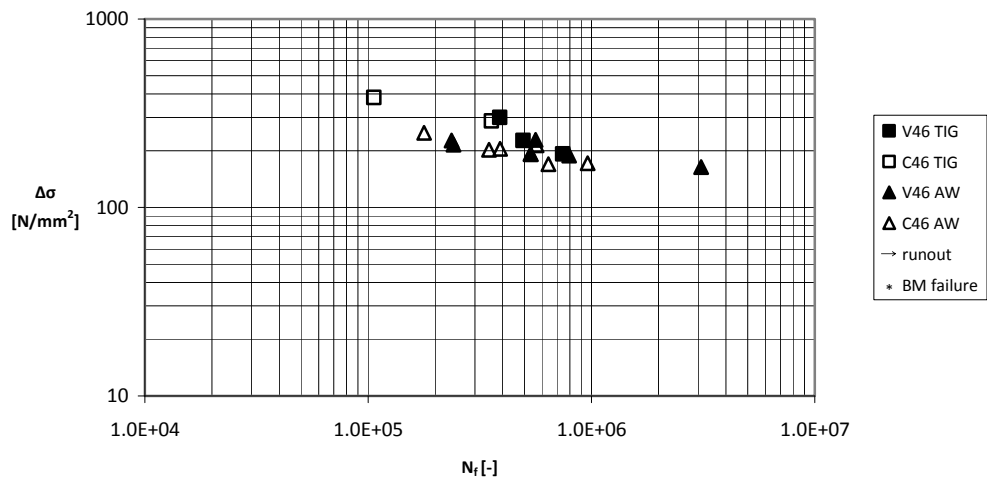


figure 9.25 Comparison of TIG-dressed and as welded data, adjusted data

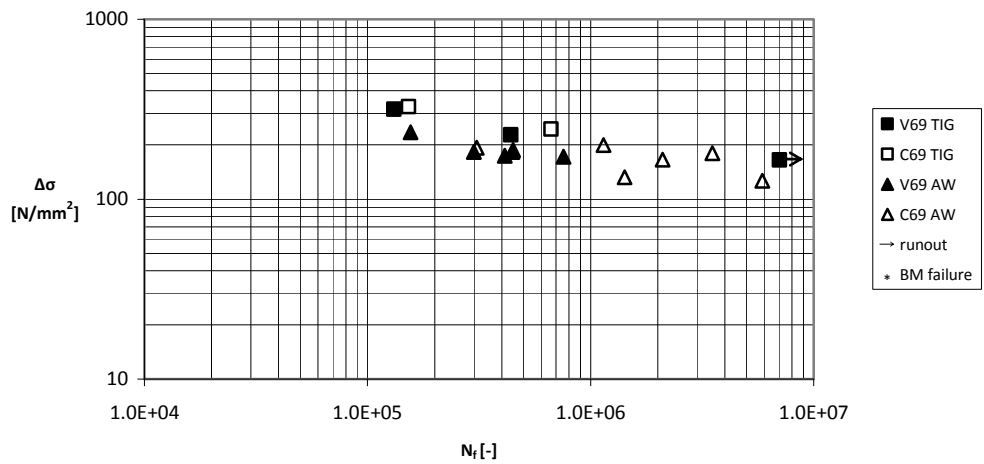


figure 9.26 Comparison of TIG-dressed and as welded data, adjusted data

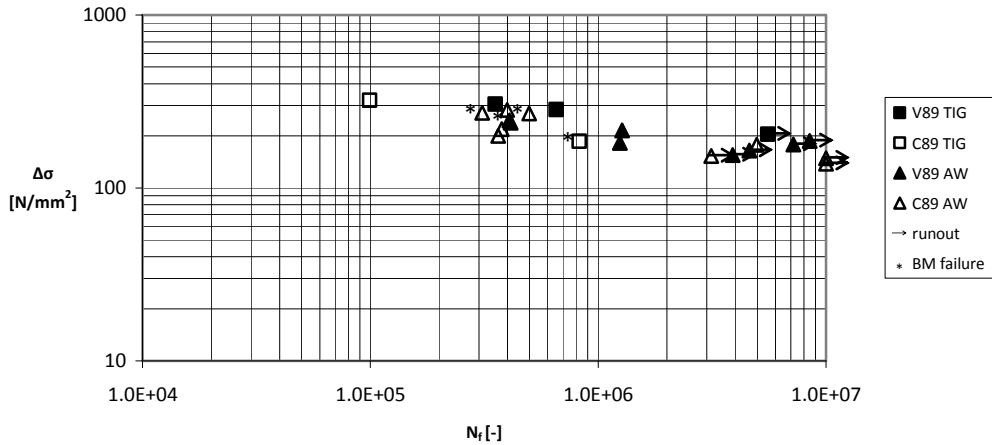


figure 9.27 Comparison of TIG-dressed and as welded data, adjusted data

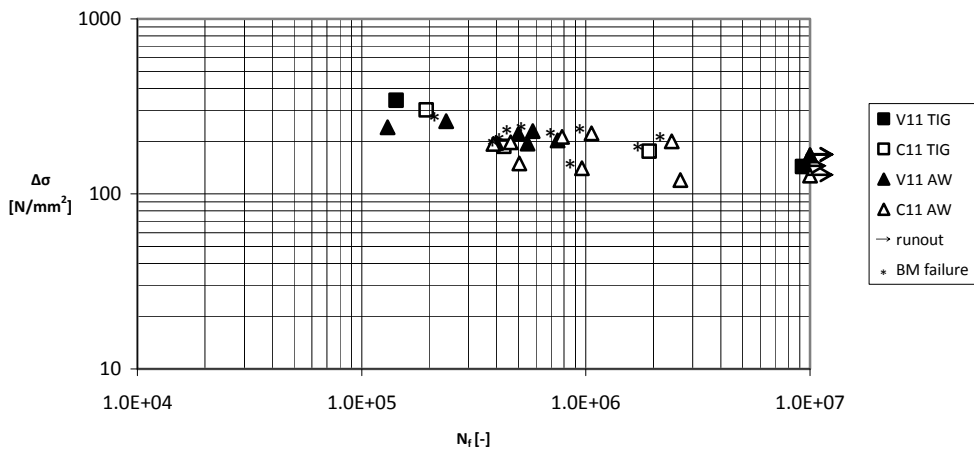


figure 9.28 Comparison of TIG-dressed and as welded data, adjusted data

Crack initiation life, raw data

Because TIG-dressing is expected to influence the crack initiation life to a greater extent than the crack propagation life, the crack initiation lives of the as welded data will be compared with the crack initiation lives of the TIG-dressed data. No S-N curves are fitted to the data, but only the overall effect of TIG-dressing will be discussed.

The earlier discussed trend, where the TIG-dressed data points mainly lie in the middle and upper region becomes somewhat more distinct in figure 9.29 to figure 9.32. Another way to analyze the effect of TIG-dressing on the crack initiation time is to compare the average crack initiation life ratios (f_{Ni}) of the TIG-dressed data set and the as welded dataset. In table 9.6 this comparison is made, and based on this table it seems clear that the TIG-dressing has increased the crack initiation life. An important remark to this table must be made. The specimens tested by Pijpers were provided with three strain gauges at each weld toe, instead of two in this research, but are also wider. If a crack initiates closer to a strain gauge it can be detected earlier. Two strain gauges in Pijpers' research were placed at the edge of the specimen, where a lot of cracks were found in that research. The results in table 9.6 may be distorted due to these differences, but it is not sure to what extent these geometrical differences between the specimens influence the result.

	f_{Ni} TIG [-]	f_{Ni} AW [-]
S460	0.70	0.49
S690	0.64	0.40
S890	0.83	0.61
S1100	0.83	0.64

table 9.6 Comparison of f_{Ni} of TIG-dressed specimens and as welded specimens. Runouts are not considered

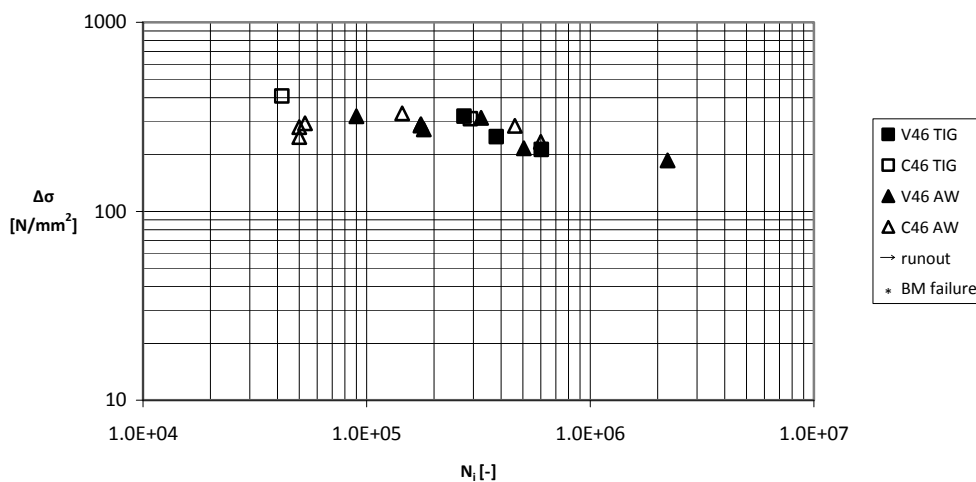


figure 9.29 Comparison of crack initiation life of TIG-dressed and as welded data, raw data

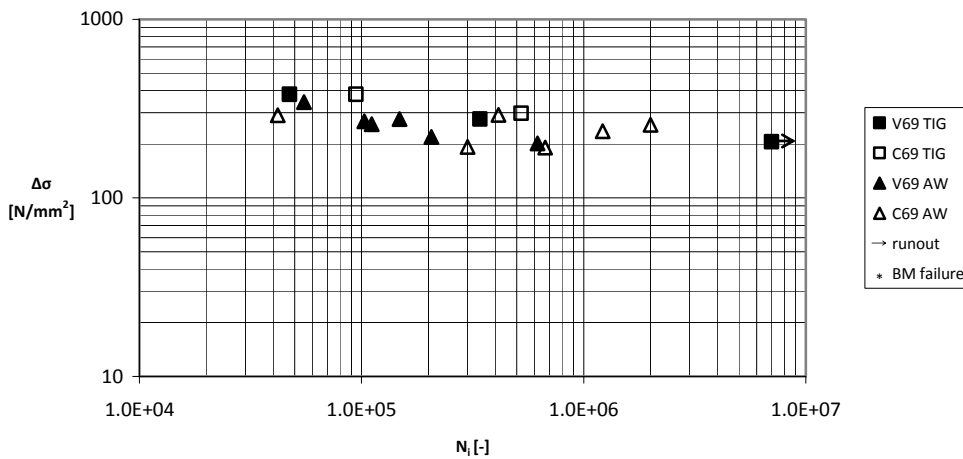


figure 9.30 Comparison of crack initiation life of TIG-dressed and as welded data, raw data

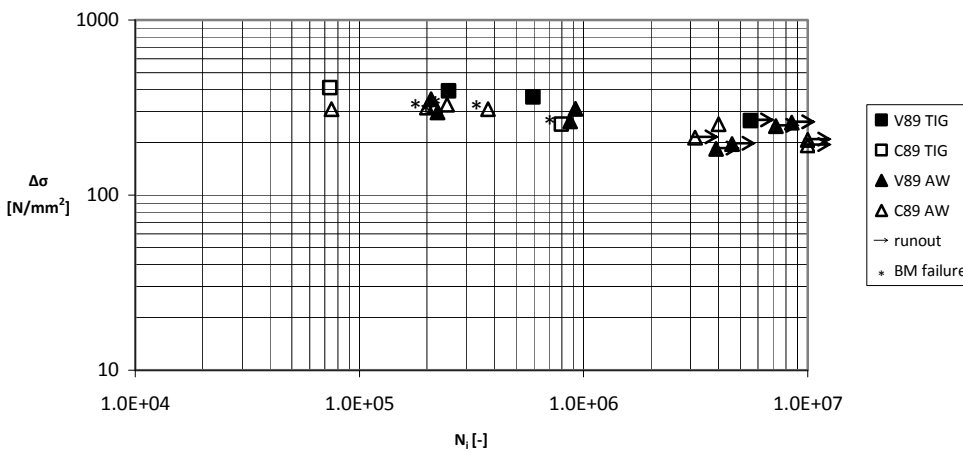


figure 9.31 Comparison of crack initiation life of TIG-dressed and as welded data, raw data

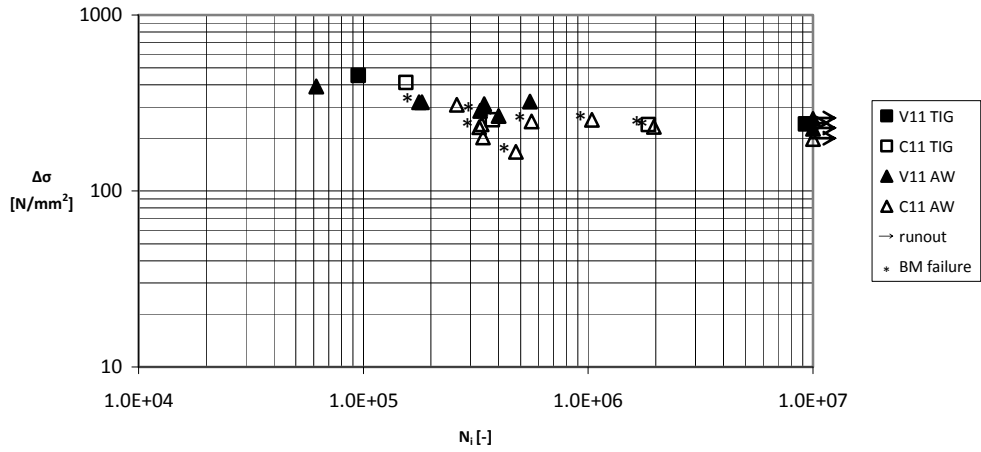


figure 9.32 Comparison of crack initiation life of TIG-dressed and as welded data, raw data

Crack initiation life, adjusted results

When the adjusted results are considered, the same effect as for raw data can be observed because the crack initiation life ratios are the same. The TIG-dressed specimens lie in the upper regions of the as welded scatter band. This effect is somewhat clearer than for the adjusted full fatigue life results.

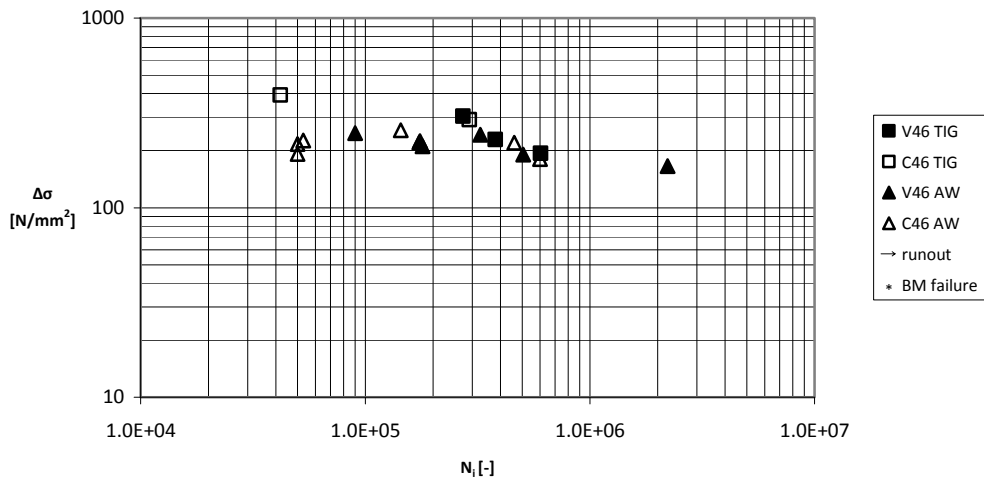


figure 9.33 Comparison of crack initiation life of TIG-dressed and as welded data, adjusted data

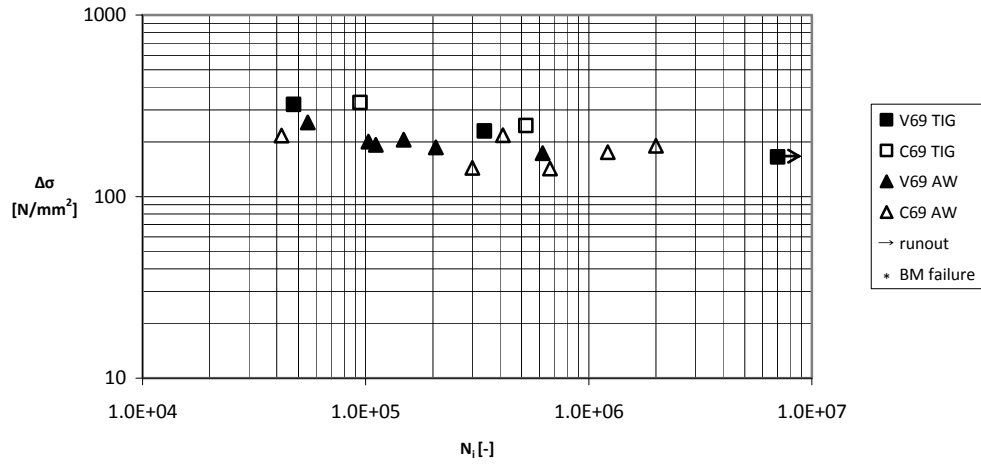


figure 9.34 Comparison of crack initiation life of TIG-dressed and as welded data, adjusted data

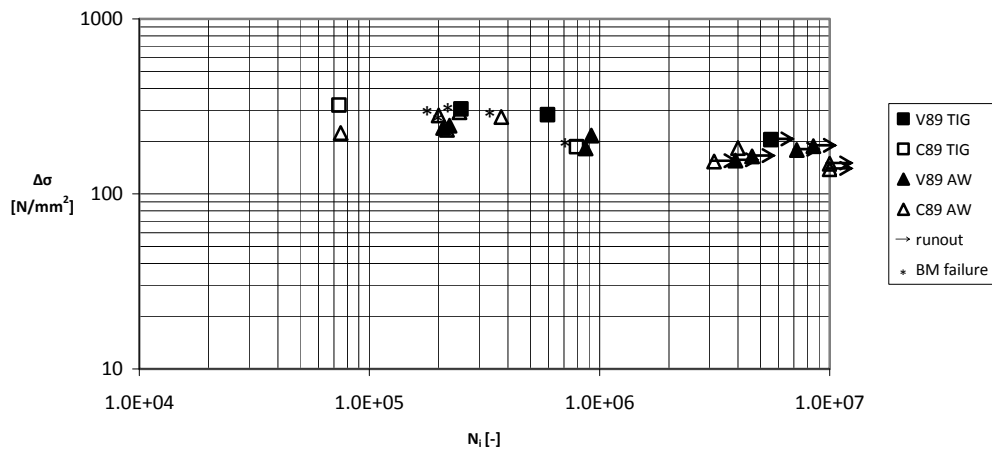


figure 9.35 Comparison of crack initiation life of TIG-dressed and as welded data, adjusted data

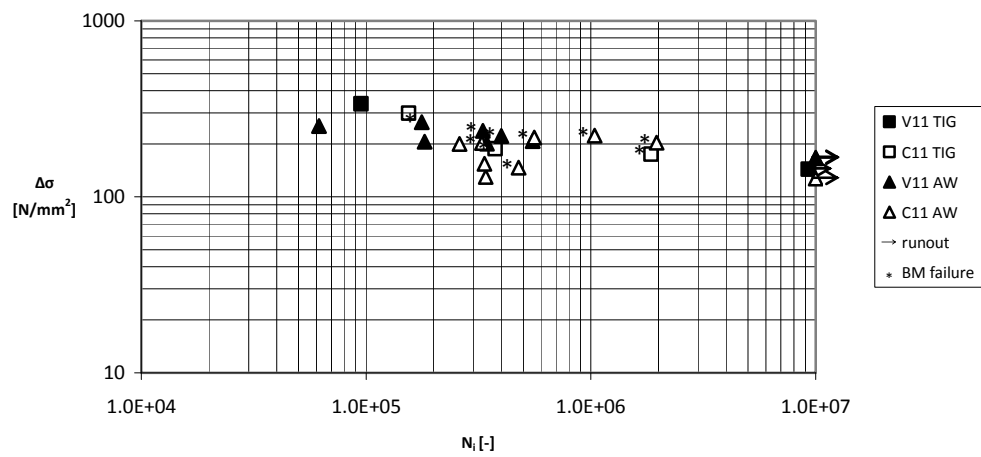


figure 9.36 Comparison of crack initiation life of TIG-dressed and as welded data, adjusted data

Discussion

The scatter plots of the raw data show little or no benefit due to TIG-dressing. When the results are adjusted according to 9.2.2, the effect of TIG-dressing seems positive, based on observations on the scatter plots. A remark must be made that the used correction factor for the loading mode has been defined as conservative by Pijpers. This means that it is possible that slightly higher fatigue strength should be attributed to the as welded results which were loaded in pure bending.

When S-N curves are fitted to the results, the TIG-dressed results show a steeper S-N curve most of the time. Because most results are located below $1 \cdot 10^6$ cycles, this steeper curve results in lower mean and characteristic stress ranges at $2 \cdot 10^6$ cycles for TIG-dressed data when compared with as welded values. When the slope of the S-N curve is fixed to a value of 3, the results for TIG-dressed data become less unfavourable, but a clear strength increase can not always be observed.

To investigate the possible positive influence of TIG-dressing in the medium cycle regime, the fitted S-N curves of both the as welded data and TIG-dressed data are plotted in figure 9.37.

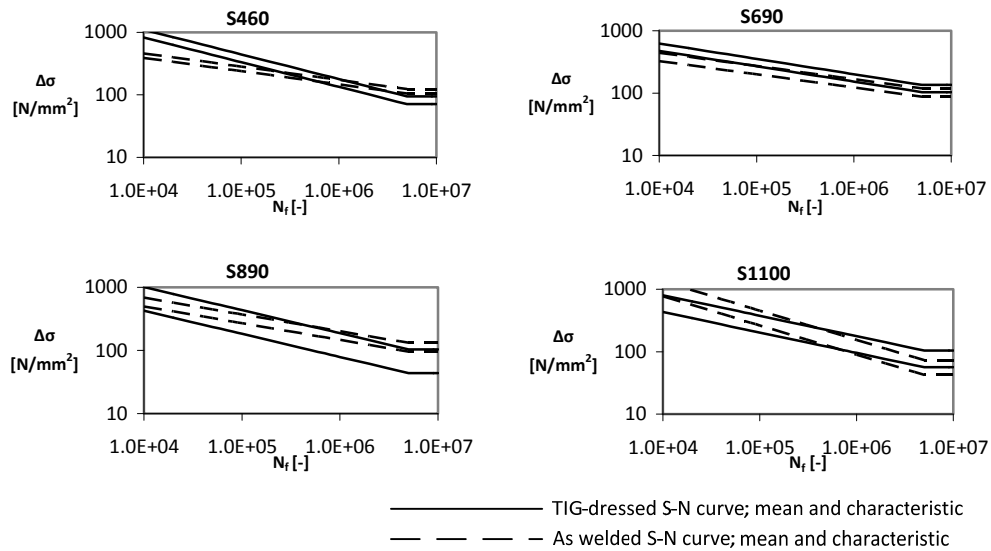


figure 9.37 Comparison of fitted S-N curves. Adjusted data, calculated slope.

From figure 9.37 can be concluded that especially in the medium cycle range a beneficial effect due to TIG-dressing can be observed for most materials. Therefore, the mean and characteristic values of the fitted S-N curves at $N=4 \cdot 10^5$ (instead of $N=2 \cdot 10^6$) are depicted in table 9.7 and figure 9.38. This table and diagram clearly show a mean fatigue strength increase due to TIG-dressing for materials S460 and S690. The two steel grades which showed a lot of failures in the base material, S890 and S1100 still perform about similar to the as welded specimens. The characteristic values of all steel grades do not always show the results as described above, but this may cohere with the smaller data set of the TIG-dressed specimens, as explained earlier.

	calculated slope			fixed slope		
	$\Delta\sigma_{\text{mean}}$ [N/mm ²]	$\Delta\sigma_{95\%}$ [N/mm ²]	m [-]	$\Delta\sigma_{\text{mean}}$ [N/mm ²]	$\Delta\sigma_{95\%}$ [N/mm ²]	m [-]
S460 TIG	257	192	2.53	260	210	3
S460 AW	211	178	4.72	217	164	3
S690 TIG	251	191	4.06	243	183	3
S690 AW	203	150	4.72	221	135	3
S890 TIG	261	110	2.73	262	156	3
S890 AW	257	187	3.77	265	181	3
S1100 TIG	239	129	3.05	239	157	3
S1100 AW	238	138	2.14	224	149	3

table 9.7 Comparison of mean and characteristic values at $4 \cdot 10^5$ cycles before and after TIG-dressing, adjusted data

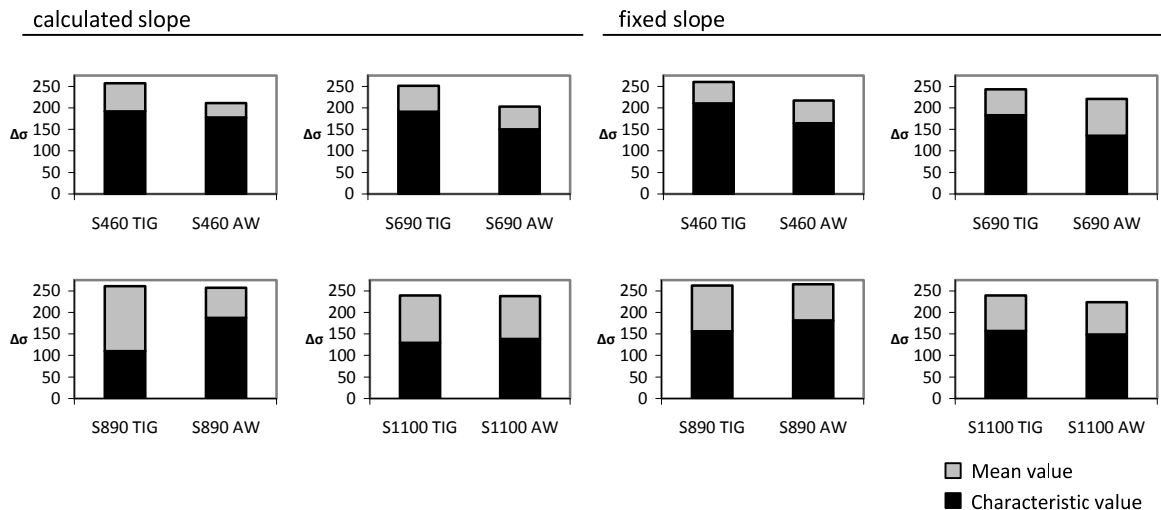


figure 9.38 Graphic overview of table 9.7: mean and characteristic stress range at $4 \cdot 10^5$ cycles, adjusted data

The exceptions to the trend described above are the data from S690 steel. Here, the data points in the scatter plot behave better and the fitted S-N curves also show a strength increase due to TIG-dressing at higher cycles ($2 \cdot 10^6$). The fitted S-N curve of the TIG-dressed data has a higher m-value than the fitted S-N curve to the as welded data in case of the raw data. When the tabulated fatigue test data are consulted (see Annex C) it can be seen that all failed S690 specimens failed at the weld toe. No base material or weld material failures have been observed in these specimens. Closer inspection of the weld leads to no additional information: the welds in S690 look similar to the welds of S460, where almost only weld material failures occurred. It may be interesting to analyze the geometry of the weld cap with the aid of the already available laser measurement data in future research. Also any changes in residual stress in the weld material may have occurred due to the TIG-dressing procedure, which, if it concerns a residual stress increase, can lead to worse fatigue behaviour of the weld material than in the as welded case.

An opposite trend can be seen in the S1100 specimens. Only one S1100 specimen has failed at the weld toe, and all others failed in the base material and the S1100 TIG-dressed data points more or less blend in with the as welded results, especially at high cycles.

It may be possible to explain these observations in the following way. TIG-dressing has improved the weld toe and removed it as 'weakest link' from the chain. For specimens where even after TIG-dressing the weld toe was the, now stronger, 'weakest link', an improvement in fatigue strength can be observed. Specimens which have 'weak links' with marginally higher fatigue strength elsewhere in the base material or weld material show only marginal improvement. If the weak link in the as welded specimen was placed outside the weld region, resulting in a base material failure, this will still be the case in the TIG-dressed situation. In that case, not improvement is observed. In the graphs of the steels that show base material failures, it can be observed that the base material failures indeed blend in with the as welded results, while the rare weld toe or weld material failures lie slightly above the as welded scatter band.

The crack initiation life of the TIG-dressed specimens seems to be improved with respect to the as welded specimens, resulting in a higher N_i/N_f ratio. However, due to differences in geometry between the TIG-dressed specimens and the as welded specimens, these results may have been distorted.

9.4.3 Comparison of data with analytical determination of fatigue strength

The used analysis method is only valid for the crack initiation life of weld toe cracks. Therefore, only the crack initiation life of specimens failed at the weld toe and runouts will be compared with the analytical results. This selection results in a relatively limited number of data points which can be compared for the TIG-dressed case, because several specimens showed other failure mechanisms than a weld toe failure (see 7.3).

Furthermore, the analysis method contains corrections for the means stress. The results of the analysis will therefore only be compared with the results of the tests corrected for means stress, thickness and loading mode.

Comparison of as welded data with model based on peak values of as welded geometry

In figure 9.39 to figure 9.49 the comparison is made between the model as described and derived in chapter 8 and the fatigue test results by Pijpers in the as welded situation. Almost all predicted results lie significantly higher than the test results. Especially the model as derived by Schijve shows very different behaviour than reality. When the knee point in the model by Schijve would be adjusted to 10^6 cycles (as is recommended for notched, not welded specimens) it would show similar results as the model derived by Hück.

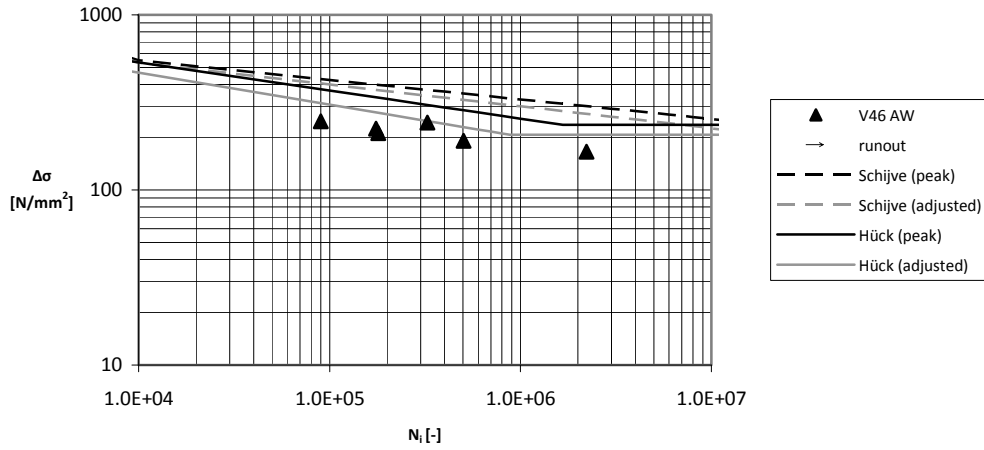


figure 9.39 Comparison of crack initiation life of V46 specimens with weld toe failure and modeled fatigue strength

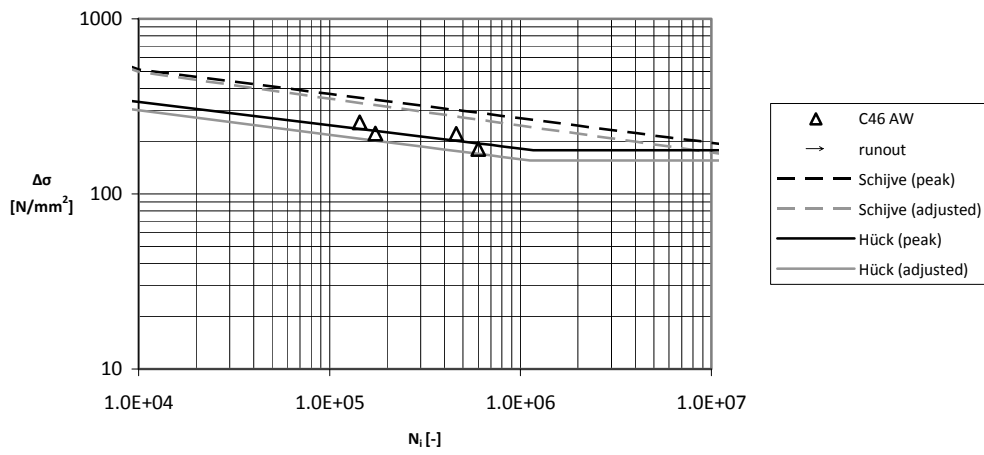


figure 9.40 Comparison of crack initiation life of C46 specimens with weld toe failure on cast side and modeled fatigue strength

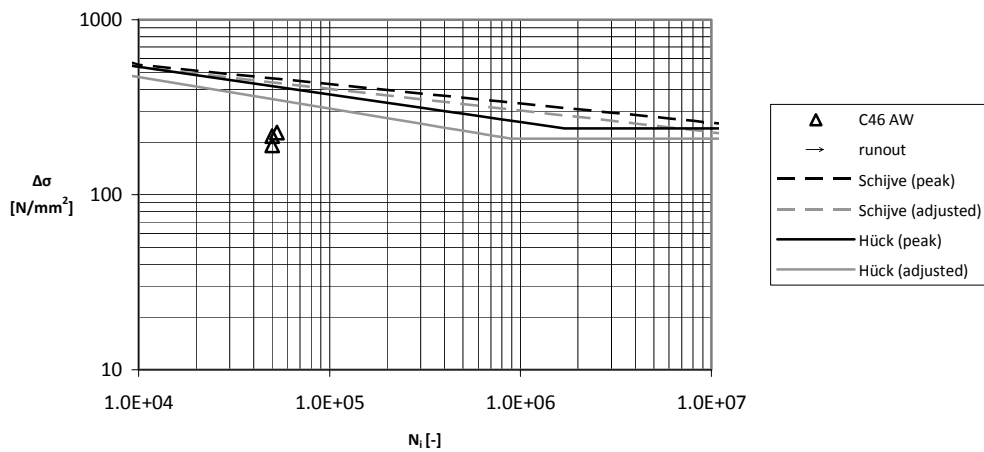


figure 9.41 Comparison of crack initiation life of C46 specimens with weld toe failure on rolled side and modeled fatigue strength

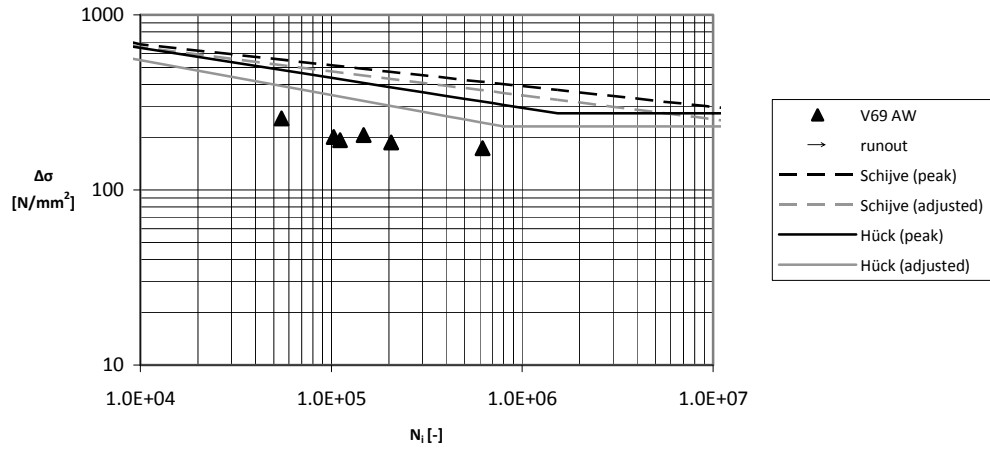


figure 9.42 Comparison of crack initiation life of V69 specimens with weld toe failure and modeled fatigue strength

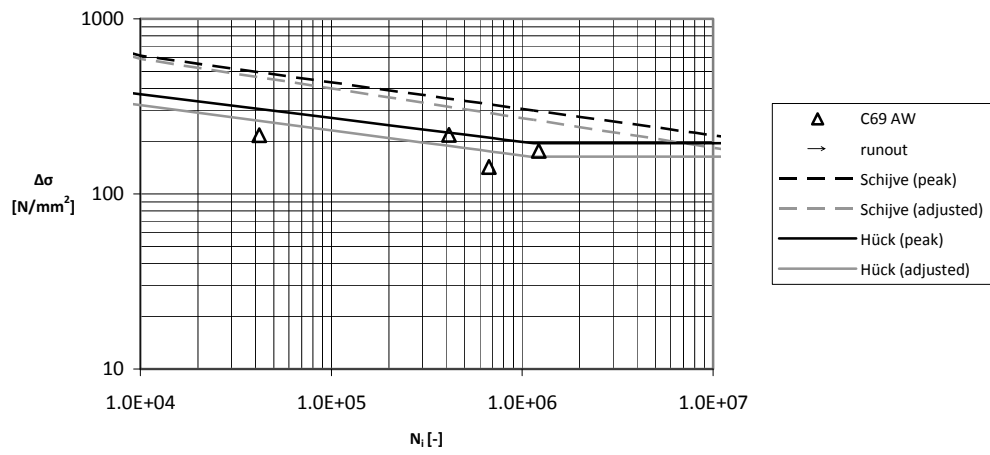


figure 9.43 Comparison of crack initiation life of C69 specimens with weld toe failure on cast side and modeled fatigue strength

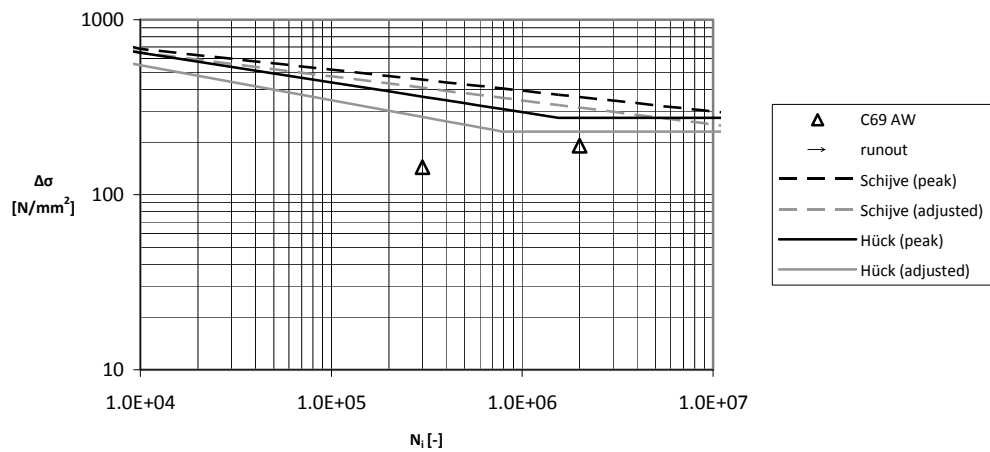


figure 9.44 Comparison of crack initiation life of C69 specimens with weld toe failure on rolled side and modeled fatigue strength

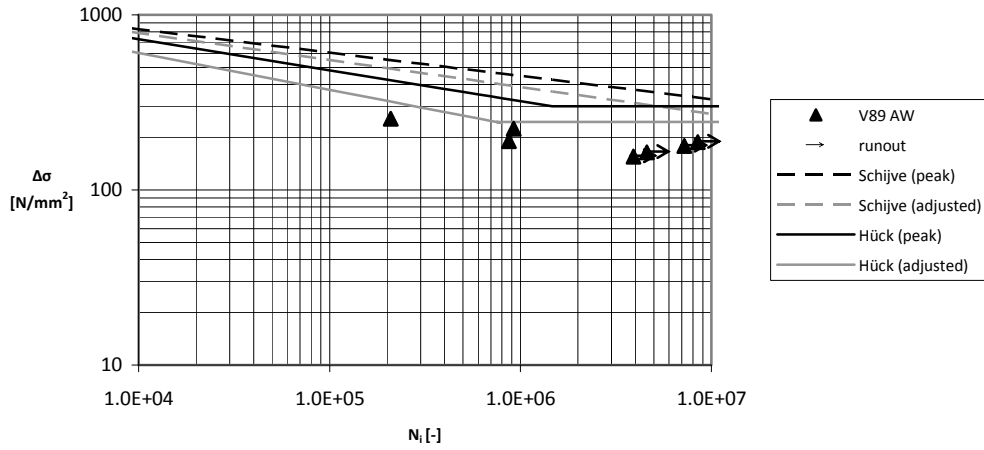


figure 9.45 Comparison of crack initiation life of V89 specimens with weld toe failure and modeled fatigue strength

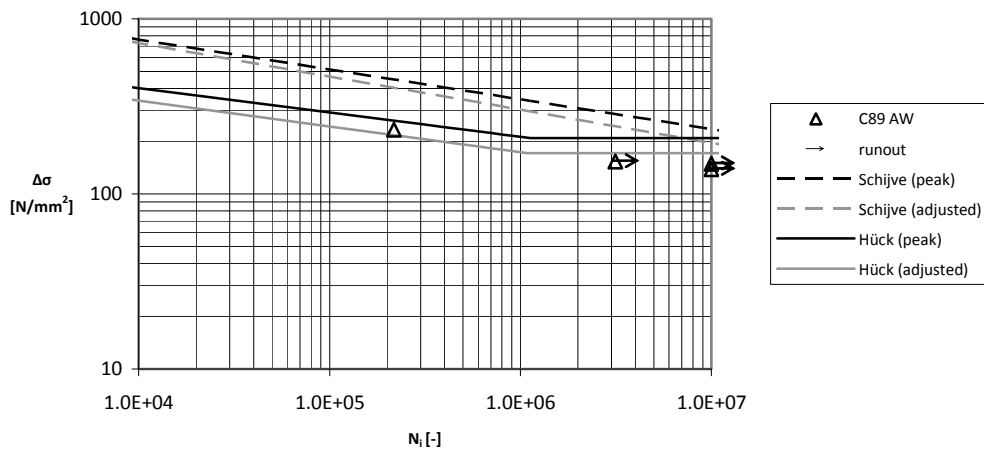


figure 9.46 Comparison of crack initiation life of C89 specimens with weld toe failure on cast side and modeled fatigue strength

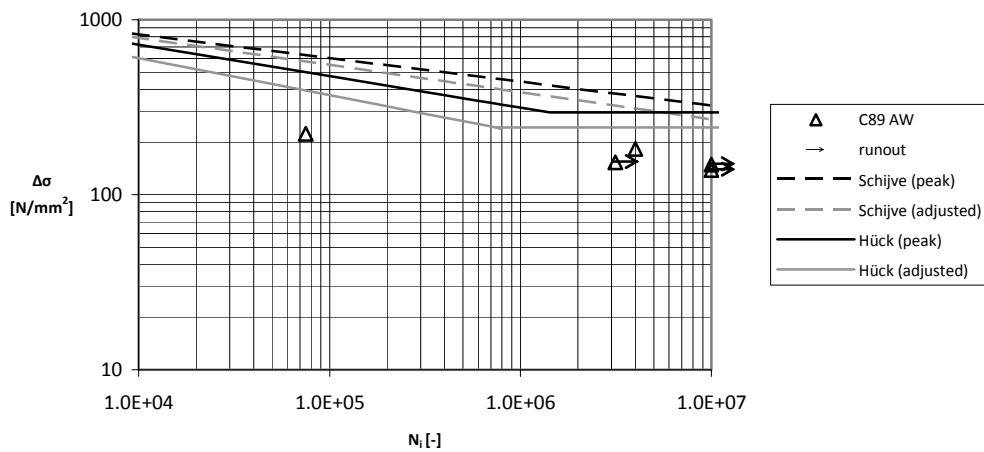


figure 9.47 Comparison of crack initiation life of C89 specimens with weld toe failure on rolled side and modeled fatigue strength

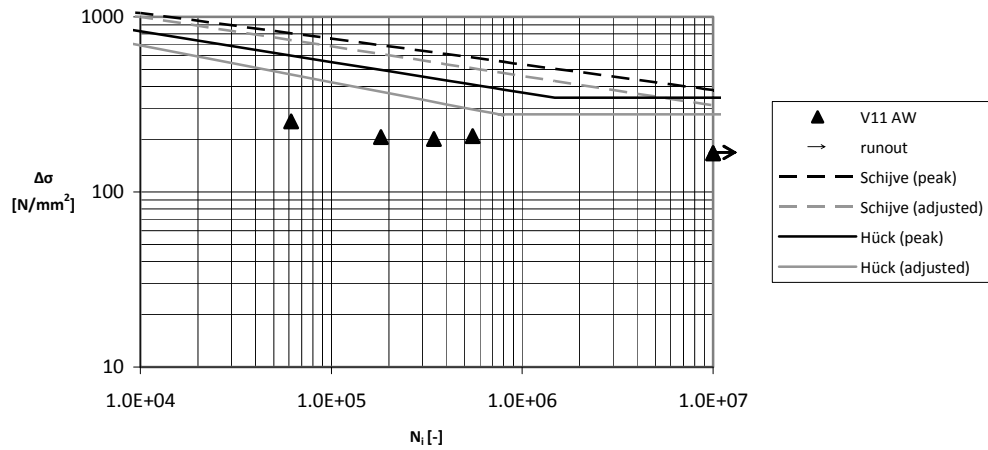


figure 9.48 Comparison of crack initiation life of V11 specimens with weld toe failure and modeled fatigue strength

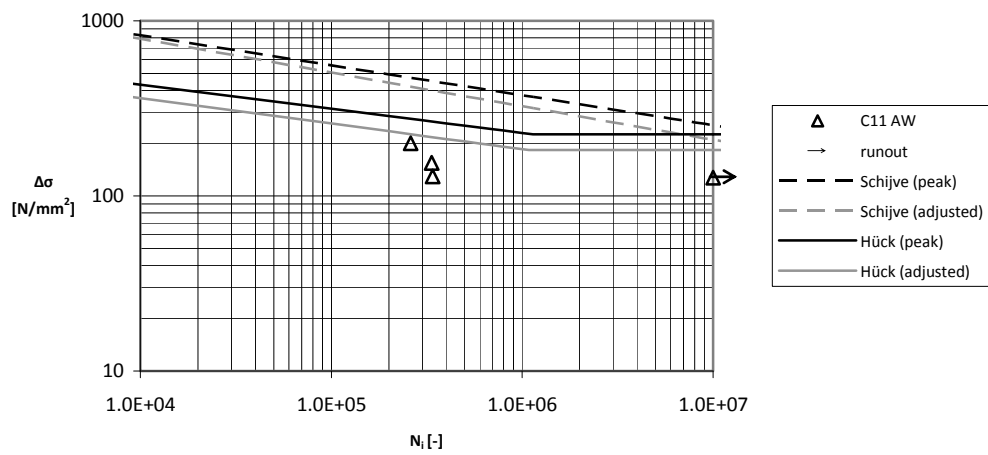


figure 9.49 Comparison of crack initiation life of C11 specimens with weld toe failure on cast side and modeled fatigue strength

Comparison of TIG-dressed data with model based on peak values of TIG-dressed geometry

In figure 9.50 to figure 9.54 the comparison is made between the model as described and derived in chapter 8 and the fatigue test results in the TIG-dressed situation. Similarly to the as welded situation, almost all predicted results lie significantly higher than the test results. It seems that the discrepancy between the model and the results is even larger in the TIG-dressed situation.

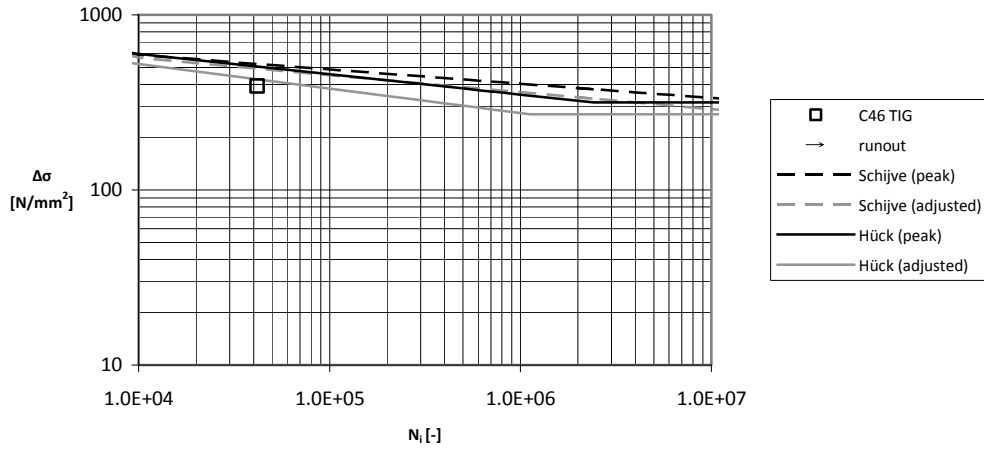


figure 9.50 Comparison of crack initiation life of C46 specimens with weld toe failure on rolled side and modeled fatigue strength

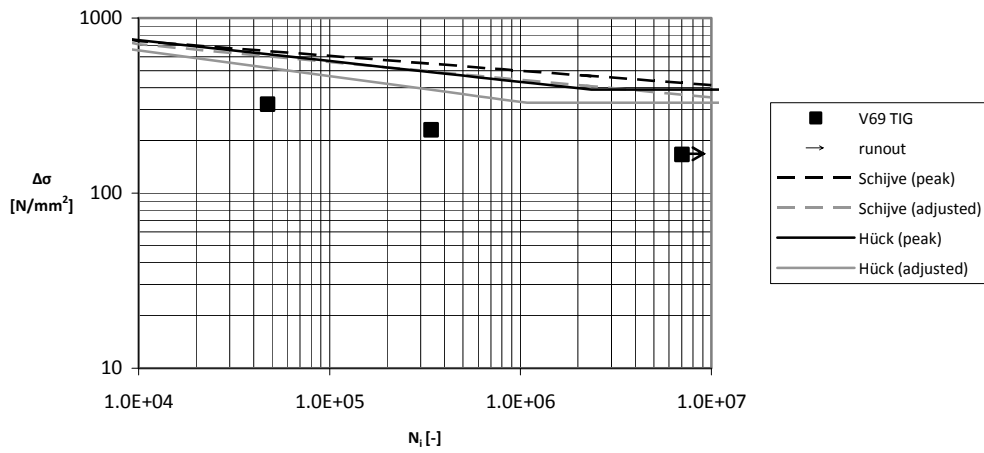


figure 9.51 Comparison of crack initiation life of V69 specimens with weld toe failure and modeled fatigue strength

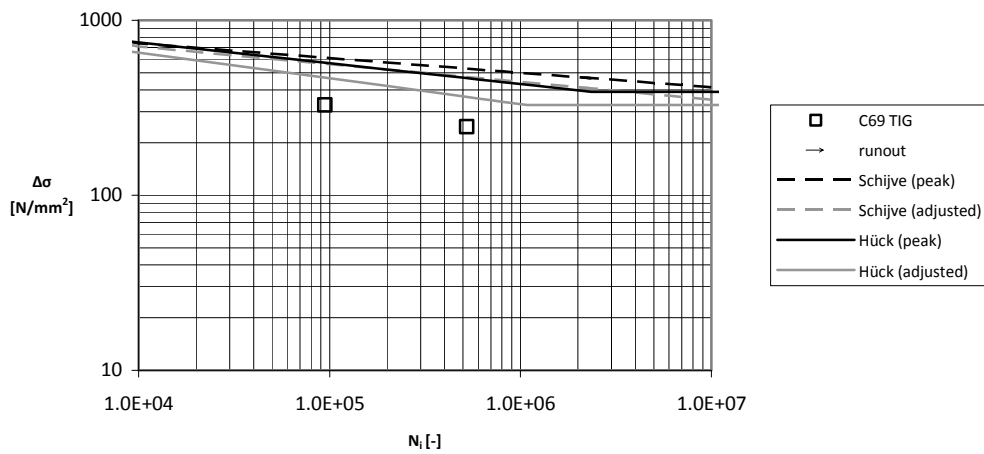


figure 9.52 Comparison of crack initiation life of C69 specimens with weld toe failure on rolled side and modeled fatigue strength

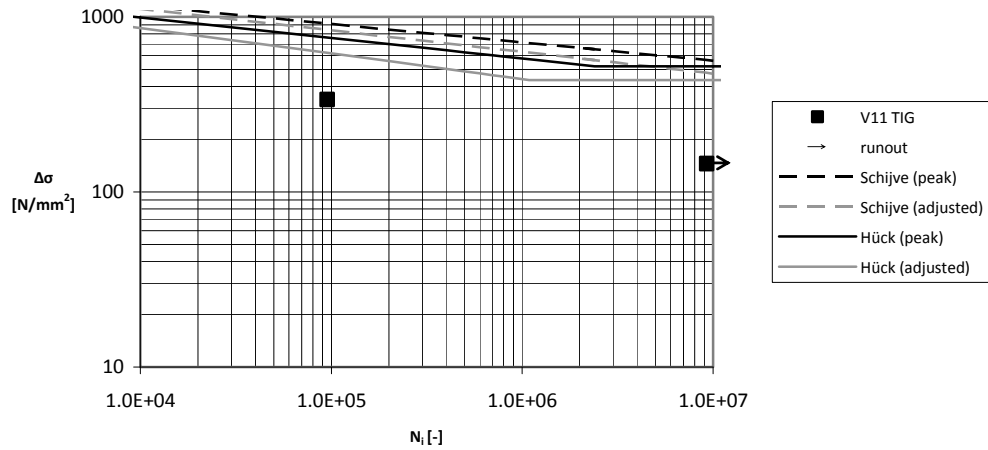


figure 9.53 Comparison of crack initiation life of V11 specimens with weld toe failure and modeled fatigue strength

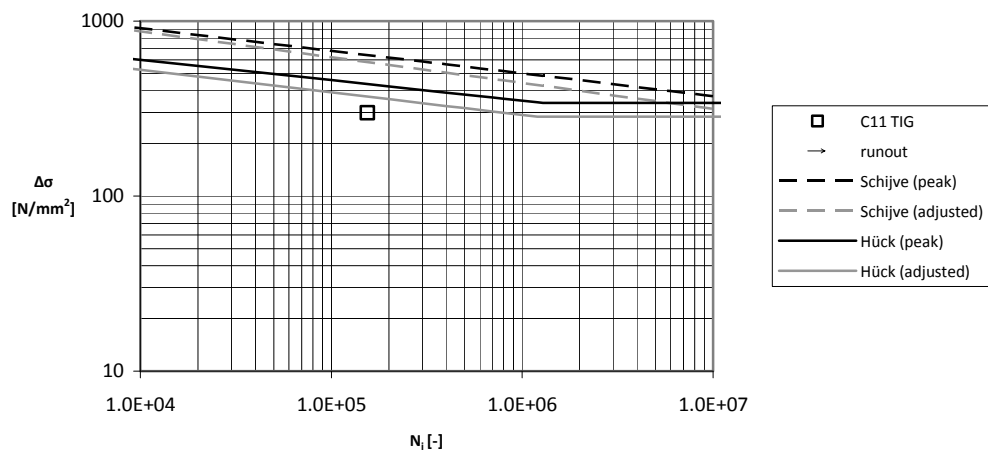


figure 9.54 Comparison of crack initiation life of C11 specimens with weld toe failure on cast side and modeled fatigue strength

Comparison of TIG-dressed data with model based on peak values of TIG-dressed geometry and as welded radius

In figure 9.55 to figure 9.59 the comparison is made between the model as described and derived in chapter 8 and the fatigue test results in the TIG-dressed situation. The results show a similar behaviour as for the previous two comparisons with the model. Because a higher stress concentration factor and fatigue notch factor is attributed to the TIG-dressed weld toes, the model and actual tests approach each other better than in the previous analysis where only peak values were considered. However, because the as welded results also did not match very well, this is no valid reason to assume that the model with peak values of the TIG-dressed geometry with an as welded radius is the best model of the TIG-dressed joint.

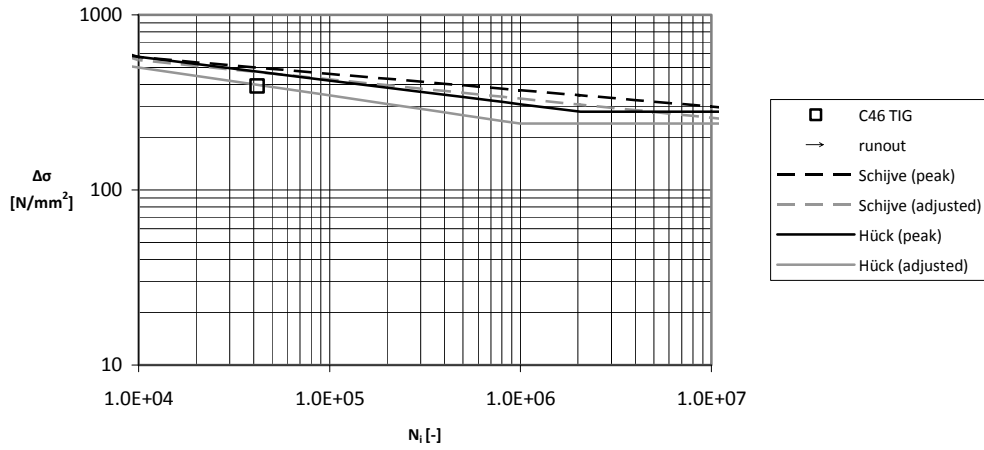


figure 9.55 Comparison of crack initiation life of C46 specimens with weld toe failure on rolled side and modeled fatigue strength

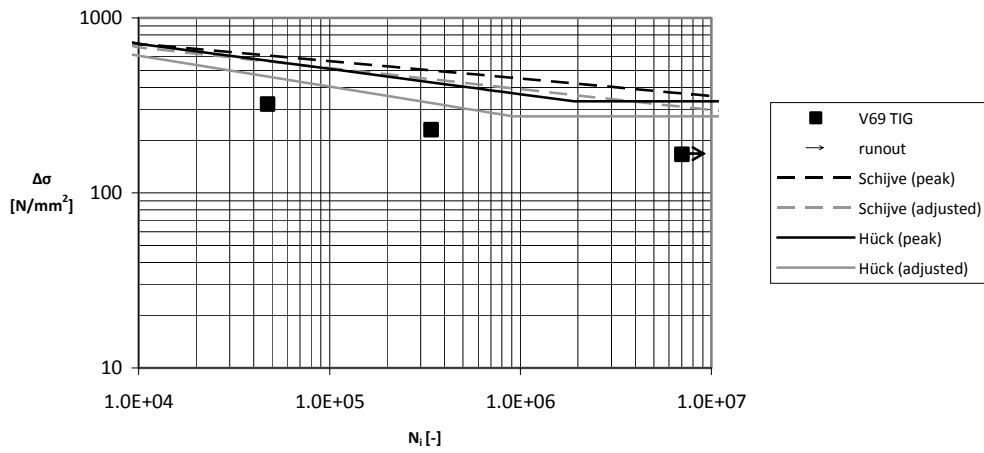


figure 9.56 Comparison of crack initiation life of V69 specimens with weld toe failure and modeled fatigue strength

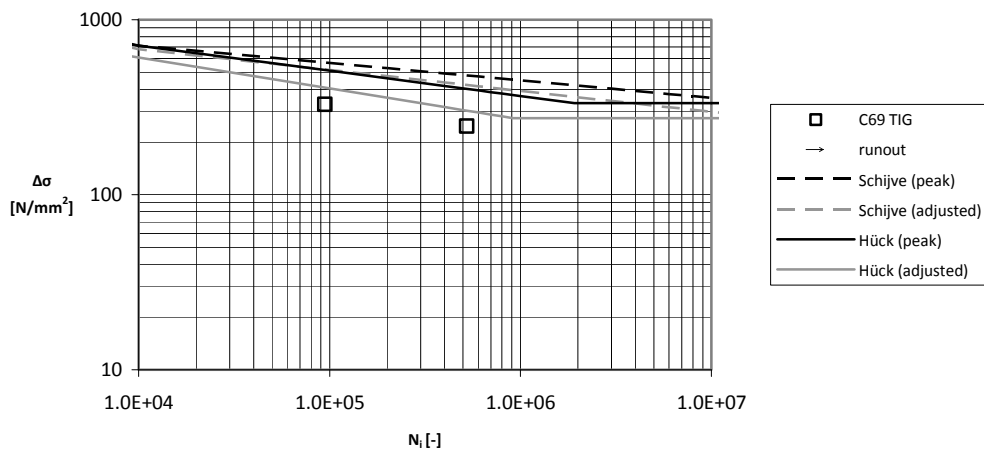


figure 9.57 Comparison of crack initiation life of C69 specimens with weld toe failure on rolled side and modeled fatigue strength

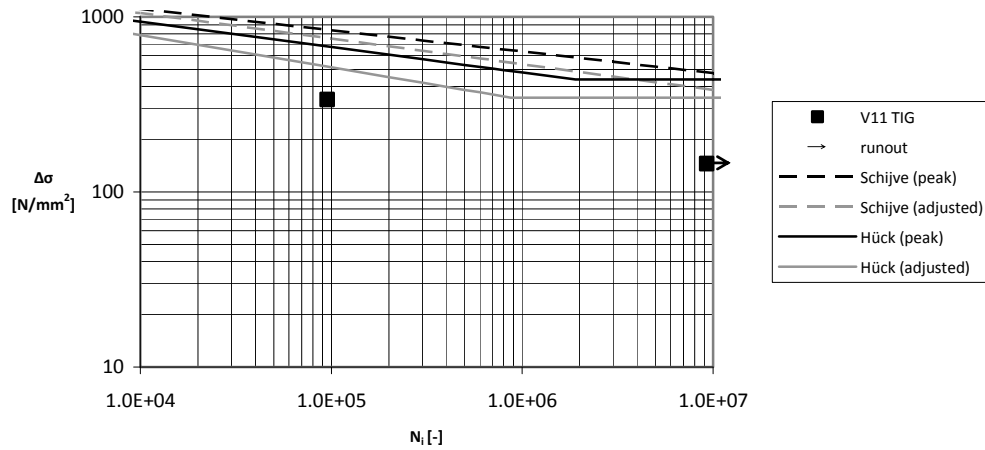


figure 9.58 Comparison of crack initiation life of V11 specimens with weld toe failure and modeled fatigue strength

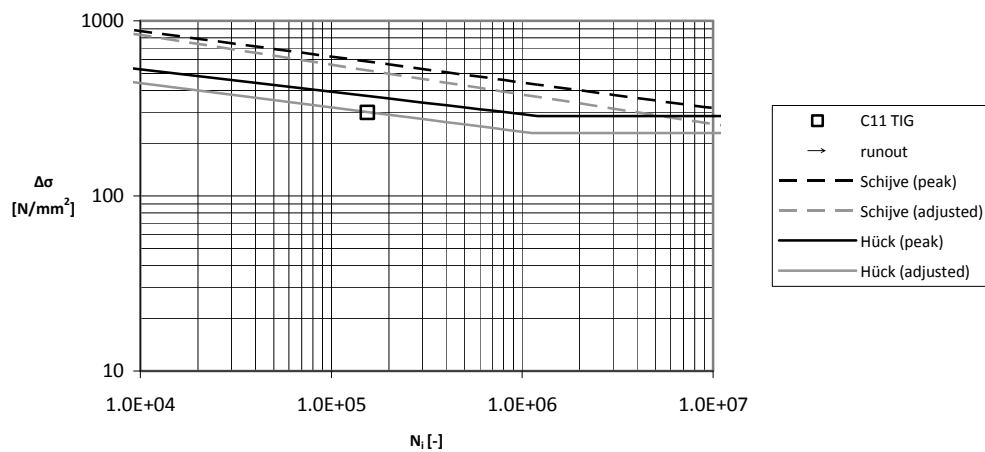


figure 9.59 Comparison of crack initiation life of C11 specimens with weld toe failure on cast side and modeled fatigue strength

Discussion

Almost all test results, both as welded and TIG-dressed show significant differences with the modelled behaviour. The as welded model seems to perform the best. Both TIG-dressed models perform a little bit worse, with the peak value model being the least dependable.

The sensitivity of the model to slight differences in the weld toe parameters is relatively limited as can be seen from the figures. The grey lines indicate a varied weld toe to an extent that the bulk of all weld toes are covered (see 8.3), but this only results in a rather small fatigue strength variation. The variation that is found is smaller than a typical fatigue test scatter band (see the figures above).

The use of the TIG-dressed model with the as welded radius instead of all peak values leads to a difference of 13-20%, depending on the steel grade. The model predicts a fatigue strength increase due to TIG-dressing of 30% for S460, which steadily increases to a 52% strength increase for S1100. This fatigue strength increase difference is partly related to the difference in K_f and is partly caused by the assumed higher absolute reduction of residual stresses in higher strength steels. Due to the inaccuracy of the model, it is very hard to rate these numbers at their true value. However, when these values are compared with figure 9.38, it seems that the model overestimates the beneficial effect of TIG-dressing.

To make a good estimation of the validity of the model for the TIG-dressed specimens, it is important that the as welded model gives good predictions of the fatigue strength. Because this is not the case, it is very hard to evaluate the accuracy of the TIG-dressed model. When these issues are set aside and only the relative difference between the as welded model and TIG-dressed model is considered, it is noticed that the test data lies further beneath the predicted line in the TIG-dressed situation than in the as welded situation. This is expected to be the other way around, because only the change in geometry

and residual stresses is incorporated in the model. The removal of weld flaws should also give a beneficial effect, which should lead to a tested fatigue resistance which is higher than the model. Unfortunately, this is not the case.

A remark must be made on the used model to determine K_f . As is explained in 3.5.1, literature recommends the use of $\rho \approx a^*$ in the determination of K_f , because this leads to the maximum value of K_f and thus the most conservative result. Because the actual geometry of the weld was measured in this study, the value of the radius to determine K_f was based on these measurements and not on the most conservative value possible. When the radius would be set at this worst case value an increase in K_f would be found, resulting in a lowering of the predicted S-N curves, thereby increasing the model accuracy. The increase of K_f can vary from a few percent for S460 for more than 30% for S1100. The actual value could not be determined because the a^* value of this material is so small, that the accompanying radius has not been modelled. The indication of 30% increase in K_f is based on the smallest radius that has been modelled. However, when this approach would be used, the measurement of the actual weld toe radius is no longer used, which partly eliminates the beneficial effect for the TIG-dressed specimens.

To omit this question, another approach could also be used. It is possible to link the fatigue notch factor to the stress gradient. This method is related to the highly stressed volume approach as discussed in 3.5.1, but has not been considered in this research. A more thorough analysis of the possibilities to determine K_f , while incorporating the measured weld profile should be subject of further investigation.

9.5 Evaluation of TIG-dressing influence

There are several indications that the TIG-dressing procedure has had a positive effect on the fatigue strength of the weld toe. First of all, a new failure mechanism has shown, which was not observed in the as welded specimens tested by Pijpers. Seven of the twenty non-excluded results showed this new failure mechanism: a crack in the weld material. Whether this is only caused by weld toe improvement, or TIG-dressing also had influence on the weld material, possibly by increasing residual stresses, may be the subject of further investigation. Other specimens still showed failure at the weld toe, but these data points can mostly be found in the upper regions or above the scatter band of the as welded specimens, thus suggesting a fatigue strength improvement. Finally, some specimens failed in the base material. Whether this base material was already a weak link in the chain before TIG-dressing or it became the weakest link after the weld toe was improved cannot be proven. However, the scatter plots in 9.4.2 show that the base material failures more or less blend in with the base material results from the as welded tests. This indicates that the observed failure location would also have been the weakest link in an as welded situation. This might be a possible explanation for the relatively poor performance of some the TIG-dressed specimens of the steel grades S890 and S1100 when compared with the fatigue strength increase of lower strength specimens. Apparently the, very likely improved, weld toe was not the weakest link, even in the as welded situation. One specimen that was excluded from the analysis, specimen V11-1, may also fall into this category. Here also a base material failure was observed, which would be the weakest link, both in the as welded state and the TIG-dressed state.

The overall trend seems to be an improvement at the weld toe as a result of TIG-dressing especially in the medium cycle regime. Clear information on the high cycle regime is not available, due to the scarcity of test data in this regime. Due to other failure mechanisms, not necessarily the whole specimen shows fatigue strength increase. If the weld toe is improved, but the next weak link only behaves marginally better, the TIG-dressing has limited influence. It must also be noted that the runout test results mostly lie in the upper region of the as welded runouts, but greatly above the fitted fatigue limits or the fatigue limits specified by codes. This is not translated into the fitted S-N curves, and therefore worth an extra remark.

The analytical results do not comply with the test data in a sufficient way to use the developed model to predict the fatigue strength of components. The test results deviate significantly from the predicted values and the modeled results are non conservative. From the analytical approach it is found that variations of the weld toe parameters within such limits that the bulk of all measured weld toes are covered, have relatively low consequences on the fatigue strength. The differences that are found when such an analysis is made are generally smaller than a typical fatigue test scatter band. To effectively predict the fatigue strength of butt welded specimens, extra research is necessary.

Because of the limited number of tests per material and the limited accuracy of the model, this report refrains from strength increase factors and only the overall trend has been described. For the same reason, and because S890 and S1100 do not show a clear strength improvement as discussed earlier, no material dependent improvement is described.

To define strength increase factors for S460 and S690, and to examine whether S890 and S1100 specimens as a whole show a strength increase more testing is necessary, especially in the high cycle regime.

10 Conclusions and recommendations

10.1 Conclusions

10.1.1 Influence of TIG-dressing of fatigue strength of butt welded specimens

- Design codes do not always incorporate a fatigue strength increase due to TIG-dressing. The fact that all TIG-dressed specimens show a fatigue strength above the design line of the considered design codes is therefore not surprising.
- When the TIG-dressed specimens are compared with similar as welded specimens, the scatter plots show a trend towards a better fatigue behaviour of the TIG-dressed specimens for all specimens which have shown failure in the weld area. For steel grades S460 and S690 this concerns almost all specimens. For the higher strength steels a lot of specimens have shown base material failure. Quantitative conclusions cannot be drawn due to the relatively small number of tests.
- The materials that have shown base material failures in the as welded condition, S890 and S1100, show little to no improvement of the fatigue strength, because any beneficial effect of the weld toe improvement can only have an effect on specimens that would not have shown base material failure in the as welded condition. The few specimens that have shown weld material failure after TIG-dressing in these steel grades generally show the above described trend towards fatigue strength improvement.
- The failure mechanism in the weld material has become much more prominent. This failure mechanism has only very rarely been observed in the as welded tests, but has been observed on a significant number of the TIG-dressed specimens. This is a very good indication that the weld toe indeed has been removed as the weakest link from the chain. Whether the weld material is simply the next weak link or has been influenced by TIG-dressing is not clear.
- The main fatigue improvement of TIG-dressed specimens is expected from improvement of the crack initiation life. When scatter plots of TIG-dressed and as welded specimens are compared, the difference between the as welded scatter band and the TIG-dressed specimens seems larger when only the crack initiation life is considered, thus confirming this expectation. It must be noted that differences in geometry of the specimens and instrumentation which were present, can distort this graph because they influence the accuracy with which the crack initiation time can be determined.

10.1.2 Influence of TIG-dressing on weld geometry of butt welded specimens

- As welded weld toe geometries of the considered specimens generally show one geometry variant. When these welds are TIG-dressed different weld toe geometries can be observed (see figure 6.9). Different variants occur in different frequencies but no single geometry variant dominates the measurements.
- The peak value of the distribution of weld toe radii increases from ~1.0 millimeter for as welded specimens to ~3.8 millimeter for TIG-dressed specimens. The TIG-dressed results also show a peak in the region of the as welded peak. The spread of weld toe radii increases due to TIG-dressing.
- The peak value of the distribution of weld toe angles decreases from ~27.8° for as welded specimens to ~15.3° for TIG-dressed specimens. The spread of the data before and after weld toe improvement is similar.
- The peak value of the distribution of undercuts is similar for the as welded specimens as for the TIG-dressed specimens and lies at 0 millimeter. The number of non-zero undercuts is somewhat larger for the TIG-dressed specimens. One specific geometry variant shows significantly deeper undercuts than all other considered weld toe geometries, both as welded as TIG-dressed. This geometry is also consistently associated with a very large weld toe radius and therefore will very likely not be the weakest link in fatigue.
- Because the width of the weld is much larger than the influence of TIG-dressing, the weld improvement has no influence on the weld height. Within one plate specimen the weld height shows only a slight variation. Larger differences in weld height between specimens were found.
- The discussed influences, with exception of the undercut influences, lead to an 'average' weld toe geometry with a lower stress concentration factor. However, due to the occurrence of a number of smaller weld toe radii in the TIG-dressed specimens, which is disproportionate with respect to the overall distribution, the theoretical improvement of the fatigue strength is not necessarily as high as is to be expected based on the average improvement.

10.1.3 Theoretical influence of changed weld geometry on behaviour of TIG-dressed specimens

- The found spread in the weld geometry data is, based on a sensitivity analysis, not likely to cause a scatter band with the width that is usually associated with fatigue testing.
- The fatigue notch factor shows reduction due to TIG-dressing with slight dependency on the material static strength. Higher strength steels show a greater reduction in fatigue notch factor, due to the difference in the parameter a^* . Further differences in fatigue strength improvement due to TIG-dressing can be sought in other factors, such as residual stress reduction. In the used model in this research the residual stress was assumed to be a fixed fraction of the yield strength, thereby increasing the fatigue strength increase differences between different steel grades
- The model shows a reduction of the fatigue notch factor due to the changed weld toe geometry, even if no improvement of the weld toe radius is achieved. This reduction is then mostly caused by a reduction of the weld toe angle.
- The model that is used shows poor accuracy for both as welded and TIG-dressed specimens. Also, the discrepancy between the model and tested specimens is not constant. Any quantitative or qualitative predictions of a fatigue strength increase due to TIG-dressing can therefore not be expressed.

10.2 Evaluation and recommendations

10.2.1 Assumptions and approximations

In this paragraph the main assumptions and approximations will be described so that the conclusions from 10.1 can be rated at their true value.

- All weld toe geometries have been analyzed together, while a few different typical geometries have been observed. One model has been used to represent all TIG-dressed geometries, leading to an approximation for typical TIG-dressed geometry type 3 (see figure 6.9).
- No probability distribution has been fit to the results of the weld toe parameters. The peak values now have been estimated based on the bar diagrams. Fitting a distribution would make an accurate calculation of the peak value of the distribution possible, but not for all data sets an accurate fit could be made. The accurate calculation of a peak value with a fitted distribution is therefore an illusion.
- When analyzing the weld toe geometry, discussion arose as to whether a large notch or a smaller notch inside this main notch should be documented. Based on various arguments, only the main notch was documented.
- This research only focuses on the geometrical improvement of TIG-dressing. Any improvement by removing weld toe flaws is not taken into account. The reduction of residual stresses is approximated, based on literature.
- The critical distance approach has not been proven in the finite life region. This research has extended the infinite life that has been determined with this approach into the finite life.
- Peterson (1974) has recommended the use of $K_{f,max}$ when determining the fatigue strength of notched specimens. This research has used the actual measured geometry.
- Correction factors for thickness, loading mode, mean stress and residual stress have been acquired from the research by Pijpers (2011). The influence of these factors can also be dependent on the weld toe geometry. In this research the same correction factors as used by Pijpers were used, although it is not certain that these factors will have exactly the same value for TIG-dressed joints.
- Various specimens have shown failure inside the weld material. This failure mechanism was not observed in the as welded joints by Pijpers (2011). Therefore, no correction factors for thickness, loading mode, mean stress and residual stress are available. These cracks have been regarded as weld toe cracks.

10.2.2 Recommendations for further research

Recommendations regarding the TIG-dressing procedure

- At some locations the TIG dressing procedure could not be executed because after grinding gas inclusions appeared. To prevent them from expanding rapidly when heated and possibly ruining the weld, these locations were not TIG-dressed. It should be investigated whether these gas inclusions would be visible on an X-ray test, and in what frequency these inclusions appear. Furthermore, it should be investigated whether welds where these inclusions have been observed can be TIG-dressed without any problems.
- Different TIG-dressed geometries have been observed (see figure 6.9). Only one of these geometries is expected and described by the IIW and other literature. Further research should determine whether these different geometries always occur for butt welded specimens. The welds that were studied in this research were relatively few in number and all executed by one person under the same conditions. To gain a more complete image of the possible geometries, these factors should be varied.

Recommendations regarding the laser measurements

- All weld geometries have been considered together after the split between as welded and TIG-dressed was made. When each weld toe parameters and their mutual dependency are recorded and coupled to one of the weld toe variants specified in figure 6.9, the value of the database will increase greatly.
- In a lot of weld toe geometries, different notches can be observed. In this study the choice is made to consider only the largest ‘main’ notch, based on a relatively quick assessment of the influence of the smaller notches. Further research should show to what extent these smaller notches influence the fatigue behaviour and should try to match the crack initiation sites on the specimens on any possible local smaller notches which may be present.
- In this research a very limited amount of parent material has been incorporated in the research to limit the measuring time. Extending the amount of measured parent material to about 10 millimeter will greatly increase the ability to accurately determine the weld toe angle, weld toe height and undercut, because all these parameters are defined with the parent material as baseline.
- A number of specimens have failed in the weld material. Although data is available of this area of the weld, the exact geometry of any present notches has not been determined. To accurately model these failures, this area of the weld should be analyzed thoroughly. This analysis may also lead to an explanation of the fact that the S460 specimens have shown a lot of weld material failures and the S690 specimens have none while they have, to the eye, a similar weld material geometry.

Recommendations regarding the fatigue testing

- To avoid runouts, most specimens were tested at relatively high stresses. This leads to an uncertain determination of the slope of the S-N curve. More tests should be done at lower stress ranges leading to failure at higher cycles
- A high uncertainty exists in the variation of the dataset due to the limited number of data points per steel grade. Additional testing should give more certainty of the actual scatter band of the TIG-dressed results.

Recommendations regarding the modelling and adjustment of the fatigue strength

- In this research an assumption was made concerning the reduction of residual stresses at the weld toe before and after TIG-dressing. Additional research on residual stresses in TIG-dressed butt welded joints is necessary to accurately model a fatigue strength increase. The residual stresses in the weld material are also interesting to measure, because an increase of residual stresses in the weld material may explain the occurrence of the extra failure mechanism in the weld material.
- When the weld toe geometries have been analyzed more thoroughly as described above, it may be possible to determine a worst case scenario by combining different weld toe parameters according to their actual occurrence and dependencies. This can lead to an accurate worst case value of K_f .
- All correction factors for thickness, mean stress and loading mode have been based on the research by Pijpers (2011). The influence of some factors depends on the weld geometry as well. Further research should investigate whether the used correction factors are also valid for TIG-dressed geometries or define new correction factors.
- All correction factors for thickness, mean stress and loading mode have been based on the research by Pijpers (2011). Because in the research by Pijpers no weld material failures were observed, no such correction factors were available for the current research. Additional research should focus on correction factors when failure is observed in the weld material.
- The developed model of the fatigue strength is inaccurate. Due to assumptions made when applying the critical distance approach, the determination of K_f may be less precise, leading to a less accurate model. Omitting these assumptions may improve model accuracy but will partly neutralize the beneficial geometrical influence of TIG-dressing. Other methods to determine the fatigue notch factor, such as the stress gradient approach, may also lead to better results.

Recommendations regarding unused data of crack monitoring and hardness measurements

- The crack monitoring data which is presented in Annex I, has not been analyzed. Although limited, this database may give insight into any influences of the TIG-dressing procedure on the crack propagation life when combined with similar measurements on as welded specimens from Pijpers (2011). This calculation could also be used to verify the measured number of cycles to crack initiation.
- The hardness measurements show rather different results than found in literature. Based on observations, interesting conclusions can be drawn if a relation can be made between hardness and fatigue strength. A more thorough research of more TIG-dressed specimens can lead to more conclusive results.

Annex A: References

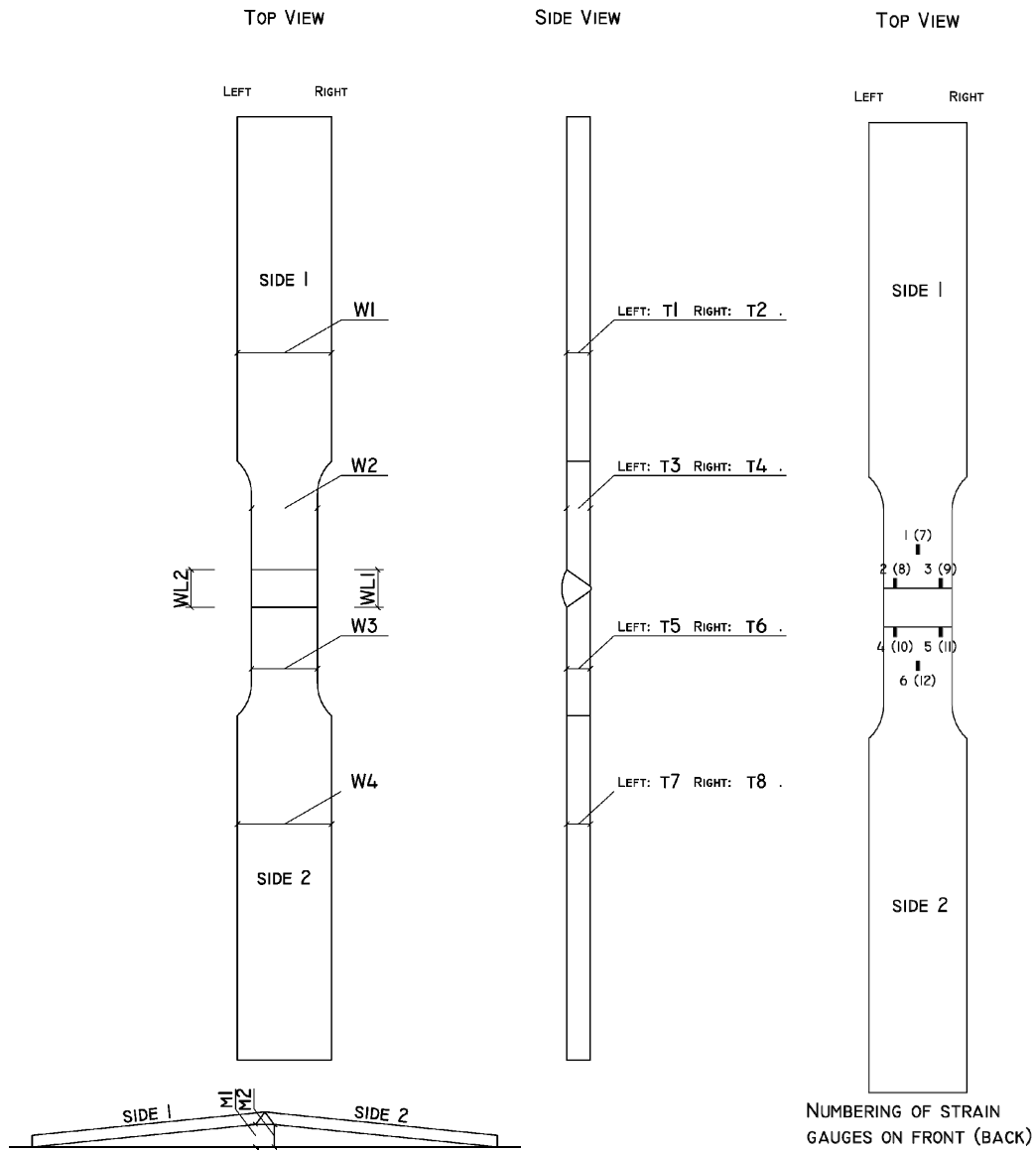
- [1] Anami, K and Miki, C. 'Fatigue strength of welded joints made of high-strength steels', *Progress in Structural Engineering and Materials*, Vol. 3, pp. 86-94, 2001
- [2] Anthes, R.J. Volker Kottgen, V.B. Seeger, T. 'Kerbformzahlen von Stumpfstoßen und Doppel-T-stößen', *Schweißen und schneiden*, vol. 45 no. 12 pp. 685-688, 1993
- [3] Brozzetti, J., Hirt, M. A., Ryan, I. Sedlacek, G. Smith, I.F.C. 'Background information on fatigue design rules – Statistical evaluation' Chapter 9, document 9.01, Eurocode 3 Editorial group, 1989
- [4] Dahle, T. 'Design fatigue strength of TIG-dressed welded joints in high-strength steels subjected to spectrum loading', *International Journal of Fatigue*, Vol. 20, No. 9, pp. 677-681, 1998
- [5] EngineeringArchives.com, 2008
- [6] ESDEP – Lecture WG12: Fatigue
- [7] FME-CWM – Constructiestaalsoorten met hoge sterkte, VM-publication 125, 2008
- [8] Gudehus, H. Zenner, H. 'Leitfaden für Betriebsfestigkeitsrechnung', *Verlag Stahleisen GmbH*, 1999
- [9] Gurney, T.R. 'Fatigue of welded structures', *Cambridge University Press*, 1979
- [10] Haagensen, P.J. and Maddox, S.J. 'IIW Recommendations on Post Weld Improvement of Steel and Aluminium Structures, *IIW document XIII-1815-00*, 2001
- [11] Haagensen, P.J. Drågen, A. Slind, T. and Ørjasæter, O. 'Prediction of the improvement in fatigue life of welded joints due to grinding, TIG dressing, weld shape control and shot peening', *Proceedings of the 3rd International ECSC Offshore Conference on Steel in Marine Structures (SIMS '87)*, Delft, 1987
- [12] Haibach, E. 'Betriebsfestigkeit – Verfahren und Daten zur Bauteilberechnung', *Springer-Verlag*, 2006
- [13] Hildebrand, J. Starcevic, I. Werner, F. Heinemann, H. and Köhler, G. 'Numerical simulation of TIG-dressing of welded joints' *Joint International Conference on Computing and Decision Making in Civil and Building Engineering*, Montréal, 2006
- [14] Hobbacher, A. 'Recommendations for fatigue design of welded joints and components, *IIW document XIII-2151-07/XV-1254-07*, 2007
- [15] Hück, M., Thrainer, L., Schütz, W. 'Berechnung von Wöhlerlinien für Bauteile aus Stahl, Stahlguss und Grauguss – Synthetische Wöhlerlinien', Bericht Nr. ABF 11 (Zweite Überarbeitete Fassung), Verlag Stahleisen, 1981
- [16] Huo, L. Wang, D. Zhang, Y. 'Investigation of the fatigue behaviour of the welded joints treated by TIG dressing and ultrasonic peening under variable-amplitude load', *International Journal of Fatigue*, Vol. 27 pp. 95-101, 2005
- [17] Janssen, M. Zuidema, J. Wanhill, R.J.H. 'Fracture Mechanics', *Delft University Press*, 2002
- [18] Kuguel, R. 'A relation between theoretical stress concentration factor and fatigue notch factor deduced from the concept of highly stressed volume', *Proceedings of ASTM 61*, 732-744, 1961
- [19] Lopez Martinez, L. Lin, R. Wang, and Blom, A.F. 'Investigation of residual stresses in as-welded and TIG-dressed specimens to static/spectrum loading' *Proceedings of NESCO: "Welded High-Strength Steel Structures"*, Stockholm, 1997
- [20] Maddox, S.J. 'Fatigue strength of welded structures', *Abington Publishing*, 1991
- [21] NEN-EN 1993-1-9, Eurocode 3: Design of steel structures – Part 1-9: Fatigue, 2006
- [22] NEN-EN 1993-1-12, Eurocode 3: Design of steel structures – Part 1-12: Additional rules for the extension of EN 1993 up to steel grades S700, 2007
- [23] NEN-EN-ISO 5817, Welding – Fusion welded joints in steel, nickel, titanium and their alloys (beam welding excluded) – Quality levels for imperfections, 2007
- [24] Neuber H. 'Kerbspannungslehre', *Springer Verlag*, 1937
- [25] Neuber H. 'Theory of Notch Stresses', *Ann Arbor Mich*, 1946
- [26] Neuber H. 'Über die Berücksichtigung der Spannungskonzentration bei Festigkeitsberechnungen', *Konstruktion*, Vol 20, No. 7, pp. 245-251, 1968
- [27] NPR-CEN/TS 13001-3-1, Cranes – General Design – Part 3-1: Limit states and proof of competence of steel structures, 2005
- [28] Pedersen, M.M. Mouritsen, O.Ø. Hansen, M.R. and Andersen J.G. 'Experience with the Notch Stress Approach for Fatigue Assessment of Welded Joints' *Proceedings of the Swedish Conference on Light Weight Optimized Welded Structures, Borlänge*, 2010
- [29] Pedersen, M.M. Mouritsen, O.Ø. Hansen, M.R. Andersen J.G. and Wenderby, J. 'Comparison of Post Weld Treatment of High Strength Steel Welded Joints in Medium Cycle Fatigue', *IIW document XIII-2272-09*, 2009
- [30] Peterson, R.E. 'Stress concentration factors', *New York, John Wiley*, 1974
- [31] Pijpers, R.J.M. Kolstein, M.H. Romeijn, A. and Bijlaard, F.S.K. 'Fatigue experiments on very high strength steel base material and transverse butt welds', *Advanced steel construction*, Vol, 5, No. 1, 14-32, 2009
- [32] Pijpers, R.J.M. Kolstein, M.H. 'Fatigue strength of truss girders made of Very High Strength Steel', as presented on the: 13th *International Symposium on Tubular Structures*, pp. 499-505, 2010

- [33] Pijpers, R.J.M. 'Fatigue strength of welded connections made of very high strength cast and rolled steels', Dissertation, *M2I*, 2011
- [34] Radaj, D. Sonsino, C.M. and Fricke, W. 'Fatigue assessment of welded joints by local approaches – second edition', *Woodhead publishing limited*, 2006
- [35] Romeijn, A. 'Lecture notes CT5126 – Fatigue', *Delft University of Technology*, 2006
- [36] Siebel, E. and Stieler, M., 'Ungleichförmige Spannungsverteilung bei schwingender Beanspruchung', *VDI-Zeitschrift*, Vol. 97, No. 5, pp. 121-126, 1993
- [37] Schijve, J. 'Fatigue of Structures and Materials', *Kluwer Academic Publishers*, 2001,
- [38] Sonsino, C.M., 'Zur Bewertung des Schwingfestigkeitsverhaltens von Bauteilen mit Hilfe örtlicher Beanspruchungen', *Konstruktion*, 1993, Vol. 45, pp. 25-33, 1993
- [39] Tricoteaux, A. Fardoun, F. Degallaix, S. Sauvage, F. 'Fatigue crack initiation life prediction in high strength structural steel welded joints', *Fatigue and Fracture of Engineering Materials*, Vol. 18, No. 2 pp. 189-200, 1995
- [40] Wanhill, R.J.H. 'Durability analysis using short and long fatigue crack growth data', *Proceedings of the International Conference on Aircraft Damage Assessment and and Repair*, Melbourne, 1991
- [41] Wortel, H van. 'Integrity of High Strength Steel Structures; Final Report of Work Package: Fabrication', *TNO Report*, 2006

Annex B: Test specimens

On the following pages the geometry of the produced test specimens will be depicted.

The geometry of tested specimens is tabulated for each specimen separately. The figure below gives guidance to the location of the various measurements.



	W1	W2	W3	W4	W11	W12	M1	M2	T1	T2	T3	T4	T5	T6	T7	T8	Side 1	Side 2
V46-1	99-100	70	70	100-101	49	51	7.7	7.4	25.4	25.3	25.3	25.1	25.3	25.1	25.5	25.7	Rolled	Rolled
V46-2	99-101	70	70	100-101	50	51	8.0	8.3	25.5	25.6	25.3	25.2	25.3	25.4	25.5	25.5	Rolled	Rolled
V46-3	101-103	70	70	102-106	51	49	8.0	7.7	25.5	25.6	25.2	25.1	25.3	25.1	25.5	25.4	Rolled	Rolled
V69-1	102-106	70	70	101-102	45	48	4.8	4.3	24.6	24.6	24.5	24.5	24.4	24.5	24.6	24.6	Rolled	Rolled
V69-2	103-106	70	70	104-105	44	46	6.1	6.7	24.6	24.6	24.4	24.5	24.5	24.4	24.6	24.7	Rolled	Rolled
V69-3	104-109	70	70	107-111	45	43	6.7	6.7	24.8	25.0	24.6	24.6	24.6	24.7	24.7	24.7	Rolled	Rolled
V89-1	99-97	70	70	98-100	44	45	3.9	4.1	24.6	24.6	24.6	24.7	24.7	24.6	24.9	24.7	Rolled	Rolled
V89-2	98-99	70	70	91-98	42	42	4.2	3.8	24.7	24.7	24.6	24.6	24.7	24.7	24.7	24.7	Rolled	Rolled
V89-3	99-100	70	70	101-104	44	42	3.8	3.2	24.7	24.7	24.6	24.5	24.6	24.6	24.7	24.7	Rolled	Rolled
V11-1	98-99	70	70	98-99	39	38	2.7	2.3	19.9	20.0	20.0	20.0	19.8	19.8	19.9	19.9	Rolled	Rolled
V11-2	102-103	70	70	92-103	35	36	5.0	4.6	20.0	20.0	20.1	19.9	20.0	19.9	20.1	20.0	Rolled	Rolled
V11-3	104-106	70	70	102-105	30	32	4.3	4.3	20.1	20.1	19.8	20.0	19.8	19.8	20.0	19.9	Rolled	Rolled
C46-1	104-109	70	70	100-101	51	51	9.6	7.7	25.5	25.6	25.5	25.4	27.1	27.0	27.0	27.1	Rolled	Cast
C46-2																		
C46-3	105	70	70	105-111	49	49	8.4	6.5	25.4	25.5	25.1	25.1	26.9	27.2	28.1	29.1	Rolled	Cast
C69-1	106	70	70	107-112	53	51	7.1	8.5	26.0	25.7	26.0	25.9	24.7	24.7	24.7	24.7	Cast	Rolled
C69-2	103-105	70	70	102-103	49	51	6.4	7.6	26.0	25.9	25.6	25.6	24.5	24.6	24.7	24.7	Cast	Rolled
C69-3	105-108	70	70	104-105	48	48	8.4	7.4	24.7	24.5	24.4	24.5	25.4	25.4	25.7	25.3	Rolled	Cast
C89-1	102-103	70	70	102-104	44	44	?	?	24.3	24.8	24.4	24.6	24.4	24.5	24.5	24.6	Rolled	Cast
C89-2	103-104	70	70	97-98	45	44	3.3	3.0	24.7	24.7	24.4	24.6	24.3	24.4	23.7	23.7	Rolled	Cast
C89a-1	104-105	70	70	101-106	45	44	4.3	3.2	24.8	24.9	24.7	24.7	23.9	23.9	23.7	24.1	Rolled	Cast
C11-1	98	70	70	97-99	43	42	3.5	3.4	20.2	20.1	20.0	20.1	20.9	20.9	21.3	21.2	Rolled	Cast
C11-2	99-100	70	70	100-101	40	44	2.5	2.4	20.0	20.1	20.0	20.0	20.8	20.7	21.2	21.0	Rolled	Cast
C11-3	97-99	70	70	97-100	41	41	1.1	1.0	20.0	20.0	20.0	20.1	20.5	20.3	20.7	20.7	Rolled	Cast

Remarks:

- All measurements in millimeters
- C46-2: bent due to test rig error
- C69-2: weld root is ground smooth due to lack of TIG dressing
- C89-2: large defects are removed and filled in with weld material. Specimens is, even after treatment, not entirely defect free, based on visual inspection

Annex D: Material certificates



CONFÉDÉRATION EUROPÉENNE
D'ORGANISMES DE CONTRÔLE

Technischer Überwachungs-Verein
Saarland e.V.



Abnahmeprüfzeugnis (EN 10204 – 3.1C)
Inspection Certificate
Certificat de Réception
Certificato Collaudo Materiali

Besteller – Customer – Acheteur – Committente:

Mercon Steel Structures B.V.
Krinkelwinkel 6-8, NL 4202 LN Gorinchem

Hersteller – Manufacturer – Fabricant – Produttore:

Dillinger Hütte/Werk Dillingen
AG der Dillinger Hüttenwerke
66748 Dillingen

Prüf-Nr.-Inspection No. -

Certificat No./no. di collaudo 6022/04/0814

Teil-Part-Partie-Parte: -

Blatt-Nr.-Sheet No.-Page No.-Pag-No: 1

Bestell-Nr.-Order No.-No de la commande-No. dell'ordine

8000-00/1501

vom – dated- date – in data:

Werks-Nr. – Works No – No usine – Commessa No.:

287702

Prüfgegenstand – Article – Produit-Prodotta: Plate, hot rolled

Prüfgrundlagen/Anforderungen - Technical requirements/Demand – Spécification techniques/Exigences - Norma di controllo/Requisiti:

Customer's requirements: BR-2GZZZZ-MT-SPE-0004 Rev.D1

Werkstoff-Material-Matière-Materiale: entsprechend-according to-suivant-secondo:

Ausgabe-Edition-Edizione:

Type I S460G2+M EN 10225

8.01

Lieferzustand-State of delivery-Etat de livraison-Stato di fornitura:

TM

Erschmelzungsart-Melting process-Procédé d'élaboration-Procedimento di elaborazione: Y*

*vacuum degassed

Kennzeichnung – Marking – Marquage – Punzonatura:

Werkstoff - Material

Matière – Materiale:

Type I S460 G2+M Z35

melting process

heat no.

test no.

Herstellerzeichen – Brand of the manufacturer:

Marque du fabricant – Marchio del produttore



Stempel des Sachverständigen-Inspector's stamp

Poinçon de l'expert-Punzone dell'ispettore.



Umfang der Lieferung – Extent of material delivery – Liste descriptive – Descrizione della fornitura:

Pos.-Nr. Item N° Poste-N° N° pos.	Stückzahl Number of Qty Numero pezzi	Gegenstand-Article-Désignation du produit-Tipo di prodotto	Schmelze -Nr. Heat N° N° Coulée N° Colata	Probe Nr. Test N° N° d'éprouvette N° di prova
001	2	Project: „AIOC 2“ Plate 25,00 x 3000 x 14800 mm	61312	99407
	2		61312	99409
	2		61314	99403
	2		61314	99405
002	1	<u>Plate 25,00 x 3000 x 14800 mm</u>	61320	99315
	2		61320	99316
	2		61320	99317

Zusätzliche Angaben – Additional remarks – Autres remarques – Osservazione:

Tolerances: EN 10029 Cl. B/91

Die gestellten Anforderungen sind lt. Anlagen erfüllt – The requirements are fulfilled as per annex.

Les conditions imposées sont satisfaites suivant annexes.

I risultati sono conformi al requisiti richiesti come da allegati delle prove

Sulzbach, den 4. April 2005

(Ort-Location-Lieu-Localita, Datum-Date-Data)

(Der Sachverständige-Inspector-
L'expert – L'ispettore)

Dipl.-Ing. Krämer

Anlagen-Annexes-Allegati:

1) Ergebnis der Prüfungen - Test results – Résultats des essais – Risultati

Weitere Anlagen in 1) Other annex in 1) – Autres annexes en 1) – Altri allegati in 1)

CEOCCONFÉDÉRATION EUROPÉENNE
D'ORGANISMES DE CONTRÔLE**Abnahmeprüfzeugnis
Inspection Certificate
Certificat de Réception
Certificato Collaudo Materiali****Technischer-Überwachungs-Verein
SAARLAND e.V.**Prüf-Nr.: 6022/04/0814
Inspection No
Certificat No
No di CollaudoTeil - Blatt Nr. 4
Part Sheet No
Partie Page No
Parte Pag No**Umfang der Lieferung - Condition of material delivery - Liste descriptive - Ammontare della fornitura:**

Pos.-Nr. Item N° Poste-N° N° pos.	Stückzahl Number of Qte Numero pezzi	Gegenstand-Article-Désignation du produit-Tipo di prodotto	Schmelze-Nr. Heat N° N° Coulée N° Colata	Probe Nr. Test N° N° d'éprouvette N° di prova
013	1	Plate 75,00 x 2500 x 11600 mm	61064	92299
	1		61064	92300
	1		61064	92301
	1		61064	92302
014	1	Plate 75,00 x 2500 x 11600 mm	61065	92291
	1		61065	92292
015	1	Plate 100,00 x 2000 x 6500 mm	61191	97693

Zusätzliche Angaben - Additional remarks - Autres remarques - Osservazione:

Die gestellten Anforderungen sind lt. Anlagen erfüllt - The requirements are fulfilled as per annex -
Les conditions imposées sont satisfaites suivant annexes -
I risultati sono conformi ai requisiti richiesti come da allegati.Sulzbach, den 4. April 2005
(Ort-Location-Lieu-Localita, Datum-Date-Data)

Anlagen-Annexes-Allegati:

1.) Ergebnis der Prüfungen - Test results - Résultats des essais - Risultati delle prove
Weitere Anlagen in 1) Other annexes in 1) - Autres annexes en 1) - Altri allegati in 1)

 (Der Sachverständige-Inspector- L'expert - L'ispettore)
Dipl.-Ing. Krämer

Erläuterungen siehe Rückseite/Explications voir au verso/See reverse for explanations (www.dillinger.biz/certificate)

A02	ABNAHMEPRUEFFPROTOKOLL	3.2	DIN EN 10204	-	EN 10204	-	DIN 50049	A09	Advice of dispatch No./ Date of dispatch	160519-19.11.04	A08/ Manufacturer's order/ A03 Certificate No.	287702-001	Sheet	1/...
	PROCES-VERBAL DE RECEPTION	3.2	NF EN 10204								B01 Product	SHOT BLASTED PLATES, PAINT		
	INSPECTION REPORT	3.2	BS EN 10204	-	ISO 10474						ED			
A05	Established inspecting body	A06 Purchaser	MERCON STEEL, CORINCH		A07.1 No.	8000-00/1501								
	TUVV	Final receiver	MERCON STEEL, GORINCH		A07.2 No.									

B02/ Steel grade **TYPE-I-S460G2+M+Z35**
 B03 Specifications **EN-10225:01**
BR-2GZZZ-MT-SPE-0004:REV.D1
EN-10164:93

B01-B99 Product description

B09 Item No.	B10 Quantity	B11 Thickness	B12 Width	B13 Length	B14 Mass theoretical KG	B04 Delivery condition	B08 Heat No.	B07 Rolled plate No./ Test No.	B16 Customer reference
02	1	25,00	x 3000	x 14800	8714	TMCP	61320	99316-01	ANNEX: 2.1 to test no.: 6022 / 0 4 / 0 3 1 4 TÜV SAARLAND e.V.
02	1	25,00	x 3000	x 14800	8714	TMCP	61320	99316-02	
02	1	25,00	x 3000	x 14800	8714	TMCP	61320	99317-01	
02	1	25,00	x 3000	x 14800	8714	TMCP	61320	99317-02	
**	4				34856				
05	1	35,00	x 3000	x 14800	12199	TMCP	61125	88603-01	
05	1	35,00	x 3000	x 14800	12199	TMCP	61125	88604-01	
05	1	35,00	x 3000	x 14800	12199	TMCP	61125	88607-01	
05	1	35,00	x 3000	x 14800	12199	TMCP	61125	88610-01	
05	1	35,00	x 3000	x 14800	12199	TMCP	61125	88615-01	
05	1	35,00	x 3000	x 14800	12199	TMCP	61125	88618-01	
**	6				73194				
06	1	35,00	x 3000	x 14800	12199	TMCP	61126	96003-01	
06	1	35,00	x 3000	x 14800	12199	TMCP	61126	96004-01	
06	1	35,00	x 3000	x 14800	12199	TMCP	61126	96005-01	
06	1	35,00	x 3000	x 14800	12199	TMCP	61126	96006-01	
**	4				48796				
07	1	40,00	x 3000	x 14800	13942	TMCP	61126	95998-01	
07	1	40,00	x 3000	x 14800	13942	TMCP	61126	95999-01	
07	1	40,00	x 3000	x 14800	13942	TMCP	61126	96000-01	
07	1	40,00	x 3000	x 14800	13942	TMCP	61126	96001-01	
07	1	40,00	x 3000	x 14800	13942	TMCP	61126	96002-01	
**	5				69710				

A04  Trademark

201/202 We hereby certify, that the above mentioned materials have been delivered in accordance with the terms of order.

CHECKED
 Technischer Überwachungs-Verein
 Saarland e.V.
 Druckgüterherstellung

[Signature]
 B. MUELLER
 Der Werkstoffverständige

AHB
 Inspection department

AG der Dillinger Hüttenwerke
 Postfach 1580, D-66748 Dillingen/Saar

Inspector's stamp: *[Stamp]* Date: 22.11.04

A01 ML 1

Erläuterungen siehe Rückseite/Explications voir au verso/See reverse for explanations (www.dillinger.biz/certificate)

A02	ABNAHMEPRUEFPROTOKOLL	3.2	DIN EN 10204	-	EN 10204	-	DIN 50049	A09	Advice of dispatch No./ Date of dispatch	160519-19.11.04	A08/ Manufacturer's order/ A03 Certificate No.	287702-001	Sheet
	PROCES-VERBAL DE RECEPTION	3.2	NF EN 10204								B01 Product	2/...	
	INSPECTION REPORT	3.2	BS EN 10204	-	ISO 10474						SHOT BLASTED PLATES, PAINT ED		
A05	Established inspecting body	A06 Purchaser	MERCON STEEL, GORINCH		A07.1 No.	8000-00/1501							
	TUVV	Final receiver	MERCON STEEL, GORINCH		A07.2 No.								
B02/	Steel grade	TYPE-I-S460G2+M+Z35											
B03	Specifications	EN-10225:01 BR-2GZZZZ-MT-SPE-0004:REV.D1 EN-10164:93											

B01-B99 Product description

B09 Item No.	B10 Quantity	B11 Thickness	B12 Width	B13 Length	B14 Mass theoretical KG	B04 Delivery condition	B08 Heat No.	B07 Rolled plate No./ Test No.	B16 Customer reference
08	1	40,00	x 3000	x 14800	13942	TMCP	61126	95996-01	
08	1	40,00	x 3000	x 14800	13942	TMCP	61126	95997-01	
08	1	40,00	x 3000	x 14800	13942	TMCP	61127	95897-01	
08	1	40,00	x 3000	x 14800	13942	TMCP	61127	95899-01	
08	1	40,00	x 3000	x 14800	13942	TMCP	61127	95991-01	
08	1	40,00	x 3000	x 14800	13942	TMCP	61127	95992-01	
08	1	40,00	x 3000	x 14800	13942	TMCP	61127	95993-01	
08	1	40,00	x 3000	x 14800	13942	TMCP	61127	95994-01	
**	8				111536				
09	1	50,00	x 3030	x 15400	18315	TMCP	61065	92295-01	
09	1	50,00	x 3030	x 15400	18315	TMCP	61065	92296-01	
09	1	50,00	x 3030	x 15400	18315	TMCP	61065	92297-01	
**	3				54945				
10	1	50,00	x 3030	x 15400	18315	TMCP	61066	92281-01	
10	1	50,00	x 3030	x 15400	18315	TMCP	61066	92284-01	
10	1	50,00	x 3030	x 15400	18315	TMCP	61068	92280-01	
**	3				54945				
11	1	60,00	x 2600	x 11400	13960	TMCP	61072	92255-01	
11	1	60,00	x 2600	x 11400	13960	TMCP	61072	92256-01	
11	1	60,00	x 2600	x 11400	13960	TMCP	61072	92257-01	
**	3				41880				
12	1	60,00	x 2600	x 11400	13960	TMCP	61066	92285-01	
12	1	60,00	x 2600	x 11400	13960	TMCP	61066	92287-01	

A04 201/202 We hereby certify, that the above mentioned materials have been delivered in accordance with the terms of order.

CHECKED
Technischer Überwachungs-Verein
Sondernd 2.V
Druckgeräteeinstellung

[Signature]
B. MUELLER
Inspector

AG der Dillinger Hüttenwerke
Postfach 1580, D-66748 Dillingen/Saar
Inspection department

ADH

Inspector's stamp Date 22.11.04 ML 1

Erläuterungen siehe Rückseite/Explications voir au verso/See reverse for explanations (www.dillinger.biz/certificate)

A02	ABNAHMEPRUEFFPROTOKOLL	3.2	DIN EN 10204	-	EN 10204	-	DIN 50049	A03	Advice of dispatch No./ Date of dispatch	160519-19.11.04	A08/ Manufacturer's order/ A03 Certificate No.	287702-001	Sheet	
PROCES-VERBAL DE RECEPTION 3.2 NF EN 10204 INSPECTION REPORT 3.2 BS EN 10204 - ISO 10474														
A05	Established inspecting body	A06	Purchaser	MERCON STEEL, GORINCH	A07.1	No.	8000-00/1501						B01	Product
TUVC		Final receiver		MERCON STEEL, GORINCH	A07.2	No.							SHOT BLASTED PLATES, PAINT ED	
B02	Steel grade	TYPE-I-S460G2+M+Z35												
B03	Specifications	EN-10225:01 BR-2G2ZZZ-MT-SPE-0004:REV.D1 EN-10164:93												

B01-B99 Product description

B09	B10	B11	B12	B13	B14	B04	B08	B07	B16
Item No.	Quantity	Thickness	Width	Length	Mass theoretical	Delivery condition	Heat No.	Rolled plate No./ Test No.	Customer reference
No.		MM			KG				
**	2				27920				
13	1	75,00	x 2500	x 11600	17074	TMCP	61064	92299-01	
13	1	75,00	x 2500	x 11600	17074	TMCP	61064	92301-01	
13	1	75,00	x 2500	x 11600	17074	TMCP	61064	92302-01	
**	3				51222				
***	41				569004				

B04 Further information about delivery condition / Heat treatment of plates

ITEM NO.: 02,05-14
 TMCP = THERMOMECHANICAL CONTROL PROCESS

B06 Marking

ITEM NO.: 02,05-14
 STEEL GRADE TYPE I S460G2+M Z35
 HEAT NO. / TRADEMARK / ROLLED PLATE NO. - TEST NO. / INSPECTOR'S STAMP

C10-C29 Tensile test

B09	B08	B07	B05	C01	C02/	C03	C10	C11	C12	C13	C14-C15	Z
Item No.	Heat No.	Rol. plate/ Test No.	Reference condition	Temp	GRC	MPA	RT	MPA	RM	A	RP02/RM	%
No.				GRC		RP02				LO-5D		%
02	61320	99316		K4	Q	RT	469		545	31,0	0,86	58,8
02	61320	99317		K2	S	RT			590			62,0
				K2	S	RT			594			68,7
				K2	S	RT			594			
				K4	Q	RT	483		567	27,1	0,85	

A04 Z01/Z02 We hereby certify, that the above mentioned materials have been delivered in accordance with the terms of order.

CHECKED

Technischer Überwachungs-Verein
Saarland e.V.
Druckguss-Herstellung

Inspector

B. Moeller
B. MOELLER
Der Werksachverständige

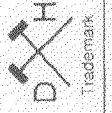
Inspector's stamp

Date 22.11.04

ML 1

AHB

AG der Dillinger Hüttenwerke
Postfach 1580, D-66748 Dillingen/Saar
inspection department



Erläuterungen siehe Rückseite/Explications voir au verso/See reverse for explanations (www.dillinger.biz/certificate)

A02	ABNAHMEPRUEFPROTOKOLL PROCES-VERBAL DE RECEPTION INSPECTION REPORT	3.2 DIN EN 10204 - EN 10204 - DIN 50049 3.2 NF EN 10204 3.2 BS EN 10204 - ISO 10474	A09	Advice of dispatch No./ Date of dispatch	160519-19.11.04	A08/ Manufacturer's order/ A03 Certificate No.	287702-001	Sheet	4/...
A05	Established inspecting body TUV	A06 Purchaser MERCON STEEL, GORINCH	A07.1 No.	8000-00/1501		B01 Product	SHOT BLASTED PLATES, PAINT ED		
B02/	Steel grade	Final receiver	A07.2 No.						
B03	Specification	TYPE-I-S460G2+M+Z35 EN-10225:01 BR-2CZZZZ-MT-SPE-0004:REV.D1 EN-10164:93							

C10-C29 Tensile test

B09	B08	B07	B05	C01	C02/	C03	C10	C11	C12	C13	A	C14-C15	Z
No.	Item	Heat No.	Ref./plate/ Test No.	Temp.	GR.C	Temp.	MPA	RP02	RM	%	LO=6D	RP02/RM	%
05	61125	88603		K2 S	RT				631		24,7	0,88	70,4
				K2 S	RT				631		25,9	0,88	72,4
				K2 S	RT				623		22,9	0,88	70,3
				K4 Q	RT		553		631		24,7	0,88	
				K4 Q	RT		558		632		25,9	0,88	
				K4 Q	RT		543		614		22,9	0,88	
				K4 Q	RT		561		629		26,5	0,89	
				K4 Q	RT		517		593		23,3	0,87	
				K4 Q	RT		517		592		23,9	0,87	
				K2 S	RT				578				72,3
				K2 S	RT				579				73,8
				K2 S	RT				581				70,2
				K4 Q	RT		494		577		24,4	0,86	
				K4 Q	RT		510		590		23,3	0,86	
				K4 Q	RT		528		617		23,3	0,86	
				K4 Q	RT		538		626		22,8	0,86	
				K2 S	RT				579				68,4
				K2 S	RT				580		23,9	0,87	70,6
				K2 S	RT				581		23,9	0,87	68,5
				K4 Q	RT		506		580		23,9	0,87	
				K4 Q	RT		508		585		23,9	0,87	
				K4 Q	RT		566		638		24,0	0,89	
				K2 S	RT				600				70,8

A04

Z01/Z02 We hereby certify, that the above mentioned materials have been delivered in accordance with the terms of order.

CHECKED
 Technischer Überwachungs-Verein
 Saarland e.V.
 Druckgeräta Herstellung
 Inspector

B. MUELLER
 Der Werksschwerstände

Inspector's stamp

AG der Dillinger Hüttenwerke
 Postfach 1580, D-66748 Dillingen/Saar
 Inspection department

Date 22.11.04

ML 1

Erklärungen siehe Rückseite/Explications voir au verso/See reverse for explanations (www.dillinger.biz/certificate)

A02	ABNAHMEPRUEFPROTOKOLL	3.2	DIN EN 10204	-	EN 10204	-	DIN 50049	A09	Advice of dispatch No./Date of dispatch	160519-19.11.04	A08/ Manufacturer's order/A03 Certificate No.	287702-001	Sheet
	PROCES-VERBAL DE RECEPTION	3.2	NF EN 10204								B01 Product	5/...	
	INSPECTION REPORT	3.2	BS EN 10204	-	ISO 10474						SHOT BLASTED PLATES, PAINT ED		
A05	Established inspecting body		MERCON STEEL, GORINCH	A07.1 No.	8000-00/1501								
	TUVV		MERCON STEEL, GORINCH	A07.2 No.									
B02/	Steel grade		TYPE-I-S460G2+M+Z35										
B03	Specifications		EN-10225:01										
			BR-2GZZZZ-MT-SPE-0004:REV.D1										
			EN-10164:93										

C10-C29 Tensile test

B09 Item No.	B08 Heat No.	B07 Rol.plate/ Test No.	B05 Reference condition	C01	C02/ C01	C03 Temp. GR.C	C10	C11 MPA RP02	C12 RM	C13	A % LO=5D	C14-C16 RP02/RM	Z %
09	61065	92295		K2 S	RT				606				71,7
				K2 S	RT				604		24,0	0,88	67,2
				K4 Q	RT			551	628				
09	61065	92297		K4 Q	RT			558	635		23,5	0,88	
10	61066	92282 *		K4 Q	RT			554	625		24,0	0,89	
10	61066	92284		K4 Q	RT			557	627		23,0	0,89	
10	61068	92280		K2 S	RT				603				62,0
				K2 S	RT				600		24,0	0,89	67,3
				K2 S	RT			556	600				69,5
11	61072	92256		K4 Q	RT				582				57,6
				K2 S	RT				581				57,5
				K2 S	RT				583				68,0
				K4 Q	RT			524	609		23,8	0,86	65,1
11	61072	92257		K4 Q	RT			516	601		24,8	0,86	56,4
12	61066	92285		K2 S	RT				584				50,1
				K2 S	RT				584				
				K2 S	RT				583				
				K4 Q	RT			533	610		24,3	0,87	
12	61066	92287		K4 Q	RT			535	618		22,9	0,87	
12	61066	92289 *		K4 Q	RT			542	620		22,9	0,87	
13	61064	92299		K2 S	RT				581				42,9
				K2 S	RT				576				48,2

A04

Z01/Z02 We hereby certify, that the above mentioned materials have been delivered in accordance with the terms of order.

CHECKED

Technische Überwachungs-Verein Saarland e.V.

DRIC: Inspektor B. MUELLER

AG der Dillinger Hüttenwerke
Postfach 1580, D-66748 Dillingen/Saar
Inspection department

Inspector's stamp: Date: 22.11.04

Der Werksachverständige: ML 1

Erläuterungen siehe Rückseite/Explications voir au verso/See reverse for explanations (www.dillinger.biz/certificate)

A02	ABNAEMPRUEFFROKOLL	3.2	DIN EN 10204	-	EN 10204	-	DIN 50049	A09	Advice of dispatch No./ Date of dispatch	160519-19.11.04	A08/ Manufacturer's order/ A03 Certificate No.	287702-001	Sheet	6/...
PROCES-VERBAL DE RECEPTION		3.2	NF EN 10204											
INSPECTION REPORT		3.2	BS EN 10204	-	ISO 10474									
A05 Established inspecting body		A06 Purchaser		A07.1 No		A07.2 No		B01 Product						
TUVC		MERCON STEEL, GORINCH		8000-00/1501		SHOT BLASTED PLATES, PAINT								
Final receiver		ED												

B02/ Steel grade
TYPE-I-S460G2+M+Z35
 B03 Specifications
 EN-10225:01
 BR-2GZZZ-MT-SPE-0004:REV.D1
 EN-10164:93

C10-C29 Tensile test

B09 Item No.	B08 Heat No.	B07 Rol.plate/ Test No.	B05 Reference condition	C01	C02/ C03	C10	C11	C12	C13	A %	C14-C15	Z %
				Temp. GRC	Temp. GRC	MPA	RP02	RM		L0=5D	RP02/RM	
13	61064	92299	K2 S	RT		521		577		25,2		42,4
13	61064	92302	K4 Q	RT		524		599		23,8		
14	61065	92291 *	K4 Q	RT		529		605		23,3		

C40-C49 Impact test

B09 Item No.	B08 Heat No.	B07 Rol.plate/ Test No.	B05 Reference condition	C01	C02/ C03	C01	C03	C40	C41	C44	C46	C43
				Temp. GRC	Temp. GRC	Temp. GRC	Temp. GRC	Type of specimen	Specimen width	Testing method	Energy Joule	Average value
02	61320	99316	K4	Q2	-40	-40	-40	CHP-V	40	AV	242	244
02	61320	99317	K4	Q2	-40	-40	-40	CHP-V	40	AV	236	222
05	61125	88603	K4	Q2	-40	-40	-40	CHP-V	40	AV	258	270
05	61125	88615	K4	Q2	-40	-40	-40	CHP-V	40	AV	286	271
06	61126	96005	K4	Q2	-40	-40	-40	CHP-V	40	AV	309	296
06	61126	96006	K4	Q2	-40	-40	-40	CHP-V	40	AV	287	281
07	61126	95999	K4	Q2	-40	-40	-40	CHP-V	40	AV	323	309
07	61126	96001	K4	Q2	-40	-40	-40	CHP-V	40	AV	336	331
08	61126	95996	K4	Q2	-40	-40	-40	CHP-V	40	AV	318	316
08	61126	95997	K4	Q2	-40	-40	-40	CHP-V	40	AV	310	307
08	61127	95899	K4	Q2	-40	-40	-40	CHP-V	40	AV	280	280
08	61127	95945 *	K4	Q2	-40	-40	-40	CHP-V	40	AV	257	255
08	61127	95992	K4	Q2	-40	-40	-40	CHP-V	40	AV	317	319
08	61127	95994	K4	Q2	-40	-40	-40	CHP-V	40	AV	297	298
09	61065	92293 *	K4	QM	-40	-40	-40	CHP-V	40	AV	277	278
			K4	Q2	-40	-40	-40	CHP-V	40	AV	284	297

A04 Z01/Z02 We hereby certify, that the above mentioned materials have been delivered in accordance with the terms of order.

CHECKED
 Technischer Überwachungs-Verein
 Saarland e.V.
 Druck-Inspektorwerkstatt

AHB
 AG der Dillinger Hüttenwerke
 Postfach 1580, D-66748 Dillingen/Saar
 Inspection department

Der Werkstoffverständige **B. MUELLER** Inspector's stamp Date 22.11.04 ML 1

Erläuterungen siehe Rückseite/Explications voir au verso/See reverse for explanations (www.dillinger.biz/certificate)

A02	ABNAHMEPRÜFPROTOKOLL	3.2	DIN EN 10204	-	EN 10204	-	DIN 50049	A09	Advance of dispatch No./ Date of dispatch	A08/ Manufacturer's order/ A03 Certificate No	Sheet
	PROCES-VERBAAL DE RECEPTION	3.2	NF EN 10204						160519-19.11.04	287702-001	7/...
	INSPECTION REPORT	3.2	BS EN 10204	-	ISO 10474					B01 Product	
A05	Established inspecting body TUVC	A06 Purchaser	MERCON STEEL, GORINCH	A07.1 No.	8000-00/1501					SHOT-BLASTED PLATES, PAINT	
		Final receiver	MERCON STEEL, GORINCH	A07.2 No.						ED	
B02/	Steel grade	TYPE-I-S460G2+M+Z35									
B03	Specifications	EN-10225:01 BR-2GZZZZ-MT-SPE-0004:REV.D1 EN-10164:93									

C40-C49 Impact test

B09 Item No.	B08 Heat No.	B07 Rol.plate/ Test No.	B05 Reference condition	C01	C02/ C01	C03 Temp. G.R.C.	C41 Specimen width	C40 Type of specimen	C44 Testing method	C46 Energy Joule	C45 individual values AV-J	C43 Average value
09	61065	92295		K4 QM	Q2	-40	CHP-V	CHP-V	AV 266	600	231	281
09	61065	92297		K4 QM	Q2	-40	CHP-V	CHP-V	AV 312	600	308	296
10	61066	92282	*	K4 QM	Q2	-40	CHP-V	CHP-V	AV 307	600	324	316
10	61066	92284	*	K4 QM	Q2	-40	CHP-V	CHP-V	AV 299	600	293	311
10	61068	92280		K4 QM	Q2	-40	CHP-V	CHP-V	AV 239	600	199	275
11	61072	92256		K4 QM	Q2	-40	CHP-V	CHP-V	AV 258	600	271	245
11	61072	92257		K4 QM	Q2	-40	CHP-V	CHP-V	AV 220	600	260	315
12	61066	92285		K4 QM	Q2	-40	CHP-V	CHP-V	AV 237	600	256	278
12	61066	92287		K4 QM	Q2	-40	CHP-V	CHP-V	AV 219	600	235	256
12	61066	92289	*	K4 QM	Q2	-40	CHP-V	CHP-V	AV 289	600	302	281
13	61064	92299	*	K4 QM	Q2	-40	CHP-V	CHP-V	AV 240	600	205	236
13	61064	92302		K4 QM	Q2	-40	CHP-V	CHP-V	AV 296	600	274	260
				K4 QM	Q2	-40	CHP-V	CHP-V	AV 251	600	257	266
				K4 QM	Q2	-40	CHP-V	CHP-V	AV 301	600	290	295
				K4 QM	Q2	-40	CHP-V	CHP-V	AV 251	600	277	253
				K4 QM	Q2	-40	CHP-V	CHP-V	AV 235	600	209	210
				K4 QM	Q2	-40	CHP-V	CHP-V	AV 312	600	299	270
				K4 QM	Q2	-40	CHP-V	CHP-V	AV 246	600	256	238
				K4 QM	Q2	-40	CHP-V	CHP-V	AV 266	600	221	289
				K4 QM	Q2	-40	CHP-V	CHP-V	AV 234	600	208	234
				K4 QM	Q2	-40	CHP-V	CHP-V	AV 314	600	276	259
				K4 QM	Q2	-40	CHP-V	CHP-V	AV 224	600	226	205
				K4 QM	Q2	-40	CHP-V	CHP-V	AV 214	600	205	214
				K4 QM	Q2	-40	CHP-V	CHP-V	AV 136	600	179	218

A04 Z01/Z02 We hereby certify, that the above mentioned materials have been delivered in accordance with the terms of order.

CHECKED
Technischer Überwachungs-Verein
Saarland e.V.
Druckgeräte-Herstellung

AG der Dillinger Hüttenwerke
Postfach 1580, D-66748 Dillingen/Saar
Inspection department

B. MUELLER
Der Werkssachverständige

Inspector's stamp Date 22.11.04 ML I

Erläuterungen siehe Rückseite/Explications voir au verso/See reverse for explanations (www.dillinger.biz/certificate)

A02	ABNAHMEPRUEFFPROTOKOLL	3.2	DIN EN 10204	-	EN 10204	-	DIN 50049	A09	Advice of dispatch No./ Date of dispatch	160519-19.11.04	A08/ Manufacturer's order/ A03 Certificate No	287702-001	Sheet	8/...
	PROCES-VERBAL DE RECEPTION	3.2	NF EN 10204											
	INSPECTION REPORT	3.2	BS EN 10204	-	ISO 10474									
A05	Established inspecting body	A06	Purchaser	MERCON STEEL, GORINCH	A071	No.	8000-00/1501							
	TUVV		Final receiver	MERCON STEEL, GORINCH	A072	No.								

B02/ Steel grade **TYPE-I-S460G2+M+Z35**
 B03/ Specific-
 tions EN-10225:01
 BR-2GZZZZ-MT-SPE-0004:REV.D1
 EN-10164:93

C40-C49 Impact test

B09	B06	B07	B05	C01	C02/	C03	C41	C40	C44	C46	C45	C42	C43
Item	Heat No.	Roll plate/ Test No.	Reference condition	K4	QM	GR.C	Temp. width	Type of specimen	Testing method	Energy Joule	AV	AV-J	Average value
14	61065	92291	*	K4	QM	-40	-40	CHP-V		600	AV 190	238	221
			*	K4	Q2	-40	-40	CHP-V		600	AV 256	239	253

C66-C68 Supplementary tests on test samples
 ITEM NO.: 02.05-14
 DEEP ETCH TESTING AS PER DH-STANDARD <= 2B: SATISFACTORY.

C70-C99 Chemical composition % - Heat analysis

B08	C70	C	SI	MN	P	S	N	CU	MO	NI	CR	V	AS	SN
61064	Y	0,058	0,212	1,60	0,011	0,0004	0,0037	0,265	0,163	0,462	0,026	0,001	0,021	0,000
61065	Y	0,057	0,216	1,62	0,012	0,0005	0,0033	0,265	0,160	0,470	0,027	0,001	0,020	0,001
61066	Y	0,054	0,184	1,63	0,009	0,0008	0,0047	0,260	0,161	0,460	0,024	0,000	0,019	0,001
61068	Y	0,054	0,210	1,61	0,013	0,0009	0,0042	0,265	0,154	0,467	0,039	0,001	0,020	0,000
61072	Y	0,054	0,197	1,59	0,012	0,0007	0,0037	0,264	0,159	0,468	0,038	0,000	0,020	0,000
61125	Y	0,080	0,166	1,60	0,012	0,0008	0,0043	0,168	0,102	0,403	0,029	0,000	0,020	0,000
61126	Y	0,074	0,210	1,59	0,013	0,0008	0,0038	0,171	0,100	0,406	0,029	0,001	0,020	0,000
61127	Y	0,075	0,179	1,57	0,012	0,0009	0,0041	0,170	0,099	0,388	0,042	0,001	0,019	0,000
61320	Y	0,082	0,211	1,59	0,012	0,0011	0,0039	0,170	0,095	0,326	0,034	0,002	0,020	0,000

A04

Z01/Z02 We hereby certify, that the above mentioned materials have been delivered in accordance with the terms of order.

CHECKED

Technischer Überwachungs-Verein
 Saarland e.V.
 Druckgerätee-Herstellung

B. Müller
 Der Werkssachverständige

Inspector's stamp

AG der Dillinger Hüttenwerke
 Postfach 1580, D-66748 Dillingen/Saar
 Inspection department

ADB

Date 22.11.04

ML

A01

Erläuterungen siehe Rückseite/Explications voir au verso/See reverse for explanations (www.dillinger.biz/certificate)

A02	ABNAHMEPRUEFPROTOKOLL	3.2	DIN EN 10204	-	EN 10204	-	DIN 50049	A09	Advice of dispatch No./ Date of dispatch	160519-19.11.04	A08/ Manufacturer's order/ A03 Certificate No	287702-001	Sheet	9/...
PROCES-VEREAL DE RECEPTION 3.2 NF EN 10204 INSPECTION REPORT 3.2 BS EN 10204 - ISO 10474														
A05	Established inspecting body	MERCON STEEL, GORINCH A071 No. 8000-00/1501												
TUVV	Final receiver	MERCON STEEL, GORINCH A072 No.												
B02/ Steel grade	TYPE-I-S460G2+M+Z35													
B03	Specifications	EN-10225:01 BR-2CZZZZ-MT-SPE-0004:REV.D1 EN-10164:93												

C70-C99 Chemical composition % - Heat analysis

	C70	TI	PB	B	SB	CA	BI	AL-T
B08 Heat	61064	Y 0,003	0,000	0,0001	0,0010	0,0034	0,0001	0,044
	61065	Y 0,003	0,000	0,0001	0,0010	0,0022	0,0001	0,043
	61066	Y 0,002	0,000	0,0002	0,0013	0,0025	0,0001	0,036
	61068	Y 0,002	0,000	0,0000	0,0013	0,0022	0,0001	0,038
	61072	Y 0,002	0,000	0,0001	0,0014	0,0029	0,0001	0,033
	61125	Y 0,001	0,000	0,0001	0,0006	0,0034	0,0001	0,032
	61126	Y 0,002	0,000	0,0001	0,0007	0,0032	0,0001	0,030
	61127	Y 0,002	0,000	0,0001	0,0006	0,0034	0,0001	0,034
	61320	Y 0,002	0,000	0,0000	0,0010	0,0026	0,0001	0,039

C94 Heat analysis Carbon equivalent / Alloying restrictions

B08 Heat	61064	FO-A1= 11,89	FO-02= 0,41	FO-31= 0,18	FO-51= 0,022	FO-52= 0,025	FO-55= 0,92
	61065	FO-A1= 13,03	FO-02= 0,41	FO-31= 0,18	FO-51= 0,021	FO-52= 0,024	FO-55= 0,92
	61066	FO-A1= 7,66	FO-02= 0,41	FO-31= 0,18	FO-51= 0,019	FO-52= 0,021	FO-55= 0,91
	61068	FO-A1= 9,05	FO-02= 0,41	FO-31= 0,17	FO-51= 0,021	FO-52= 0,023	FO-55= 0,93
	61072	FO-A1= 8,92	FO-02= 0,41	FO-31= 0,17	FO-51= 0,020	FO-52= 0,022	FO-55= 0,93
	61125	FO-A1= 7,44	FO-02= 0,41	FO-31= 0,19	FO-51= 0,020	FO-52= 0,021	FO-55= 0,70
	61126	FO-A1= 7,89	FO-02= 0,40	FO-31= 0,18	FO-51= 0,021	FO-52= 0,023	FO-55= 0,71
	61127	FO-A1= 8,29	FO-02= 0,40	FO-31= 0,18	FO-51= 0,020	FO-52= 0,022	FO-55= 0,70
	61320	FO-A1= 10,00	FO-02= 0,39	FO-31= 0,18	FO-51= 0,022	FO-52= 0,024	FO-55= 0,54

A01 Z01/Z02 We hereby certify, that the above mentioned materials have been delivered in accordance with the terms of order.

CHECKED

Technischer Überwachungs-Verein
Saarland e.V.
Druckgeräte-Herstellung

B. Müller

B. MUELLER
Der Werkssachverständige

Inspector's stamp

AG der Dillinger Hüttenwerke
Postfach 1580, D-66748 Dillingen/Saar
Inspection department

Date 22.11.04

ML 1



Erläuterungen siehe Rückseite/Explications voir au verso/See reverse for explanations (www.dillinger.biz/certificate)

A02	ABNAHMEPRUEFPROTOKOLL	3.2	DIN EN 10204	-	EN 10204	-	DIN 50049	A09	Advice of dispatch No./ Date of dispatch	160519-19.11.04	A08/ Manufacturer's order/ A03 Certificate No.	287702-001	Sheet
	PROCES-VERBAL DE RECEPTION	3.2	NF EN 10204								B01 Product	10/....	
	INSPECTION REPORT	3.2	BS EN 10204	-	ISO 10474						SHOT BLASTED PLATES, PAINT		
A06	Established inspecting body	A06 Purchaser	MERCON STEEL, GORINCH	A07.1 No.	8000-00/1501						ED		
	TUVV	Final receiver	MERCON STEEL, GORINCH	A07.2 No.									

B02/ Steel grade **TYPE-I-S460G2+M+Z35**
 B03 Specifications **EN-10225:01**
BR-2GZZZZ-MT-SPE-0004:REV.D1
EN-10164:93

C70-C99 Chemical composition % - Product analysis

B08 Heat	B07 Test No.	C01	C	Si	Mn	P	S	N	CU	MO	NI	CR	V	NB	TI	B
61064	92299	K4	0,059	0,207	1,58	0,010	0,0004	0,0034	0,264	0,162	0,463	0,024	0,001	0,019	0,003	0,0000
61064	92302	K4	0,062	0,209	1,57	0,009	0,0005	0,0036	0,265	0,163	0,459	0,024	0,000	0,019	0,003	0,0000
61065	92291	K4	0,056	0,207	1,60	0,011	0,0009	0,0030	0,262	0,158	0,470	0,026	0,002	0,018	0,003	0,0000
61065	92293	K4	0,056	0,209	1,60	0,011	0,0005	0,0044	0,264	0,163	0,467	0,025	0,000	0,019	0,003	0,0000
61065	92295	K4	0,054	0,220	1,59	0,012	0,0006	0,0026	0,270	0,162	0,465	0,026	0,000	0,019	0,003	0,0000
61065	92297	K4	0,056	0,215	1,61	0,011	0,0004	0,0027	0,262	0,160	0,467	0,025	0,001	0,019	0,003	0,0000
61066	92282	K4	0,052	0,181	1,60	0,009	0,0008	0,0042	0,259	0,159	0,453	0,022	0,000	0,019	0,001	0,0000
61066	92284	K4	0,052	0,182	1,61	0,009	0,0007	0,0042	0,258	0,160	0,454	0,022	0,000	0,019	0,001	0,0000
61066	92285	K4	0,055	0,186	1,60	0,009	0,0006	0,0040	0,256	0,156	0,458	0,024	0,001	0,018	0,002	0,0000
61066	92287	K4	0,057	0,205	1,58	0,011	0,0009	0,0035	0,265	0,161	0,466	0,025	0,001	0,019	0,003	0,0000
61066	92289	K4	0,055	0,193	1,60	0,009	0,0006	0,0039	0,258	0,156	0,462	0,025	0,001	0,018	0,002	0,0000
61068	92280	K4	0,055	0,188	1,60	0,009	0,0008	0,0039	0,257	0,156	0,460	0,027	0,002	0,019	0,001	0,0000
61068	92280	K4	0,055	0,182	1,60	0,009	0,0010	0,0036	0,258	0,158	0,453	0,027	0,000	0,019	0,002	0,0000
61072	92256	K4	0,053	0,192	1,56	0,011	0,0007	0,0037	0,263	0,154	0,464	0,039	0,002	0,019	0,002	0,0001
61072	92257	K4	0,058	0,200	1,57	0,012	0,0010	0,0034	0,266	0,152	0,462	0,038	0,000	0,019	0,002	0,0001
61125	88603	K4	0,077	0,165	1,59	0,012	0,0009	0,0036	0,165	0,099	0,407	0,027	0,000	0,020	0,001	0,0000
61125	88615	K4	0,079	0,163	1,59	0,011	0,0005	0,0042	0,163	0,099	0,404	0,028	0,000	0,020	0,001	0,0000
61126	95995	K4	0,071	0,212	1,58	0,012	0,0007	0,0037	0,171	0,097	0,400	0,028	0,001	0,021	0,003	0,0000
61126	95996	K4	0,073	0,203	1,57	0,013	0,0007	0,0035	0,174	0,100	0,403	0,028	0,000	0,020	0,003	0,0000
61126	95999	K4	0,068	0,208	1,58	0,013	0,0007	0,0031	0,172	0,099	0,408	0,029	0,001	0,020	0,003	0,0000
61126	96000	K4	0,069	0,198	1,57	0,012	0,0006	0,0041	0,170	0,098	0,404	0,029	0,002	0,020	0,002	0,0000
61126	96002	K4	0,072	0,202	1,58	0,012	0,0007	0,0037	0,171	0,100	0,406	0,028	0,001	0,020	0,003	0,0001
61126	96005	K4	0,077	0,198	1,56	0,012	0,0014	0,0041	0,169	0,100	0,402	0,029	0,000	0,020	0,002	0,0000
61127	95899	K4	0,074	0,174	1,57	0,012	0,0007	0,0042	0,166	0,097	0,390	0,041	0,001	0,019	0,002	0,0000
61127	95945	K4	0,074	0,172	1,57	0,012	0,0007	0,0040	0,167	0,098	0,391	0,041	0,002	0,019	0,002	0,0000

A04

Z01/Z02 We hereby certify, that the above mentioned materials have been delivered in accordance with the terms of order.

CHECKED

Technischer Überwachungs-Verein Saarland e.V.

Druckgeräte Herstellung

Inspector

AHB

AG der Dillinger Hüttenwerke
Postfach 1580, D-66748 Dillingen/Saar
Inspection department

Inspector's stamp

Date 22.11.04

ML 1

Erläuterungen siehe Rückseite/Explications voir au verso/See reverse for explanations (www.dillinger.biz/certificates)

A02	ABNAHMEPRÜFPROTOKOLL	3.2	DIN EN 10204	-	EN 10204	-	DIN 50049	A09	Advice of dispatch No./ Date of dispatch	160519-19.11.04	A08/ Manufacturer's order/ A03 Certificate No.	287702-001	Sheet
	PROCES-VERBAAL DE RECEPTION	3.2	NF EN 10204								B01 Product	12/...	
	INSPECTION REPORT	3.2	BS EN 10204	-	ISO 10474						SHOT BLASTED PLATES, PAINT ED		
A05	Established inspecting body	A06 Purchaser	MERCON STEEL, GORINCH	A071 No.	8000-00/1501								
	TUVV	Final receiver	MERCON STEEL, GORINCH	A072 No.									
B02/ Steel grade	TYPE-I-S460G2+M+Z35												
B03 Specifications	EN-10225:01												
	BR-2CZZZZ-MT-SPE-0004:REV.D1												
	EN-10164:93												

C70-C99 Chemical composition % - Product analysis

B08 Heat	B07 Test No.	AL-T												
61126	95999	K4 0,033												
61126	96000	K4 0,031												
61126	96002	K4 0,031												
61126	96005	K4 0,029												
61127	95899	K4 0,036												
61127	95945	K4 0,037												
61127	95992	K4 0,033												
61127	95994	K4 0,034												
61320	99316	K4 0,039												
61320	99317	K4 0,038												

C94 Product analysis Carbon equivalent / Alloying restrictions

B08 Heat	B07 Test No.	FO-51=	FO-52=	FO-55=	FO-31=	FO-02=	FO-01=	FO-02=	FO-01=	FO-02=	FO-01=	FO-02=	FO-01=	FO-02=
61064	92299	0,020	0,023	0,023	0,18	0,41	0,41	0,41	0,41	0,41	0,41	0,41	0,41	0,41
61064	92302	0,019	0,022	0,022	0,18	0,41	0,41	0,41	0,41	0,41	0,41	0,41	0,41	0,41
61065	92291	0,020	0,023	0,023	0,18	0,41	0,41	0,41	0,41	0,41	0,41	0,41	0,41	0,41
61065	92293	0,019	0,022	0,022	0,17	0,41	0,41	0,41	0,41	0,41	0,41	0,41	0,41	0,41
61065	92295	0,019	0,022	0,022	0,18	0,41	0,41	0,41	0,41	0,41	0,41	0,41	0,41	0,41
61065	92297	0,020	0,023	0,023	0,17	0,40	0,40	0,40	0,40	0,40	0,40	0,40	0,40	0,40
61066	92282	0,019	0,022	0,022	0,17	0,40	0,40	0,40	0,40	0,40	0,40	0,40	0,40	0,40
61066	92284	0,019	0,022	0,022	0,17	0,40	0,40	0,40	0,40	0,40	0,40	0,40	0,40	0,40
61066	92285	0,019	0,021	0,021	0,17	0,41	0,41	0,41	0,41	0,41	0,41	0,41	0,41	0,41
61066	92287	0,020	0,023	0,023	0,18	0,41	0,41	0,41	0,41	0,41	0,41	0,41	0,41	0,41
61066	92289	0,019	0,021	0,021	0,17	0,41	0,41	0,41	0,41	0,41	0,41	0,41	0,41	0,41
61068	92280	0,021	0,022	0,022	0,17	0,41	0,41	0,41	0,41	0,41	0,41	0,41	0,41	0,41

Z01/Z02 We hereby certify, that the above mentioned materials have been delivered in accordance with the terms of order.

CHECKED

Technischer Überwachungs-Verein Saarland e.V.

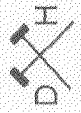
Druckgeräteherstellung

AG der Dillinger Hüttenwerke
Postfach 1580, D-66748 Dillingen/Saar
Inspection department

AHB

B. MUELLER
Der Werksachverständige

Inspector's stamp Date 22.11.04 ML I



Erläuterungen siehe Rückseite/Explications voir au verso/See reverse for explanations (www.dillinger.biz/certificate)

A02	ABNAHMEPRÜFPROTOKOLL	3.2	DIN EN 10204	-	EN 10204	-	DIN 50049	A09	Advice of dispatch No./ Date of dispatch	160519-19.11.04	A03	Manufacturer's order/ Certificate No	287702-001	Sheet	13/....
	PROCES-VERBAL DE RECEPTION	3.2	NF EN 10204								B01	Product	SHOT BLASTED PLATES, PAINT		
	INSPECTION REPORT	3.2	BS EN 10204	-	ISO 10474								ED		
A05	Established inspecting body	A06	Purchaser	MERCON STEEL, GORINCH	A07.1	No.	8000-00/1501								
	TUVV		Final receiver	MERCON STEEL, GORINCH	A07.2	No.									
B02/	Steel grade	TYPE-I-S460G2+M+Z35													
B03	Specifications	EN-10225:01													
		BR-2GZZZZ-MT-SPE-0004:REV.D1													
		EN-10164:93													

C94 Product analysis Carbon equivalent / Alloying restrictions

B08	B07	Test No.	C01	FO-02=	FO-31=	FO-51=	FO-52=	FO-55=
61068	92280	K4 FO-A1=	9,72	0,41	0,17	0,019	0,021	0,90
61072	92256	K4 FO-A1=	9,73	0,40	0,17	0,021	0,023	0,92
61072	92257	K4 FO-A1=	10,29	0,41	0,18	0,019	0,021	0,92
61125	88603	K4 FO-A1=	9,17	0,41	0,18	0,020	0,021	0,70
61125	88615	K4 FO-A1=	7,86	0,41	0,19	0,020	0,021	0,69
61126	95995	K4 FO-A1=	8,65	0,40	0,18	0,022	0,023	0,70
61126	95996	K4 FO-A1=	9,43	0,40	0,18	0,020	0,023	0,71
61126	95999	K4 FO-A1=	10,65	0,40	0,18	0,021	0,024	0,71
61126	96000	K4 FO-A1=	7,56	0,39	0,18	0,022	0,024	0,70
61126	96002	K4 FO-A1=	8,38	0,40	0,18	0,021	0,024	0,71
61126	96005	K4 FO-A1=	7,07	0,40	0,18	0,020	0,022	0,70
61127	95899	K4 FO-A1=	8,57	0,40	0,18	0,020	0,022	0,69
61127	95945	K4 FO-A1=	9,25	0,40	0,18	0,021	0,023	0,70
61127	95992	K4 FO-A1=	10,31	0,41	0,19	0,020	0,022	0,71
61127	95994	K4 FO-A1=	8,95	0,40	0,18	0,020	0,022	0,69
61320	99316	K4 FO-A1=	10,54	0,38	0,18	0,019	0,021	0,52
61320	99317	K4 FO-A1=	10,27	0,38	0,18	0,019	0,021	0,51

C94 Carbon equivalent formula / Alloying restrictions

- FO-A1 = AT/N
- FO-02 = C+(MN/6)+(CR+MO+V)/5+(NI+CU)/15
- FO-31 = C+SI/30+(MN+CR+CU)/20+MO/15+V/10+NI/60+5B
- FO-51 = V +NB
- FO-52 = V +NB+TI
- FO-55 = CU+MO+NI+CR

A04		<p>Der Werkssachverständige</p> <p>B. MUELLER</p>	<p>Inspector's stamp</p> <p>AHB</p>	<p>Date</p> <p>22.11.04</p>	<p>ML</p> <p>1</p>
A01	<p>AG der Dillinger Hüttenwerke</p> <p>Postfach 1580, D-66748 Dillingen/Saar</p> <p>Inspection department</p>				
<p>Z01/Z02 We hereby certify, that the above mentioned materials have been delivered in accordance with the terms of order</p> <p>CHECKED</p> <p>Technischer Überwachungs-Verein Saarland e.V.</p> <p>Druckgeräte Herstellung</p>					

Erläuterungen siehe Rückseite/Explications voir au verso/See reverse for explanations (www.dillinger.biz/certificate)

A02	ABNAHMEPRUEFFPROTOKOLL	3.2	DIN EN 10204	-	EN 10204	-	DIN 50049	A09	Advice of dispatch No./ Date of dispatch	160519-19.11.04	A08/ Manufacturer's order/ A03 Certificate No	287702-001	Sheet
	PROCES-VERBAL DE RECEPTION	3.2	NF EN 10204								B01 Product	14	
	INSPECTION REPORT	3.2	BS EN 10204	-	ISO 10474						SHOT BLASTED PLATES, PAINT ED		
A05	Established inspecting body TUVV	A06 Purchaser	MERCON STEEL, GORINCH	A07.1 No	8000-00/1501								
		Final receiver	MERCON STEEL, GORINCH	A07.2 No									

B02/ Steel grade TYPE-I-S460G2+M+Z35

B03 Specifications EN-10225:01

BR-2GZZZ-MT-SPE-0004:REV.D1

EN-10164:93

D01 Checking of marking, surface, shape and dimensions

ITEM NO.: 02.05-12

RESULT OF MARKING, SURFACE, SHAPE AND DIMENSIONS: NO REMARKS

SURFACE AS PER EN-10225

THICKNESS AS PER EN-10029-B:91

LENGTH AND WIDTH AS PER EN-10029:91

FLATNESS AS PER EN-10029-T4L:91

ITEM NO.: 13-14

RESULT OF MARKING, SURFACE, SHAPE AND DIMENSIONS: NO REMARKS

SURFACE AS PER EN-10225

THICKNESS AS PER EN-10029-B:91

LENGTH AND WIDTH AS PER EN-10029:91

FLATNESS AS PER EN-10029-T5L:91

D02 Ultrasonic testing

ITEM NO.: 02.05-14

UT-SPECIFICATION : EN-10160 CLASS S1 AND E1

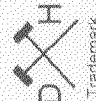
SCANNING PLAN BODY : LONGITUDINALLY SCAN LINES SPACING 100 MM

EDGES : 100 MM

PERSONNEL QUALIFICATION : LEVEL 2 IN ACCORDANCE TO EN 473

THE TEST RESULTS MEET THE REQUIREMENTS OF THE ORDER.

A04



A01 Z02 We hereby certify that the above mentioned materials have been delivered in accordance with the terms of order

CHECKED

Technischer Überwachungs-Verein
Saarland e.V.
Druckguss-Handwerk
Inspector

B. MUELLER

Der Werksachverständige

Inspector's stamp



AG der Dillinger Hüttenwerke
Postfach 1580, D-66748 Dillingen/Saar
Inspection department

Date 22.11.04

ML

1



27094

Erläuterungen siehe Rückseite/Explications voir au verso/See reverse for explanations (www.dillinger.de/certificate)

A02	INSPECTION CERTIFICATE 3.2 AS PER EN 10204:2004 INSPECTION REPORT 3.2 AS PER EN 10204:1991+A1:1995 + AS PER ISO 10474:1991	A10	Advice of dispatch No./ Date of dispatch 276253-17.10.07	A08/	Manufacturer's order/ Certificate No. 325651-001	Sheet 1/...
A05	Established inspecting body LR ANCOFERWALDRAM, OOSTE A07.1 No. 3020947 Final receiver ANCOFERWALDRAM, OOSTE A07.2 No.	B01	Product HOT ROLLED PLATES			
B02/	Steel design. DILLIMAX690T					
B03	Any suppl. requirements DILLING-E04:03					

B01-B99 Description of the product

B14	B08	B09	B10	B11	B12	B04	B07.2	B07.1	A09
Item No.	Number of pieces	Thickness	Width	Length	Theoretical mass	Product delivery condition	Heat No.	Rolled plate No./ Test No.	Purchaser article number
01	1	12,00	X 2055	X 12000	2367	Q+A	312005	35772-01	
01	1	12,00	X 2055	X 12000	2367	Q+A	312005	35772-02	
01	1	12,00	X 2055	X 12000	2367	Q+A	312005	35772-03	
01	1	12,00	X 2055	X 12000	2367	Q+A	312005	35772-04	
01	1	12,00	X 2055	X 12000	2367	Q+A	312005	35772-05	
01	1	12,00	X 2055	X 12000	2367	Q+A	312005	35772-06	
**	6				14202				
02	1	12,00	X 2500	X 12000	2880	Q+A	312005	35821-01	
02	1	12,00	X 2500	X 12000	2880	Q+A	312005	35821-02	
02	1	12,00	X 2500	X 12000	2880	Q+A	312005	35821-03	
**	3				8640				
03	1	15,00	X 2055	X 12000	2959	Q+A	311913	26829-01	
03	1	15,00	X 2055	X 12000	2959	Q+A	311913	26829-02	
03	1	15,00	X 2055	X 12000	2959	Q+A	311913	26829-03	
03	1	15,00	X 2055	X 12000	2959	Q+A	311913	26829-04	
**	4				11836				
04	1	15,00	X 2500	X 12000	3600	Q+A	311911	26839-02	
04	1	15,00	X 2500	X 12000	3600	Q+A	311911	26839-03	
**	2				7200				
05	1	20,00	X 2055	X 12000	3946	Q+A	311913	26826-01	
05	1	20,00	X 2055	X 12000	3946	Q+A	311913	26826-02	
05	1	20,00	X 2055	X 12000	3946	Q+A	311913	26826-03	
**	3				11838				

A04 Z01/Z02/Z03 We hereby certify, that the above mentioned materials have been delivered in accordance with the terms of order.

H.-J. Cyrancki
Stuttgart Office
Lloyd's Register EMEA

23. Okt. 2007
Inspector

STU
710282

B. MUELLER
Test House Manager

AHB

AG der Dillinger Hüttenwerke
Postfach 1580, D-66748 Dillingen/Saar
Inspection department

Inspector's stamp Date 17.10.07 EDI HK 1

A01



Erläuterungen siehe Rückseite/Explications voir au verso/See reverse for explanations (www.dillinger.de/certificate)

A02 INSPECTION CERTIFICATE 3.2 AS PER EN 10204:2004
 INSPECTION REPORT 3.2 AS PER EN 10204:1991+A1:1995 + AS PER ISO 10474:1991

A10 Advice of dispatch No./ Date of dispatch
 276253-17.10.07

A08/ Manufacturer's order/ A03 Certificate No.
 325651-001

Sheet
 2/...

A05 Established inspecting body LR ANCOFERWALDRAM, OOSTE A07.1 No. 3020947
 Final receiver ANCOFERWALDRAM, OOSTE A07.2 No.

B02/ Steel design. DILLIMAX 690T
 B03 Any suppl. requirements DILLING-E04:03

B01-B99 Description of the product

B14 Item No.	B08 Number of pieces	B09 Thickness	B10 Width	B11 Length	B12 Theoretical mass	B04 Product delivery condition	B07.2 Heat No.	B07.1 Rolled plate No./ Test No.	A09 Purchaser article number
06	1	20,00	X 2500	X 12000	4800	Q+A	311915	26787-02	
06	1	20,00	X 2500	X 12000	4800	Q+A	311915	26787-03	
**	2				9600				
07	1	25,00	X 2055	X 12000	4932	Q+A	311913	26798-02	
07	1	25,00	X 2055	X 12000	4932	Q+A	311913	26798-03	
**	2				9864				
08	1	25,00	X 2500	X 12000	6000	Q+A	311915	26764-02	
09	1	25,00	X 3000	X 12000	7200	Q+A	311915	26797-01	
09	1	25,00	X 3000	X 12000	7200	Q+A	311915	26797-02	
**	2				14400				
10	1	30,00	X 2055	X 12000	5918	Q+A	312416	18514-01	
10	1	30,00	X 2055	X 12000	5918	Q+A	312416	18514-02	
**	2				11836				
11	1	30,00	X 2500	X 12000	7200	Q+A	312416	12124-02	
11	1	30,00	X 2500	X 12000	7200	Q+A	312416	12124-03	
**	2				14400				
19	1	45,00	X 2055	X 12000	8878	Q+A	312700	41320-01	
19	1	45,00	X 2055	X 12000	8878	Q+A	312700	41320-02	
**	2				17756				
20	1	45,00	X 2500	X 12000	10800	Q+A	312700	40991-01	
21	1	50,00	X 2055	X 12000	9864	Q+A	312700	41321-01	
21	1	50,00	X 2055	X 12000	9864	Q+A	312700	41321-02	
**	2				19728				

A04

2017/202/203 We hereby certify, that the above mentioned materials have been delivered in accordance with the terms of order.

H.-J. Cyranski
 Stuttgart Office
 Lloyd's Register EMEA Inspector

[Signature]

B. MUELLER
 Test House Manager

AHB

AG der Dillinger Hüttenwerke
 Postfach 1580, D-66748 Dillingen/Saar
 Inspection department

Inspector's stamp Date 17.10.07 EDI HK 1



Erläuterungen siehe Rückseite/Explications voir au verso/See reverse for explanations (www.dillinger.de/certificate)

A02 INSPECTION CERTIFICATE 3.2 AS PER EN 10204:2004 INSPECTION REPORT 3.2 AS PER EN 10204:1991+A1:1995 + AS PER ISO 10474:1991		A10 Advice of dispatch No./ Date of dispatch 276253-17.10.07	A08/ Manufacturer's order/ A03 Certificate No. 325651-001	Sheet 3/...					
A05 Established inspecting body LR ANCOFERWALDRAM, OOSTE A07.1 No. 3020947 Final receiver ANCOFERWALDRAM, OOSTE A07.2 No.		B01 Product HOT ROLLED PLATES							
B02/ Steel design. DILLIMAX690T									
B03 Any suppl. requirements DILLING-E04:03									
B01-B99 Description of the product									
B14 Item No.	B08 Number of pieces	B09 Thickness	B10 Width	B11 Length	B12 Theoretical mass	B04 Product delivery condition	B07.2 Heat No.	B07.1 Rolled plate No./ Test No.	A09 Purchaser article number
24	1	60,00	x 2500	x 12000	14400	Q+A	312700	40898-01	
***	35				182500				
B06 Marking of the product									
ITEM NO.: 01-11,13,19-24 STEEL DESIGNATION DILLIMAX690T HEAT NO. / TRADEMARK / ROLLED PLATE NO. - TEST NO. / INSPECTOR'S STAMP									
C10-C29 Tensile test									
B14 Item No.	B07.2 Heat No.	B05 Reference	(heat) treatment	C01 C02/ C03 C01 Temp. G.R.C.	C10 C11 MPA REH	C12 C13 RM	A % L0=50	C14-C15	
02	312005	35799 *		K4 Q RT	750	794	19,0		
03	311913	26829		K4 Q RT	846	848	18,1		
04	311911	26839		K4 Q RT	805	829	18,2		
05	311913	26826		K4 Q RT	788	831	18,4		
06	311915	26787		K4 Q RT	807	851	16,8		
07	311913	26798		K4 Q RT	798	842	17,1		
08	311915	26764		K4 Q RT	792	843	17,9		
10	312416	18514		K4 Q RT	837	861	16,1		
13	312416	18603 *		K4 Q RT	803	848	16,4		
20	312700	40991		K4 QV RT	827	872	17,0		
22	312700	40855 *		K4 QV RT		844	19,4		
23	312700	40895 *		K4 QV RT		862	17,2		

A04 Z01Z02/Z03 We hereby certify, that the above mentioned materials have been delivered in accordance with the terms of order.

H.-J. Cyrancki
Stuttgart Office
Lloyd's Register EMEA

D&H
Manufacturer's mark

[Signature]
Inspector

[Signature]
B. MUELLER
Test House Manager



AG der Dillinger Hüttenwerke
Postfach 1580, D-66748 Dillingen/Saar
Inspection department

Inspector's stamp Date 17.10.07 EDI HK 1

A01



Erläuterungen siehe Rückseite/Explications voir au verso/See reverse for explanations (www.dillinger.de/certificate)

A02 INSPECTION CERTIFICATE 3.2 AS PER EN 10204:2004
 INSPECTION REPORT 3.2 AS PER EN 10204:1991+A1:1995 + AS PER ISO 10474:1991

A10 Advice of dispatch No./ Date of dispatch
 276253-17.10.07

A08/ Manufacturer's order/ Certificate No.
 325651-001

A05 Established inspecting body A06 Purchaser ANCOFERWALDRAM, OOSTE A07.1 No. 3020947
 LR Final receiver ANCOFERWALDRAM, OOSTE A07.2 No.

B02/ Steel design. DILLIMAX690T
 B03 Any suppl. requirements DILLING-E04:03

A03 Sheet
 4/...

B01 Product
 HOT ROLLED PLATES

C10-C29 Tensile test

B14 Item No.	B07.2 Heat No.	B05 Rol.plate/ Test No.	Reference (heat) treatment	C01 C02/ C03 Temp. G.R.C	C10 C11 MPA REH	C12 C13 RM	C14-C15 A % L0=5D
24	312700	41139 *		K4 QV RT	762	835	17,0

C40-C49 Impact test

B14 Item No.	B07.2 Heat No.	B07.1 Rol.plate/ Test No.	B05 Reference (heat) treatment	C01 C02/ C03 Temp. G.R.C	C40 C41 Type of test piece	C44 Testing method	C46 Energy Joule	C45 Individual values AV=J	C43 Mean value
02	312005	35799 *		K4 QO -40	CHP-V		600	AV 176	153
03	311913	26829		K4 QO -40	CHP-V		600	AV 194	194
04	311911	26839		K4 QO -40	CHP-V		600	AV 177	162
05	311913	26826		K4 QO -40	CHP-V		600	AV 178	182
06	311915	26787		K4 QO -40	CHP-V		600	AV 181	194
07	311913	26798		K4 QO -40	CHP-V		600	AV 154	177
08	311915	26764		K4 QO -40	CHP-V		600	AV 109	105
10	312416	18514		K4 QO -40	CHP-V		600	AV 132	103
13	312416	18603 *		K4 QO -40	CHP-V		600	AV 91	83
20	312700	40991		K4 QV -40	CHP-V		600	AV 207	213
22	312700	40855 *		K4 QV -40	CHP-V		600	AV 208	216
23	312700	40895 *		K4 QV -40	CHP-V		600	AV 97	129
24	312700	41139 *		K4 QV -40	CHP-V		600	AV 50	94

A04 Z01/Z02/Z03 We hereby certify, that the above mentioned materials have been delivered in accordance with the terms of order.

H.-J. Cyrancki
 Stuttgart Office
 Lloyd's Register EMEA

Lloyd's Register

B. MUELLER
 Test House Manager

AG der Dillinger Hüttenwerke
 Postfach 1580, D-66748 Dillingen/Saar
 Inspection department

Inspector's stamp
 Date 17.10.07 EDI

Inspector
 HK 1



Erläuterungen siehe Rückseite/Explications voir au verso/See reverse for explanations (www.dillinger.de/certificate)

A02	INSPECTION CERTIFICATE 3.2 AS PER EN 10204:2004	A10	Advice of dispatch No./ Date of dispatch	A08/ Manufacturer's order/ A03 Certificate No.	Sheet
	INSPECTION REPORT 3.2 AS PER EN 10204:1991+Al:1995 + AS PER ISO 10474:1991		276253-17.10.07	325651-001	5/...
A05	Established inspecting body	A06	Purchaser	B01	Product
LR			ANCOFERWALDRAM, OOSTE		HOT ROLLED PLATES
			Final receiver		
			ANCOFERWALDRAM, OOSTE		
B02/	Steel design. DILLIMAX690T	A07.1	No. 3020947		
B03	Any suppl. requirements DILLING-E04:03	A07.2	No.		

C70-C99 Chemical composition % - Heat analysis

	C70	C	SI	MN	P	S	N	CU	MO	NI	CR	V	NB	TI	B
B07.2 Heat															
311911	Y	0,165	0,275	1,29	0,010	0,0006	0,0039	0,014	0,111	0,045	0,027	0,000	0,024	0,003	0,0019
311913	Y	0,170	0,289	1,29	0,010	0,0008	0,0027	0,023	0,101	0,024	0,024	0,000	0,024	0,004	0,0019
311915	Y	0,160	0,282	1,28	0,011	0,0007	0,0042	0,024	0,099	0,032	0,025	0,000	0,024	0,003	0,0019
312005	Y	0,134	0,265	1,43	0,011	0,0011	0,0035	0,016	0,007	0,023	0,301	0,001	0,020	0,002	0,0017
312416	Y	0,168	0,275	1,29	0,011	0,0005	0,0031	0,017	0,207	0,032	0,304	0,000	0,029	0,002	0,0018
312700	Y	0,164	0,269	1,29	0,009	0,0011	0,0045	0,018	0,247	0,116	0,304	0,001	0,027	0,002	0,0019

C70

B07.2 Heat

	ZR	AL-T
311911	0,0002	0,079
311913	0,0002	0,077
311915	0,0002	0,080
312005	0,0002	0,054
312416	0,0002	0,081
312700	0,0002	0,077

C94 Heat analysis Carbon equivalent / Alloying restrictions

	FO-02=	FO-51=
B07.2 Heat		
311911	0,41	0,02
311913	0,41	0,02
311915	0,40	0,02
312005	0,44	0,02
312416	0,49	0,03
312700	0,50	0,03

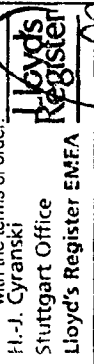
B07.2 Heat

A04



Manufacturer's mark

Z01/Z02/Z03 We hereby certify, that the above mentioned materials have been delivered in accordance with the terms of order.



H.-J. Gyrancki
Stuttgart Office
Lloyd's Register EMFA

B. Mueller

B. MUELLER
Test House Manager



AG der Dillinger Hüttenwerke
Postfach 1580, D-66748 Dillingen/Saar
Inspection department

Inspector's stamp

Date 17.10.07 EDI

HK 1

A01



Erläuterungen siehe Rückseite/Explications voir au verso/See reverse for explanations (www.dillinger.de/certificate)

<p>A02 INSPECTION CERTIFICATE 3.2 AS PER EN 10204:2004 INSPECTION REPORT 3.2 AS PER EN 10204:1991+A1:1995 + AS PER ISO 10474:1991</p>	<p>A10 Advice of dispatch No./ Date of dispatch 276253-17.10.07</p>	<p>A08/ Manufacturer's order/ A03 Certificate No. 325651-001</p> <p>Sheet 6</p>
<p>A05 Established inspecting body LR</p>	<p>A06 Purchaser ANCOFERWALDRAM, OOSTE A07.1 No. 3020947</p> <p>Final receiver ANCOFERWALDRAM, OOSTE A07.2 No.</p>	<p>B01 Product HOT ROLLED PLATES</p>
<p>B02/ Steel design. DILLIMAX690T</p> <p>B03 Any suppl. requirements DILLING-E04:03</p>		
<p>C94 Carbon equivalent formula / Alloying restrictions</p> <p>FO-02 = C+ (MN/6) + (CR+MO+V) / 5+ (NI+CU) / 15</p> <p>FO-51 = V +NB</p>		
<p>D01 Marking and identification, surface appearance, shape and dimensional properties</p> <p>ITEM NO.: 01-11,13,19-24</p> <p>RESULT OF MARKING, SURFACE, SHAPE AND DIMENSIONS: NO REMARKS</p> <p>SURFACE AS PER EN-10163-A2</p> <p>THICKNESS AS PER EN-10029-A</p> <p>LENGTH AND WIDTH AS PER EN-10029</p> <p>FLATNESS AS PER EN-10029-T4H</p>		
<p>Z01-Z99 Confirmations</p> <p>ITEM NO.: 01-11,13,19-24</p> <p>TERMS AND CONDITIONS OF A. M. SOCIETY (A05) APPLY: LLOYDS REGISTER EMEA</p>		
<p>A04</p> 	<p>Z01/Z02/Z03 We hereby certify, that the above mentioned materials have been delivered in accordance with the terms of order.</p> <p>H.-J. Cyranski Stuttgart Office Lloyd's Register EMEA</p> 	<p>AG der Dillinger Hüttenwerke Postfach 1580, D-66748 Dillingen/Saar Inspection department</p> <p>AHB</p> <p>Inspector's stamp Date 17.10.07 EDI</p> <p>Test House Manager B. MUELLER</p> 



Erläuterungen siehe Rückseite/Explications voir au verso/See reverse for explanations (www.dillinger.de/certificate)

A02	ABNAHMEPRUEFZEUGNIS 3.1 NACH EN 10204:2004	A09	Versandanzeige-Nr. und Datum	A08/ Werksauftrags-/ A03	Beschreibungs-Nr.	Blatt
	ABNAHMEPRUEFZEUGNIS 3.1.B NACH EN 10204:1991+A1:1995 UND NACH ISO 10474:1991		220135-17.07.06		309782-007	1/...
A05	Aussteller Abnahmeorgan	A06	Besteller	B01	Erzeugnis	
	DH		A07.1 Nr.		GROBBLECHE	
	Empfänger		A07.2 Nr.			

B02/	Stahlsorte	DILLIMAX890T				
B03	Lieferbedingungen	DILLING-D04:03				

B01-B99 Beschreibung des Erzeugnisses									
B09 Pos. Nr.	B10 Stückzahl	B11 Dicke	B12 Breite	B13 Länge	B14 Gewicht errechnet KG	B04 Lieferzustand	B08 Schmelzen-Nr.	B07 Walztafel-/ Proben-Nr.	B16 Kundenkennzeichen
14	1	25,00	x 2000	x 12000	4710	Q+A	283468	95607-02	ANSOFER WALDFAM STEELPLATES B.V. The Schürdenweg Tel. 0162-491547 Fax 0162-423733 e-mail: theo.schoonhoven@dws.dillinger.biz
14	1	25,00	x 2000	x 12000	4710	Q+A	283468	95607-03	
**	2				9420				
***	2				9420	Verwogenes	Gewicht: 9500 KG		

B06 Kennzeichnung

POSITION-NR.: 06,14

STAHLSORTE DILLIMAX965T DILLIMAX890T

SCHMELZEN-NR. / HERSTELLERZEICHEN / WALZTADEL-NR. - PROBEN-NR. / ABNAHMEPRUEFSTEMPEL

C10-C29 Zugversuch							
B09 Pos. Nr.	B07 Schmelzen- Walztafel-/ Proben-Nr.	B05 Probenbehandlung	C01 C02/ C01 Temp. GRC	C10 C11 MPA RP02	C12 RM	C13 A %	C14-C15 L0=5D
06	283468	95603 *	K4 Q	RT 1000	1065	16,1	
14	283468	95607	K4 Q	RT 985	1051	14,3	

C40-C49 Kerbschlagbiegeversuch									
B09 Pos. Nr.	B08 Schmelzen- Nr.	B07 Walztafel-/ Proben-Nr.	B05 Probenbehandlung	C01 C02/ C01 Temp. GRC	C40 Probenform	C44 Prüfverfahren	C46 Energie Joule	C45 Einzelwerte AV=J	C43 Mittelwert
06	283468	95603 *		K4 Q0 -40	CHP-V		600	AV 37	34 37
14	283468	95607		K4 Q0 -40	CHP-V		600	AV 39	30 38

A04

Z01/Z02 Es wird bestätigt, dass die Lieferung den Vereinbarungen bei der Bestellung entspricht.

QM-System: Zertifiziert nach ISO 9001

Herstellerzeichen

B. MUELLER
Der Abnahmebeauftragte

AG der Dillinger Hüttenwerke
Postfach 1580, D-66748 Dillingen/Saar
Abnahme

Abnahmeprüfstempel Datum 17.07.06

RD 1



Erläuterungen siehe Rückseite/Explications voir au verso/See reverse for explanations (www.dillinger.de/certificate)

A02 ABNAHMEPRÜFZEUGNIS 3.1 NACH EN 10204:2004 ABNAHMEPRÜFZEUGNIS 3.1.B NACH EN 10204:1991+A1:1995 UND NACH ISO 10474:1991 MATERIAL TEST REPORT (MTR)	A09 Versandanzeige-Nr. und Datum 220135-17.07.06	A08/ Werksauftrags-/ A03 Bescheinigungs-Nr. 309782-007	Blatt 2
A05 Aussteller Abnahmeorgan DH A06 Besteller Empfänger	A07.1 Nr. 206 2037217 A07.2 Nr.	B01 Erzeugnis GROBBLECHE	

B02/ Stahlsorte DILLIMAX890T
B03 Lieferbedingungen DILLING-D04:03

C70-C99 Chemische Zusammensetzung % - Schmelzenanalyse

B08 Schmelze	C70	C	SI	MN	P	S	AL	CU	MO	NI	CR	V	NB	B
283468	Y	0,168	0,281	0,88	0,012	0,0008	0,074	0,024	0,511	0,980	0,494	0,041	0,011	0,0022

C94 Schmelzenanalyse C-Äquivalent / Legierungsbegrenzung

B08 Schmelze	FO-02=	0,59	FO-51=	0,05
283468				

C94 Formel C-Äquivalent / Legierungsbegrenzung

FO-02 = C + (MN/6) + (CR+MO+V) / 5 + (NI+CU) / 15
FO-51 = V + NB

D01 Prüfung von Kennzeichnung, Oberfläche, Form und Maßen

POSITION-NR. : 06,14
 ERGEBNIS DER PRUEFUNG VON KENNZEICHNUNG, OBERFLAECHE, FORM UND MASSEN : OHNE FEHLERBEFUND
 OBERFLAECHE NACH DIN-EN10163-A2
 DICKE NACH DIN-EN10029-A:91
 LAENGE UND BREITE NACH DIN-EN10029:91
 EBENHEIT NACH DIN-EN10029-T4H:91

AGROFOR VERWERTUNGSTECHNIK GMBH
 1120 Subdorfsweg
 Tel 0162 - 401647
 Fax 0162 - 420733
 contact@agrofor.com oder wart@aws.dillinger.de

A04	Z01/Z02 Es wird bestätigt, dass die Lieferung den Vereinbarungen bei der Bestellung entspricht.	A01
	QM-System: Zertifiziert nach ISO 9001	AG der Dillinger Hüttenwerke Postfach 1580, D-66748 Dillingen/Saar Abnahme
Der Herstellerzeichen		Abnahmeprüfstempel Datum 17.07.06
	B. MUELLER Der Abnahmebeauftragte	RD 1



DILLINGER HÜTTE

Erläuterungen siehe Rückseite/Explications voir au verso/See reverse for explanations

A02 ABNAHMEPRUEFZEUGNIS CERTIFICAT DE RECEPTION INSPECTION CERTIFICATE	3.1.B 3.1.B 3.1.B	DIN EN 10204 - NF EN 10204	EN 10204	-	DIN 50049	A09 Versandanzeige-Nr. und Datum	13484-01.09.99	A08/Werkauftrags-/ A03 Bescheinigungs-Nr.	208290-001	Blatt	1/...
--	-------------------------	-------------------------------	----------	---	-----------	-------------------------------------	----------------	--	------------	-------	-------

A05 Aussteller DH	Abnahmeorgan Empfänger	A06 Besteller A07.1 Nr.	A06 Besteller A07.2 Nr.	B01 Erzeugnis GROBBLECHE
----------------------	---------------------------	----------------------------	----------------------------	-----------------------------

B02/ Stahlsorte B03 Lieferbe- dingungen	DILLIMAX1100 DH-D55-A/99
---	-----------------------------

B01-B99 BESCHREIBUNG DES ERZEUGNISSES											
B09 Pos. Nr.	B10 Stckz	B11 Dicke	B12 x Breite	B13 x Laenge	B14 Gewicht errechnet	B04 Lieferzustand	B08 Schmelze Nr.	B07 Walztafel/ Proben-Nr.	B16 Kundenkennzeichen		
		MM	MM	MM	KG						
02	4	12,00	x 2000	x 12000	9044	Q +A	81618	47437			
03	3	15,00	x 2500	x 12000	10599	Q +A	81618	47348			
04	2	20,00	x 3000	x 12000	11304	Q +A	81618	47347			
***	9				30947	Verwogenes Gewicht:		31527 KG			

B06 KENNZEICHNUNG

POSITION-NR.: 01-04
 STAHLSORTE DILLIMAX 1100
 SCHMELZEN-NR. / HERSTELLERZEICHEN / WALZTAPEL-NR. / PROBEN-NR. / ABNAHMEPRUEFSTEMPEL

C10-C29 ZUGVERSUCH											
B09 Pos. Nr.	B08 Schmelze	B07 Walztafel/ Proben-Nr.	B05 Probenbehandlung	C01 C02/ C03 C01	C02/ C03 Temp. RE	C12 RM	C13 AZ	C14 LO=	C15		
				K Q				5D			
01	81618	27054	*	K Q		1385					
02	81618	47437		K Q		1374		11,4			
04	81618	47347		K Q		1373		11,0			

C40-C49 KERBSCHLAGBIEGEVERSUCH											
B09 Pos. Nr.	B08 Schmelze	B07 Walztafel/ Proben-Nr.	B05 Probenbehandlung	C01 C02/ C03 C01	C02/ C03 Temp. GR.C	C40 Breite	C41 Probenform	C45/C42 Einzelwerte	C43 Mittelwert		
				K Q		CHP-V	AV=J	AV			
01	81618	27054	*	K Q	-40	5,0	CHP-V	AV 23	21	24	23
02	81618	47437		K Q	-40		CHP-V	AV 29	29	29	29
04	81618	47347		K Q	-40		CHP-V	AV 31	28	27	29

A04 Z01/Z02 Es wird bestätigt, dass die Lieferung den Vereinbarungen bei der Bestellung entspricht.

OM-System: Zertifiziert nach ISO 9001 seit 14. März 1990
 AG der Dillinger Hüttenwerke
 Postfach 1580, D-66748 Dillingen/Saar
 Abnahme



Herstellerzeichen
 B. MUELLER
 Der Werkssachverständige - Abnahmepfifstempel Datum 02.09.99
 RD 1



DILLINGER HÜTTE

Erläuterungen siehe Rückseite/Explications voir au verso/See reverse for explanations

A02 ABNAHMEPRUEFZEUGNIS CERTIFICAT DE RECEPTION INSPECTION CERTIFICATE		3.1.B DIN EN 10204 - EN 10204 - DIN 50049 3.1.B NF EN 10204 3.1.B BS EN 10204 - ISO 10474	MILL. TEST REPORT	A09 Versandanzeige-Nr. und Datum 13484-01.09.99	A08/Werksauftrags-/ A03 Bescheinigungs-Nr. 208290-001	Blatt 2
--	--	---	-------------------	---	---	------------

A05 Aussteller DH	Abnahmeorgan / A06 Besteller Empfänger	A07.1 Nr. A07.2 Nr.	801 Erzeugnis GROBBLECHE
----------------------	---	------------------------	-----------------------------

B02/ Stahlsorte **DILLIMAX1100**
 B03 Lieferbe- **DH-D55-A/99**
 dingungen

----- C70-C99 CHEMISCHE ZUSAMMENSETZUNG Z - SCHMELZENANALYSE -----
 C70

B08 Schmelze Nr.	C	SI	MN	P	S	AL	MO	NI	CR	V	NB	B	FO-51
81618	Y	0,271	0,87	0,012	0,0004	0,061	0,46	1,95	0,47	0,02	0,013	0,0016	0,03

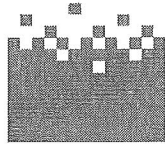
----- C94 FORMEL C-AEQUIVALENT / LEGIERUNGSBEGRENZUNG -----
 FO-51 = V +NB

----- D01 PRUEFUNG VON KENNZEICHNUNG, OBERFLAECHE, FORM UND MASSEN -----
 POSITION-NR.: 01-04

ERGEBNIS DER PRUEFUNG VON KENNZEICHNUNG, OBERFLAECHE, FORM UND MASSEN: OHNE FEHLERBEFUND
 OBERFLAECHE NACH DIN-EN10163-A2
 DICKE NACH DIN-EN10029-A/91
 LAENGE UND BREITE NACH DIN-EN10029/91
 EBENHEIT NACH DIN-EN10029-T4H/91

AG der Dillinger Hüttenwerke
 1580 Dillingen/Saar
 Tel. 063 426733
 Fax 063 426733
 e-mail: treibschneidwerk@aws.dillingen.de

A04 	Z01/Z02 Es wird bestätigt, daß die Lieferung den Vereinbarungen bei der Bestellung entspricht. QM-System: Zertifiziert nach ISO 9001 seit 14. März 1990	AG der Dillinger Hüttenwerke Postfach 1580, D-66748 Dillingen/Saar Abnahme AHB	Der Werksachverständige B. MUELLER	Abnahmeprüfstempel Datum 02.09.99	RD 1
---------	---	---	---------------------------------------	--------------------------------------	------



Friedrich Wilhelms-Hütte Stahlguss GmbH
Postfach. 45466 Mülheim an der Ruhr

Delft University of Technology
Att: Richard Pijpers
PhD researcher
P.O. Box 5049
2600 GA Delft
Netherlands

Mülheim an der Ruhr, den 23.07.08

Inspection certificate 3.1

according to EN 10204

Item	Piece	Description of Casting	Drawing-No.	Pattern-No	Customer-No.
010	3	Test plates for welding and fatigue strength test 1000x500x25			

Material:	G20Mn5	Customers order No.:	Del.-No.:
Order-No.:		Date of delivery:	

Compliance with the specified quality level has tested applying the following methods:

1) External condition: (x) Magnet particle test 2) Internal condition: (x) Ultrasonic test
() Liquid penetrant test () Radiographic test

Chemical analysis

Item	Piece	Heat	Date of Casting	C %		Si %		Mn %		P %		S %		Cr %		Mo %		Ni %		V %	
				Min	Max	Min	Max	Min	Max	Min	Max	Min	Max	Min	Max	Min	Max	Min	Max	Min	Max
				010	1	S1319A	6/08-1	0,21	0,56	1,45	0,013	0,002	0,15	0,13	0,20						
010	1	S1319A	6/08-2	0,21	0,56	1,45	0,013	0,002	0,15	0,13	0,20										
010	1	S1319A	6/08-3	0,21	0,56	1,45	0,013	0,002	0,15	0,13	0,20										

Physical properties

Item	Piece	Date of Casting	Yield-/ 0,2-strength N/mm2	Tensile-strength N/mm2	Elongation %	Reduktion of area %	Shape of specimen: ISO-V				HB 2)
							Temp. -40°C	Joule	Temp. °C	Joule 1)	
010	1	6/08-1	510	622	25,6	64,0	85	116	92	98	185
010	1	6/08-2	485	599	27,0	64,0	131	90	80	100	180
010	1	6/08-3	512	611	26,6	67,5	104	111	84	100	180

- 1) Average values from 3 single values
2) Min/Max – values

Impact values at RT: 172-181 Joule ISO-V

Heat treatment: 940°C/water
+680°C/water

The requirements are fulfilled!

Friedrich-Ebert-Straße 125
45473 Mülheim an der Ruhr
Telefon: (0208) 4518
Telefax: (0208) 451-73 03


FRIEDRICH WILHELMS-HÜTTE STAHLGUSS GmbH
Inspector steel foundry



Friedrich Wilhelms-Hütte Stahlguss GmbH
Postfach. 45466 Mülheim an der Ruhr

Delft University of Technology
Att: Richard Pijpers
PhD researcher
P.O. Box 5049
2600 GA Delft
Netherlands

Mülheim an der Ruhr, den 27.10.08

Inspection certificate 3.1

according to EN 10204

Item	Piece	Description of Casting	Drawing-No.	Pattern-No	Customer-No.
010	3	Test plates for welding and fatigue strength test 1000x500x35			

Material:	G22NiMoCr5-6	Customers order No.:	Del.-No.:
Order-No.:		Date of delivery:	

Compliance with the specified quality level has tested applying the following methods:

1) External condition: (x) Magnet particle test 2) Internal condition: (x) Ultrasonic test
() Liquid penetrant test () Radiographic test

Chemical analysis

Item	Piece	Heat	Date of Casting	C %	Si %	Mn %	P %	S %	Cr %	Mo %	Ni %	V %
			Min									
			Max									
010	1	S1605B	9/08-1	0,23	0,47	0,96	0,011	0,002	0,80	0,57	0,20	
010	1	S1605B	9/08-2	0,23	0,47	0,96	0,011	0,002	0,80	0,57	0,20	
010	1	S1605B	9/08-3	0,23	0,47	0,96	0,011	0,002	0,80	0,57	0,20	

Physical properties

Item	Piece	Date of Casting	Yield-/ 0,2- strength N/mm2	Tensile- strength N/mm2	Elonga- tion %	Reduktion of area %	Shape of specimen:ISO-V				HB 2)	
							Temp. -40°C	Joule 1)	Temp. °C	Joule 1)	mid	
010	1	9/08-1	1126	1185	12,6	40,7	28	35	35	33	366	
010	1	9/08-2	1113	1163	12,8	42,4	41	37	40	39	363	
010	1	9/08-3	1118	1171	12,6	42,2	34	31	31	32	363	

- 1) Average values from 3 single values
2) Min/Max – values

Impact values at RT: 86-75 Joule ISO-V

Heat treatment: 920°C/water
+545°C/water

The requirements are fulfilled!

Friedrich-Ebert-Straße 125
45473 Mülheim an der Ruhr
Telefon: (0208) 4518
Telefax: (0208) 451-73 03


FRIEDRICH WILHELMS-HÜTTE STAHLGUSS GmbH
Inspector steel foundry

Annex E: Production data sheets TIG Dressing

On the following pages the production data sheets from the TIG-dressing are displayed. Unfortunately some of the comments are in Dutch language.

1

PRODUCTION DATA SHEET for WELD TOE IMPROVEMENT by TIG DRESSING



International Institute of
Welding
Commission XIII

WELDING SPECIFICATION

Base material: Scpgo
Filler material: _____
Welding procedure No: CPg

COMPONENT

Type: _____
Identification: CPg 9

EQUIPMENT

Make and model: Newppi
Power capacity: 2500 Amp
Electrode diameter: 3,2
Gas cup diameter: 10 mm
Shielding gas: ARGON 4.6

SKETCH OR PHOTO

yes

TREATMENT DATA

Dressing position (1G, 2G) etc: 1G
Preheat temperature: 50°C
Gas flow rate: 15 L/min
Work angle, sideways: 60-90°
Work angle, weld direction: 10°
Travel speed (S): 172 mm/PM
Voltage (V): 17-18 Current (I): 250 amp
Heat input: $H = \frac{60 \times S \times I}{1000 \times V} =$ _____
(kJ/mm)

INSPECTION

Visual Photo Geometry
measurements

Equipment: Leunk

REMARKS

Voorverwarming 50°C
Voorvermen 2e laag 125°
Grondlaag 200 AMP 2x

TOE GEOMETRY MEASUREMENTS

Spacing of measurement points (mm): _____

Max. Min. Mean

Toe radius (mm): _____

Groove depth (mm): _____

Measurements report: _____

OPERATOR

Experience: a). Hours: _____ b). Length of weld treated: 15g mm

Operator's name: G. Groenenberg

Date: 28/06/11

9

PRODUCTION DATA SHEET for WELD TOE IMPROVEMENT by TIG DRESSING



International Institute of
Welding
Commission XIII

WELDING SPECIFICATION

Base material: S 46
Filler material: _____
Welding procedure No: C46

COMPONENT

Type: _____
Identification: C46

EQUIPMENT

Make and model: Uemppi
Power capacity: 2500 Amp
Electrode diameter: 3.2
Gas cup diameter: 10 mm
Shielding gas: Argon 4.6

SKETCH OR PHOTO

TREATMENT DATA

Dressing position (1G, 2G) etc: 1G
Preheat temperature: 50°C
Gas flow rate: 15 L/min
Work angle, sideways: 60° - 90° C
Work angle, weld direction: 10°
Travel speed (S): 172,5 mm/min
Voltage (V): _____ Current (I): 250 Amp
Heat input: $H = \frac{60 \times 1}{1000 \times 1} = \underline{1.5 \text{ kJ/mm}}$
(kJ/mm)

INSPECTION

Visual Photo Geometry
measurements

Equipment: lunix

REMARKS

C46 1/2 G. et steel

Root → 200 Amp.
15.2 Volt

↳ 115 mm/min

TOE GEOMETRY MEASUREMENTS

Spacing of measurement points (mm): _____

Max. Min. Mean

Toe radius (mm): _____

Groove depth (mm): _____

Measurements report: _____

OPERATOR

Experience: a). Hours: _____ b). Length of weld treated: 345 mm

Operator's name: G. Groenenberg

Date: 28/06/11

3

PRODUCTION DATA SHEET for WELD TOE IMPROVEMENT by TIG DRESSING



International Institute of
Welding
Commission XIII

WELDING SPECIFICATION

Base material: S 690 -
Filler material: _____
Welding procedure No: C69 Tig dressing

COMPONENT

Type: _____
Identification: C 69

EQUIPMENT

Make and model: Kemp
Power capacity: 2500 AMP
Electrode diameter: 2.2
Gas cup diameter: 10 mm
Shielding gas: ARGON 4.6

SKETCH OR PHOTO

TREATMENT DATA

Dressing position (1G, 2G) etc: 1G
Preheat temperature: 100°
Gas flow rate: 15 L P/m
Work angle, sideways: 60 - 90°
Work angle, weld direction: 10°
Travel speed (S): 172 mm/Pm
Voltage (V): 17-18 Current (I): 250 AMP
Heat input: $H = \frac{60 \times S \times I}{1000 \times V} =$ _____
(kJ/mm)

INSPECTION

Visual Photo Geometry
measurements

Equipment: _____

REMARKS

green legentlas
in m POREUSITÄT

TOE GEOMETRY MEASUREMENTS

Spacing of measurement points (mm): _____

Max. Min. Mean

Toe radius (mm): _____

Groove depth (mm): _____

Measurements report: _____

OPERATOR

Experience: a). Hours: _____ b). Length of weld treated: 343 mm

Operator's name: GROENENBERG

Date: 29.6.2011

4

PRODUCTION DATA SHEET for WELD TOE IMPROVEMENT by TIG DRESSING



International Institute of
Welding
Commission XIII

WELDING SPECIFICATION

Base material: S 1100
Filler material: _____
Welding procedure No: Tig dressing

COMPONENT

Type: _____
Identification: C 11

EQUIPMENT

Make and model: Kempp.
Power capacity: 250 Amp
Electrode diameter: 3.2 mm
Gas cup diameter: 10 mm
Shielding gas: ARGON 4.6

SKETCH OR PHOTO

TREATMENT DATA

Dressing position (1G, 2G) etc: 1G
Preheat temperature: 125°C
Gas flow rate: 15 L P/min
Work angle, sideways: 60-90°
Work angle, weld direction: 10°
Travel speed (S): 172
Voltage (V): 17-18 Current (I): 250 Amp
Heat input: $H = \frac{60 \times S \times I}{1000 \times V} =$ _____
(kJ/mm)

INSPECTION

Visual Photo Geometry
measurements

Equipment: _____

REMARKS

GROND LANG 200 AMP
15.2 ~~15.5~~ V
Speed 115 mm/P.min

TOE GEOMETRY MEASUREMENTS

Spacing of measurement points (mm): _____

Max. Min. Mean

Toe radius (mm): _____

Groove depth (mm): _____

Measurements report: _____

OPERATOR

Experience: a). Hours: _____ b). Length of weld treated: 332 mm

Operator's name: G. Groenenberg

Date: 29-6-2011

5A

PRODUCTION DATA SHEET

for WELD TOE IMPROVEMENT by
TIG DRESSING



International Institute of
Welding
Commission XIII

WELDING SPECIFICATION

Base material: S 890
Filler material: _____
Welding procedure No: Tig dressing

COMPONENT

Type: C89
Identification: _____

EQUIPMENT

Make and model: Kemppi
Power capacity: 250 Amp
Electrode diameter: 3.2 mm
Gas cup diameter: 10 mm
Shielding gas: Argon 4.6

SKETCH OR PHOTO

TREATMENT DATA

Dressing position (1G, 2G) etc: 1G
Preheat temperature: 125°C
Gas flow rate: 15 L P/min
Work angle, sideways: 60-90°
Work angle, weld direction: 10°
Travel speed (S): 179 mm P/min
Voltage (V): 17.2 Current (I): 250 AMP
Heat input: $H = \frac{60 \times S \times I}{1000 \times V} =$ _____
(kJ/mm)

INSPECTION

Visual Photo Geometry
measurements

Equipment: _____

REMARKS

GRONDLAG 5-1
200 AMP
15.2 VOLT

GRONDLAG 5-2
ONVOLDOENDE DIK
VOOR TIG DRESSING

TOE GEOMETRY MEASUREMENTS

Spacing of measurement points (mm): _____

Max. Min. Mean

Toe radius (mm): _____

Groove depth (mm): _____

Measurements report: _____

OPERATOR

Experience: a). Hours: _____ b). Length of weld treated: 315 mm

Operator's name: Greenenberg

Date: 29-6-2011

6

PRODUCTION DATA SHEET

for WELD TOE IMPROVEMENT by
TIG DRESSING



International Institute of
Welding
Commission XIII

WELDING SPECIFICATION

Base material: S 690
Filler material: _____
Welding procedure No: _____

COMPONENT

Type: _____
Identification: V69

EQUIPMENT

Make and model: Kemppi
Power capacity: 250 Amp
Electrode diameter: 3.2
Gas cup diameter: 10 mm
Shielding gas: ARGON 4.6

SKETCH OR PHOTO

TREATMENT DATA

Dressing position (1G, 2G) etc: 1G
Preheat temperature: 100 °C
Gas flow rate: 15 L P/min
Work angle, sideways: 60-90°
Work angle, weld direction: 10°
Travel speed (S): 172 mm P/min
Voltage (V): 17-18 Current (I): 250
Heat input: $H = \frac{60 \times S \times I}{1000 \times V} =$ _____
(kJ/mm)

INSPECTION

Visual Photo Geometry
measurements

Equipment: _____

REMARKS

Regenlas
100 °C
250 AMP
15.2 V

TOE GEOMETRY MEASUREMENTS

Spacing of measurement points (mm): _____

Max. Min. Mean

Toe radius (mm): _____

Groove depth (mm): _____

Measurements report: _____

OPERATOR

Experience: a). Hours: _____ b). Length of weld treated: 337 mm

Operator's name: Greenenborg

Date: 30-6-2011

57

PRODUCTION DATA SHEET for WELD TOE IMPROVEMENT by TIG DRESSING



International Institute of
Welding
Commission XIII

WELDING SPECIFICATION

Base material: S 460
Filler material: _____
Welding procedure No: Tig dressing

COMPONENT

Type: _____
Identification: V 46

EQUIPMENT

Make and model: Kempp. 2500 w
Power capacity: 250 Amp
Electrode diameter: 3.2 mm
Gas cup diameter: 10 mm
Shielding gas: Argon 4.6

SKETCH OR PHOTO

TREATMENT DATA

Dressing position (1G, 2G) etc: 1G
Preheat temperature: 50 °C
Gas flow rate: 15 l / min
Work angle, sideways: 60-90 °
Work angle, weld direction: 10 °
Travel speed (S): 172 mm / min
Voltage (V): 12-18 Current (I): 250 Amp
Heat input: $H = \frac{60 \times S \times I}{1000 \times V} =$ _____
(kJ/mm)

INSPECTION

Visual Photo Geometry
measurements

Equipment: _____

REMARKS

GRONDLAG
180 Amp
13-14 V
VOORWARMEN 50 °C
Note LAAG Amperage i.v.m.
geringe doorlas

TOE GEOMETRY MEASUREMENTS

Spacing of measurement points (mm): _____

Max. Min. Mean

Toe radius (mm): _____

Groove depth (mm): _____

Measurements report: _____

OPERATOR

Experience: a). Hours: _____ b). Length of weld treated: 337 mm

Operator's name: G. Groenewberg

Date: 30-6-2011

8

PRODUCTION DATA SHEET

for WELD TOE IMPROVEMENT by
TIG DRESSING



International Institute of
Welding
Commission XIII

WELDING SPECIFICATION

Base material: S 890
Filler material: _____
Welding procedure No: _____

COMPONENT

Type: _____
Identification: V 89

EQUIPMENT

Make and model: Kemppi 2500 W
Power capacity: 250 AMP
Electrode diameter: 3.2 mm
Gas cup diameter: 10 mm
Shielding gas: Argon 4.6

SKETCH OR PHOTO

TREATMENT DATA

Dressing position (1G, 2G) etc: 1G
Preheat temperature: 125 °C
Gas flow rate: 15 L / P/min
Work angle, sideways: 60-90°
Work angle, weld direction: 10°
Travel speed (S): 170 mm P/min
Voltage (V): 17-18 Current (I): 250 Amp
Heat input: $H = \frac{60 \times S \times I}{1000 \times V} =$ _____
(kJ/mm)

INSPECTION

Visual Photo Geometry
measurements

Equipment: _____

REMARKS

Grondslag (grilling)
200 Amp
15.2 Volt
Voorarm 125 °C

TOE GEOMETRY MEASUREMENTS

Spacing of measurement points (mm): _____

Max. Min. Mean

Toe radius (mm): _____

Groove depth (mm): _____

Measurements report: _____

OPERATOR

Experience: a). Hours: _____ b). Length of weld treated: 323 mm

Operator's name: G. Groenewegen

Date: 30-6-2011

9

PRODUCTION DATA SHEET for WELD TOE IMPROVEMENT by TIG DRESSING



International Institute of
Welding
Commission XIII

WELDING SPECIFICATION

Base material: S 1100
Filler material: _____
Welding procedure No: Tig dressing

COMPONENT

Type: _____
Identification: V11

EQUIPMENT

Make and model: Kemppi 2500 W
Power capacity: 250 AMP
Electrode diameter: 3.2 mm
Gas cup diameter: 10 mm
Shielding gas: Argon 4.6

SKETCH OR PHOTO

TREATMENT DATA

Dressing position (1G, 2G) etc: 1G
Preheat temperature: 125°
Gas flow rate: 15 l P/min
Work angle, sideways: 60-90°
Work angle, weld direction: 10°
Travel speed (S): 1.77 mm P/m
Voltage (V): 17-18 Current (I): 250
Heat input: $H = \frac{60 \times S \times I}{1000 \times V} =$ _____
(kJ/mm)

INSPECTION

Visual Photo Geometry
measurements

Equipment: _____

REMARKS

TOE GEOMETRY MEASUREMENTS

Spacing of measurement points (mm): _____

Max. Min. Mean

Toe radius (mm): _____

Groove depth (mm): _____

Measurements report: _____

OPERATOR

Experience: a). Hours: _____ b). Length of weld treated: 337 mm

Operator's name: G. Gruenewberg

Date: 30-6-2011

Annex F: Matlab scripts to process weld geometry data

Splitting of laser position and measured data and subtracting a plane.

```

%split A in X, Y en Z values
gr=size(A);
rijen_m=gr(1,1);
kolommen_n=gr(1,2);
Xs=A(1,:);
X=Xs(1,2:kolommen_n(1,1)); %create vector containing x-values
Ys=A(:,1);
Y=Ys(2:rijen_m(1,1),1); %create vector containing y-values
Zster=A(2:rijen_m(1,1),2:kolommen_n(1,1)); %extract Z values

%Construct a plane to level the weld cross sections at 0
x1=0; %first point to equal to zero
y1=7;
z1=1.4481;

x2=53; %second point to equal to zero
y2=7;
z2=0.1411;

x3=0; %third point to equal to zero
y3=140;
z3=0.7353;

gridsizeX=0.01; %define grid size of data
gridsizeY=7;

F=[x1 y1 1; x2 y2 1; x3 y3 1]; v=[z1; z2; z3];
abc=F\v;

VLAK=zeros(rijen_m(1,1)-1,kolommen_n(1,1)-1);
for n=1:(kolommen_n(1,1)-1)
    for m=1:(rijen_m(1,1)-1)
        xwaarde=X(1,n);
        ywaarde=Y(m,1);
        VLAK(m,n)=abc(1,1)*xwaarde+abc(2,1)*ywaarde+abc(3,1);
    end;
end;

%Substract created plane from Z values
Z=(Zster-VLAK)*-1;

%Plot Weld
surf(X,Y,Z,'LineWidth',0.1,'LineStyle','-') %create 3D plot
title('Weld geometry'), xlabel('Dimension across the weld'),
ylabel('Dimension along the weld'), axis equal;

clear Xs Ys Zster x1 y1 x2 y2 x3 y3 z1 z2 z3 xwaarde ywaarde VLAK gr m n
abc F v;

```

Determining the weld toe radius

```

%define optimisation boundaries
ondergrens=46; %lower boundary, use steps of size: [gridsizex]
bovengrens=47; %upper boundary, use steps of size: [gridsizex]
apphmid=2; %estimate of height of circle midpoint6
hoogtegrid=2.5; %height of grid in mm
breedtegrid=2.5; %width of grid in mm
gridstap=0.025; %grid spacing

%building of the grid
lgrid=breedtegrid/gridstap+1;
hgrid=hoogtegrid/gridstap+1;
hcoor=zeros(1,lgrid);
vcoor=zeros(hgrid,1);
for k=1:lgrid
    hcoor(1,k)=(bovengrens+ondergrens)/2-breedtegrid/2+(k-1)*gridstap;
end
for l=1:hgrid
    vcoor(l,1)=apphmid+hoogtegrid/2-(l-1)*gridstap;
end

%build two vectors to show the grid
vectorgridplothor=hcoor;
m=1;
while m<hgrid;
    vectorgridplothor=[vectorgridplothor hcoor];
    m=m+1;
end
vectorgridplotver=vcoor(1,1)*ones(1,lgrid);
mm=2;
while mm<hgrid+1;
    hulpvector=vcoor(mm,1)*ones(1,lgrid);
    vectorgridplotver=[vectorgridplotver hulpvector];
    mm=mm+1;
end
scatter(vectorgridplothor,vectorgridplotver,'.g')
axis equal
hold on;

%for all gridpoints, calculate distance to all data points within
%optimisation boundaries, determine average distance and deviation
Mafw=zeros(hgrid,lgrid);
Mstr=zeros(hgrid,lgrid);
vanscancol=round(ondergrens/gridsizex+1);
totscancol=round(bovengrens/gridsizex+1);
scanpointsx=X(1,vanscancol:totscancol);
scanpointsy=Z(rij,vanscancol:totscancol);
grscptx=size(scanpointsx);
afst=zeros(grscptx(1,2),1);

for q=1:hgrid
    for r=1:lgrid
        for t=1:grscptx(1,2)
            afst(t,1)=sqrt((hcoor(1,r)-scanpointsx(1,t))^2+(vcoor(q,1)-
scanpointsy(1,t))^2);
        end
    end
end

```

```

        gem=mean (afst);
        vgem=gem*ones (grscptx (1,2),1);
        afw=afst-vgem;
        Mstr (q,r)=gem;
        Mafw (q,r)=sum (abs (afw));
    end
end

%find minimum value in matrix Mr
[minpercol,rijentry]=min (Mafw);
[mintot,colentry]=min (minpercol);
entryrijcol=[rijentry (1,colentry) colentry];

%find calculated optimum radius and midpoint coordinates
ropt=Mstr (entryrijcol (1,1),entryrijcol (1,2));
afwijkingvangem=Mafw (entryrijcol (1,1),entryrijcol (1,2));
xopt=hcoor (1,entryrijcol (1,2));
yopt=vcoor (entryrijcol (1,1),1);

%draw optimum midpoint
scatter (xopt,yopt,'or');

%draw circle
for tel=1:1000
    cirkelx (tel)=ropt*cos (tel/100)+xopt;
    cirkely (tel)=ropt*sin (tel/100)+yopt;
end
plot (cirkelx, cirkely);
clear cirkelx cirkely grscptx afst afw vgem Mstr Mafw minpercol rijentry
colentry afwijkingvangem;
clear ondergrens bovengrens apphmid hoogtegrid breedtegrid gridstap lgrid
hgrid hcoor vcoor;
clear k l vectorgridplothor vectorgridplotver mintot entryrijcol
afwijkingvangem tel;

```

Determining the weld toe angle

```

%determine weld toe angle
vanmoe=44; %start of straight parent material, use steps of size
[gridsizex]
totmoe=45; %end of straight parent material, use steps of size [gridsizex]
vanlas=50; %start of straight weld material, use steps of size [gridsizex]
totlas=52; %end of straight weld material, use steps of size [gridsizex]

vanhoekmoecol=round (vanmoe/gridsizex+1);
tothoekmoecol=round (totmoe/gridsizex+1);
vanhoekklascol=round (vanlas/gridsizex+1);
tothoekklascol=round (totlas/gridsizex+1);

Xmoepoints=X (1,vanhoekmoecol:tothoekmoecol);
Zmoepoints=Z (rij,vanhoekmoecol:tothoekmoecol);
Xlaspoints=X (1,vanhoekklascol:tothoekklascol);
Zlaspoints=Z (rij,vanhoekklascol:tothoekklascol);

moe=polyfit (Xmoepoints,Zmoepoints,1);
las=polyfit (Xlaspoints,Zlaspoints,1);

%plot of both fitted lines

```

```

xmoe=vanmoe:gridsize:totmoe;
zmoe=moe(1)*xmoe+moe(2);
plot(xmoe,zmoe)
hold on;
xlas=vanlas:gridsize:totlas;
zlas=las(1)*xlas+las(2);
plot(xlas,zlas);

hoekmoe=atand(moe(1));    %angle of parent material with horizontal
hoeklas=atand(las(1));   %angle of weld material with horizontal
hoekverschil=abs(hoeklas-hoekmoe); %angle between parent material and
weld
clear vanhoekmoecol tohoekmoecol vanhoeklascol tohoeklascol Xmoepoints
Xlaspoints Zlaspoints moe las xmoe zmoe xlas zlas hoekmoe hoeklas;

```

Determining the weld height

```

%determine undercut of weld in relation to parent material
left=3.; %left location of parent material, use steps of size [gridsize]
right=50; %right location parent material, use steps of size [gridsize]
vanh=5; %start of area under investigation for weld height use steps of
size [gridsize]
toth=52; %end of area under investigation for weld height use steps of size
[gridsize]

%construct reference line
leftcol=round(left/gridsize+1);
rightcol=round(right/gridsize+1);
leftz=Z(rij,leftcol);
rightz=Z(rij,rightcol);
xline=[left right];
zline=[leftz rightz];
parent=polyfit(xline,zline,1);
plot(xline,zline);

%determine distance of weld to reference line
vanhcol=round(vanh/gridsize+1);
tothcol=round(toth/gridsize+1);
scanpointsx=X(1,vanhcol:tothcol);
scanpointsz=Z(rij,vanhcol:tothcol);
grscptx=size(scanpointsx);
Dist=zeros(1,grscptx(1,2));
for dtel=1:grscptx(1,2);
    Dist(1,dtel)=scanpointsz(1,dtel)-
    (parent(1,1)*scanpointsx(1,dtel)+parent(1,2));
end
weldheight=max(Dist);
clear left right vanh toth leftcol rightcol leftz rightz xline zline
parent;
clear scanpointsx scanpointsz vanhcol tothcol grscptx Dist;

```

Determining the undercut

```

%determine undercut of weld in relation to parent material
vanmoe=48; %start of straight parent material, use steps of size
[gridsize]
totmoe=49; %end of straight parent material, use steps of size [gridsize]

```

```

vancut=47; %start of area under investigation for undercut use steps of
size [gridsizex]
totcut=51; %end of area under investigation for undercut use steps of size
[gridsizex]

vancutmoecol=round(vanmoe/gridsizex+1);
totcutmoecol=round(totmoe/gridsizex+1);
vancutweldcol=round(vancut/gridsizex+1);
totcutweldcol=round(totcut/gridsizex+1);

Xmoepoints=X(1,vancutmoecol:totcutmoecol);
Zmoepoints=Z(rij,vancutmoecol:totcutmoecol);
moe=polyfit(Xmoepoints,Zmoepoints,1);

scanpointsx=X(1,vancutweldcol:totcutweldcol);
grscptx=size(scanpointsx);
scanpointsz=Z(rij,vancutweldcol:totcutweldcol);

reflijnx=X(1,vancutweldcol:totcutweldcol);
for reftel=1:grscptx(1,2)
    reflijnz(1,reftel)=moe(1)*scanpointsx(1,reftel)+moe(2);
end
plot(scanpointsx,reflijnz);

Dist=zeros(1,grscptx(1,2));
for dtel=1:grscptx(1,2)
    Dist(1,dtel)=reflijnz(1,dtel)-scanpointsz(1,dtel);
end
undercut=max(Dist);
clear vanmoe tot moe vancut totcut vancutmoecol totcutmoecol vancutweldcol;
clear totcutweldcol Xmoepoints Zmoepoints moe scanpointsx grscptx;
clear scanpointsz reflijnx reftel reflijnz Dist dtel;

```


Annex G: Collaboration with TNO: Acoustic emission

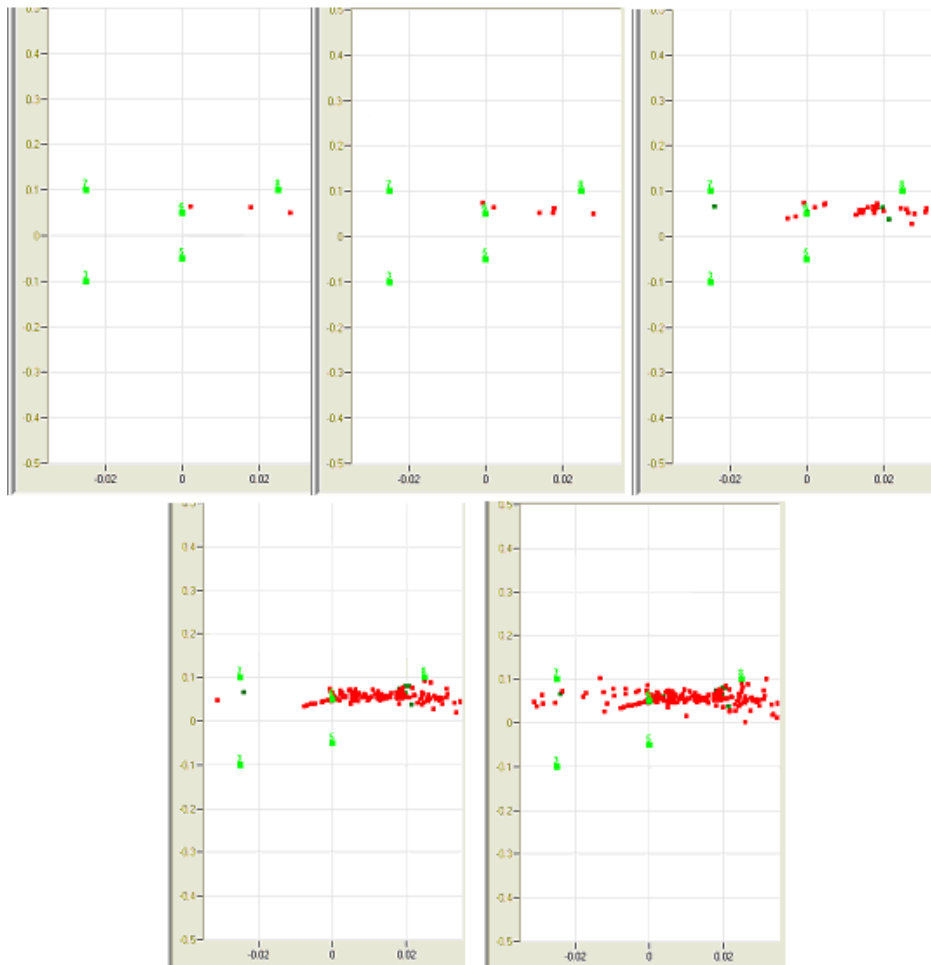
In this research the location of cracks and crack initiation time have been determined with the aid of strain gauges. Another possibility is the use of the acoustic emission of the steel when a crack is growing. To detect these sound emissions of the steel, sensors have been applied on a number of specimens. To reduce background noise from the hydraulics of the testing rig, plasticine dampers have been applied. The resulting test setup can be seen in figure G.1.



figure G.1 Left: test setup with sensors and dampers applied to the specimen. Right: close up of three sensors without any cables attached and two dampers made of plasticine, pretensioned with bicycle tires.

Due to the nature of the testing rig a very high background noise level was measured. This can be damped by the dampers as depicted in figure G.1 or by placing insulating material between the clamps of the test rig. Because the considered rig is an axial test rig which uses clamping to fix the specimens, the second option for background noise reduction was not possible. The dampers are able to reduce the background noise to a certain extent, but not always to the desired level, depending on the thickness of the specimen and the magnitude of the applied load and frequency.

The sensors are able to locate a crack via triangulation of the signal at different sensors. The software then produces a summation of all 'hits' which results in an image as can be seen in figure G.2. This location of the crack can only be done in a rather coarse manner because of the relatively large size of the sensors in relation to the weld. In practice, larger structures will be observed and smaller sensors are available.



**figure G.2 Increase of 'hits' during the test of a specimen from the first hit (top left) to the final crack (bottom right)
The green symbols represent the sensors on both sides on the weld, the red dots are hits.**

Most results of the experiment are of limited importance for the current research. For these results reference is made to TNO publications on the matter. It is however very interesting to compare the crack initiation time as defined in this research and the crack initiation time as found with the acoustic emission. In this way, the crack initiation time as defined by the method of deviating strain gauges can be evaluated. Unfortunately these results are not available at the publishing date of this report.

If additional research is done on the matter, it would be very insightful to obtain the reports of TNO which contain several practical tips. Further testing should, when possible, be done in such a testing rig, that damping of the background noise is possible by placing isolation material between the rig and the specimen (i.e. a bending test).

Annex H: Hardness Measurements

From each plate material one strip of residual material has been polished. Pijpers (2011) has shown on similar specimens from the same material that the hardness does not vary significantly over the height of the specimen, but only shows differences between the different material states (fusion zone FZ, heat affected zone HAZ and base material BM). From each specimen the as welded situation is plotted. All measurements are executed after TIG-dressing, but only in the middle of the specimen, which is assumed to be out of the influence of TIG-dressing.

Then, the comparison with the effect of TIG dressing is made. The different zones that occur after the initial welding process (FZ, HAZ and BM) can each separately be influenced by the TIG dressing, by being remelted or heat affected. In the diagrams the different zones that occur after initial welding are stated as the 'as welded' situation, and the effects of TIG-dressing (melting of heat affecting) on these original zones are plotted for comparison. For example: figure H.4 shows datapoints which were in the BM zone after welding. Some areas of the BM zone have been influenced by TIG dressing, denoted by TIG Fluid Zone and TIG Heat Affected Zone. These points are plotted in white and grey. Because of the complex geometry of the different zones after TIG-dressing, the X-axis in these comparison diagrams has no meaning, the diagram is simply a comparison of different measured values.

An example of the as welded state of a specimen is shown in figure H.1. The effect of TIG-dressing is shown in figure H.2. Note that in figure H.2 the fluid zone of TIG-dressing at the cap side of the weld extends into the as welded FZ, HAZ and BM. This is in reality not always the case. Similar remarks can be made at the other fluid zones and heat affected zones.

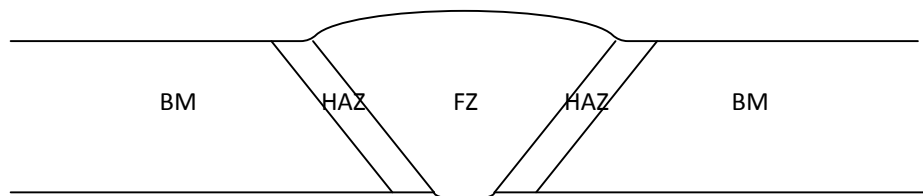


figure H.1 Zones in the as welded specimens

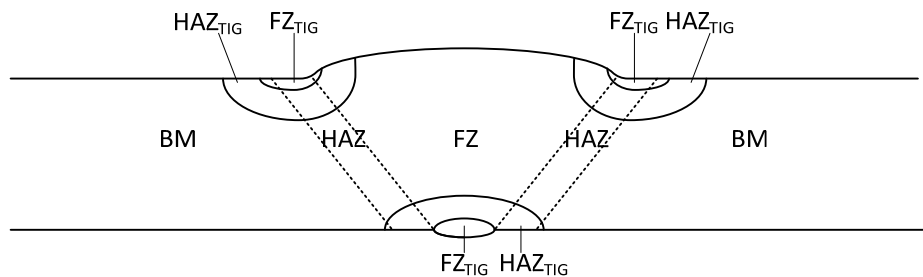


figure H.2 Effect of TIG-dressing

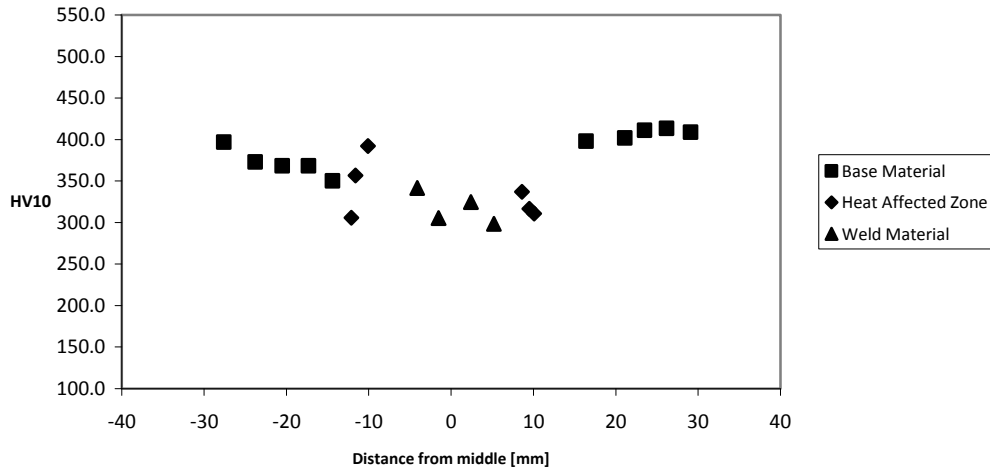


figure H.3 C11: As welded. Cast material on the left, rolled material on the right side of the weld

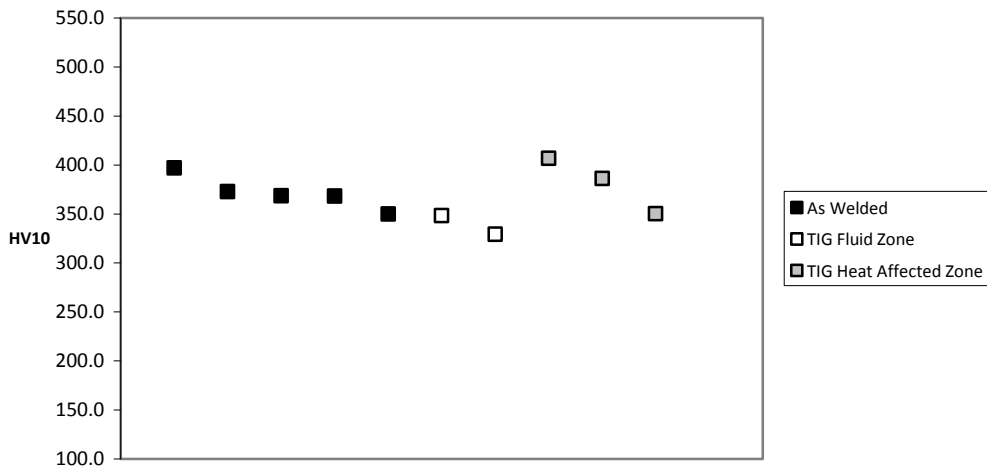


figure H.4 C11: Base material before and after TIG-dressing [Cast]

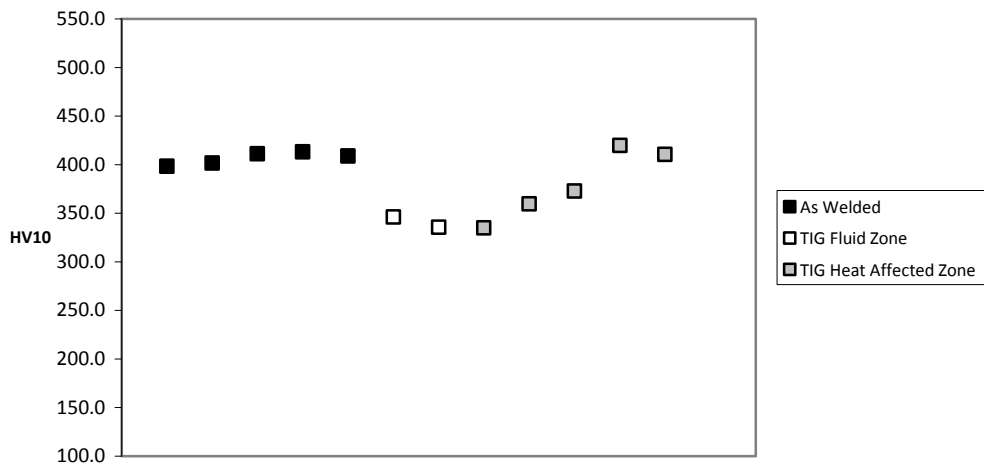


figure H.5 C11: Base material before and after TIG-dressing [Rolled]

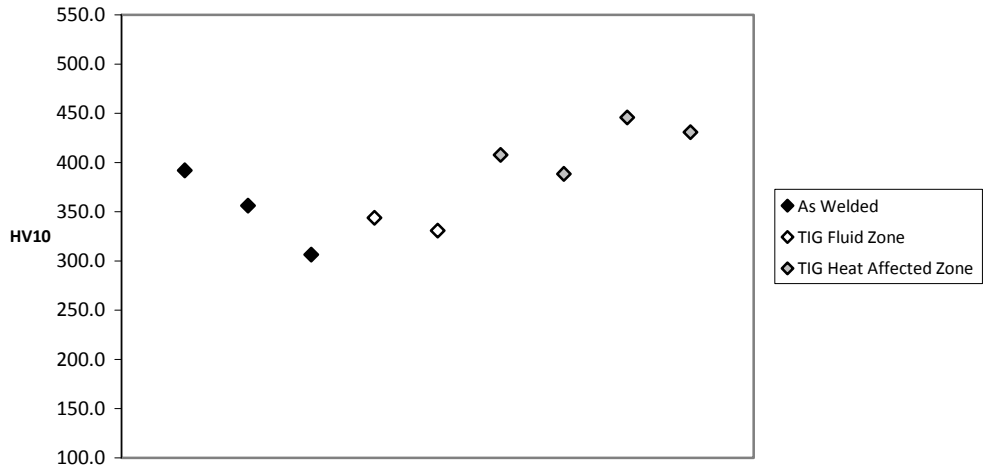


figure H.6 C11: Heat affected zone before and after TIG-dressing [Cast]

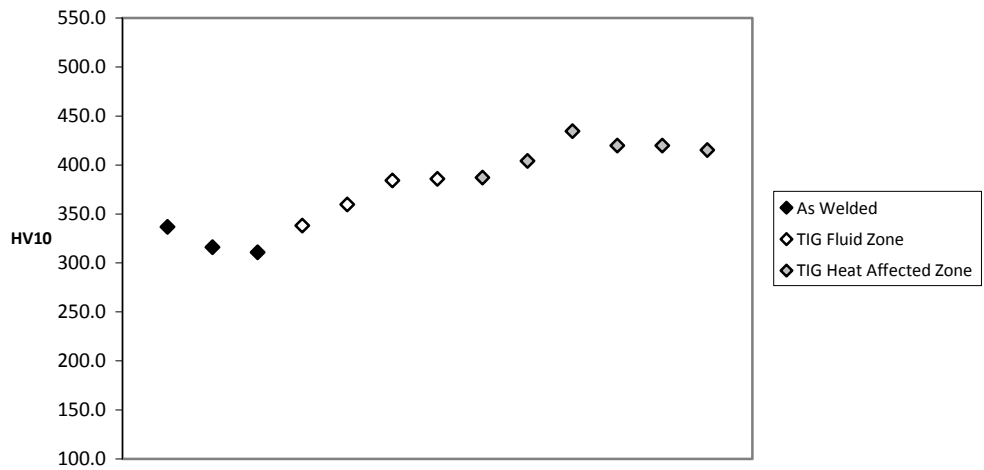


figure H.7 C11: Heat affected zone before and after TIG-dressing [Rolled]

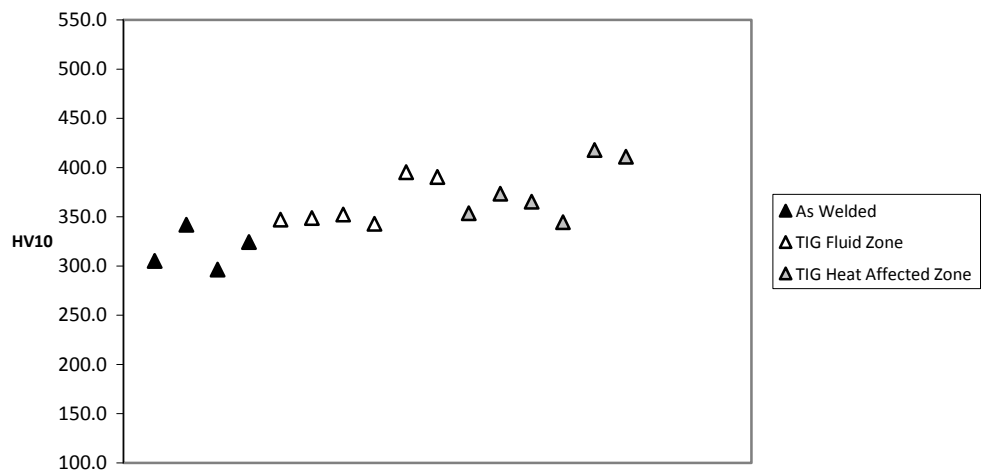


figure H.8 C11: Fluid zone before and after TIG-dressing

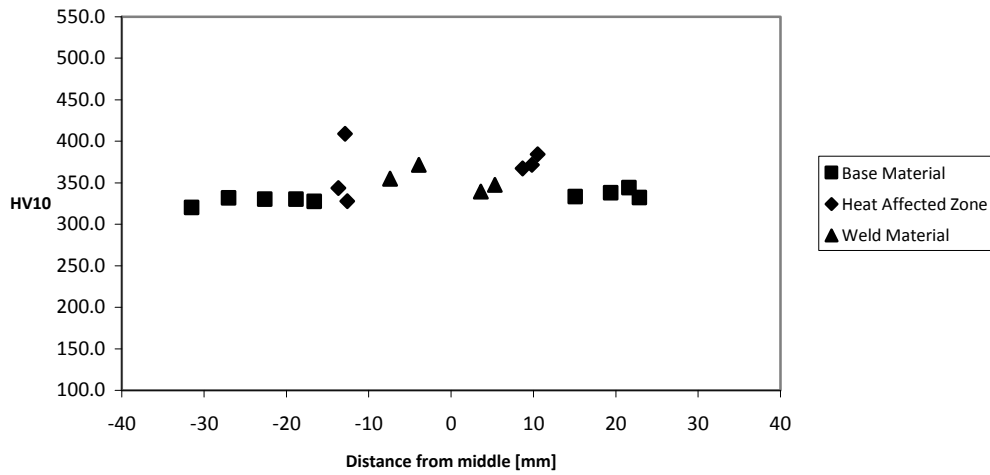


figure H.9 C89: As welded. Cast material on the left, rolled material on the right side of the weld

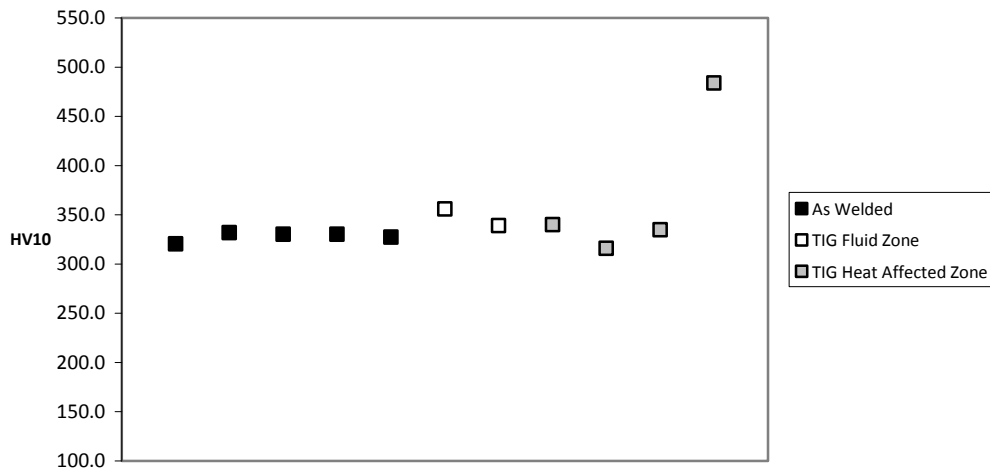


figure H.10 C89: Base material before and after TIG-dressing [Cast]

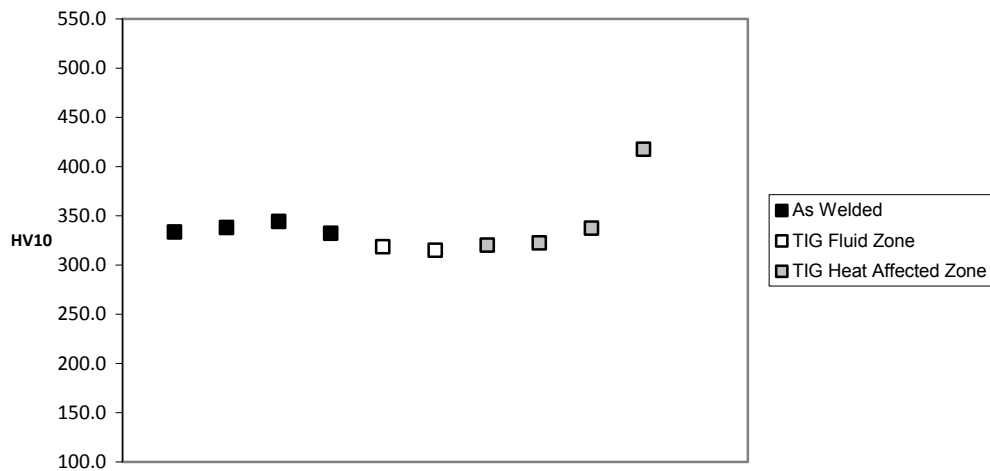


figure H.11 C89: Base material before and after TIG-dressing [Rolled]

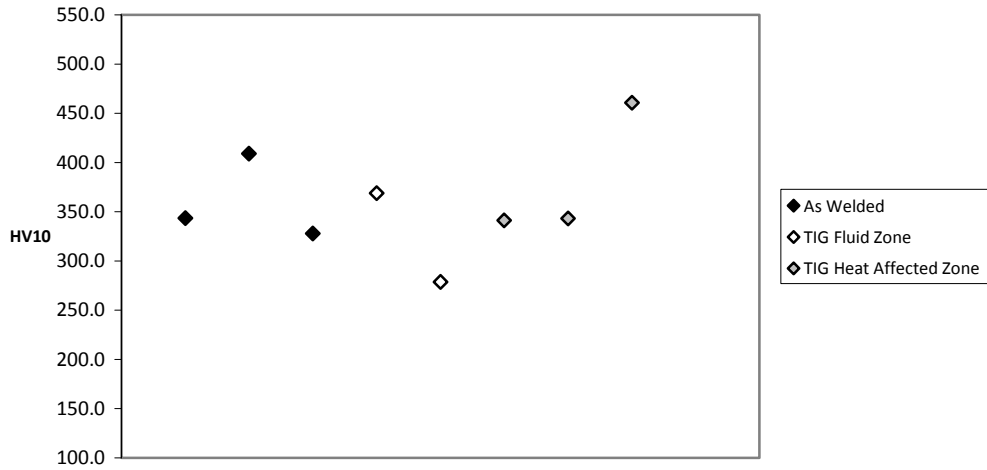


figure H.12 C89: Heat affected zone before and after TIG-dressing [Cast]

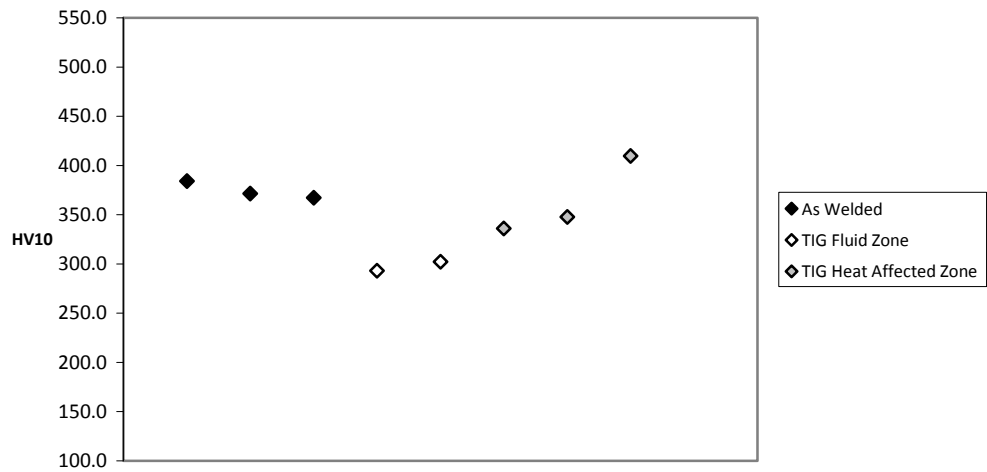


figure H.13 C89: Heat affected zone before and after TIG-dressing [Rolled]

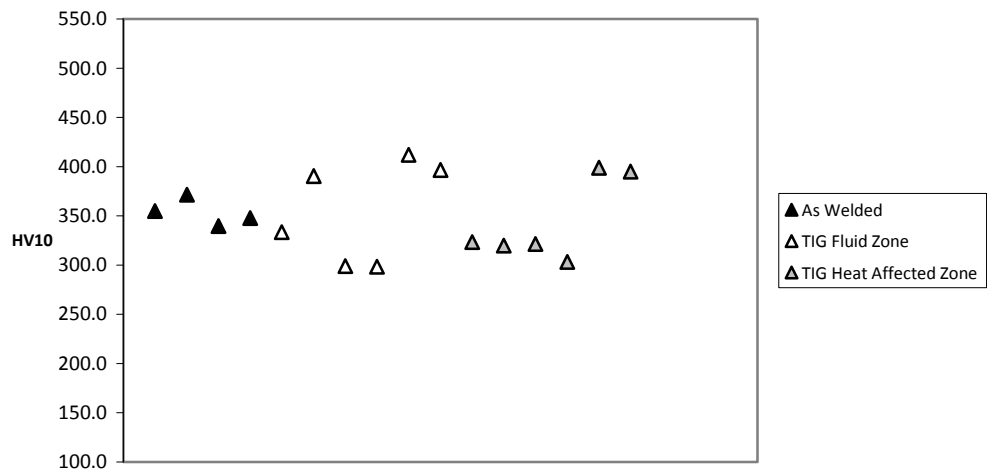


figure H.14 C89: Fluid zone before and after TIG-dressing

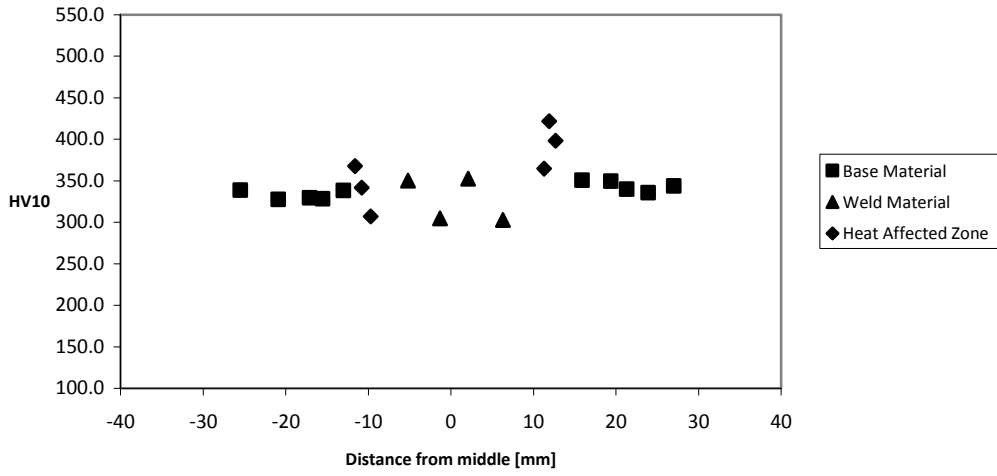


figure H.15 C89a: As welded. Cast material on the right, rolled material on the left side of the weld

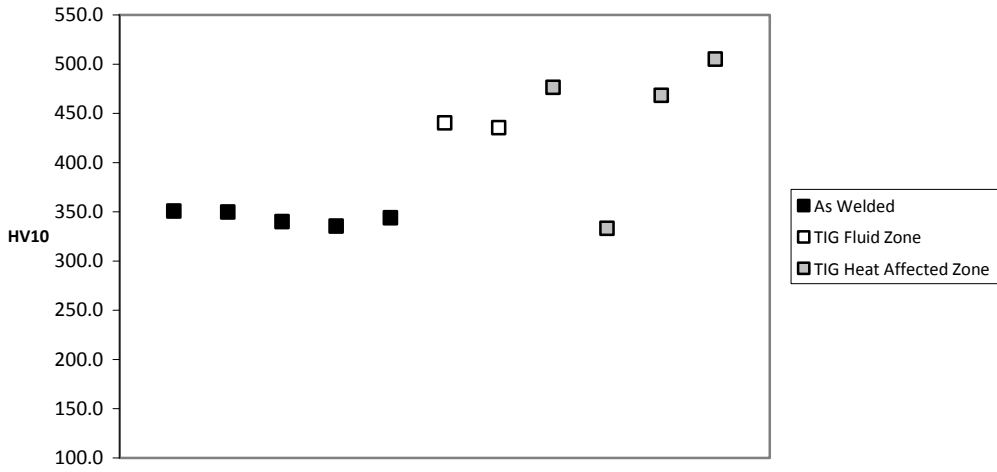


figure H.16 C89a: Base material before and after TIG-dressing [Cast]

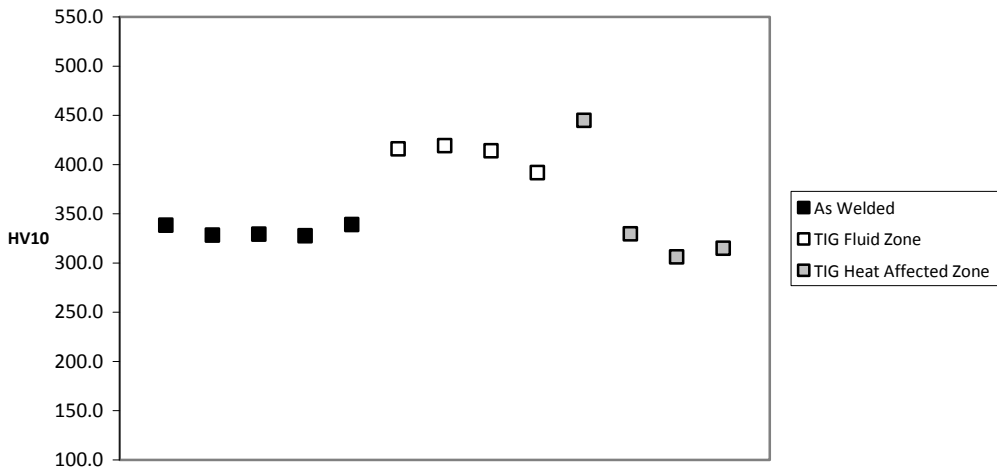


figure H.17 C89a: Base material before and after TIG-dressing [Rolled]

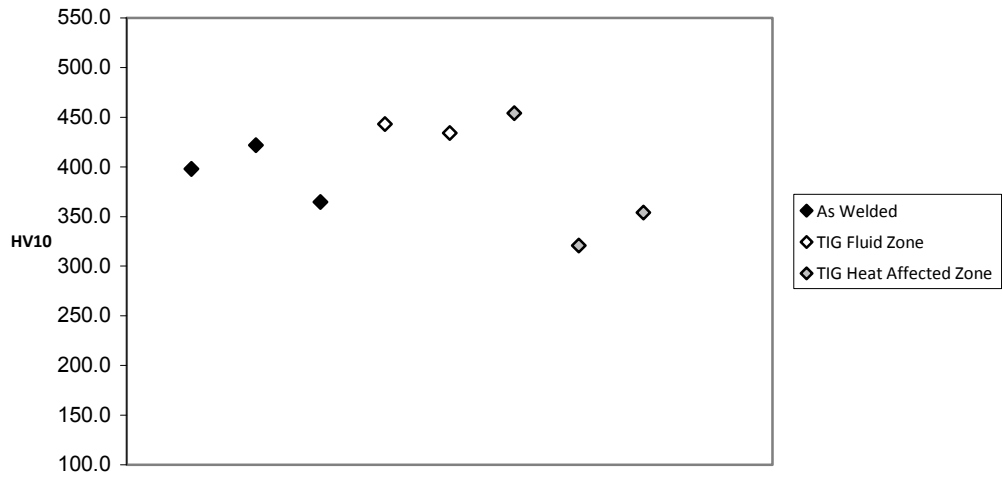


figure H.18 C89a: Heat affected zone before and after TIG-dressing [Cast]

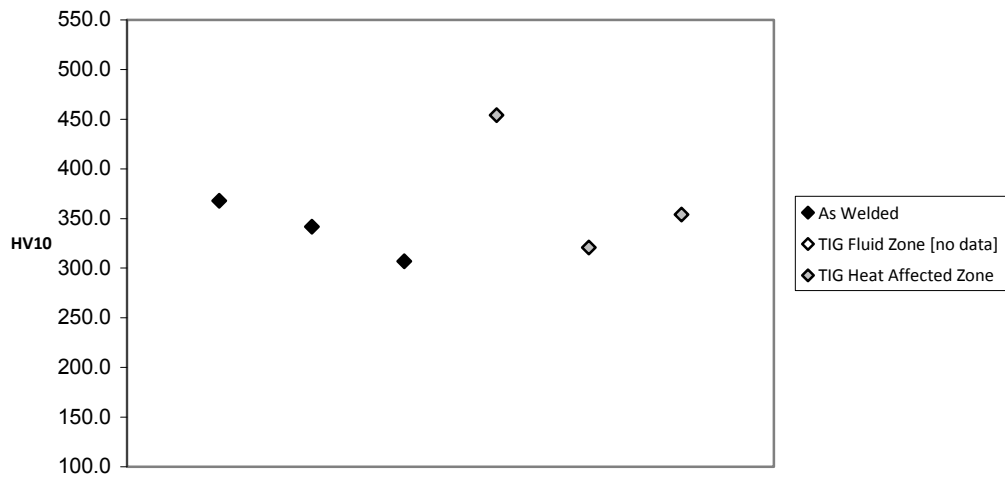


figure H.19 C89a: Heat affected zone before and after TIG-dressing [Rolled]

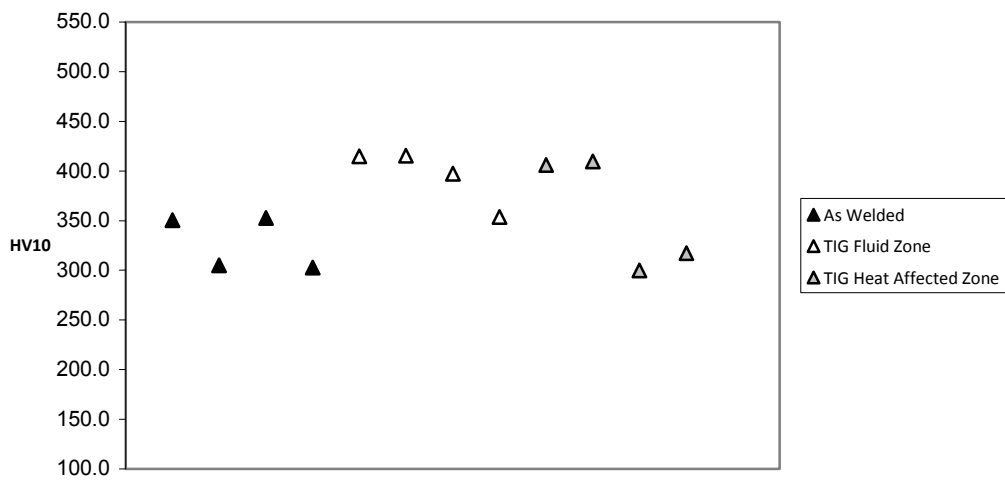


figure H.20 C89a: Fluid zone before and after TIG-dressing

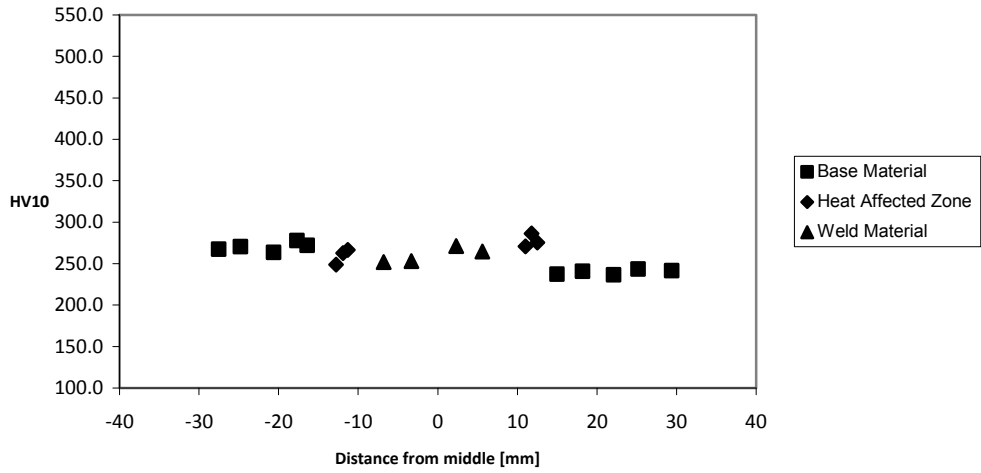


figure H.21 C69: As welded. Cast material on the right, rolled material on the left side of the weld

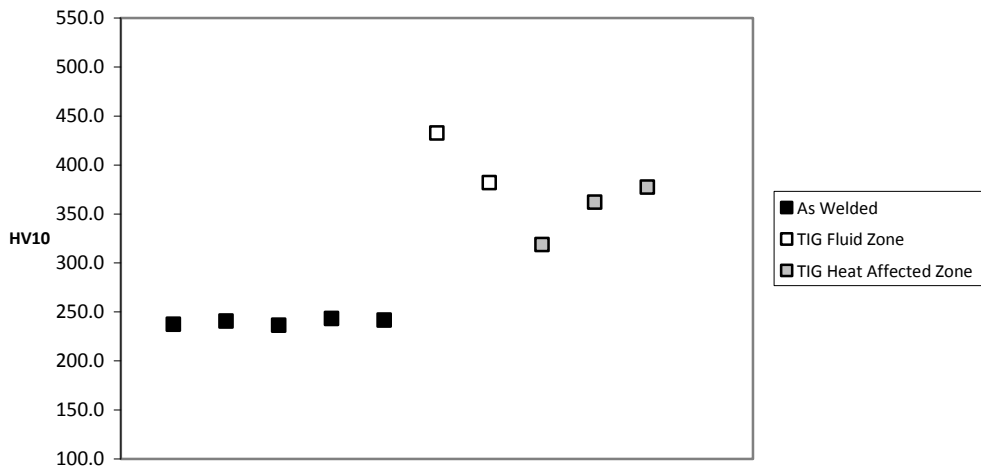


figure H.22 C69: Base material before and after TIG-dressing [Cast]

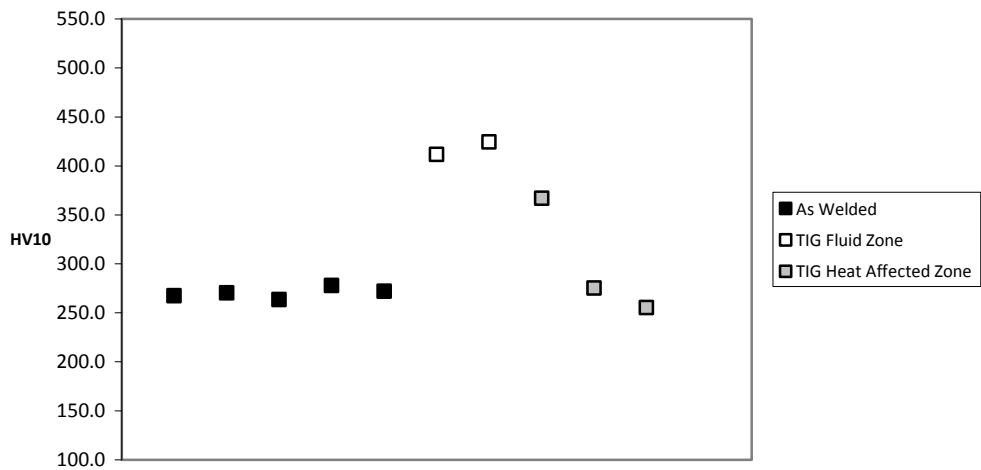


figure H.23 C69: Base material before and after TIG-dressing [Rolled]

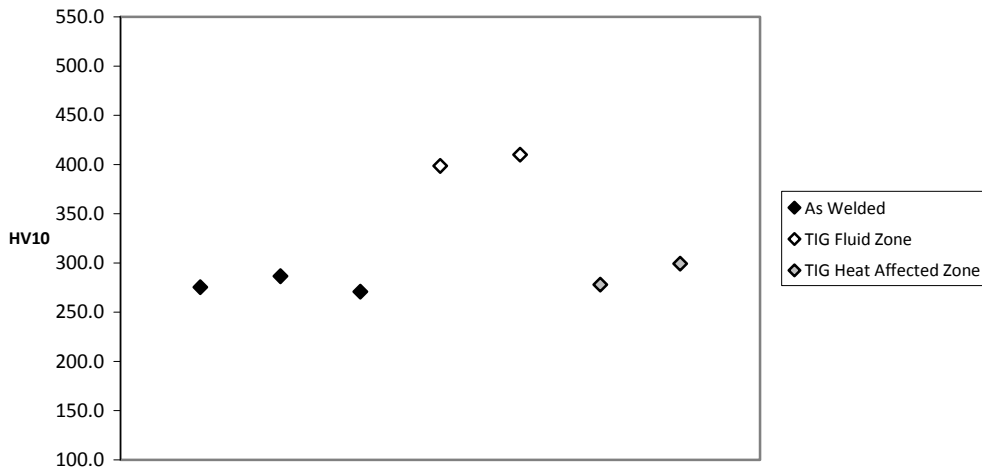


figure H.24 C69: Heat affected zone before and after TIG-dressing [Cast]

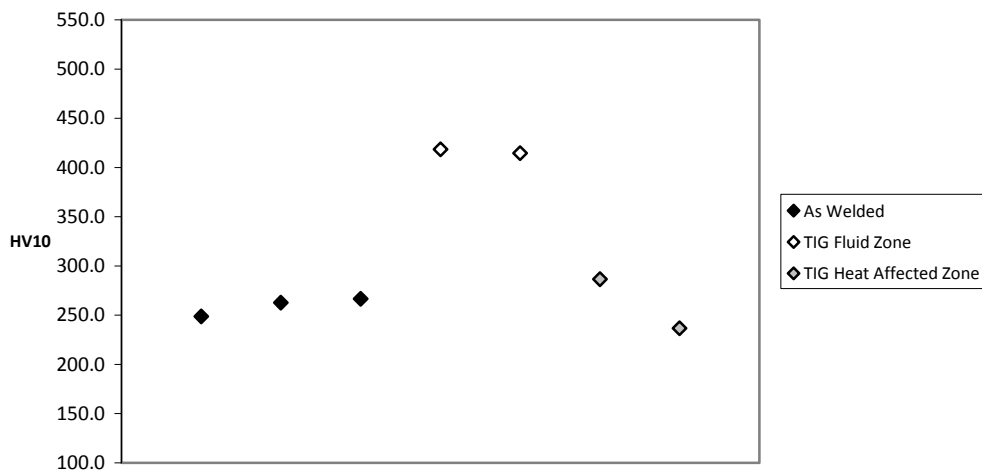


figure H.25 C69: Heat affected zone before and after TIG-dressing [Rolled]

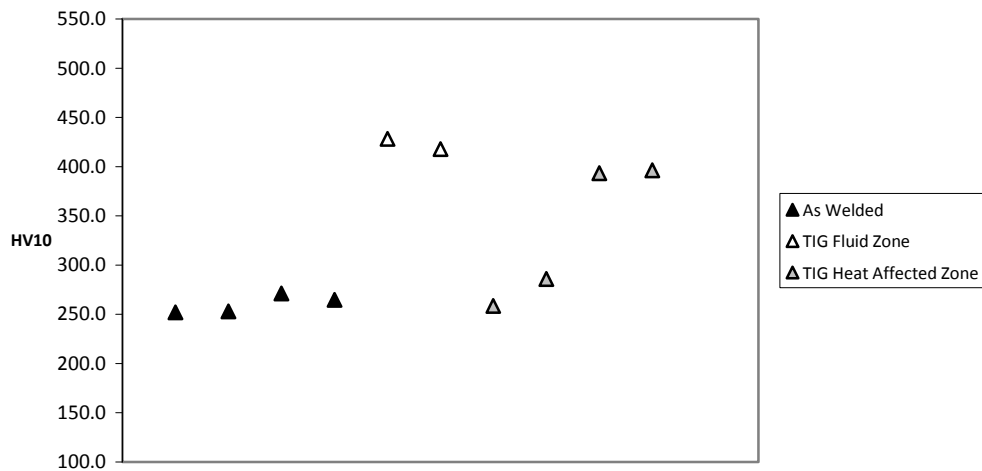


figure H.26 C69: Fluid zone before and after TIG-dressing

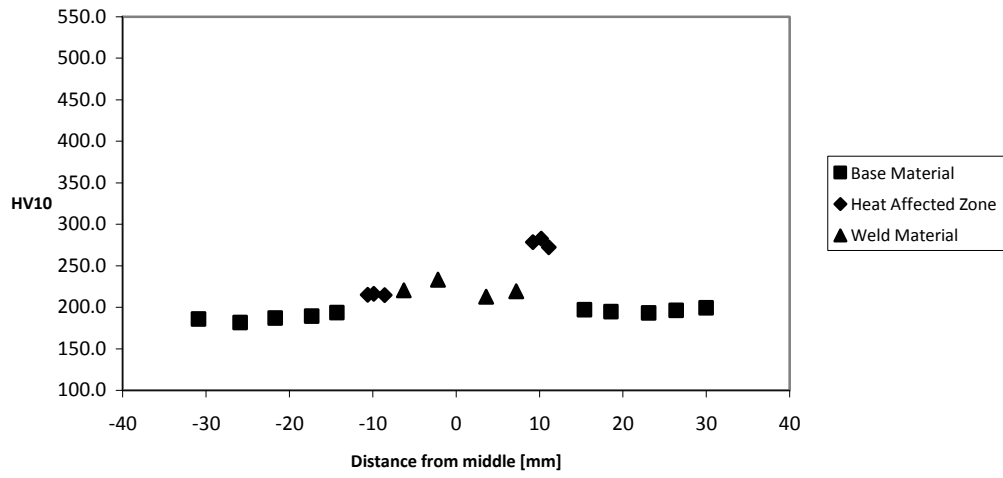


figure H.27 C46: As welded Cast material on the right, rolled material on the left side of the weld

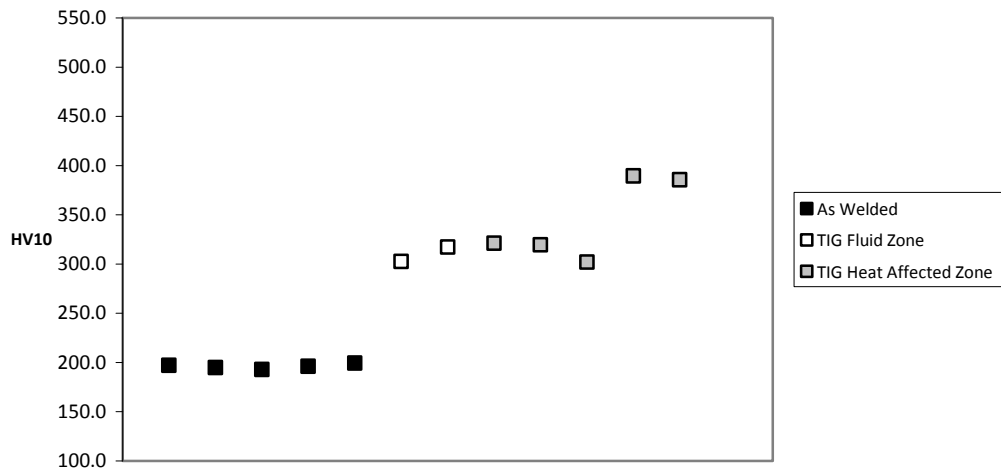


figure H.28 C46: Base material before and after TIG-dressing [Cast]

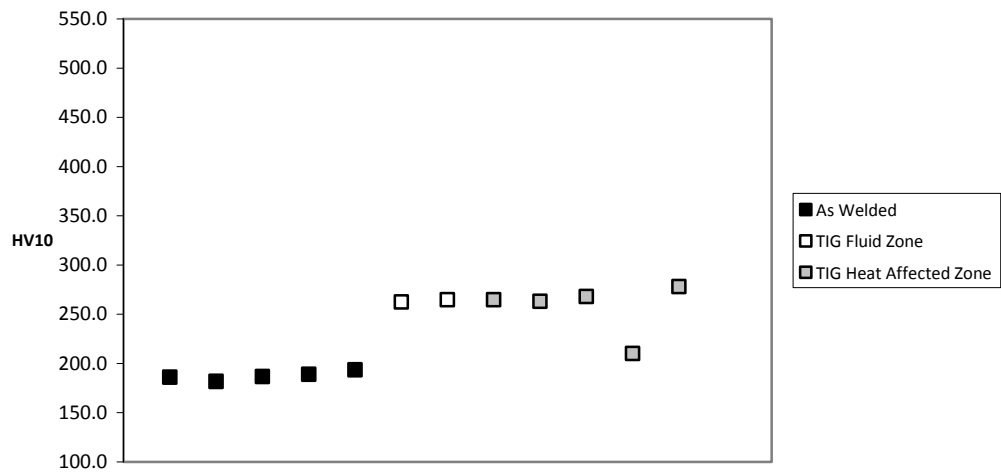


figure H.29 C46: Base material before and after TIG-dressing [Rolled]

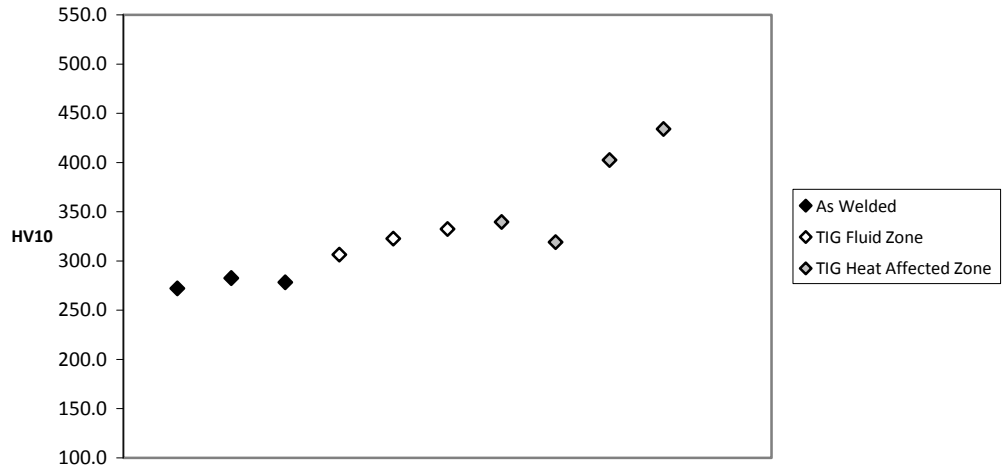


figure H.30 C46: Heat affected zone before and after TIG-dressing [Cast]

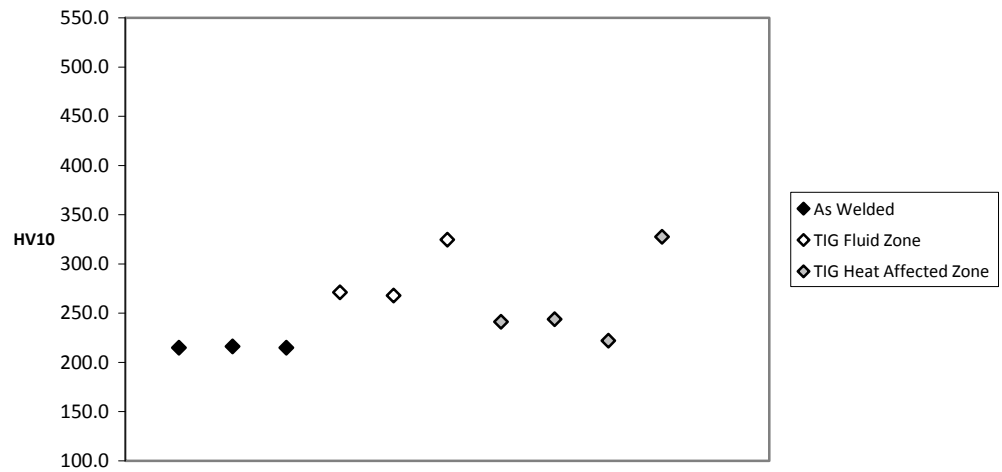


figure H.31 C46: Heat affected zone before and after TIG-dressing [Rolled]

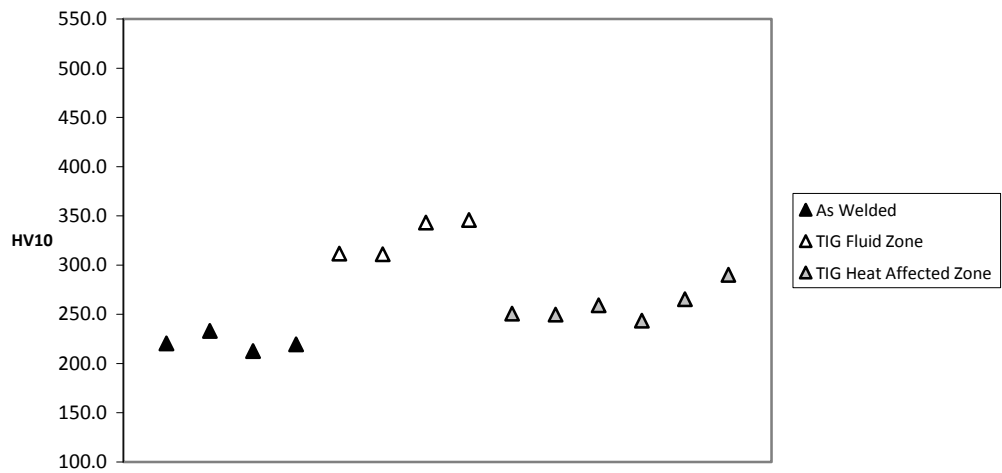


figure H.32 C46: Fluid zone before and after TIG-dressing

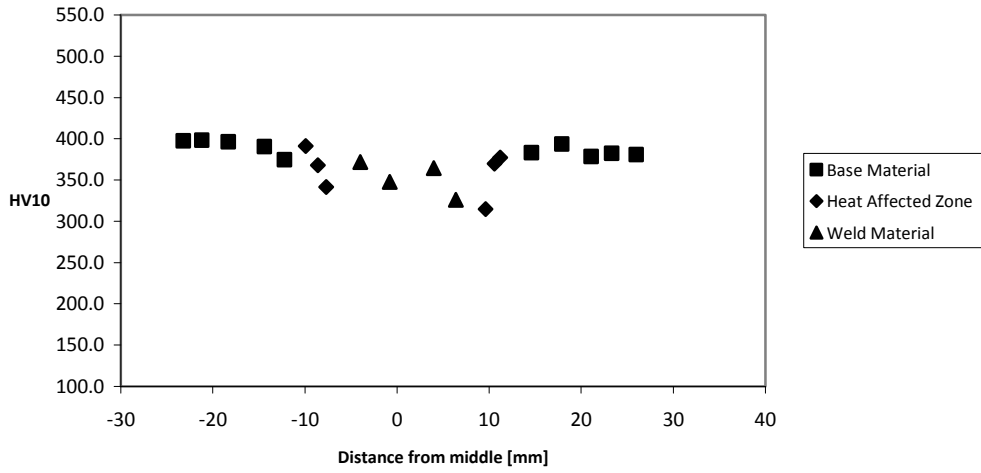


figure H.33 V11: As welded

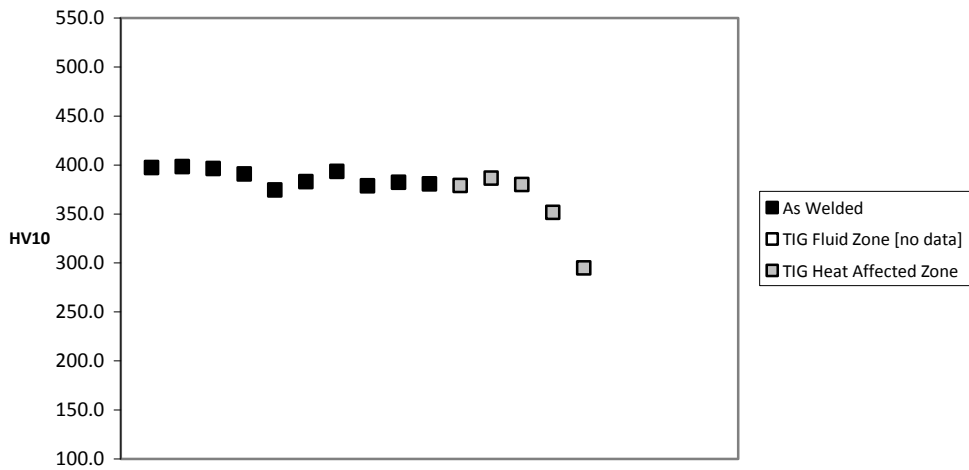


figure H.34 V11: Base material before and after TIG-dressing

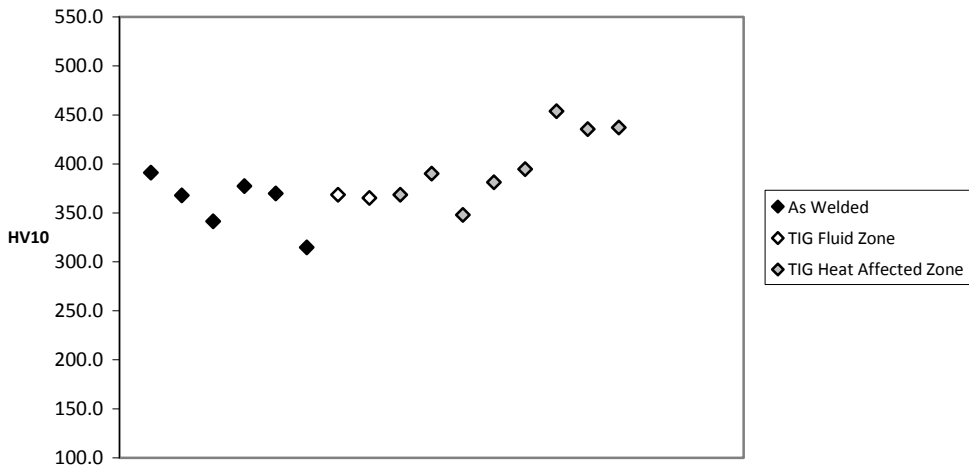


figure H.35 V11: Heat affected zone before and after TIG-dressing

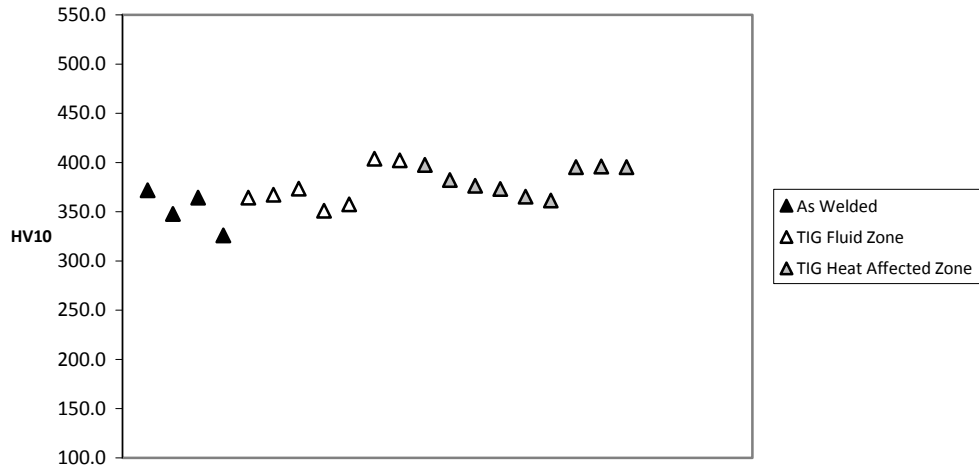


figure H.36 V11: Fluid zone before and after TIG-dressing

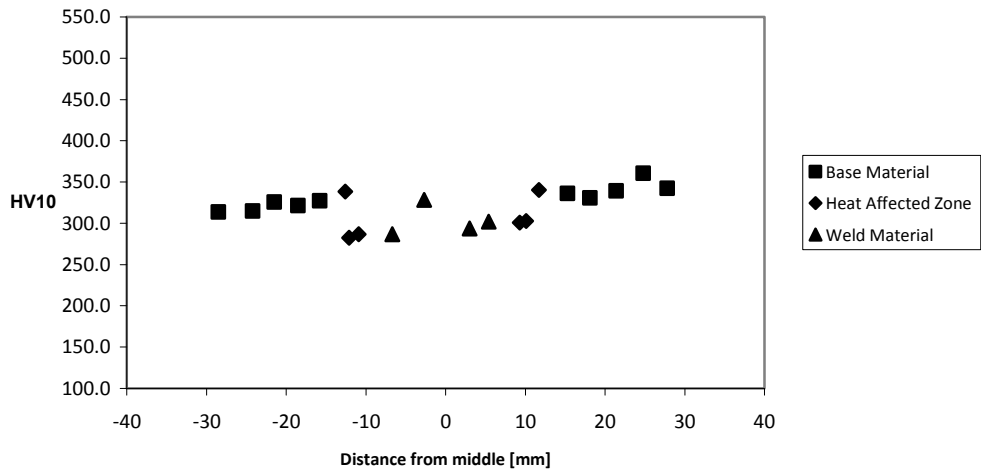


figure H.37 V89: As welded

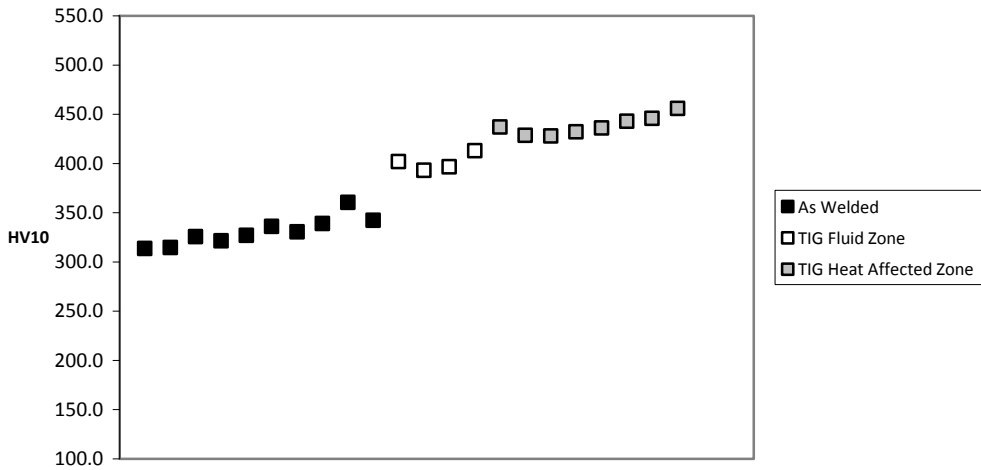


figure H.38 V89: Base material before and after TIG-dressing

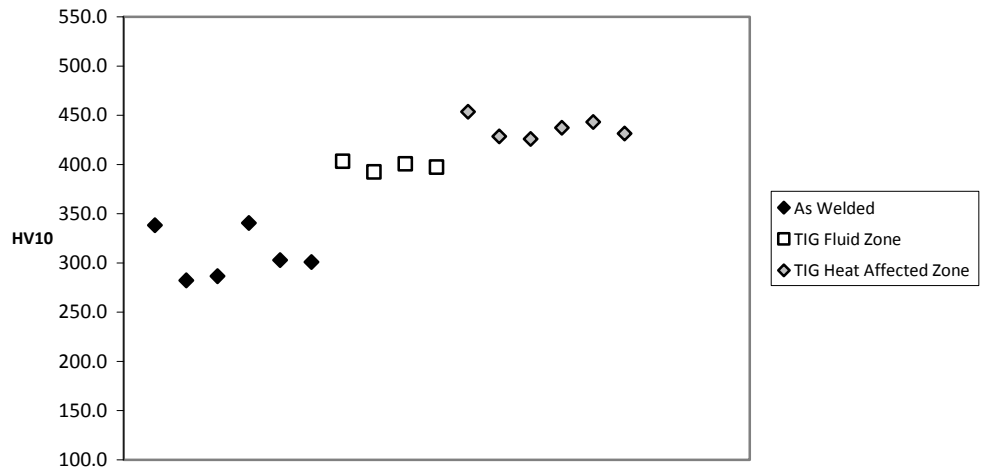


figure H.39 V89: Heat affected zone before and after TIG-dressing

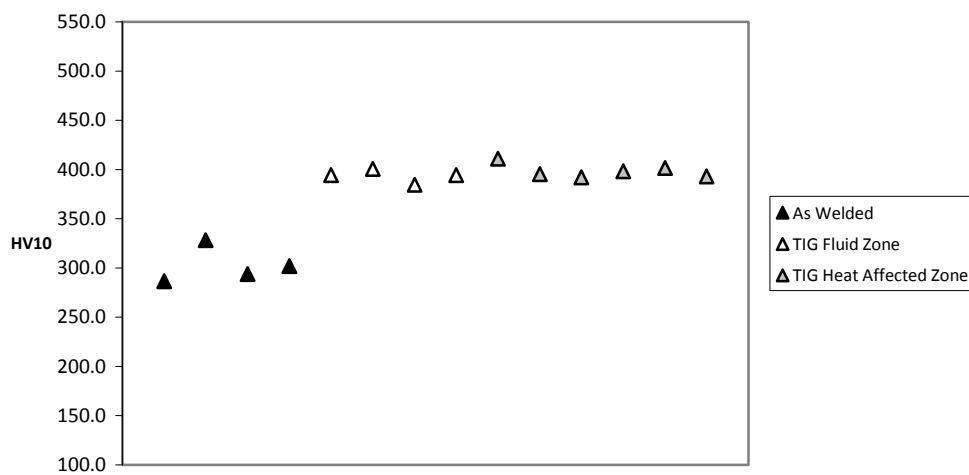


figure H 40 V89: Fluid zone before and after TIG-dressing

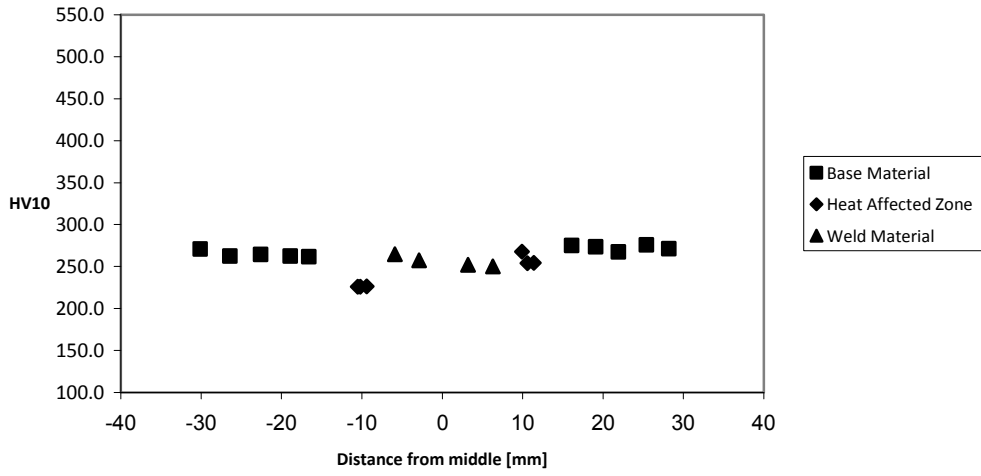


figure H.41 V69: As welded

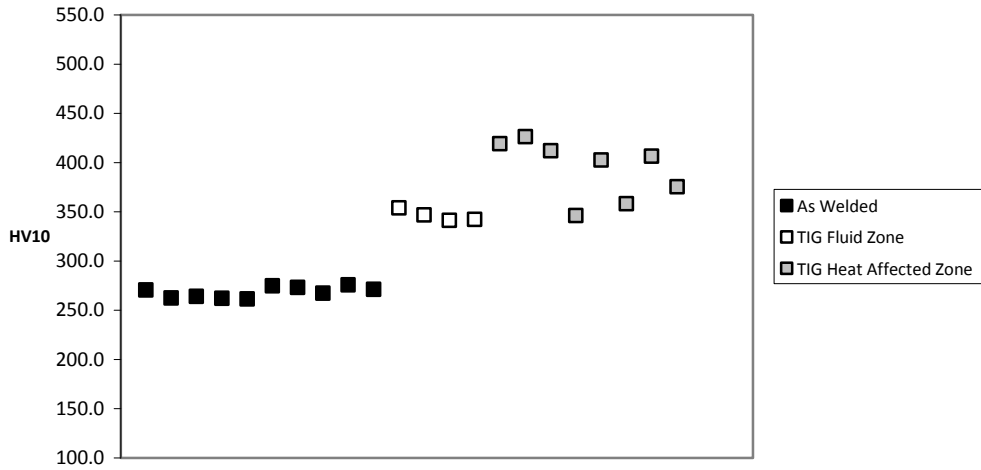


figure H.42 V69: Base material before and after TIG0-dressing

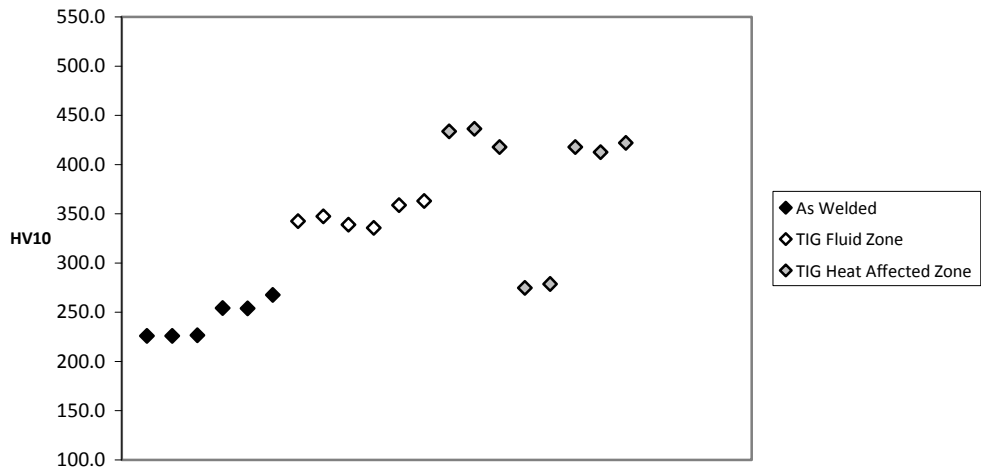


figure H.43 V69: Heat affected zone before and after TIG-dressing

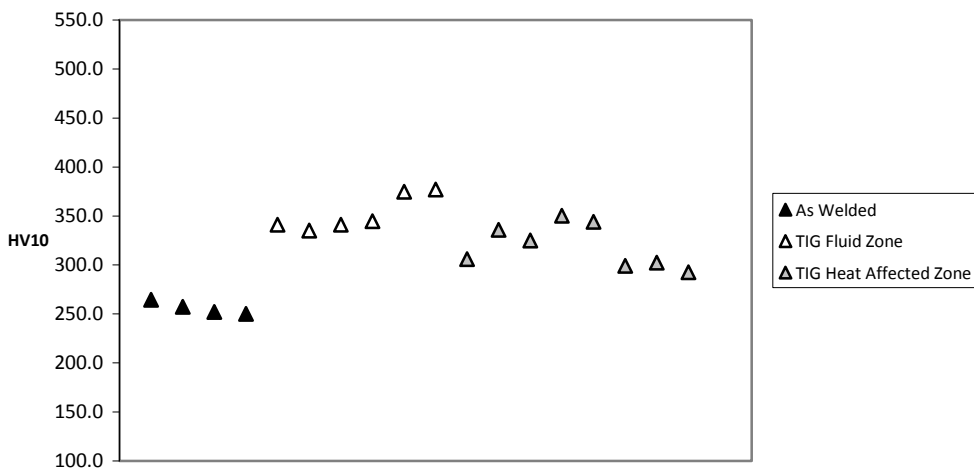


figure H.44 V69: Fluid zone before and after TIG-dressing

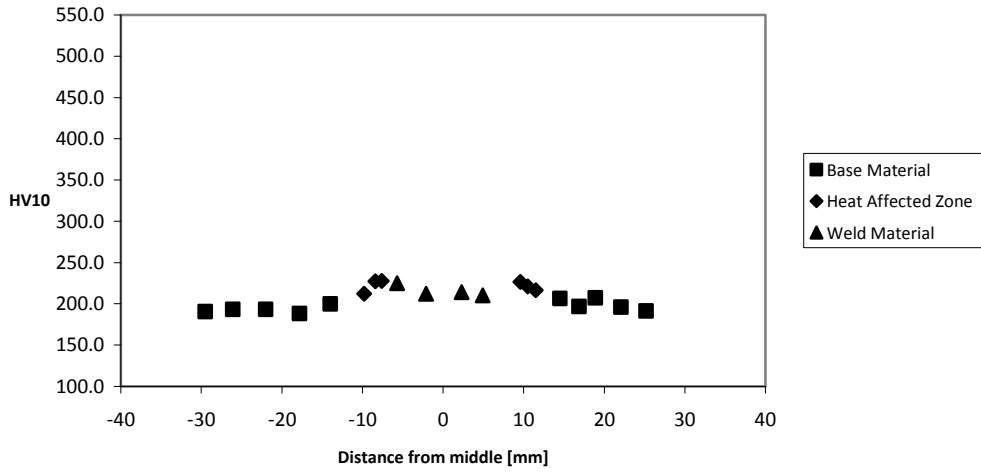


figure H.45 V46: As welded

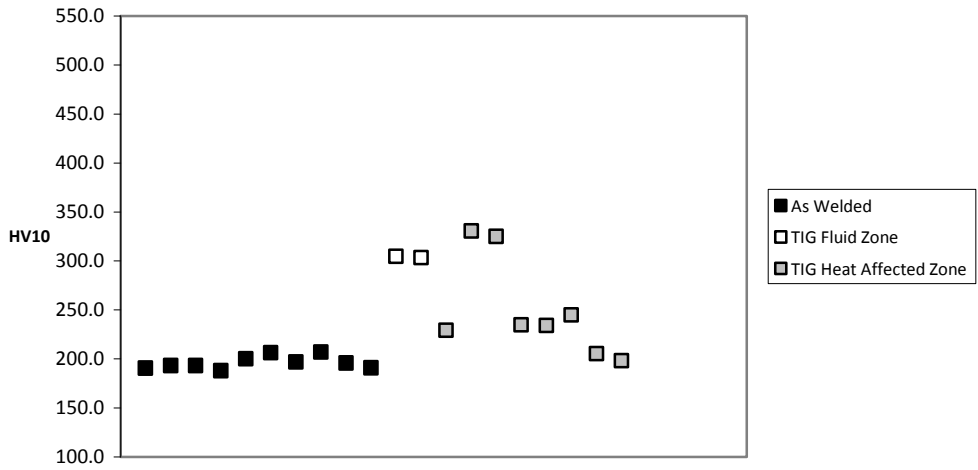


figure H.46 V46: Base material before and after TIG-dressing

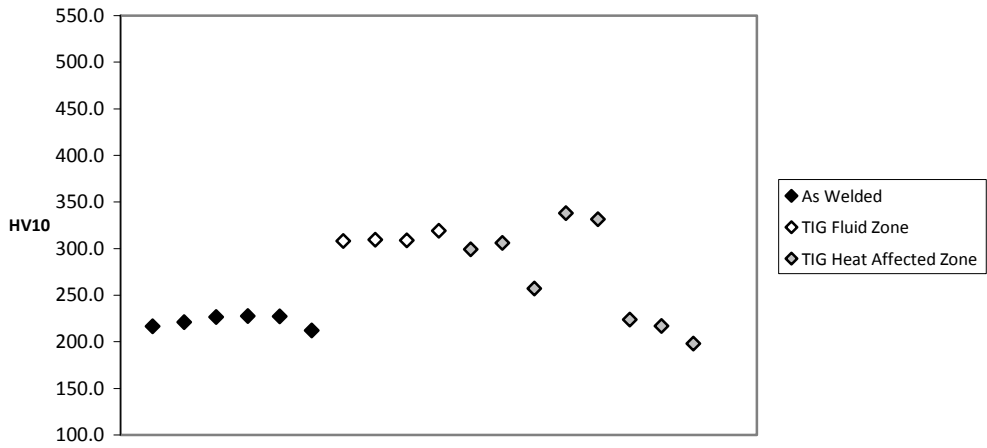


figure H.47 V46: Heat affected zone before and after TIG-dressing

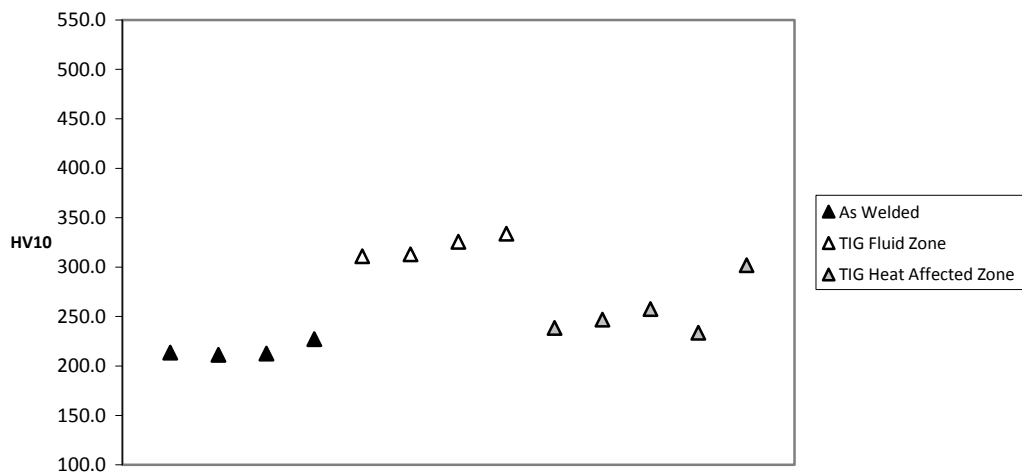


figure H.48 V46: Fluid zone before and after TIG-dressing

Annex I: Crack monitoring results

In the following diagrams the results of the crack monitoring are plotted. All values are given in the crack dimensions a and c . For edge cracks this is equal to the length and diameter of the crack, for surface cracks the actual crack width is $2 \cdot c$. Only the specimens which have shown usable results are plotted. Note that the crack depth a measured from surface measurements can differ from the crack marking measurements because the depth of the crack at the side is not necessarily the same as the maximum depth anywhere in the cross section. In case of a rerun specimen, only the second test is considered.

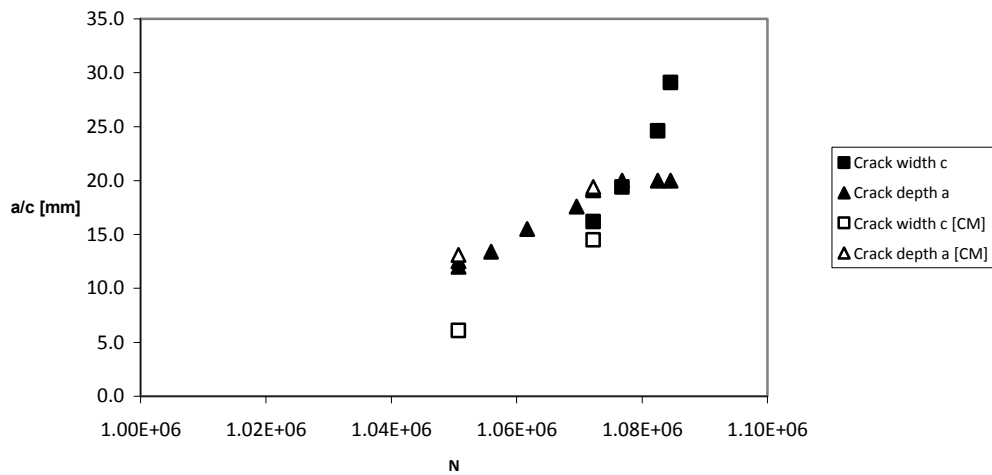


figure I.1 Crack propagation data of specimen C11-2

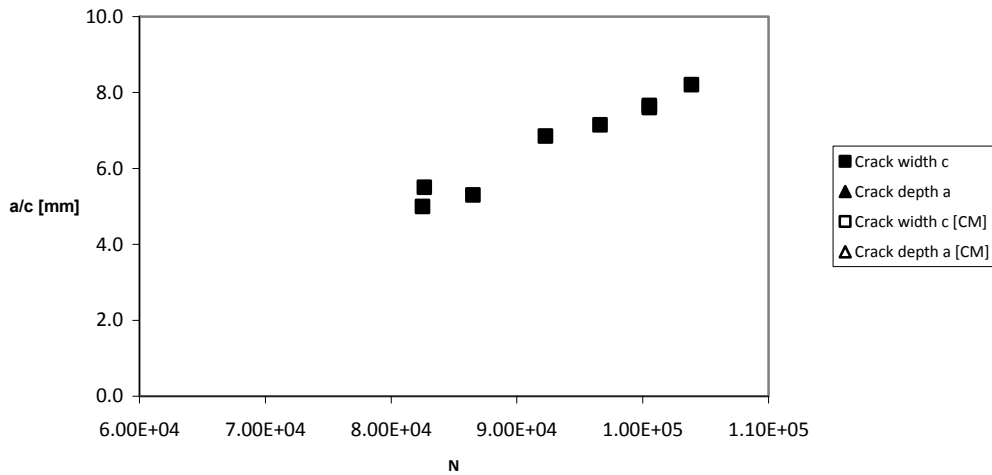


figure I.2 Crack propagation data of specimen C89-2

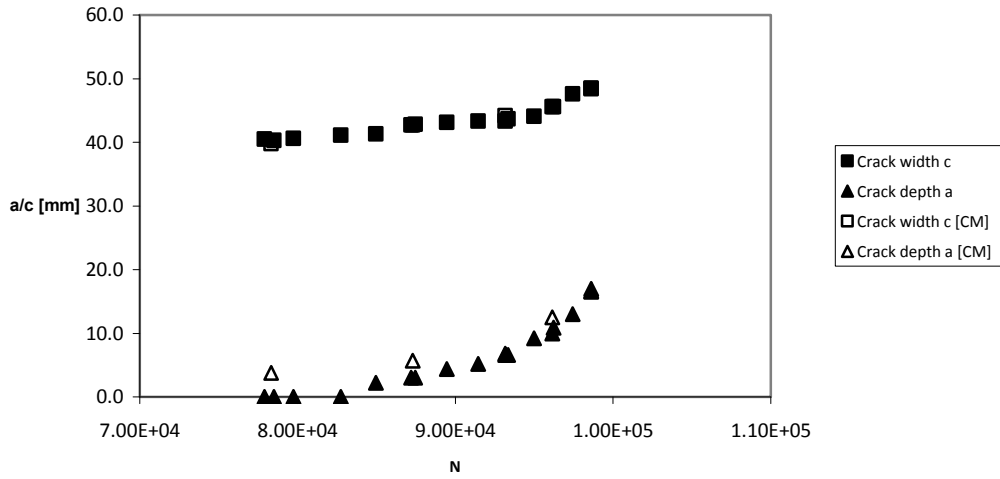


figure I.3 Crack propagation data of specimen C89a-1

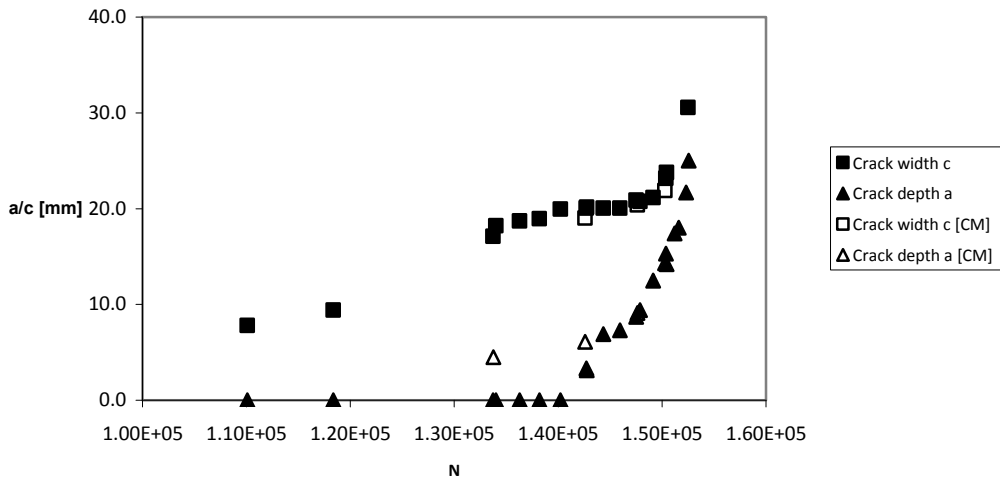


figure I.4 Crack propagation data of specimen C69-1

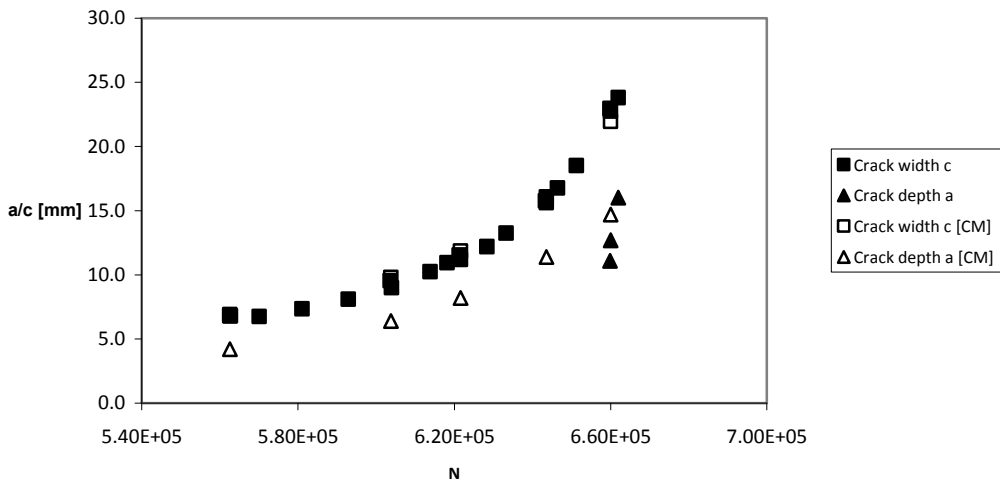


figure I.5 Crack propagation data of specimen C69-2

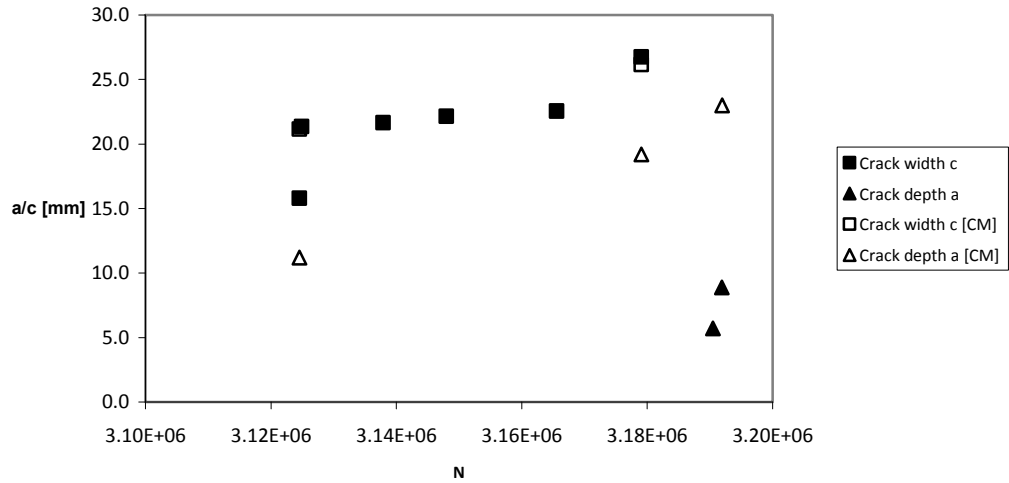


figure I.6 Crack propagation data of specimen C69-1

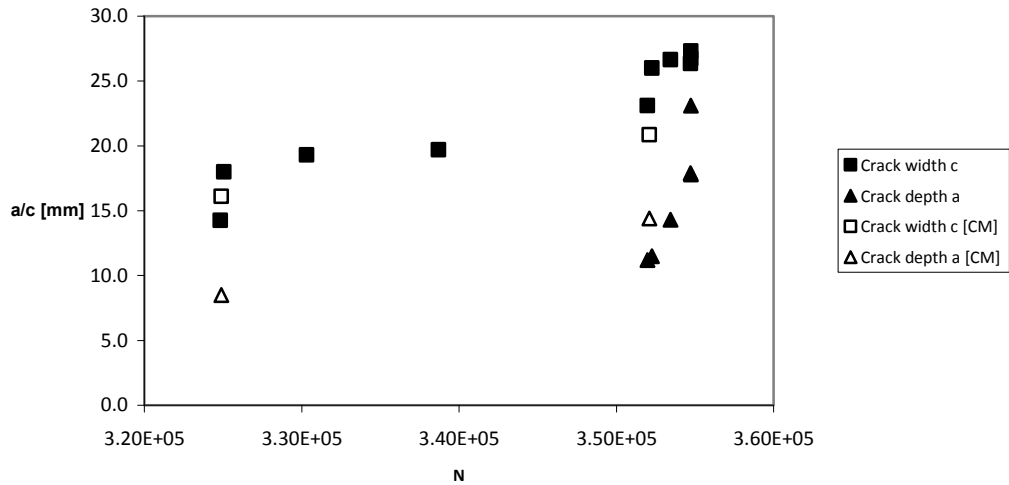


figure I.7 Crack propagation data of specimen C46-1

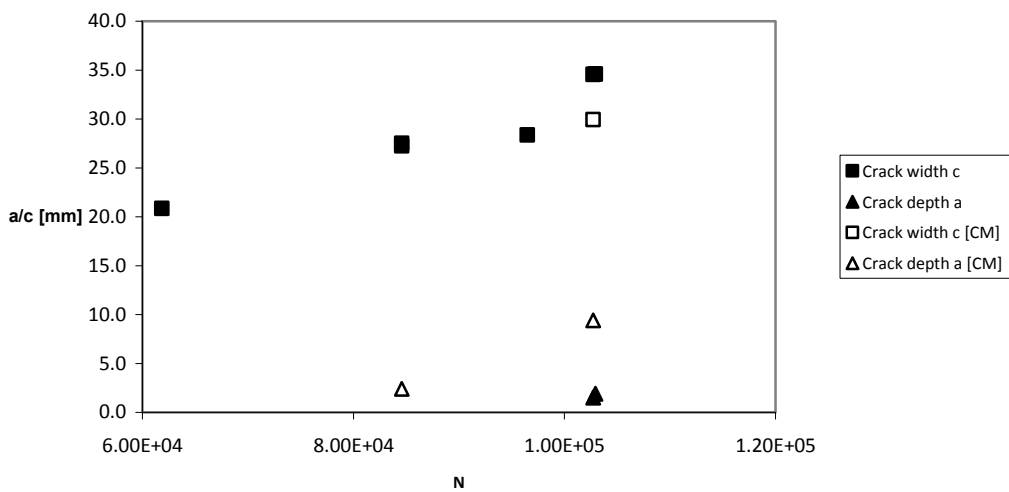


figure I.8 Crack propagation data of specimen C46-3

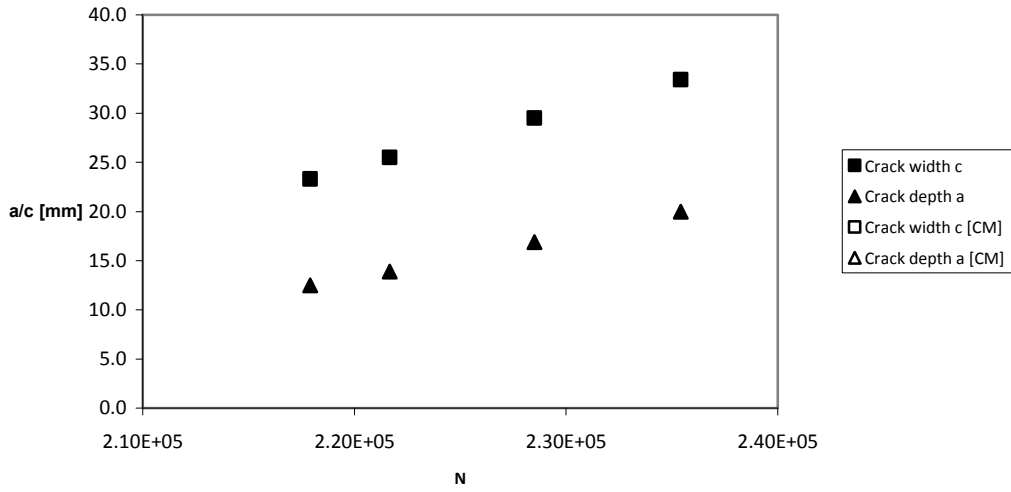


figure I 9 Crack propagation data of specimen V11-1

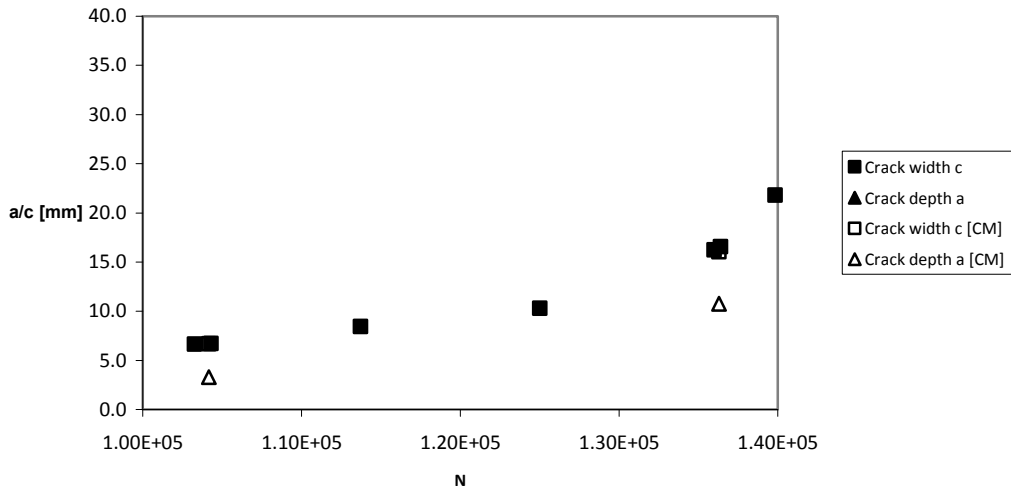


figure I 10 Crack propagation data of specimen V11-2

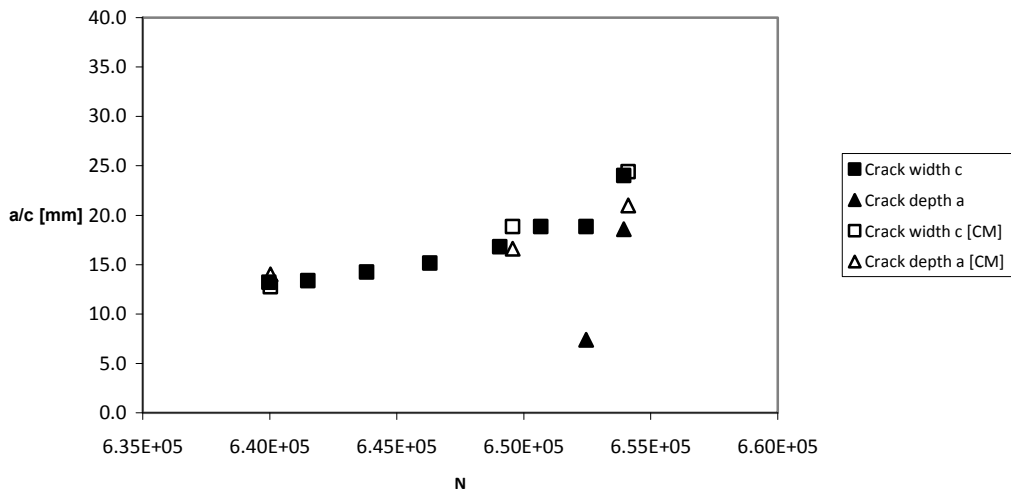


figure I 11 Crack propagation data of specimen V89-1

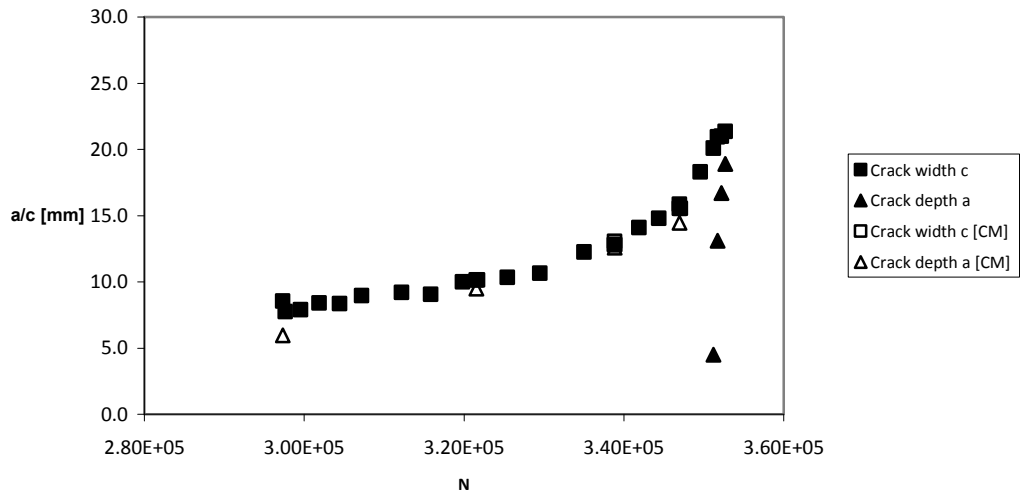


figure I 12 Crack propagation data of specimen V89-3

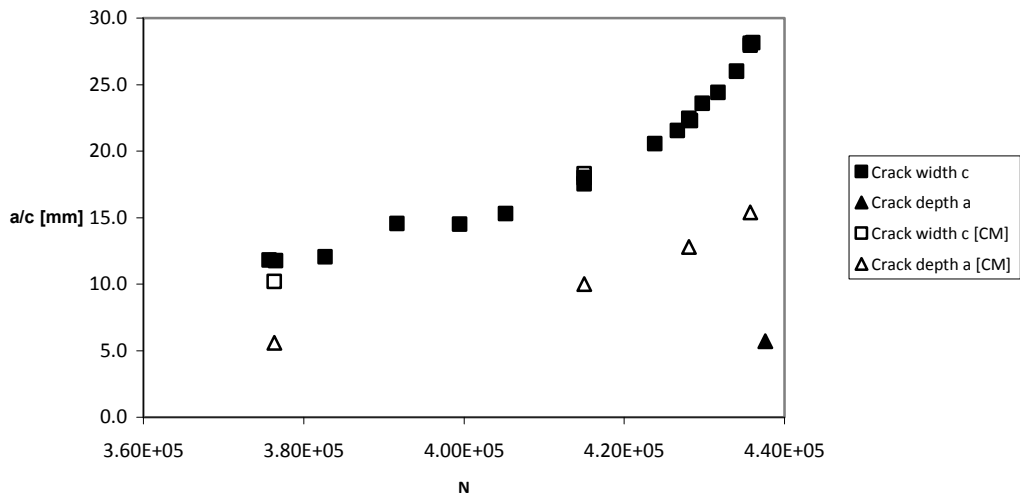


figure I 13 Crack propagation data of specimen V69-2

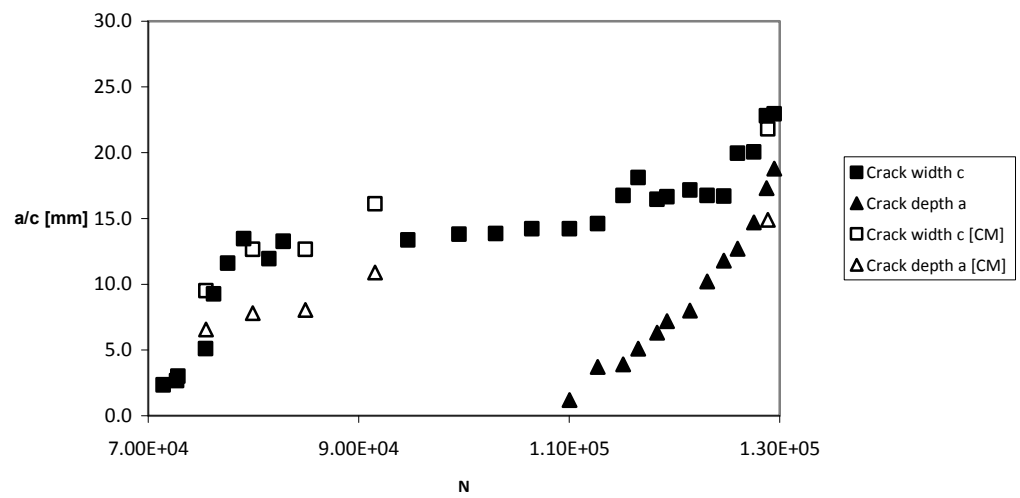


figure I 14 Crack propagation data of specimen V69-3

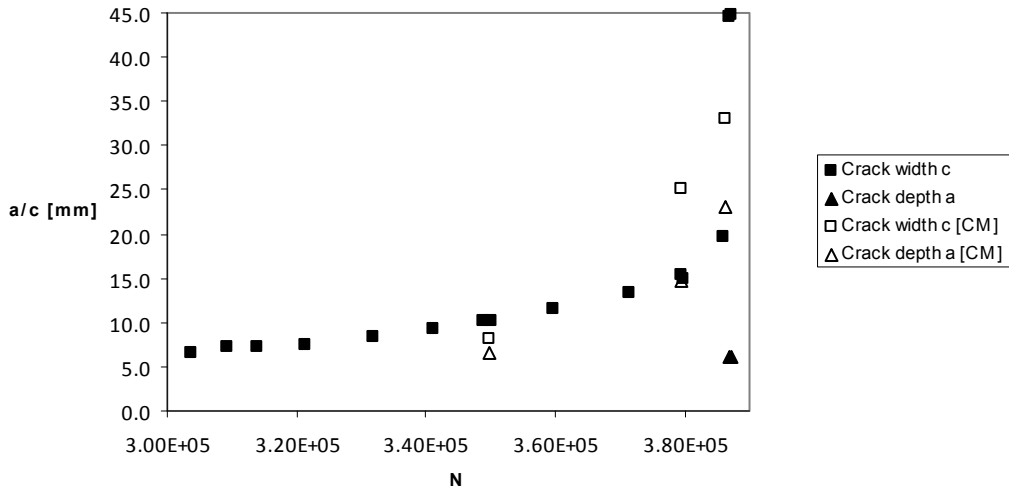


figure I 15 Crack propagation data of specimen V46-1

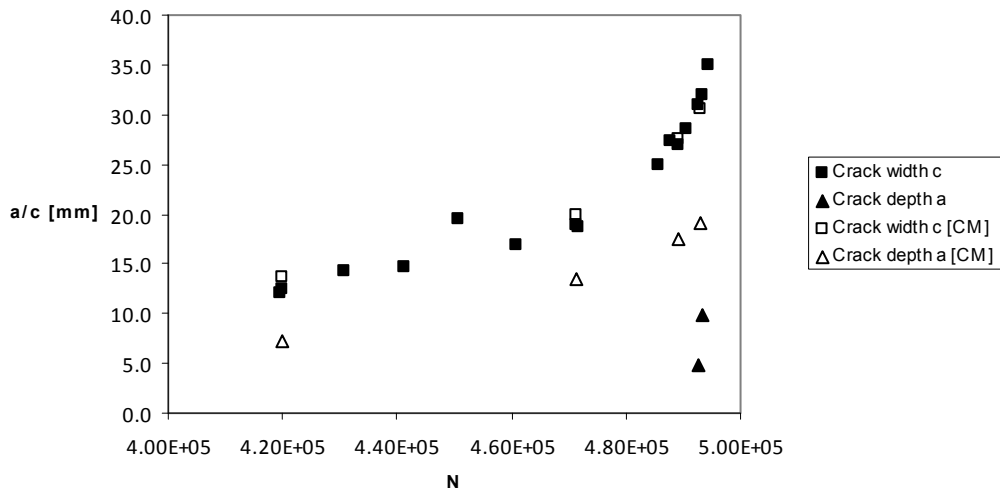


figure I 16 Crack propagation data of specimen V46-2

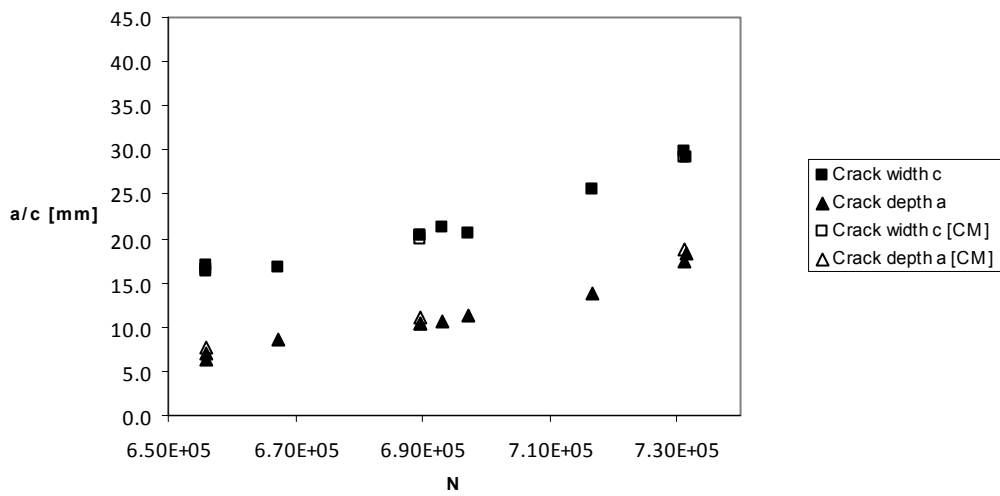


figure I 17 Crack propagation data of specimen V46-3

Annex J: Diana Model

The model that was used needs to be easily adjustable to calculate the stress concentration factor for different weld toe geometries. To achieve this, an excel sheet was designed which generates a list of TNO Diana commands, based on the given input parameters. The sheet offers the possibility to alter the geometry, but also the meshing division of the different contour lines. Because of the large changes in geometry, the meshing division needs to be changed in such a way that the automatic meshing generator in TNO Diana can find a suitable mesh.

In this annex, only two geometries will be covered, with the following parameters:

Radius:	2 mm
Weld toe angle:	15.3 degrees
Weld height:	3 mm
Length:	100 mm
Thickness:	25 mm
Undercut:	0 mm or 0.1 mm

Any different geometries are simply an alteration of the described procedure. The difference between the two considered geometries is the occurrence of an undercut, which slightly alters the model build up. The model is constrained in horizontal direction and all rotations on the right side. A horizontal line load is applied on the left side of the model.

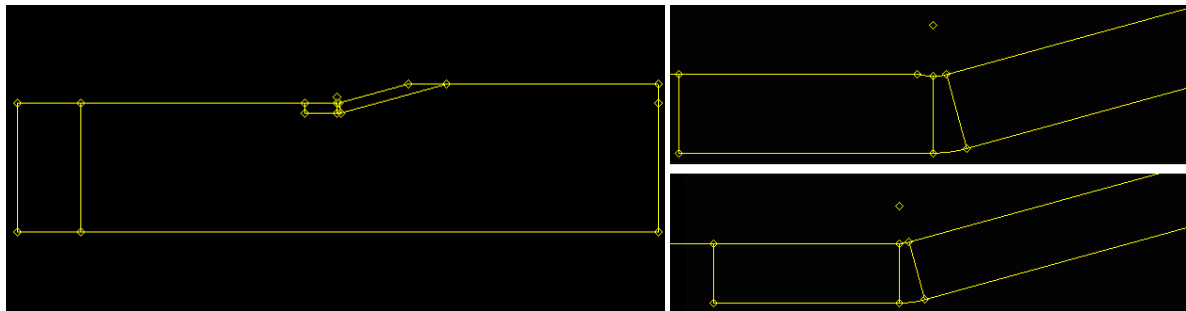


figure J.1 Left: overview of the contour lines and meshing aid lines of the model. Right: detail of weld toe with undercut (top) and without undercut (bottom)

In between the meshing aid lines (as seen in the details in figure J.1) and in the left rectangular section to which the load is applied a mapped mesh is used. This results in a mesh similar to the one depicted in figure 8.1. Finally, the Diana commands to construct the mesh of figure J.1 with undercut are show below.

```
FEMGEN Annex_UC
PROPERTY FE-PROG DIANA STRUCT_PE
yes;

UTILITY SETUP UNITS LENGTH MILLIMETER
UTILITY SETUP UNITS MASS KILOGRAM
UTILITY SETUP UNITS FORCE NEWTON
UTILITY SETUP UNITS TIME SECOND
UTILITY SETUP UNITS TEMPERATURE CELSIUS
CONSTRUCT SPACE TOLERANCE ABSOLUTE 0.0005
MESHING DIVISION DEFAULT 2

!define basic weld shape
GEOMETRY POINT P1 0 0 0
GEOMETRY POINT P2 100 0 0
GEOMETRY LINE STRAIGHT L1 P1 P2
GEOMETRY POINT P3 0 25 0
GEOMETRY LINE STRAIGHT L2 P1 P3
GEOMETRY POINT P4 50 25 0
GEOMETRY LINE STRAIGHT L3 P3 P4
GEOMETRY POINT P5 100 25 0
GEOMETRY POINT H 100 28 0
GEOMETRY LINE STRAIGHT L4 P2 P5
```

GEOMETRY LINE STRAIGHT L5 P5 H

GEOMETRY LINE ANGLE CL6 L5 90 H XY 100
 GEOMETRY LINE ANGLE CL7 L3 15.3 P4 XY 40
 GEOMETRY POINT INTERSECT P8 CL6 CL7
 UTILITY DELETE LINES CL6 CL7
 YES ;
 GEOMETRY LINE STRAIGHT L6 H P8
 GEOMETRY LINE STRAIGHT L7 P4 P8

!define weld root notch
 GEOMETRY LINE PARALLEL CL1 L7 P6 2
 GEOMETRY POINT INTERSECT CP1 CL1 L3
 GEOMETRY LINE ANGLE CL2 CL1 0 CP1 xy 7.20043217846358
 GEOMETRY LINE CIRCLE P11 2
 GEOMETRY LINE PERPENDIC CL3 L7 P11 P15 10
 GEOMETRY POINT INTERSECT P20 CL3 L11
 UTILITY DELETE LINES L7
 YES ;

GEOMETRY POINT INTERSECT P21 L3 L10
 GEOMETRY LINE STRAIGHT L12 P20 P8
 GEOMETRY LINE STRAIGHT L13 P3 P21
 GEOMETRY LINE ARC L14 P21 P15 P11
 GEOMETRY LINE ARC L15 P15 P20 P11
 UTILITY DELETE LINES CL3 CL1 L9 L8 CL2 L3 L10 L11
 YES ;
 UTILITY DELETE POINTS P16 P13 P9 P10 P6 P7 CP1 P14 P12 P4
 YES ;

!renaming in orderly fashion
 UTILITY NAME L13 L3
 UTILITY NAME L4 L9
 UTILITY NAME L5 L8
 UTILITY NAME L6 L7
 UTILITY NAME L12 L6
 UTILITY NAME L15 L5
 UTILITY NAME L14 L4
 UTILITY NAME P2 P9
 UTILITY NAME P3 P2
 UTILITY NAME P21 P3
 UTILITY NAME P15 P4
 UTILITY NAME P8 P6
 UTILITY NAME P5 P8
 UTILITY NAME P20 P5
 UTILITY NAME H P7
 UTILITY NAME P11 PCENTER

!create meshing aid lines
 GEOMETRY LINE CIRCLE PCENTER 5
 GEOMETRY LINE PERPENDIC CL1 L6 PCENTER P20 20
 GEOMETRY POINT INTERSECT P12 CL1 L19
 UTILITY NAME P20 P11
 UTILITY DELETE LINES L16 L17 L18 L19
 YES
 GEOMETRY LINE ARC L11 P11 P12 PCENTER
 GEOMETRY LINE ANGLE CL2 L6 0 P12 XY 40
 GEOMETRY POINT INTERSECT P13 CL2 L7
 UTILITY DELETE LINES CL1 CL2
 YES
 UTILITY DELETE POINTS P17 P18 P19 P21 P22
 YES

GEOMETRY LINE STRAIGHT L12 P12 P13
 GEOMETRY LINE ANGLE L10 L1 180 P11 XY 10
 GEOMETRY LINE PERPENDIC CL1 L10 P23 PCENTER 10
 GEOMETRY POINT INTERSECT P10 L3 CL1
 UTILITY DELETE LINES CL1
 YES
 GEOMETRY LINE STRAIGHT L13 P23 P10
 UTILITY DELETE POINTS P24
 YES
 GEOMETRY LINE STRAIGHT L14 P4 P11
 GEOMETRY LINE STRAIGHT I15 P5 P12
 UTILITY DELETE LINES L3 L7
 YES
 GEOMETRY LINE STRAIGHT L3 P2 P10
 GEOMETRY LINE STRAIGHT L7 P13 P7
 GEOMETRY LINE STRAIGHT L16 P10 P3
 GEOMETRY LINE STRAIGHT L17 P6 P13
 UTILITY DELETE LINES L3
 YES
 GEOMETRY POINT P16 10 25 0
 GEOMETRY LINE STRAIGHT L20 P2 P16
 GEOMETRY LINE STRAIGHT L3 P16 P10
 GEOMETRY POINT P17 10 0 0
 UTILITY DELETE LINES L1
 YES
 GEOMETRY LINE STRAIGHT L1 P17 P9
 GEOMETRY LINE STRAIGHT L18 P1 P17
 GEOMETRY LINE STRAIGHT L19 P17 P16

!create surface

GEOMETRY SURFACE 4SIDES SURF1 L1 +L9 L8 +L7 +L12 +L11 +L10 +L13

 L3 L19
 GEOMETRY SURFACE 4SIDES SURF2 L10 L14 +L4 L16 L13
 GEOMETRY SURFACE 4SIDES SURF3 L11 L15 L5 L14
 GEOMETRY SURFACE 4SIDES SURF4 L12 L17 L6 L15
 GEOMETRY SURFACE 4SIDES SURF5 L18 L19 L20 L2

!boundary conditions

PROPERTY BOUNDARY CONSTRAINT L8 1456
 PROPERTY BOUNDARY CONSTRAINT L9 1456

!loading

PROPERTY LOADS PRESSURE LO1 1 L2 -100 X

!materials

PROPERTY MATERIAL S1100 ELASTIC ISOTROP 210000 0.3
 PROPERTY MATERIAL S890 ELASTIC ISOTROP 210000 0.3
 PROPERTY MATERIAL S690 ELASTIC ISOTROP 210000 0.3
 PROPERTY MATERIAL S460 ELASTIC ISOTROP 210000 0.3
 PROPERTY ATTACH ALL MATERIAL S1100

!properties

PROPERTY PHYSICAL TH1 GEOMETRY THINFSHL 1
 PROPERTY ATTACH ALL TH1

!meshing

CONSTRUCT SET SURFS APPEND SURFACES ALL
 MESHING TYPES SURF1 CQ16E
 MESHING TYPES SURF2 CQ16E
 MESHING TYPES SURF3 CQ16E
 MESHING TYPES SURF4 CQ16E
 MESHING TYPES SURF5 CQ16E

MESHING DIVISION LINE L1 90
MESHING DIVISION LINE L2 40
MESHING DIVISION LINE L3 -998
MESHING DIVISION LINE L4 10
MESHING DIVISION LINE L5 8
MESHING DIVISION LINE L6 660
MESHING DIVISION LINE L7 660
MESHING DIVISION LINE L8 10
MESHING DIVISION LINE L9 40
MESHING DIVISION LINE L10 248
MESHING DIVISION LINE L11 8
MESHING DIVISION LINE L12 660
MESHING DIVISION LINE L13 30
MESHING DIVISION LINE L14 530
MESHING DIVISION LINE L15 530
MESHING DIVISION LINE L16 -538
MESHING DIVISION LINE L17 30
MESHING DIVISION LINE L18 10
MESHING DIVISION LINE L19 40
MESHING DIVISION LINE L20 10
MESHING OPTIONS ALGORITHM PAVING SURF1
MESHING OPTIONS ALGORITHM MAPPED SURF2
MESHING OPTIONS ALGORITHM MAPPED SURF3
MESHING OPTIONS ALGORITHM MAPPED SURF4
MESHING OPTIONS ALGORITHM MAPPED SURF5
MESHING GENERATE ALL

EYE FRAME